TESIS DE LA UNIVERSIDAD DE ZARAGOZA

2023

98

Ignacio Gimeno Alonso

Quantum circuits based on artificial magnetic molecules

Director/es
Luis Vitalla, Fernando

ISSN 2254-7606

Prensas de la Universidad
Universidad Zaragoza

ISSN 2254-7606

Universidad Zaragoza
1542

Tesis Doctoral

QUANTUM CIRCUITS BASED ON ARTIFICIAL MAGNETIC MOLECULES

Autor

Ignacio Gimeno Alonso

Director/es

Luis Vitalla, Fernando

UNIVERSIDAD DE ZARAGOZA
Escuela de Doctorado

Programa de Doctorado en Física

2023

Universidad Zaragoza
1542

Tesis Doctoral

QUANTUM CIRCUITS BASED ON ARTIFICIAL MAGNETIC MOLECULES

Autor

Ignacio Gimeno Alonso

Director/es

Luis Vitalla, Fernando María

UNIVERSIDAD DE ZARAGOZA
Escuela de Doctorado

Programa de Doctorado en Física
2022

Contents

Agradecimientos

Me gustaría expresar mi agradecimiento en primer lugar a mi director, Dr. Fernando Luis Vitalla, por su apoyo y guía durante el desarrollo de esta tesis. Ha compartido su conocimiento conmigo, y siempre me ha dado consejo cuando lo he necesitado durante todo este tiempo.

En segundo lugar me gustaría agradecer a mis compañeros de Q-MAD y del Departamento de Física de la Materia Condensada por hacerme pasar buenos ratos durante el café y en el laboratorio, haciendo el trabajo mucho más ameno.

Tampoco me puedo olvidar de mi familia y amigos. Sobre todo a Ainara, que me ha aguantado durante un confinamiento y me ha animado a seguir adelante incluso en los momentos más difíciles.

Por último, quiero agradecer la financiación de esta tesis, llevada a cabo por el Proyecto RTI2018-096075-B-C21 financiado por MCIN/ AEI /10.13039/501100011033/ y por FEDER Una manera de hacer Europa. Porque comer es importante.

Resumen

Desde comienzos del siglo XXI se ha investigado en el desarrollo de distintos tipos de bits cuánticos, también conocidos como qubits. Por un lado, se ha trabajado en la fabricación de qubits basados en circuitos cuánticos superconductores. Estos sistemas, en los cuales un circuito superconductor se acopla a un resonador coplanar mediante un campo eléctrico o magnético de microondas, presentan una capacidad de cableado elevada al trabajar con circuitos eléctricos, mientras que el escalado a sistemas con un número cada vez mayor de qubits es complicado debido a las pequeñas diferencias entre qubits producidas durante su fabricación. Gracias a su fácil cableado, los ordenadores cuánticos más desarrollados hasta la fecha emplean distintas variantes de estos tipos de qubits, destacando los de IBM y Google, que emplean un tipo de qubit de carga conocido como transmón.

Un segundo tipo de qubit que también muestra características muy prometedoras consiste en emplear sistemas microscópicos, como por ejemplo espines alojados en cristales moleculares. Estos qubits presentan ciertas ventajas frente a los qubits superconductores, como un elevado grado de reproducibilidad (al ser sistemas moleculares dos qubits pueden ser idénticos) que otorga un gran potencial de escalado a esta tecnología. Sin embargo, la comunicación entre qubits se complica respecto a los qubits superconductores.

Un tercer tipo de sistemas, los cuales se han estudiado en esta tesis, consisten en la combinación de las dos clases de qubits anteriores. En estos sistemas híbridos, la información estaría codificada en el estado de espín de las moléculas, mientras que su manipulación y la comunicación entre moléculas se realizaría mediante el empleo de circuitos superconductores (resonadores y líneas de transmisión). Mediante la explotación de lo mejor de ambos tipos de qubits, superconductores y moleculares, podríamos conseguir sistemas fácilmente escalables y con un elevado grado de diseño gracias a las posibilidades que se abren al emplear moléculas para codificar la información.

En esta tesis se han pretendido optimizar dos parámetros críticos a la hora de fabricar un futuro ordenador cuántico basado en la combinación de moléculas magnéticas y circuitos superconductores: el acoplo entre los espines moleculares y los circuitos superconductores; y la coherencia de las moléculas magnéticas (el tiempo que dura un estado del espín antes de sufrir cambios debido a su entorno). Para que una molécula magnética sea una buena candidata a qubit, debe cumplir que su acoplo a los circuitos superconductores, equivalente a la velocidad a la que se podría leer y modificar su estado de espín, sea mayor que su tiempo de coherencia. Existen dos vías para conseguir este objetivo: mejorar la integración de las moléculas en los dispositivos superconductores, y buscar sistemas moleculares con tiempos de coherencia suficientemente elevados. En el trabajo aquí presentado se exploran ambas vías, comprobando a la vez si las distintas moléculas empleadas cumplen el resto de condiciones necesarias para poder codificar un qubit (existencia de al menos dos niveles de energía entre los cuales se puedan realizar transiciones, anarmonicidad del espectro). Este trabajo está dividido fundamentalmente en tres partes.

Aumento del campo magnético de microondas generado por los circuitos cuánticos superconductores

En esta parte de la tesis se buscan formas de aumentar el campo magnético de microondas generado por los resonadores superconductores. Para ello se muestran dos técnicas complementarias. En primer lugar, se estudia el efecto de la fabricación de una nanoconstricción mediante haz localizado de iones (FIB) en el centro de un resonador coplanar superconductor (capítulo 4). Al confinar la corriente que pasa por el resonador en una región muy pequeña, se espera que el campo magnético de microondas, y con ello el acoplo, aumente considerablemente. Se presenta un estudio del acoplo colectivo espín-fotón alcanzado con este circuito en función de distintos parámetros como la anchura de la nanoconstricción (que se reduce hasta los 50 nm), la temperatura del sistema o la cantidad de espines depositados en el circuito.

En segundo lugar, se introduce un nuevo diseño de resonador, resultado de combinar las cavidades 3D con los resonadores coplanares superconductores (sección 4.8). Este resonador, diseñado por el equipo de Andreas Angerer de la Universidad Técnica de Viena, presenta un diseño en el cual la inductancia se reduce considerablemente respecto a los resonadores coplanares. En principio, esto debería aumentar el campo magnético local generado por el resonador respecto a los coplanares, algo que se comprueba en esta sección. Por último, se combina este resonador con las nanoconstricciones introducidas anteriormente, en un intento de aumentar al máximo el acoploindividual espín-fotón.

Empleo de moléculas magnéticas con tiempos de coherencia elevados

La segunda parte de la tesis (capítulo 5) introduce un estudio del acoplo entre moléculas del radical libre PTM_r, que presenta tiempos de coherencia elevados incluso a temperatura ambiente, y resonadores de parámetros concentrados (LERs). Estos circuitos consisten en un condensador en paralelo con un inductor, lo que permite manipular los valores de capacidad e inductancia por separado. Con ello, es posible aumentar el campo magnético de microondas generado mientras se controla la frecuencia de resonancia. Esto, combinado con la elevada coherencia que se espera de las moléculas de PTM_r, podría permitir alcanzar el régimen de acoplo fuerte a una molécula sin necesidad de conseguir acoplos excesivamente elevados. En este capítulo se muestra un estudio del acoplo y la decoherencia de las muestras en función de la cantidad de espines acoplados, así como de la temperatura. También se comprueba si la intensidad del campo magnético de microondas generado por los resonadores varía considerablemente con la inductancia y con la forma de acoplar los resonadores a la línea de transmisión que los alimenta (inductiva o capacitivamente).

En esta parte también se estudia la mejora del acoplo espín-fotón al reducir el inductor de estos resonadores a un único hilo corto, a la vez que se les fabrica una nanoconstricción en ella. Se comprueba la diferencia entre el acoplo alcanzado con los resonadores con baja inductancia sin constricción y con una constricción de anchura 50 nm fabricada en el inductor, estudiando si es posible alcanzar un acoplo coherente con estos sistemas.

Acoplo de transiciones de reloj a circuitos cuánticos

En esta última parte se realiza una caracterización física de dos moléculas que presentan transiciones de reloj de espín: HoW_{10} y 1^{VO} (capítulo 6). En estas transiciones los sistemas se encuentran más aislados de su entorno, siendo posible aumentar su coherencia enormemente frente a otras transiciones de espín. Para realizar este estudio se muestran medidas de susceptibilidad magnética, calor específico, resonancia paramagnética electrónica (EPR) y espectroscopía de banda ancha.

En la caracterización del HoW_{10}, que debe presentar un acoplo elevado debido a su alto valor de espín electrónico $J = 8$, se realiza en primer lugar un estudio de sus niveles de energía en función del campo magnético aplicado. Con esta información, se comprueba la evolución del acoplo espín-fotón con el campo magnético y la temperatura, observando si se produce un aumento del acoplo en las transiciones de reloj debido al solapamiento máximo entre las funciones de onda involucradas. Por último, se discute la idoneidad de este sistema a la hora de codificar un qubit de espín según su diagrama de energías y el comportamiento de sus transiciones de reloj.

Respecto al 1^{VO}, se estudia su posible uso como qudit de 16 niveles, para lo cual se comprueba el comportamiento de los niveles de energía presentes en la molécula. Para que el sistema sea un buen candidato se deben cumplir dos condiciones: su diagrama de energías debe ser anarmónico, y se deben poder realizar operaciones universales, es decir, generar cualquier estado final a partir de cualquier estado inicial mediante una secuencia de pulsos electromagnéticos. Mediante medidas de espectroscopía de banda ancha, EPR y simulaciones numéricas, se comprueba el cumplimiento de ambas condiciones en función del campo magnético aplicado, discutiendo formas de aumentar la regíon de campo en la cual el sistema sea idóneo para codificar un qudit. Por último, se muestra un estudio del acoplo a LERs de las distintas transiciones de reloj que aparecen en la molécula 1^{VO} en la región de bajo campo. Se muestran los resultados de las medidas de espectroscopía de banda ancha, con las cuales se ha comparado la evolución del acoplo espín-fotón y la decoherencia en muestras concentradas y diluidas.

1 Introduction

Richard Feynman was the first to propose the idea of applying the laws of quantum physics to perform computational tasks in 1982.[1] David Deutsch then generalised the notion of a Turing machine to the quantum realm, introducing the notion of a universal quantum computer. In this system, the bit (the classical unit of information) is replaced by the quantum bit or qubit. The quantum superposition principle allows the qubit to be in any superposition state $a|0\rangle + b|1\rangle$, instead of being in just one of the two states 0 or 1 as a classical bit. This "quantum parallelism" is the key property of a quantum computer, which provides access to an exponentially larger set of states to process information. It makes it possible to simulate quantum systems that classical computers cannot afford due to their size. It could also solve new tasks, as creating true random numbers,[2] and improve others such as the database searching,[3] and prime number factorisation.[4]

There are four main conditions that need to be fulfilled when a quantum computer wants to be fabricated. These conditions are the following:

- Find suitable quantum systems, equivalent to a quantum two level system, to encode the qubits. Many physical systems, such as nuclear and molecular spins,[5;6] NV centers in diamond,[7] or photons in cavities,[8] satisfy this condition. Artificial systems with this property can be also fabricated. Some examples are the superconducting quantum circuits,[9] or semiconducting quantum dots.[10]
- The qubits of a quantum processor must be addressable, *i.e.* we should be able to distinguish which of the qubits is performing a given operation.[11] In case of having quantum systems with more than two levels, or qudits, this addressability expands to the operations within the qudit itself.
- Mechanisms to initialize and manipulate individual qubits, as well as to entangle multiple qubits creating quantum logic gates, are needed.[12] Electromagnetic radiation is a natural and efficient method to achieve these requirements, being possible to transfer quantum information between qubits by means of photons.
- A good qubit candidate must show a long enough coherence time to perform multiple operations before the information stored in it is lost due to the interaction with its environment. In general, improving coherence worsens the condition of easily manipulating the qubits, since the more isolated the qubit is from its environment, the more difficult it is to interact with it.

The possibility of using photons to manipulate and read out the qubit states and to communicate remote qubits with each other makes the study of the interaction between the electromagnetic radiation and qubit candidates critical. This field is known as cavity quantum electrodynamics (cavity QED).[13;14] It consists of the study of the interaction between photons confined in a resonant cavity and a quantum system, for example a two level system. For a device like this to be useful for quantum computing, the qubit-photon coupling strength must be higher than the decoherence rates of both the cavity and the qubit. This situation is known as the strong coupling regime, and it is necessary to perform several operations with the qubits before losing the information and to read out the result. Many different cavity QED systems, like Rydberg

atoms or quantum dots, have been studied, reaching the strong coupling regime with some of them.[13;15;16]

In the systems based on cavity QED, the qubit-photon coupling is proportional to the intensity of the microwave electromagnetic field generated by the cavity. A promising way to increase this coupling strength is to reduce the effective mode volume of the microwave field, that increases the electromagnetic energy density and thus the coupling. This volume can be reduced down to the 2D limit by using microwave integrated circuits as cavities. This approach is known as circuit quantum electrodynamics (circuit QED).[17] Some of the most successful qubits, like the charge qubit or the flux qubit, coupled to a superconducting coplanar waveguide resonator through the microwave electric or magnetic field respectively,[18] belong to this field. With these systems, the strong coupling regime and entanglement between different qubits have been achieved.[19;20;21]

Today, microwave resonators form the basis of most architectures based on superconducting qubits, such as those bein developed by IBM and Google among others. Yet, scaling up such schemes to the level required to carry up computations of practical interest (10^8 qubits for the implementation of Shor's factorisation algorithm with quantum error correction) remains challenging. A way to increase the density of qubits in a quantum processor is to make use of microscopic systems. Spins embedded in solid hosts are one of the simplest and most natural choices to realize such qubits.[22;23] Their quantized spin projections can encode the logic qubit states whereas operations between them can be induced via the application of microwave radiation pulses, using well-established magnetic resonance protocols. Some examples of this type of qubit are ensembles of NV centers[24] or magnetic molecules.[25;26;27] NV centers act as $S = 1$ spins, while magnetic molecules show a great variety of electronic and nuclear spin values that can be exploited. In addition, each molecule could act as multiple coupled qubits or, in general, as a d-dimensional qudit, being possible to implement quantum error correction algorithms in a single molecule or even use it as a universal quantum processor.[28;29;30]

This approach faces the challenge of wiring-up different molecules into a scalable architecture. A promising technology is to use microwave photons, trapped in on-chip superconducting resonators to mediate molecule-molecule interactions.[20;31;32;33;34] Working with high-spin molecules helps maximizing the spin-photon coupling, as required for such applications.[32] However, it also tends to enhance decoherence, as their interactions with fluctuating hyperfine and dipolar magnetic fields also become stronger.[35;36] Yet, the coupling of a single molecule to superconducting circuits is far too weak.

A "cheap" way to avoid this problem is to work with a crystal of perfectly aligned molecules. This gives rise to a collective enhancement of the coupling to photons proportional to $\sqrt{N}$. This allows crystals formed by these molecules to act as quantum memories.[37;38;39] Molecular crystals with more than two energy levels can also act as proof of concept representations of qudit codes that exploit the Hilbert space defined by each molecule spin states.

If the strong coupling regime between superconducting circuits and individual molecules were achieved, it would be possible to design a quantum processor that combines both systems like the one shown in Fig. 1.1 Here, each individual molecule would be placed at nanoconstrictions of coplanar superconducting resonators, where the local magnetic field is maximum. Transmission lines would tune in and out of resonance with the resonator each molecule, allowing the communication between distant qubits. This system would be easily scalable and it would show the attractiveness of embedding quantum error correction algorithms within each individual molecule.

The main goal of this thesis has been to develop and test different and complementary ways of enhancing the single spin-photon coupling and coherence of our systems, trying to achieve the strong coupling regime between magnetic molecules and superconducting circuits. Several

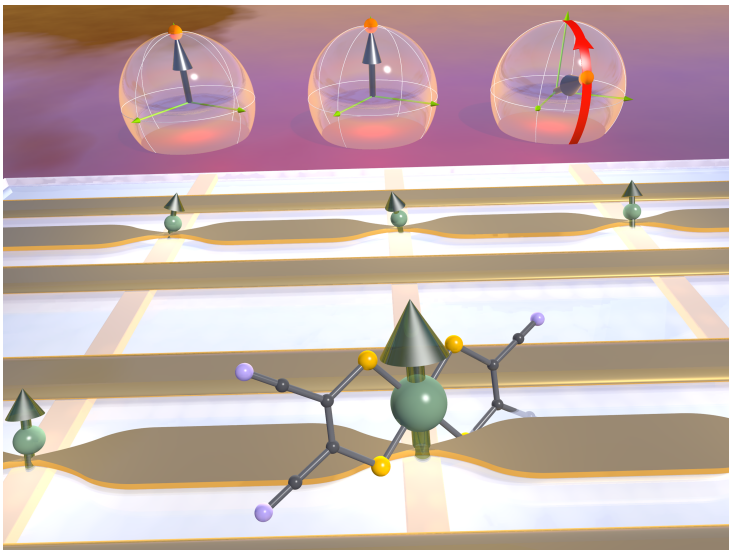

Figure 1.1: Possible architecture for a quantum processor that combines magnetic molecules with superconducting coplanar waveguides and resonators.[33] Each spin could be tuned by local magnetic fields generated by the transmission lines, while the resonators would generate the qubit operations and the entanglement between several qubits, and read out the results

approaches have been studied for optimizing our devices:

- Reduce the size of the inductor line to squeeze the photon magnetic field.
- Optimise the design of the circuits to enhance the local magnetic field.
- Optimise the molecular spin states. Usually, increasing the number of molecules in a sample also increases the dipolar coupling between molecules, and thus the decoherence of the system. A solution to this problem, that could allow us to use concentrated samples with high spin maintaining still high coherence values, is to encode the qubit in superposition states that are formed at level anticrossings. These anticrossings are known as clock transitions.[40;41;42] Here, dipolar decoherence vanishes at first order, showing a remarkable stability against magnetic field fluctuations. Some examples of clock transitions found in molecular materials show that spin coherence times present a sharp increase near each of these transitions.[41;42;43]

This thesis is organised as follows:

- In chapter 2 we introduce the main experimental techniques used during this work.
- In chapter 3 we derive most of the equations used to analyse the results obtained during this thesis. We also show the dependence of the spin-photon coupling on different parameters of the superconducting circuits and the magnetic molecules, which helps finding ways to improve it.
- Chapter 4 is dedicated to the experimental study of the effect of a nanoconstriction fabricated on the central line of superconducting coplanar resonators. We test the evolution of the spin-photon coupling between these circuits and a free radical while changing different parameters, like the nanoconstriction width or temperature. We also introduce a new type of resonator which combines properties of coplanar resonators and 3D cavities.

- In chapter 5 we present the free radical PTM_r, that shows high coherence even at room temperature. We study the coupling between ensembles of this molecules and low-inductance LC resonators, designed to maximize the microwave magnetic field. We finally combine these devices with the nanoconstrictions introduced in chapter 4, testing the enhancement of the spin-photon coupling in these resonators.
- In chapter 6 we perform a complete experimental study of the physical properties of two molecules, HoW_{10} and $\mathbf{1^{VO}}$, that show spin-clock transitions. The effect that the presence of such avoided level crossings has on the spin states and on the spin-photon coupling is characterised. We also test if the molecule $\mathbf{1^{VO}}$ can be used as a $d = 16$ electronuclear spin qudit.
- Finally, chapter 7 is dedicated to summarizing the conclusions obtained in this work.

Bibliography

[1] R. P. Feynman. Simulating physics with computers. *International Journal of Theoretical Physics*, 21:467–488, 1982.

[2] Y. Jian, M. Ren, E. Wu, G. Wu, and H. Zeng. Two-bit quantum random number generator based on photon-number-resolving detection. *Review of Scientific Instruments*, 82:073109, 2011.

[3] L. K. Grover. Quantum Mechanics Helps in Searching for a Needle in a Haystack. *Physical Review Letters*, 79:325–328, 1997.

[4] P. W. Shor. Algorithms for quantum computation: discrete logarithms and factoring. In *Proceedings 35th Annual Symposium on Foundations of Computer Science*, pages 124–134, November 1994.

[5] F. Jelezko, T. Gaebel, I. Popa, M. Domhan, A. Gruber, and J. Wrachtrup. Observation of Coherent Oscillation of a Single Nuclear Spin and Realization of a Two-Qubit Conditional Quantum Gate. *Physical Review Letters*, 93:130501, 2004.

[6] J. R. Friedman, M. P. Sarachik, J. Tejada, and R. Ziolo. Macroscopic measurement of resonant magnetization tunneling in high-spin molecules. *Physical Review Letters*, 76:3830, 1996.

[7] J. R. Weber, W. F. Koehl, J. B. Varley, A. Janotti, B. B. Buckley, C. G. Van de Walle, and D. D. Awschalom. Quantum computing with defects. *Proceedings of the National Academy of Sciences*, 107:8513–8518, 2010.

[8] F. De Martini, V. Buzek, F. Sciarrino, and C. Sias. Experimental realization of the quantum universal NOT gate. *Nature*, 419:815–818, 2002.

[9] A. O. Niskanen, K. Harrabi, F. Yoshihara, Y. Nakamura, S. Lloyd, and J. S. Tsai. Quantum Coherent Tunable Coupling of Superconducting Qubits. *Science*, 316:723–726, 2007.

[10] R. Hanson and D. D. Awschalom. Coherent manipulation of single spins in semiconductors. *Nature*, 453:1043–1049, 2008.

[11] J. M. Gambetta, A. D. Córcoles, S. T. Merkel, B. R. Johnson, J. A. Smolin, J. M. Chow, C. A. Ryan, C. Rigetti, S. Poletto, T. A. Ohki, M. B. Ketchen, and M. Steffen. Characterization of Addressability by Simultaneous Randomized Benchmarking. *Physical Review Letters*, 109:240504, 2012.

[12] E. Knill. Quantum computing. *Nature*, 463:441–443, 2010.

[13] J. M. Raimond, M. Brune, and S. Haroche. Manipulating quantum entanglement with atoms and photons in a cavity. *Reviews of Modern Physics*, 73:565–582, 2001.

[14] H. Walther, B. T. H. Varcoe, B.-G. Englert, and T. Becker. Cavity quantum electrodynamics. *Reports on Progress in Physics*, 69:1325, 2006.

[15] K. Hennessy, A. Badolato, M. Winger, D. Gerace, M. Atatüre, S. Gulde, S. Fält, E. L. Hu, and A. Imamoğlu. Quantum nature of a strongly coupled single quantum dot–cavity system. *Nature*, 445:896–899, 2007.

[16] T. Yoshie, A. Scherer, J. Hendrickson, G. Khitrova, H. M. Gibbs, G. Rupper, C. Ell, O. B. Shchekin, and D. G. Deppe. Vacuum Rabi splitting with a single quantum dot in a photonic crystal nanocavity. *Nature*, 432:200–203, 2004.

[17] A. Blais, R.-S. Huang, A. Wallraff, S. M. Girvin, and R. J. Schoelkopf. Cavity quantum electrodynamics for superconducting electrical circuits: An architecture for quantum computation. *Physical Review A*, 69:062320, 2004.

[18] Y. Makhlin, G. Schön, and A. Shnirman. Quantum-state engineering with Josephson-junction devices. *Reviews of Modern Physics*, 73:357–400, 2001.

[19] A. Wallraff, D. I. Schuster, A. Blais, L. Frunzio, R.-S. Huang, J. Majer, S. Kumar, S. M. Girvin, and R. J. Schoelkopf. Strong coupling of a single photon to a superconducting qubit using circuit quantum electrodynamics. *Nature*, 431:162–167, 2004.

[20] J. Majer, J. M. Chow, J. M. Gambetta, J. Koch, B. R. Johnson, J. A. Schreier, L. Frunzio, D. I. Schuster, A. A. Houck, A. Wallraff, A. Blais, M. H. Devoret, S. M. Girvin, and R. J. Schoelkopf. Coupling superconducting qubits via a cavity bus. *Nature*, 449:443–447, 2007.

[21] L. DiCarlo, M. D. Reed, L. Sun, B. R. Johnson, J. M. Chow, J. M. Gambetta, L. Frunzio, S. M. Girvin, M. H. Devoret, and R. J. Schoelkopf. Preparation and measurement of three-qubit entanglement in a superconducting circuit. *Nature*, 467:574–578, 2010.

[22] S. Bertaina, S. Gambarelli, A. Tkachuk, I. N. Kurkin, B. Malkin, A. Stepanov, and B. Barbara. Rare-earth solid-state qubits. *Nature Nanotechnology*, 2:39–42, 2007.

[23] D. D. Awschalom, L. C. Bassett, A. S. Dzurak, E. L. Hu, and J. R. Petta. Quantum Spintronics: Engineering and Manipulating Atom-Like Spins in Semiconductors. *Science*, 339:1174–1179, 2013.

[24] Y. Kubo, F. R. Ong, P. Bertet, D. Vion, V. Jacques, D. Zheng, A. Dréau, J.-F. Roch, A. Auffeves, F. Jelezko, J. Wrachtrup, M. F. Barthe, P. Bergonzo, and D. Esteve. Strong Coupling of a Spin Ensemble to a Superconducting Resonator. *Physical Review Letters*, 105:140502, 2010.

[25] T. D. Ladd, F. Jelezko, R. Laflamme, Y. Nakamura, C. Monroe, and J. L. O'Brien. Quantum computers. *Nature*, 464:45–53, 2010.

[26] A. Gaita-Ariño, F. Luis, S. Hill, and E. Coronado. Molecular spins for quantum computation. *Nature Chemistry*, 11:301–309, 2019.

[27] M. Atzori and R. Sessoli. The Second Quantum Revolution: Role and Challenges of Molecular Chemistry. *Journal of the American Chemical Society*, 141:11339–11352, 2019.

[28] A. Chiesa, E. Macaluso, F. Petiziol, S. Wimberger, P. Santini, and S. Carretta. Molecular Nanomagnets as Qubits with Embedded Quantum-Error Correction. *The Journal of Physical Chemistry Letters*, 11:8610–8615, 2020.

[29] F. Luis, P. J. Alonso, O. Roubeau, V. Velasco, D. Zueco, D. Aguilà, J. I. Martínez, L. A. Barrios, and G. Aromí. A dissymmetric [Gd_2] coordination molecular dimer hosting six addressable spin qubits. *Communications Chemistry*, 11:176, 2020.

[30] A. Chiesa, F. Petiziol, E. Macaluso, S. Wimberger, P. Santini, and S. Carretta. Embedded quantum-error correction and controlled-phase gate for molecular spin qubits. *AIP Advances*, 11:025134, 2021.

[31] R. J. Schoelkopf and S. M. Girvin. Wiring up quantum systems. *Nature*, 451:664–669, 2008.

[32] M. D. Jenkins, T. Hümmer, M. J. Martínez-Pérez, J. J. García-Ripoll, D. Zueco, and F. Luis. Coupling single-molecule magnets to quantum circuits. *New Journal of Physics*, 15:095007, 2013.

[33] M. D. Jenkins, D. Zueco, O. Roubeau, G. Aromi, J. Majer, and F. Luis. A scalable architecture for quantum computation with molecular nanomagnets. *Dalton Transactions*, 45:16682–16693, 2016.

[34] C. Bonizzoni, A. Ghirri, and M. Affronte. Coherent coupling of molecular spins with microwave photons in planar superconducting resonators. *Advances in Physics: X*, 3:1435305, 2018.

[35] A. Morello, P. C. E. Stamp, and I. S. Tupitsyn. Pairwise Decoherence in Coupled Spin Qubit Networks. *Physical Review Letters*, 97:207206, 2006.

[36] L. Escalera-Moreno, A. Gaita-Ariño, and E. Coronado. Decoherence from dipolar interspin interactions in molecular spin qubits. *Physical Review B*, 100:064405, 2019.

[37] A. Imamoğlu. Cavity QED Based on Collective Magnetic Dipole Coupling: Spin Ensembles as Hybrid Two-Level Systems. *Physical Review Letters*, 102:083602, 2009.

[38] J. H. Wesenberg, A. Ardavan, G. A. D. Briggs, J. J. L. Morton, R. J. Schoelkopf, D. I. Schuster, and K. Mølmer. Quantum Computing with an Electron Spin Ensemble. *Physical Review Letters*, 103:070502, 2009.

[39] D. Marcos, M. Wubs, J. M. Taylor, R. Aguado, M. D. Lukin, and A. S. Sørensen. Coupling Nitrogen-Vacancy Centers in Diamond to Superconducting Flux Qubits. *Physical Review Letters*, 105:210501, 2010.

[40] G. Wolfowicz, A. M. Tyryshkin, R. E. George, H. Riemann, N. V. Abrosimov, P. Becker, H.-J. Pohl, M. L. Thewalt, S. A. Lyon, and J. J. L. Morton. Atomic clock transitions in silicon-based spin qubits. *Nature Nanotechnology*, 8:561–564, 2013.

[41] M. Shiddiq, D. Komijani, Y. Duan, A. Gaita-Ariño, E. Coronado, and S. Hill. Enhancing coherence in molecular spin qubits via atomic clock transitions. *Nature*, 531:348–351, 2016.

[42] J. M. Zadrozny, A. T. Gallagher, and D. E. Harris, T. D. amd Freedman. A Porous Array of Clock Qubits. *Journal of the American Chemical Society*, 139:7089–7094, 2017.

[43] C. A. Collett, K.-I. Ellers, N. Russo, K. R. Kittilstved, G. A. Timco, R. E. P. Winpenny, and J. R. Friedman. A Clock Transition in the Cr_7Mn Molecular Nanomagnet. *Magnetochemistry*, 5:4, 2019.

2

Experimental Techniques

2.1 Introduction

In this chapter we introduce the main equipment and experimental techniques that have been used during this thesis work. As explained in the previous introductory chapter, we deal with the problem of optimising the coupling of molecular spins to superconducting circuits. The techniques used cover all aspects required to properly characterise each of these systems and to explore their interaction in different situations. They can be divided in several categories:

- Basic physical characterization of molecular spins
- Circuit fabrication and characterization techniques
- Deposition of molecular samples at the nanoscale
- Characterization of superconducting circuits
- Low and very low temperature equipment

2.2 Basic physical characterization of molecular spins

2.2.1 Physical Properties Measurement System: heat capacity and micro-Hall magnetometry

The Physical Properties Measurement System (PPMS) by Quantum Design is a versatile system that allows the measurement of different physical properties of a sample such as thermal and electrical conductivity, magnetization, magnetic susceptibility and heat capacity, while varying temperature, magnetic field and pressure. The two models that have been used, PPMS-9T and PPMS-14T (see Fig. 2.1), are available at the Physical Measurements Service of the University of Zaragoza.[1]

The device consists of a liquid helium dewar where a probe containing the sample is inserted. Using a ^{3}He cryostat inserted in the probe and an oven, it can work over a temperature range from 350 mK to 1100 K. A superconducting magnet cooled by the liquid helium in the dewar can apply a maximum field of 9 T or 14 T depending on the model.

(a) (b)

Figure 2.1: (a) PPMS-9T at the Servicio de Medidas Físicas. (b) PPMS probe where the puck is connected. This probe is then inserted in the PPMS.

Heat capacity measurements

When measuring heat capacity, the sample is placed on a calorimeter consisting of a sapphire sample holder, a heater and a thermometer. This experimental puck is shown in Fig. 2.2. It is thermally anchored to the PPMS probe shown in Fig. 2.1. The calorimeter itselfs is only coupled to the metal frame by the thin metal wires that carry the currents to the thermometer and the heater. This weak thermal link allows introducing thermal gradients with respect to the bath, which are at the basis of the measuring method. The whole system is introduced in the ^{3}He bath, which can cool it down to about 350 mK.

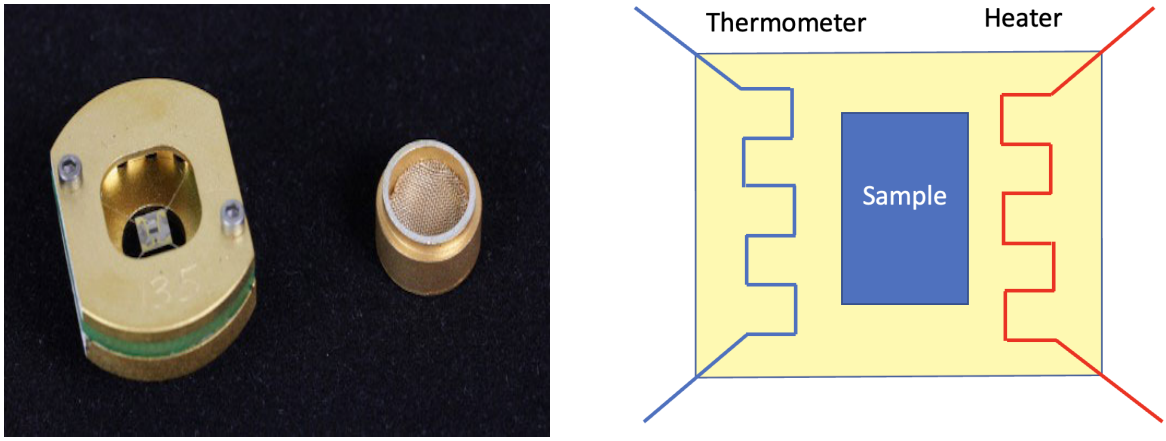

(a) (b)

Figure 2.2: (a) Photo of the calorimeters used in the PPMS and (b) its schematic representation.

The PPMS allows us to measure the heat capacity at constant pressure of a sample using a method which exploits the thermal relaxation of the sample and calorimeter ensemble.[2] A square heat power pulse is applied to the calorimeter during a controlled period of time. Its amplitude is kept low enough to ensure that the increase in the calorimeter temperature is less

than a 5% of the He bath temperature in order to avoid non-linear effects. When the input power is removed, the temperature of the sample decays back to the bath temperature. As shown by the scheme in Fig. 2.3, the system is a thermal equivalent of a RC circuit, with the heat capacity playing the role of the capacitor, the thermal resistance of the wires that of the electrical resistance. Using this equivalence, the temperature difference with the bath follows the same response as the voltage of the electric circuit subject to a current pulse with amplitude P. The evolution of the temperature while heating and cooling the calorimeter then follows the relation

$$T(t) - T_B = \frac{P}{K}\left(1 - e^{-tK/C}\right) \tag{2.1}$$

where T_B is the temperature of the bath, P is the heat power applied to the system, K is the thermal conductivity of the wires and C is the heat capacity of the sample and the calorimeter.

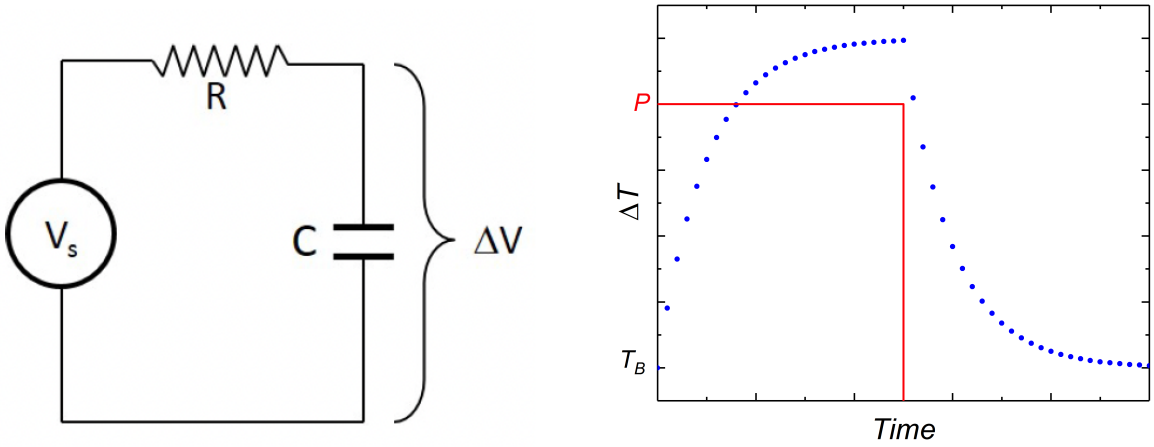

Figure 2.3: (a) Equivalent RC circuit of a calorimeter operating with the relaxation method. The voltage difference ΔV is equivalent to the temperature variation ΔT generated when a square power pulse P is applied.(b) Example of the temperature evolution of the system during a typical C_p measurement, following the application and remove of a thermal power pulse P.

This technique presents a higher sensitivity than others thanks to the fact that it measures a decay time constant τ. This also allows us to study spin relaxation changing the measurement time, as can be shown in Fig. 2.4. Here, two measurements of a vanadyl crystal were done using different measuring times, obtaining the full spin signal with the longer time and telling us that the relaxation time T_1 of this sample was longer than 0.1 s at low temperatures.

The samples measured with this system were molecular crystals with at least one flat face. They were attached to the sample holder using Apiezon N grease, which provides a good thermal contact and whose contribution to the heat capacity of the system was previously calibrated.

Micro-Hall magnetometry

Regarding the micro-Hall magnetometry technique, the sample is placed on a magnetometer made by two layers of GaAs and AlGaAs, between which the electrons are confined and a bidimensional electron gas is formed.[3] These semiconductors have a low charge carriers density, which increases the Hall coefficient and the measured signal, while the mobility of these charge carriers is very high, reducing the resistivity of the system and improving the sensitivity.

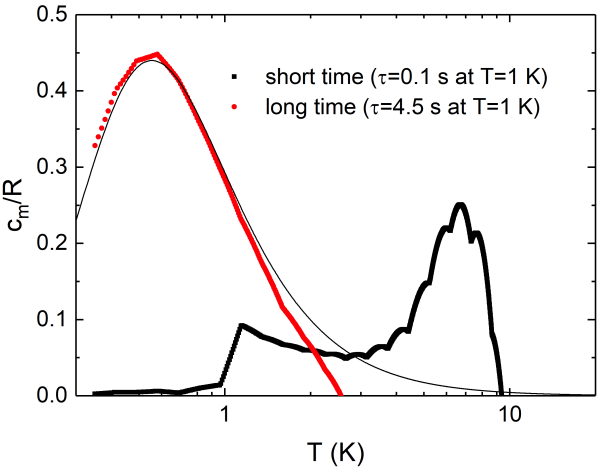

Figure 2.4: Comparison between two specific heat curves of a vanadyl crystal obtained for an applied magnetic field of 1 T. The curve that follows the theoretical dependence is the one measured with a longer measuring time.

This magnetometry technique is based on the Hall effect.[4] When an electric current flows in the presence of a magnetic field oriented perpendicular to its propagation direction, a voltage is formed, perpendicular to both (see scheme in Fig. 2.5), associated with the Lorentz force exerted by the magnetic field on the electrons. The device has several terminals. Two of them are used to introduce the current, whereas the other are used to measure voltage. When no sample is placed on any of these "crosses", the Hall voltage is then approximately the same in all of them. When a magnetic sample is placed near one of them (Fig. 2.5(b)), its magnetization generates a local magnetic field. The net voltage difference between two crosses is then proportional to the induced magnetization of the sample placed on the sheet. A scheme of this process and a photo of the magnetometer are shown in Fig. 2.5.

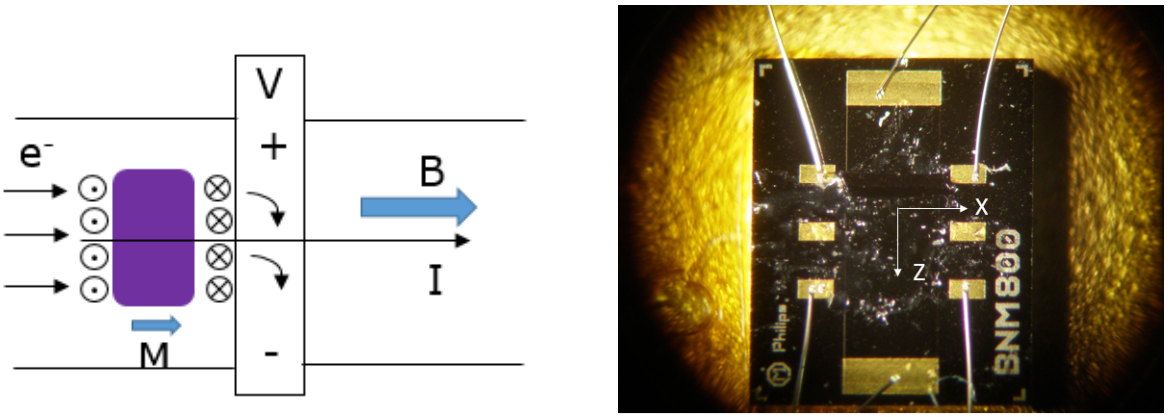

(a) **(b)**

Figure 2.5: Scheme (a) and photo (b) of the micro-Hall magnetometer

With this technique we have measured the magnetization of different samples as a function of magnetic field and time. When measuring the time-dependent magnetization, the applied field is suddenly changed from one fixed value to another, while the voltage difference is measured. An exponential fit of the voltage decay with time gives us information about the spin-lattice relaxation time T_1. Regarding the field-dependent magnetization measurements, the voltage is measured while the magnetic field is swept at a constant rate. Both types of measurements

provide information about the spin-lattice relaxation processes in a sample. An example of a time-dependent magnetization measurement performed during this thesis is shown in Fig. 2.6.

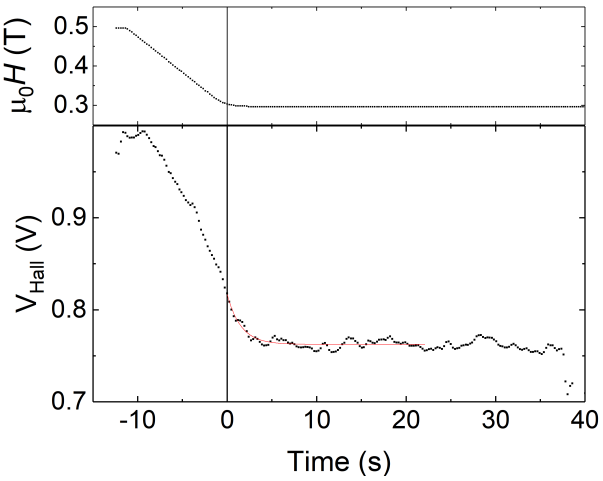

Figure 2.6: Time-dependent magnetization of a single crystal of vanadyl porphyrin molecules ($S = 1/2$), measured at 0.4 K after the application of a magnetic field of 0.3 T has been applied. Fitting the exponential decay of the magnetization, T_1 can be obtained.

2.2.2 MPMS: SQUID magnetometry

The Magnetic Properties Measurement System (MPMS) is another commercial system by Quantum Design specifically prepared for performing magnetic measurements like DC magnetization and AC susceptibility. Like the PPMS, the model we used in this thesis work (MPMS-XL, see Fig. 2.7) is available at the Physical Measurements Service of the University of Zaragoza.[1] It works inside a He^4 cryostat which allows controlling temperatures from 1.8 K to 400 K. A superconducting magnet can apply static magnetic fields up to 5 T. This system also includes an additional coil that enables applying AC magnetic fields with amplitude up to 4 Oe and frequencies from 0.1 Hz to 1.4 kHz to measure the linear AC magnetic susceptibility of the sample.

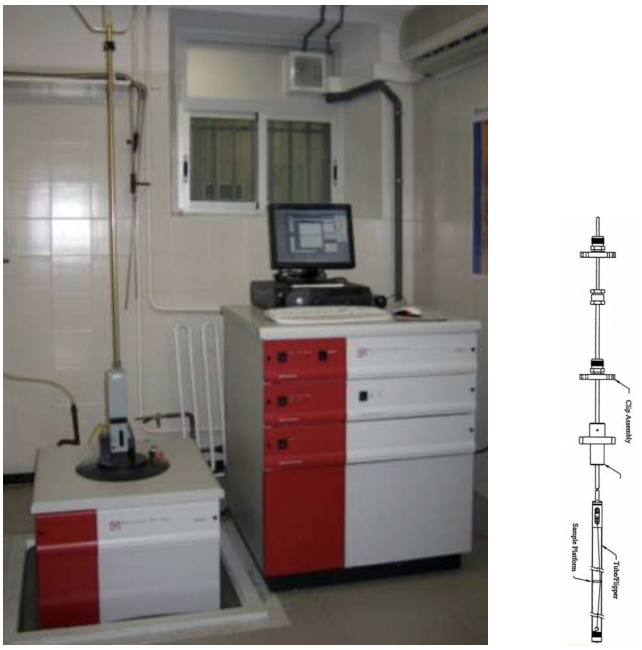

(a) **(b)**

Figure 2.7: (a) MPMS-XL at the Servicio de Medidas Físicas. (b) MPMS probe where the sample is introduced.

The main component of the MPMS is the Superconducting Quantum Interference Device (SQUID) magnetometer. SQUIDs are very sensitive flux-to-voltage converters, so they can work as low noise current amplifiers.[5;6] As can be shown in Fig. 2.8, this SQUID amplifier is connected to a NbTi second order superconducting gradiometer, made of four coils placed one above the other with the two central coils in the opposite direction to the external coils. This geometry suppresses any contribution to the signal from static external magnetic fields. The sample is inserted into a thin rod which is introduced inside the gradiometer and can travel through all its length (3 cm).

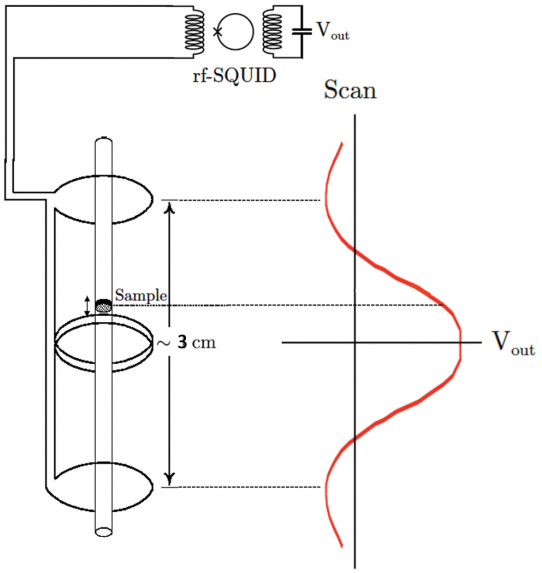

Figure 2.8: Scheme of the superconducting gradiometer coupled to the SQUID. The signal is maximum when the sample is placed in the centre of the coils.

There are two ways of measuring with the MPMS. For DC measurements (DC susceptibility and magnetization), temperature and magnetic field are fixed, and the system measures the output voltage of the SQUID as a function of the sample position in the gradiometer. The induced magnetization of the sample produces a change of the magnetic flux across the coils when moving the sample through them, being this change proportional to the sample magnetization. This technique has a sensitivity of 1×10^{-7} emu, which can be improved to 5×10^{-9} by using the RSO option that introduces an oscillation of the sample position and a lock-in detection of the voltage induced in the circuit.

For AC measurements (AC susceptibility), a low amplitude ($h_0 \lesssim 4$ Oe) AC magnetic field is applied, and an AC voltage is measured. Comparing input and output signals, it is possible to obtain the real and imaginary components of the magnetic susceptibility with a sensitivity of 10^{-8} emu.

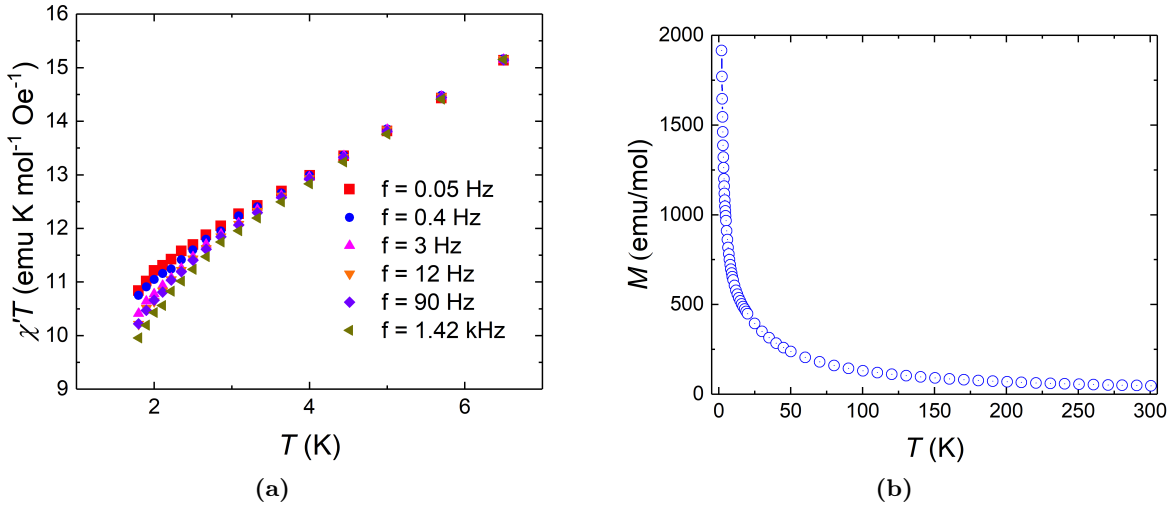

Figure 2.9: (a) AC susceptibility and (b) DC magnetization of a HoW_{10} sample.

During this thesis we have used the MPMS for measuring the AC susceptibility and DC magnetization of HoW_{10} and (VO)-porphyrin crystals, obtaining some graphs like the ones shown in Fig. 2.9. These experiments give us information about the magnetic moment and its distribution, as well as the spin lattice relaxation time scales. These measurements also allow calibrating the measurements performed with the micro-Hall sensors.

2.2.3 Electron Paramagnetic Resonance

Electron paramagnetic resonance (EPR) is a form of spectroscopy in which an oscillating magnetic field induces transitions between the different energy levels of a spin system.[7] This technique is restricted to substances with at least one unpaired electron. It is very similar to nuclear magnetic resonance (NMR), with the difference that the spins excited in EPR are those of the unpaired electrons instead of those from atomic nuclei. EPR can be useful for studying metal and organic samples with electronic transitions in the microwave frequency range (1 GHz to 100 GHz).

A typical EPR setup consists of a resonant cavity, a microwave source and an electromagnet. The paramagnetic sample is placed inside the cavity, which is continuously irradiated by the microwave source with a fixed frequency signal. At the same time, an external DC magnetic field, usually perpendicular to the cavity microwave field, is applied by the electromagnet. This external magnetic field produces the splitting of the energy levels of the sample through the Zeeman effect. When the level splitting and the energy associated to the microwave field are

tuned, the sample absorbs part of the input signal, being this absorption visible in the output signal. The position and number of the absorption lines, as well as the distance between them, give us information about the zero-field Hamiltonian, its g-factor and the hyperfine splitting.

While the method known as continuous wave EPR (CW-EPR), in which the external magnetic field is changed slowly while the cavity is continuously irradiated, can give us information about the Hamiltonian, relaxation and coherence of a spin system can be studied using pulsed EPR measurements.[8] In these experiments, a sequence of microwave pulses are applied, after which the signal emitted by the spin system is measured. The measured signal depends on the spin relaxation and coherence times T_1 and T_2, and on the applied pulse sequence.

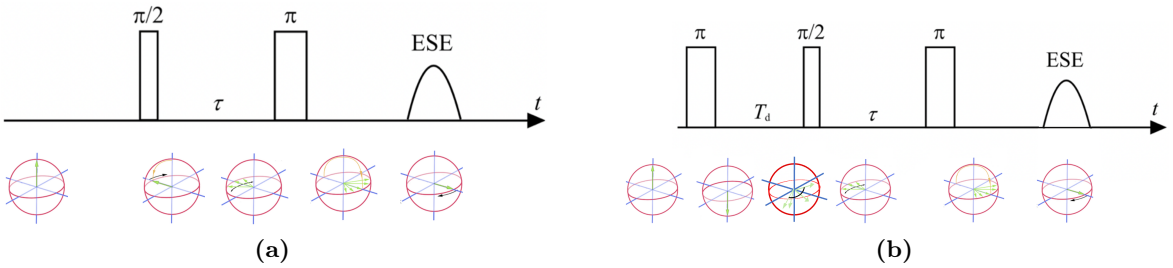

Figure 2.10: Diagram of the spin-echo sequence (a) and the ESE inversion recovery sequence (b). The first is used for measuring T_2, while the second sequence is useful for obtaining T_1.

There are many pulse sequences that can be used in pulsed EPR, but here we will focus on two, schematically shown in Fig. 2.10: the spin-echo, used for measuring T_2, and the electron spin-echo (ESE) inversion recovery, with which T_1 can be extracted. Regarding the first sequence, the external field is tuned to the transition that is going to be studied. At equilibrium, the magnetization of the spin system will be aligned with this field, along the Z direction. If a $\pi/2$ pulse is applied, the spins flip to the XY plane. Now the spins precess at the Larmor frequency, but due to local magnetic field inhomogeneities the precession speed of each individual spin is slightly different. After a time τ a π pulse is applied, placing the faster spins behind the slower ones. After another τ period, the spins are refocused and an echo is produced. The intensity of this echo decays exponentially with the value of τ and with a characteristic time scale given by T_2. Information about the decoherence time can be obtained by repeating this measurement for different values of τ.

The value of T_1 can be extracted by inversion recovery experiments. In this case, a initial π pulse that inverts the spin population is applied. After a certain delay time T_d, the previous spin-echo sequence is applied, now with a fixed τ. Here, the intensity of the measured echo decays exponentially with the time T_d separating the initial π pulse and the $\pi/2$ pulse, with a characteristic time scale given by the spin-lattice relaxation time T_1.

EPR has been used to confirm the Hamiltonian parameters obtained by broadband spectroscopy and obtain information about the spin dynamics of different systems. An example of a rotational CW-EPR spectrum measured for a vanadyl porphyrin sample (see chapter 6) is shown in Fig. 2.11.[9] In this case, a rotating mechanism was used for obtaining the spectra for different orientations of the sample. With this type of measurements, information about the Hamiltonian and the orientation of the molecules in the sample can be extracted.

The EPR system used during this thesis is an Elexsys E-580 spectrometer by Bruker Corporation, property of the University of Zaragoza (Fig. 2.12). This system allows us to take EPR spectra in both X-band (8-10 GHz) and Q-band (35 GHz), in continuous wave and pulsed modes, and is equipped with a gas-flow helium cryostat with which experiments at temperatures down to 5 K can be performed. External DC magnetic fields between 0 and

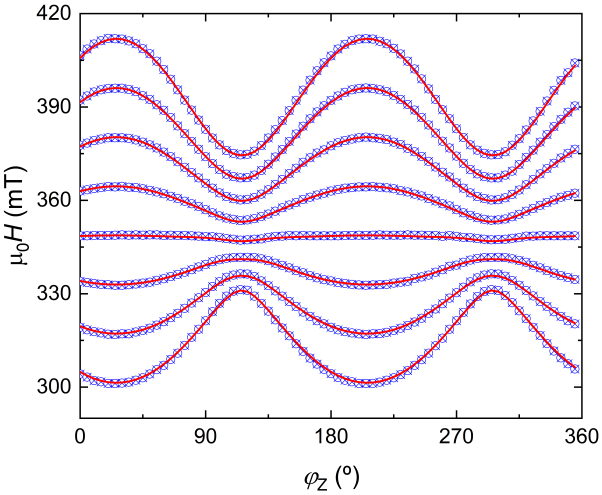

Figure 2.11: Example of a rotational diagram for a single crystal of a vanadyl porphyrin at room temperature. The empty circles represent the positions of the centre of the lines in the CW-EPR spectra upon rotating the crystal around the Z laboratory axis. Full lines are the corresponding positions calculated with the spin Hamiltonian.

1.4 T can be applied, and a rotating mechanism allows the acquisition of spectra for different orientations of the sample.

Figure 2.12: Elexsys E-580 EPR spectrometer at the University of Zaragoza.

2.3 Circuit fabrication and characterization techniques

2.3.1 Ultra-Violet Photolithography

The superconducting circuits used during this thesis have been fabricated by ultra-violet (UV) lithography explained in this section. The fabrication has been carried out at the Instituto de Nanociencia y Materiales de Aragón (INMA) and at the Centro de Astrobiología (CAB), depending on the method and the type of circuit.

UV photolithography[10] is a circuit fabrication technique with which a pattern is transferred from a mask to a substrate by means of a photosensitive resin and UV irradiation. The different mask patterns, like the one shown in Fig. 2.13, were designed using the CAD software. Once the

mask is fabricated, two different UV photolithography methods can be used for transferring its pattern to the chip: etching and lift-off (see Fig. 2.14).

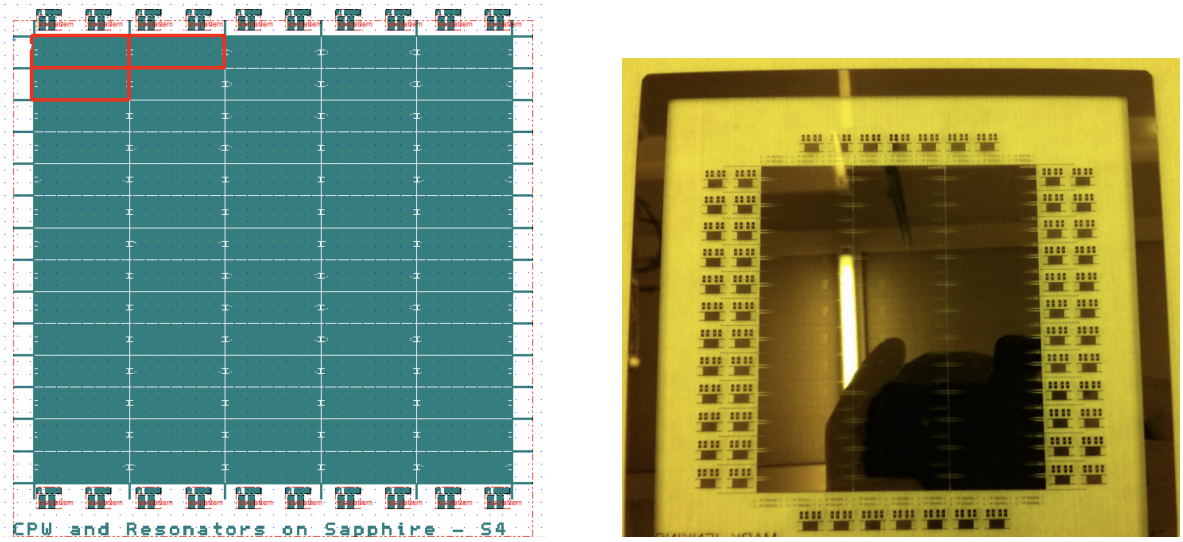

(a) **(b)**

Figure 2.13: (a) UV photolithography mask CAD design used to fabricate coplanar waveguide resonators. (b) Finished mask used for UV photolithography.

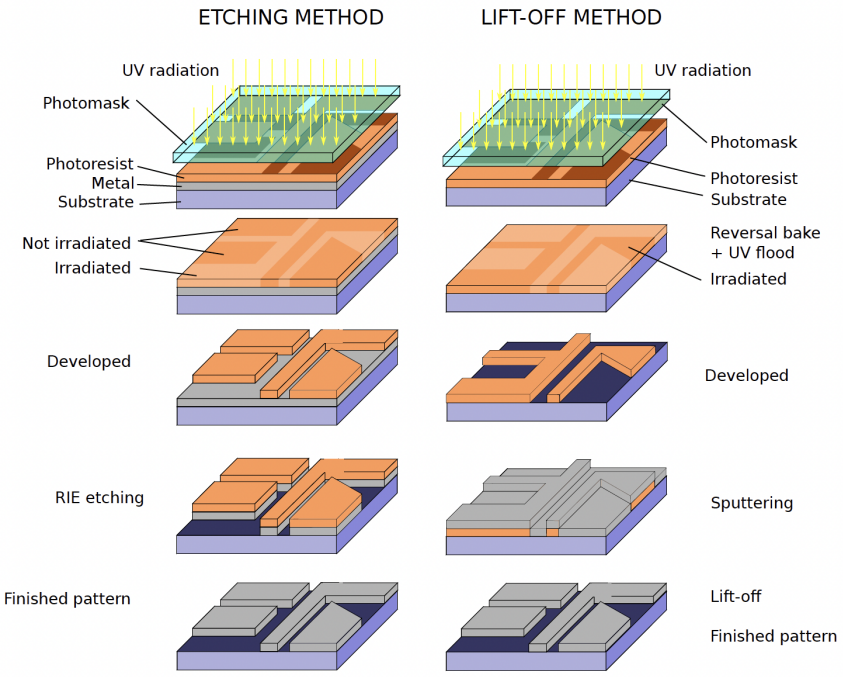

Figure 2.14: Two different UV photolithography methods. The one used at INMA is the etching method, while at CAB both methods have been used.

In both INMA and CAB, circuits are fabricated by UV lithography, but the technique varies slightly from one centre to another. The following paragraphs briefly describe both fabrication methods.

Fabrication at INMA

Coplanar superconducting waveguides and resonators have been fabricated at INMA, using the etching method shown on the left hand side of Fig. 2.14. This technique is separated in several steps that are explained here.

The first step of the etching method used in this thesis implies covering a 4 inch wide, 500 μm thick sapphire wafer with a 150 nm thick Nb layer using ion beam sputtering (IBS). After this deposition, all the steps are done under clean room conditions in order to avoid any damage and contamination of the final pattern.

In the second step, the wafer is cleaned by ultrasound stirring in acetone, isopropanol and deionized water. Then, it is heated to 120°C for 10 minutes to remove humidity. When the wafer has cooled, a layer of adhesion promoter and a 2.4 μm layer of photoresist are deposited using a spin coater. After that, the wafer is soft baked at 110°C for 50 s.

The next step implies introducing the mask and the wafer in the mask aligner for UV irradiation. Here, the mask and the wafer are aligned and placed into close contact by applying vacuum. Then, the wafer is irradiated through the mask for 20 seconds.

Once the photoresist has been exposed to UV irradiation, the exposed parts are removed. For doing this, the wafer is introduced in a solution of photoresist developer and deionized water for one minute. Then, the wafer is hard baked at 125°C for 2 minutes to harden the photoresist.

Finally, the exposed niobium is removed by reactive ion etching (RIE), attacking the wafer using SF_6 gas and O_2 plasma. The remaining photoresist is removed with acetone, obtaining the final device.

Fabrication at CAB

The fabrication of superconducting chips containing several lumped-element resonators (LERs) was carried out at CAB by Alicia Gómez, Marina Calero and Maite Magaz. UV lithography was also the technique used for this fabrication, but some steps were a bit different from the ones followed at INMA.

There are several differences between the circuit fabrication in both places. The first one is that a 100 nm thick Nb layer (instead of 150 nm) is deposited on top of a Si substrate wafer (sapphire wafer at INMA) by means of magnetron sputtering instead of IBS. The second difference is that the design is transferred to the Nb layer by means of maskless UV laser-writer lithography, using a 405 nm wavelength laser scanned over the chip surface. Finally, both positive and negative resists are used. The remaining steps are the same as in the process carried out at INMA.

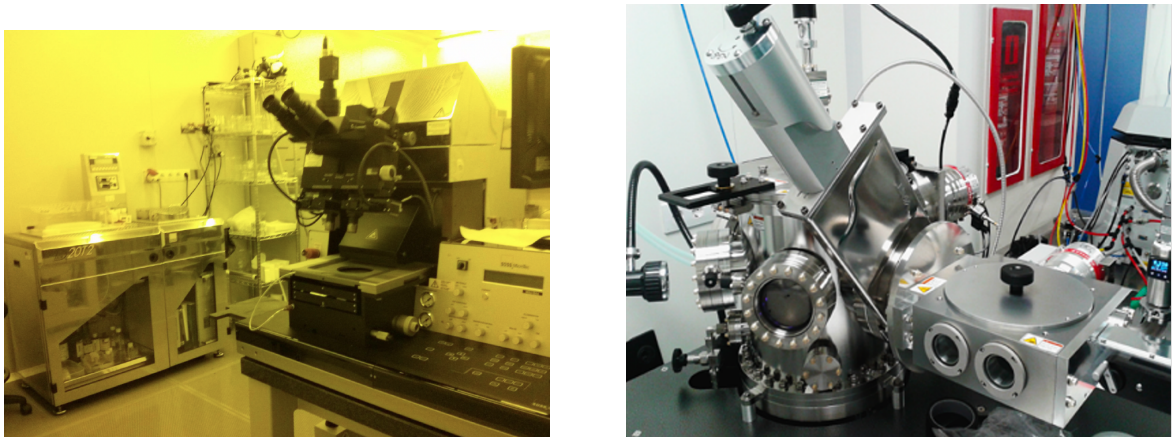

(a) (b)

Figure 2.15: (a) UV photolithography clean room at INMA with all the equipment used during the process. (b) DC Magnetron Sputtering equipment used at CAB.

The equipment used at INMA for UV photolithography, together with the DC magnetron sputtering system used at CAB, are shown in Fig. 2.15. Coplanar superconducting waveguides and resonators like the one shown in Fig. 2.16(a) were fabricated at INMA, while superconducting chips containing several lumped-element resonators (LERs) like the one shown in Fig. 2.16(b) where made at CAB. The latter process has the advantage of being more flexible to changes in the design of the circuits. Both type of circuits had the same chip size, allowing us to measure both in the liquid helium dewar as well as in the dilution refrigerator (see section 2.6).

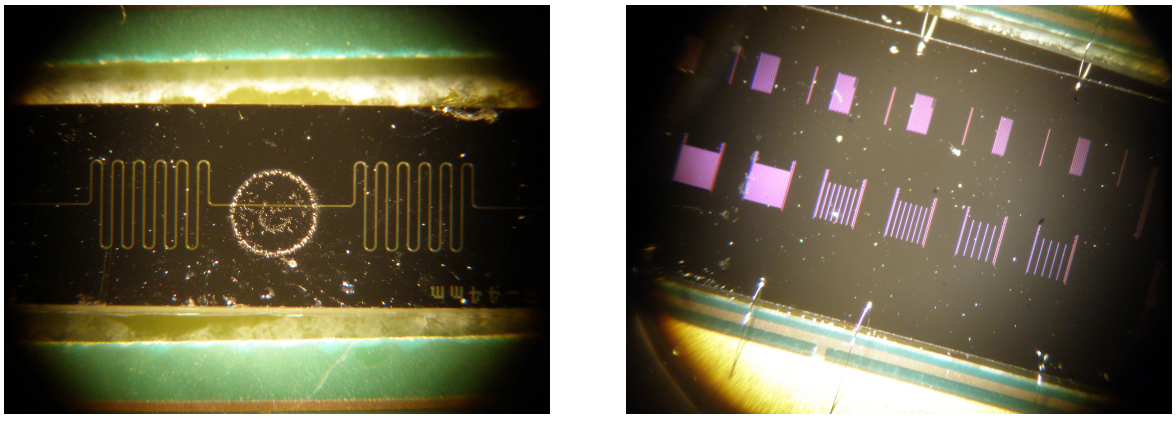

(a) (b)

Figure 2.16: Examples of a coplanar resonator (a) and a chip with several LERs (b) used during this thesis.

2.3.2 Scanning Electron Microscopy (SEM) and Focused Ion Beam (FIB)

Scanning electron microscopy (SEM) is a microscopy technique that produces images of a sample by scanning its surface with a high energy electron beam.[11] The different signals produced from the interaction between the beam and the sample include secondary electrons, backscattered electrons, characteristic x-rays, and other photons of different energies. Secondary and backscattered electrons are the most interesting signals because they provide information about the surface topography. The images present a very high resolution, down to 1 nm, and a

3D appearance due to the large depth of field of this technique.

Focused ion beam (FIB) is very similar to SEM, but instead of electrons it uses a beam of charged ions that bombards the sample surface.[12] This technique also presents a very high resolution (down to 4 nm), but due to the destruction of the surface that is scanned with the ion beam, it is more used for sample etching and for depositing different materials on the sample surface than for imaging. Nanoscale structures with a minimum size of ∼10 nm can be created. Regarding the deposition of materials, the technique is known as focused ion beam induced deposition (FIBID).[13] A precursor gas is injected near the surface of the sample, which adsorbs it. Then, the ion beam dissociates the volatile elements from the precursor gas, which are pumped away, and a deposit formed by the non-volatile components of the gas together with implanted ions remains on the surface.

The SEM/FIB system used during this thesis is an Helios Nanolab Dual Beam by FEI (see Fig. 2.17(a)) of the Laboratorio de Microscopías Avanzadas (LMA),[14] located at the Instituto de Nanociencia y Materiales de Aragón. This system consists of a 30 kV electron column and a 30 kV Ga^+ focused ion beam oriented at 52° from each other, allowing the sample to be imaged by SEM and processed by FIB or FIBID at the same time. It also has five gas injectors which allow the growth of nano-deposits with high resolution, such as W-based superconducting nano-deposits and Co-based ferromagnetic nano-deposits with a minimum lateral size of 30 nm.

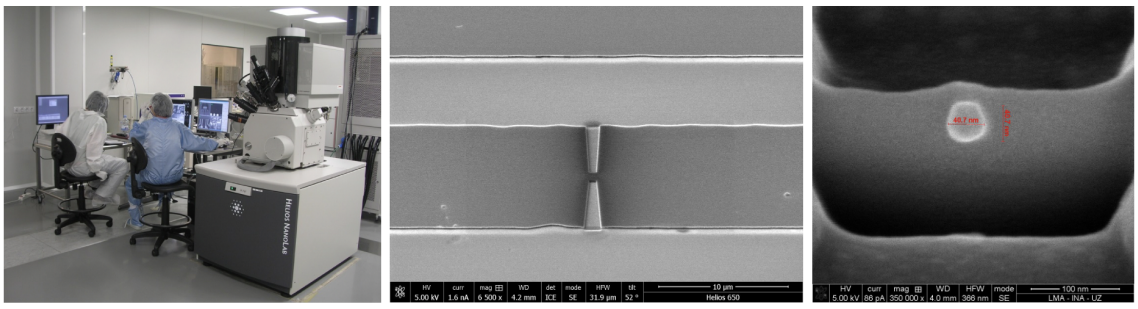

(a) (b) (c)

Figure 2.17: (a) Helios Nanolab Dual Beam 600 at the clean room of the Instituto de Nanociencia y Materiales de Aragón. (b) SEM image of a nanoconstriction fabricated on a coplanar superconducting waveguide. (c) SEM photo of a Co nanoparticle deposited on a transmission line.

A SEM image of a coplanar waveguide where a nanoconstriction has been fabricated by FIB is shown in Fig. 2.17(b). Nanoconstrictions like this have been fabricated in several resonators used during this thesis for increasing the local magnetic field produced by them, and thus improving the coupling to molecular spins (see chapter 4 for more details).

Figure 2.17(c) shows a Co nanoparticle deposited by FIBID on top of a coplanar waveguide. Experiments carried out with this sample did not show any significant signal corresponding to the coupling between the nanoparticle and the superconducting circuit, not being this approach described in this thesis.

2.4 Deposition of molecular samples at the nanoscale: dip-pen nanolithography

Dip-Pen nanolithography (DPN) is a soft lithographic technique that uses the tip of an atomic force microscope (AFM) as a pen to transfer a sample from a solution (the 'ink') to a solid substrate with a certain chemical affinity for the sample.[15] Many types of inks can be transferred

by DPN: organic molecules, polymers, colloidal particles and metal ions, achieving sub-100-nm precision depending on the sample and the substrate.[16]

In the DPN process, shown schematically in Fig. 2.18(a), a molecular ink or a dissolved solid sample is coated onto an AFM tip which transports it to the substrate. When ink and substrate are in contact, molecules flow from the tip to the substrate by capillarity, depositing the sample in drops with sizes down to 100 nm in the case of molecular inks, or μm in other cases. The size of the deposits can be reduced by controlling the relative humidity and the tip-substrate contact time.

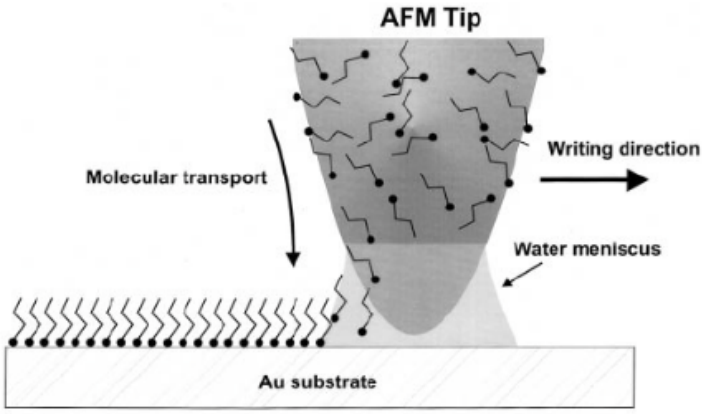

(a)

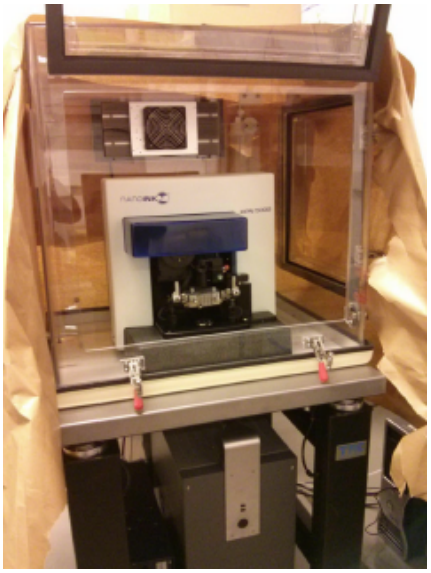

(b)

Figure 2.18: (a) Scheme of the dip-pen nanolithography.[15] (b) Nanoink DPN 5000 System at the Instituto de Nanociencia y Materiales de Aragón.

The inks used for deposition must present a high boiling point to prevent a premature drying of the ink before it is deposited on its desired location, a sufficiently large surface tension to keep them fixed on the surface, and enough viscosity for better controlling the amount of ink deposited. All these parameters can be controlled by a careful choice of solvents and additives, which also need to be soluble between them and compatible with the molecule that is going to be deposited. In the cases of the two molecules deposited by dip-pen during this thesis, the organic free radicals DPPH and PTM_r, the former ink contained dimethylformamide (DMF), glycerol

and DPPH, while the latter ink was made of polystyrene (PS), trichlorobenzene, undecanol and PTM_r.

Before making the final ink, the suitable proportion of solvents and additives needs to be determined. Inks with several proportions of these components are studied under different temperature and humidity conditions. First tests are usually made on silicon dioxide, and then characterized by AFM. This allows selecting the ink that has a better performance for the final depositions. An example of a deposition performed during this thesis is shown in Fig. 2.19, where two images of a deposition of DPPH are presented. DPPH is a free radical with $S = 1/2$, $g = 2$ and $T_2 \sim 100$ ns, widely used for calibration of Electron Paramagnetic Resonance (EPR) signals.

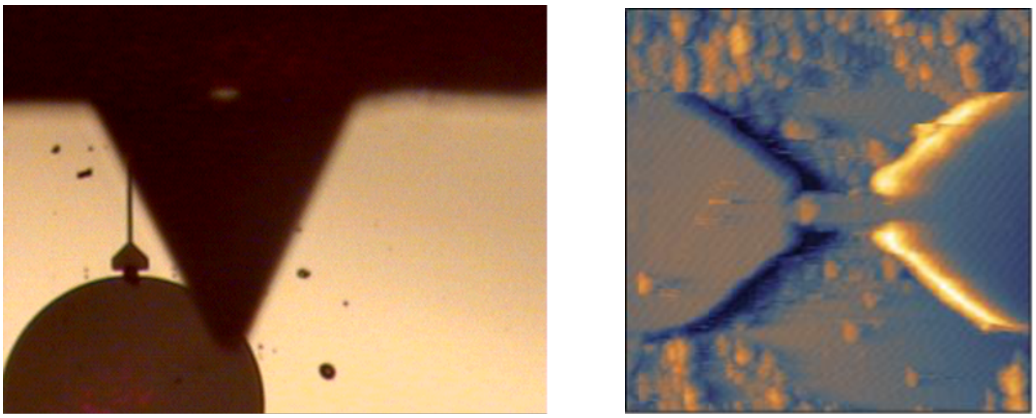

(a) **(b)**

Figure 2.19: (a) Optical microscopy and (b) AFM images of a dip-pen deposition of DPPH on a "2.5D" resonator used during this thesis.

2.5 Characterization of superconducting circuits: RF measurements

2.5.1 Chips and sample holders

The microwave transmission experiments described in this thesis were performed using on-chip superconducting circuits, transmission lines and resonators. These devices need to be connected to a printed circuit board (PCB) that holds the connectors used to introduce the input signals into the chip and collect the output signals. In this section, we briefly describe these PCBs, the instrument with which the electrical connection between the circuits and the PCBs has been made, and the coaxial cables and connectors employed.

Printed Circuit Board (PCB)

Printed circuit boards (PCBs) are electrical components consisting on one or more layers of electrical conductors, like copper, separated by insulating material.[17] A common PCB design consists of a rectangle of insulating material with metal tracks on both sides of the board. Those metal tracks designed to act as ground are connected between them, forming a common ground for all the devices connected to the PCB. Other tracks connect the different components, like connectors and chips, to each other. These devices allow us to desing more or less complex circuits in a reduced space.

A photography of one of the PCBs used during this work is shown in Fig. 2.20. It contains three holes where the different electrical components are placed: the central hole is designed for

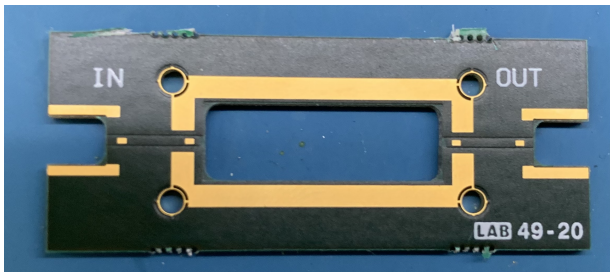

Figure 2.20: Photo of one of the PCBs used in the microwave transmission experiments described in this thesis. The superconducting circuit would be placed in the central hole, while two SMP connectors would be soldered to both sides of the PCB.

hosting the chip with the superconducting circuits, while the two holes to the left and right of the central one are prepared for solding the connectors that connect the chip with the coaxial cables. Four more holes are fabricated to screw the PCB to the cold finger of the cryostat, thus ensuring a proper thermalisation of the whole system.

The PCB is formed by a large metal plate that connects the ground of the chip and of the two connectors mounted on the board. This ground plate is covered above and below by two layers of insulating material. The central line of the chip is connected to both connectors by two metal tracks whose beginning and end are exposed. The chip is connected to these tracks by wire bonds, while the central pin of the connectors is soldered. These connectors are subminiature push-on (SMP), plug-in connectors for applications up to 40 GHz. These connectors are easy to connect and disconnect as they can be pushed against each other to make a connection and pulled apart to open the connection. The characteristic impedance of these connectors (as well as that of all superconducting circuits used in this thesis) is 50 Ω.

Transission through coplanar waveguides and resonators can be strongly affected by the existence of parasitic paths parallel to the central transmission line. These parasitic losses can be associated to regions of the PCB where the electric field density is increased, which correspond to zones in which the geometry of the transmission line varies (such as at the bondwire interface between the PCB and superconducting chip).[18] The behaviour of the superconducting circuits can be improved by using PCBs large enough so that these field inhomogeneities are sufficiently far from the chip, like the one shown in Fig. 2.20. If the PCB design satisfies this condition, these parasitic losses can be minimised, allowing the PCB to act as an almost open circuit at low frequency when there is no chip bonded to it (see Fig. 2.21).

Wire bonding

The electrical connection between our superconducting circuits and the PCBs that host them is made by wire bonding. This is a technique in which electrical connections between chips and integrated circuits are created by using bonding wires, thin wires made up of materials such as gold or aluminium.

There are two main wire bonding processes: ball bonding and wedge bonding. Both are schematically shown in Fig. 2.22. In the ball bonding process, the end of the wire is melted to form a ball. This ball is placed into contact with the bond pad while pressure, heat and ultrasounds are applied to it to weld both components. The capillary through which the wire is fed is then moved to the end point of the weld, making the wire form an arch between both points. Here a second bond is formed in the same way as the first one. Finally, the wire is broken off by being clamped and moved. This technique is shown in Fig. 2.22(a)

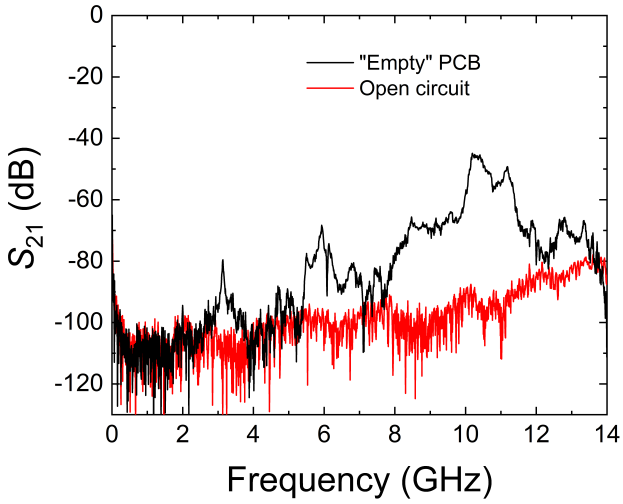

Figure 2.21: Comparison between the measured transmission through an "empty" PCB (without chip) like the one show in Fig. 2.20 and through the circuit without any PCB. Data were taken at room temperature and an input power of 0 dBm.

The wedge bonding process involves bringing a clamped wire in contact with the bond pad (Fig. 2.22(b)). The wire is then welded by the application of ultrasounds and pressure. The capillary is then moved to the second bonding point, where a second bond is formed using the same technique. The wire is finally clampled and broken by raising the capillary.

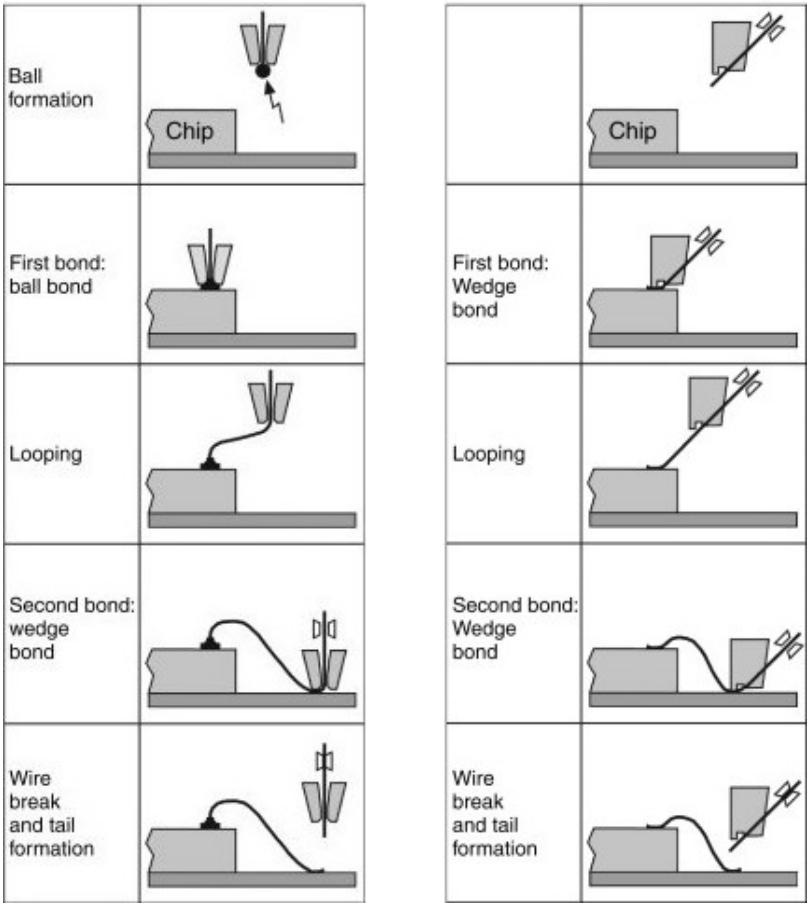

Figure 2.22: Scheme of (a) ball bonding and (b) wedge bonding methods. The one used during this work is the wedge wire bonding method.

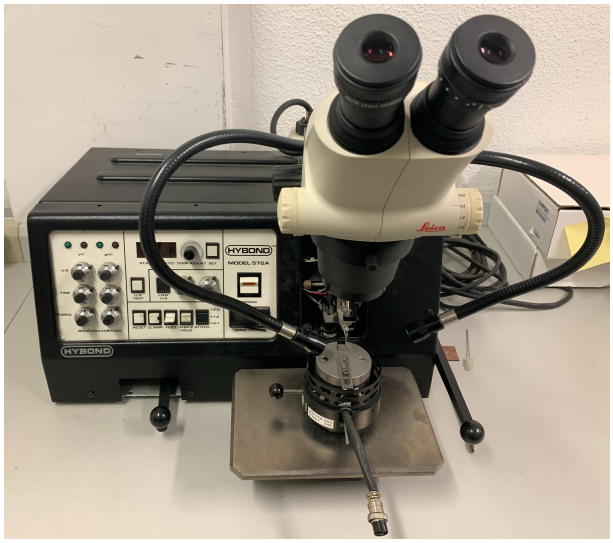

Figure 2.23: Hybond model 572A wire bonding machine at the INMA.

The wire bonding machine used for bonding the superconducting circuits shown in this thesis is a Hybond model 572A from the INMA (see Fig. 2.23). It contains independent X, Y and Z-axis controllers that allow us to accurately fabricate bondings at any point of the samples.

The parameters of the first and the second bonds (time and power of the ultrasonic pulse, and pressure applied by the capillary) can be independently modified, adapting them to the different surfaces on the PCB and the superconducting circuit. The bond wire is made up of silicon / aluminium (1% SiAl), with a diameter of 25 μm.

Coaxial cables

Depending on whether the microwave transmission experiments shown in this thesis have been carried out in a liquid helium cryostat (section 2.6.1) or in a dilution refrigerator (section 2.6.2), the coaxial cables that connect the superconducting circuits with the vector network analyser (section 2.5.2) are different.

In the case of the liquid helium cryostat, the coaxial cables are 2.15 mm semi-rigid coaxial cables made of stainless steel. As will be explained in section 2.6.1, these cables present a lower thermal conductivity than the copper ones, making the helium stored inside the cryostat last a few more days without evaporating. This reduction in helium evaporation comes at the cost of increasing circuit dissipation due to its lower electrical conductivity compared to copper.

Regarding the coaxial cables used in the dilution refrigerator, input wires are semi-rigid coaxial wires made up of a CuNi alloy or only Cu (for the connection between the chip and the mixing chamber plate). These cables are thermalised at each thermal stage in the system by a combination of attenuators and female/female bulkhead feedthroughs. Output wires are made up of a superconducting NbTi alloy. These cables allow us to recover the response of the sample to the input signal with the least possible losses.

All these cables are connected to the vector network analyser by means of subminiature version A (SMA) connectors. The characteristic impedance of both wires and SMA connectors is 50 Ω.

2.5.2 Vector network analyser

A vector network analyser (VNA) is an instrument that allows the characterization of electrical components and circuits by measuring their effect on the amplitude and phase of frequency-swept or power-swept radio-frequency signals.[19]

To understand how a network analyser works, we can make an analogy between electrical and optical waves. If we have an optical wave which strikes a system of lenses, part of the light will be reflected by the lenses surfaces, some will be absorbed by the lenses and most of it will be transmitted through them. If the system has mirrors, most of the light will be reflected. Despite the fact that wavelengths are different for light and RF signals, the behaviour and principles are the same for both. Network analysers measure the energy of incident, reflected and transmitted RF waves introduced in Fig. 2.24(a).

There are two basic types of network analizers: scalar and vector. While scalar network analysers only measure the amplitude properties of reflected and transmitted signals, vector network analysers also obtain information about the phase difference between incident, transmitted and reflected signals. A third type of network analizer, the large-signal network analyser, can study the harmonics and non-linearities of a device under large signal conditions.

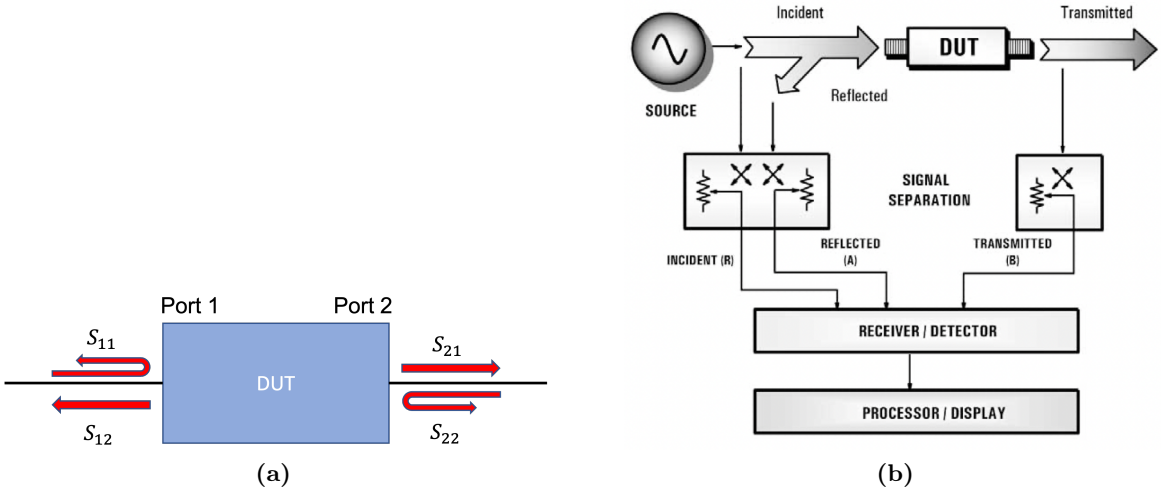

Figure 2.24: (a) Scheme of the different signals that can be measured by a VNA. S_{ij} is the signal emitted by port j when the system is fed through port i. (b) Generalized block diagram of a network analyser.[20]

A block diagram of a network analyser is shown in Fig. 2.24(b). All types of network analysers contain the four following sections:

- Signal source: It gives us the stimulus that will be introduced in the system. Frequency and power can be swept.
- Signal-separation block: This part has two main functions. It measures a portion of the input signal to provide the device a reference for ratioing, using splitters or directional couplers. It also separates the incident and reflected waves at the input of the system we are testing (Device Under Test, DUT). For this second function, directional couplers and bridges can be used.
- Signal-detection block: There are two types of detectors. Diode detectors are scalar, while tuned receivers give information about magnitude and phase of the signal and are used in VNAs.
- Processor and display for calculating and showing the results: This last block is where the measured data is formatted in order to make it easy to interpret.

During this thesis, the VNA that has been used for most of the measurements is a Rohde & Schwarz ZVB14 from the department of Electronic Engineering of the University of Zaragoza. A photo of this device can be seen in Fig. 2.25(a). This model has 4 ports that can be used simultaneously, but during this thesis only ports 1 and 2 have been used. It presents a frequency range from 10 MHz to 14 GHz, and a power range from -45 dBm to +15 dBm.[21] Figure 2.25(b) provides an example of a transmission measurement carried out during this thesis. It shows the transmission through a superconducting transmission line measured in the helium cryostat introduced in section 2.6 at a temperature of 4.2 K.

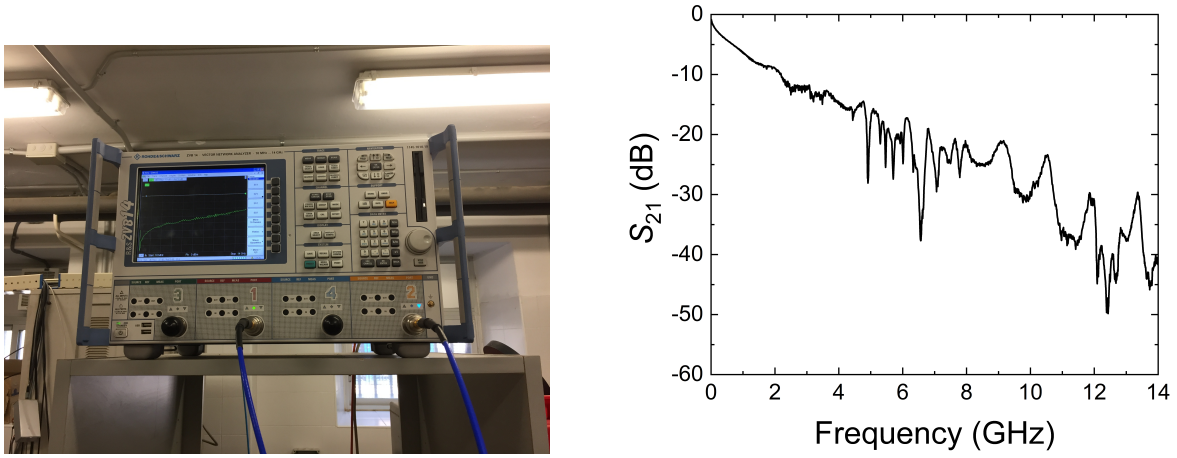

(a) **(b)**

Figure 2.25: (a) Photography of the Rohde & Schwarz ZVB14 VNA using during this thesis. (b) Example of a measurement over the full frequency range of this instrument. It shows the transmission through a superconducting coplanar transmission line coupled to a vanadyl porphyrin crystal.

2.6 Low and very low temperature equipment

2.6.1 Liquid Helium Dewar with Vector Magnet

In order to observe the quantum phenomena studied in this thesis, it is necessary to achieve very low temperatures, close to absolute zero, and to apply strong magnetic fields. During the first half of the thesis these two requirements have been fulfiled using a 90 L liquid helium dewar that hosts a superconducting vector magnet.

The 90 L capacity liquid helium dewar (Fig. 2.26(a)) has three main parts: a central chamber that contains the liquid helium, a nitrogen cooled radiation shield that protects the inner helium from external radiation, and an outer vacuum chamber that insulates the liquid helium bath and slows down the losses. The PCB holding the superconducting circuit and the magnetic materials are introduced in the helium bath, at a temperature of 4.2 K, using the 4K probe with two semi-rigid stainless steel coaxial wires terminated in SMP microwave connectors, as shown in Fig. 2.26(b). These cables allow us to connect the superconducting chips to external electronics, like the previous VNA (see section 2.5.2).

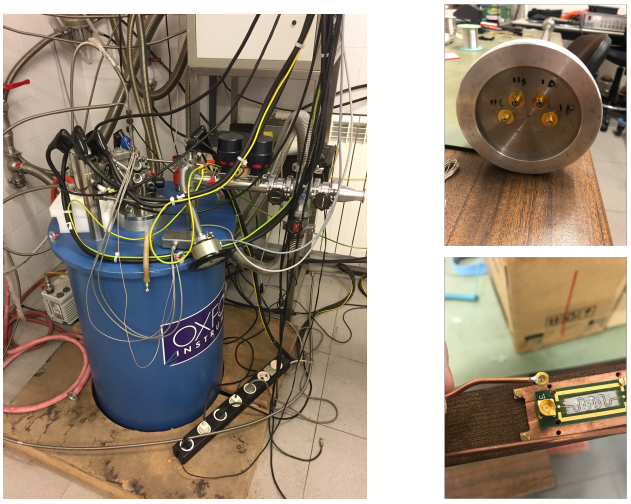

(a) **(b)**

Figure 2.26: (a) 90 L liquid helium dewar containing the superconducting vector magnet. (b) 4K probe used for RF measurements at 4.2 K

Superconducting magnets[22] are made of several coils of superconducting wire. In the superconducting state, these magnets support larger electric currents than conventional electromagnets without dissipating energy as heat, producing high magnetic fields with low power supply.

The superconducting vector magnet consists of three separated superconducting coils that apply magnetic fields along three perpendicular directions. The largest field is applied along the vertical (Z) axis and can be increased up to ±9 T. In the horizontal plane (X and Y axes) a maximum field of ±1 T can be applied. Z and X coils are fed by a model IPS120-10 power supply, while Y coil uses an IPS120-3, which cannot reverse the polarity. These power sources can work in persistent mode, in which the superconducting circuit is closed and isolated by a superconducting switch. In this mode, the field decay rate is very low, about one part in 10^4 per hour or even lower.

2.6.2 Bluefors LD250 Cryogen-Free Dilution Refrigerator with Uniaxial Magnet

While studying quantum phenomena, lower temperatures than 4.2 K are often necessary. To achieve them, a LD250 cryogen-free dilution refrigerator (DR) by Bluefors has been used.

DR systems are the only cooling devices that can achieve stable temperatures below 300 mK, reaching 10 mK or even lower temperatures. This is possible due to the properties of ^{3}He/^{4}He mixtures at low temperatures.[23] At saturated vapor pressure, pure ^{4}He presents a phase transition at 2.17 K from a normal fluid to a superfluid. Diluting the ^{4}He with ^{3}He decreases this transition temperature along the λ-line (see Fig. 2.28). At a low enough temperature, the mixture separates in two phases: a ^{3}He concentrated phase and a ^{3}He poor phase. Moving ^{3}He atoms from the concentrated to the diluted phase requires energy due to the larger enthalpy of ^{3}He atoms in the diluted phase, and in a DR this energy is taken from the mixing chamber, which gets cooled during this process.

As can be shown in Fig. 2.28, there is a finite solubility of ^{3}He in ^{4}He at absolute zero, remaining a concentration of 6.6%. This fact, which cannot be explained by classical thermodynamics, would make it feasible to cool the system down to arbitrarily low temperatures. This is not

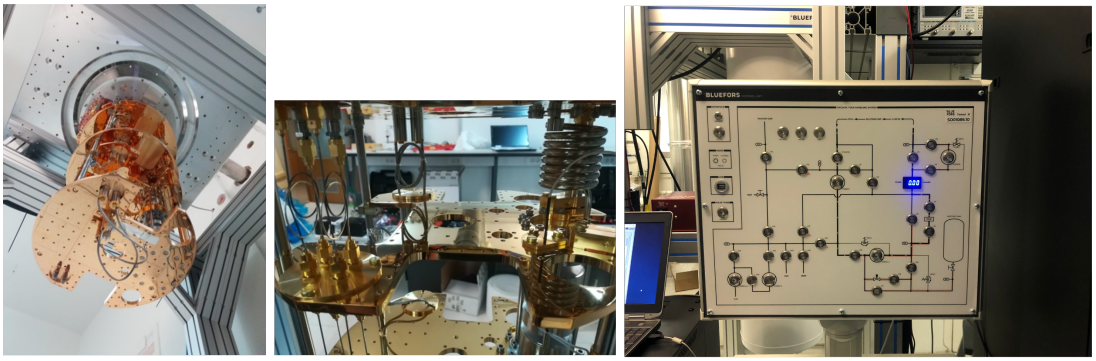

Figure 2.27: Photos of the Bluefors DR, showing the mixing chamber, where the lowest temperature is achieved (left), one of the different plates inside the fridge with the input and output superconducting wires for RF measurements (centre), and the DR control panel (right).

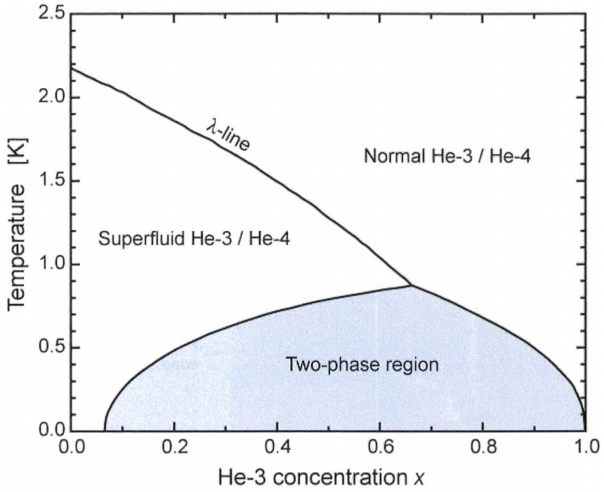

Figure 2.28: Phase diagram of ^{3}He-^{4}He mixture.

experimentally possible due to the need to recondense the removed ^{3}He, which brings a finite amount of heat to the mixture.

There are two types of dilution refrigerators: cryogen-free and non cryogen-free. A non cryogen-free DR is surrounded by a vacuum chamber and liquid helium at 4.2 K. This helium bath is used for pre-cooling the DR and the ^{3}He gas circulating through the refrigerator, and it also serves as a low temperature radiation shield.

In a cryogen-free DR like the one used in this thesis, the helium bath is not necessary. It contains a pulse tube cooler with which temperatures low enough to start the condensing cycle can be achieved. In this system, shown schematically in Fig. 2.29, the compressor produces a periodical variation of the pressure of the gas inside the system, usually helium, moving the piston left and right. When the gas goes to the right, it enters to the regenerator (a porous medium with a large specific heat) at room temperature (T_a), and leaves the regenerator at a lower temperature (T_L), transferring heat to the regenerator. Then, the gas enters to the pulse tube at low temperature and, thanks to the orifice, buffer and the heat exchanger X_3 at room temperature, when the pressure drops and the gas goes back to the left it has a temperature below T_L, hence taking heat from X_2 and cooling it.

Any DR also contains three main parts regarding the ^{3}He/^{4}He circuit: the mixing chamber, the still and the heat exchangers. These parts are shown in Fig. 2.30(a).

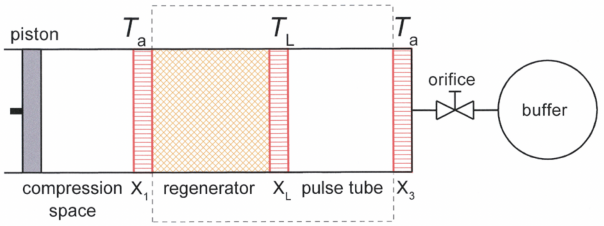

Figure 2.29: Schematic diagram of a Stirling-type single-orifice pulse tube cooler, where the different parts are labeled.[24] X_1, X_2 and X_3 are heat exchangers.

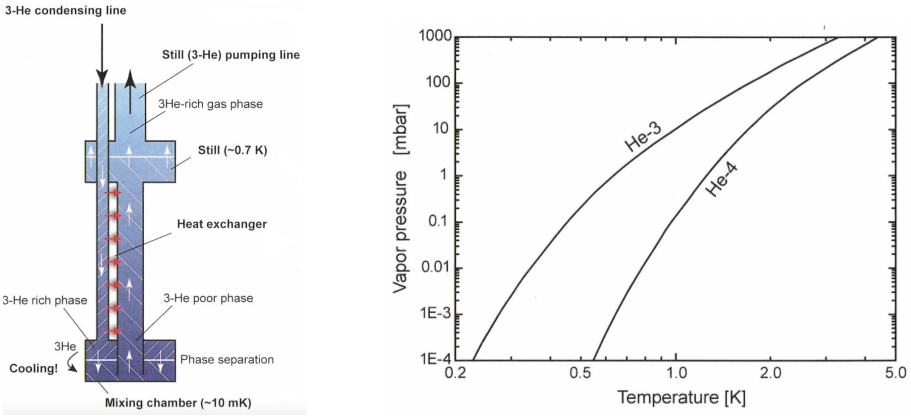

(a) **(b)**

Figure 2.30: (a) Main parts of a dilution refrigerator. (b) Vapor pressures of ^{3}He and ^{4}He.[25]

The mixing chamber is a deposit located at the bottom of the circuit where the concentrated and the diluted ^{3}He phases coexist. The ^{3}He diluted phase is denser, so it lies at the bottom while the concentrated phase is on top of it.

To cool down the system it is necessary to continuosly remove ^{3}He atoms from the diluted phase. This process is driven by the still. It is connected to the diluted phase of the mixing chamber, so part of this phase is located in the still. Due to the large difference in vapor pressure between ^{3}He and ^{4}He (see Fig. 2.30(b)), the helium pumped away from the diluted phase is almost pure ^{3}He. This produces an osmotic pressure which makes the ^{3}He atoms from the mixing chamber to flow towards the still, then forcing ^{3}He of the concentrated phase in the former pass to the diluted one. These atoms need to absorb the enthalpy of mixture from the mixing chamber, thus cooling it. The ^{3}He atoms removed from the still are returned into the condensing line of the DR after being precooled. The heat exchangers cool down the ^{3}He which returns to the mixing chamber. In these heat exchangers, the tubes which remove the ^{3}He and return it to the mixing chamber are linked to maximize the thermal contact between them. The design used in most refrigerators is shown in Fig. 2.31.

During this thesis, a new Bluefors LD250 DR was acquired and installed. It it managed as a service by the Servicio de Apoyo a la Investigación (SAI), making it accessible to all researchers. It allows performing experiments at temperatures down to 9 mK. The temperature of the system can be controlled by means of different heaters located in the mixing chamber and the still, going from 6 mK to 50 K. Three vacuum pumps (one scroll pump and two turbomolecular pumps) and a compressor are in charge of achieving the necessary vacuum inside the DR and making the mixture circulate through the circuit.

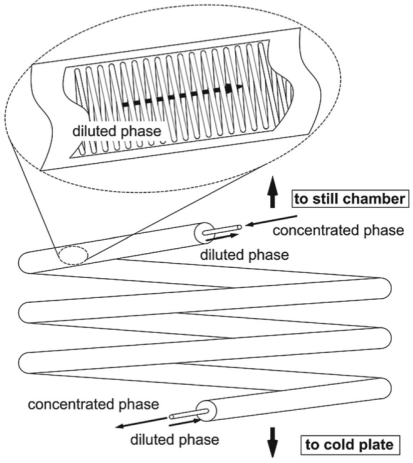

Figure 2.31: Schematic of the concentric heat exchanger.[26]

The system has a uniaxial superconducting magnet by American Magnetics located below the mixing chamber of the DR and thermally anchored to the 4.2 K plate. The magnet allows applying magnetic fields up to 1 T. The smallest field step is of order 1 G (10^{-4} T). It is fed by a model 4Q06125PS-430 high-stability power supply system and controlled by a model 430 power supply programmer.

In order to perform transmission measurements with this DR, it was necessary to carry out some preparatory work. A cold finger made of oxygen-free copper was designed and fabricated by members of our research group (Víctor Rollano, Marcos Rubín and Sergio Martínez-Losa). It consists of a rod, mechanically attached and thermally anchored to the mixing chamber, and of a wider plate that serves as the experimental stage. The PCB that holds the circuits and the magnetic samples is screwed and thermalised with Apiezon N grease to this plate, located at the centre of the magnet. We also assembled two cryogenic amplifiers inside the DR, which allow working with very low (down to -95 dBm) input powers and still obtain measurable transmission signals. The wiring of these elements to the external electronics with copper coaxial cables and its test was also performed by our team. Results of some of the measurements performed during the first tests are shown in Fig. 2.33. Figure 2.32 the DR with all these new devices and a scheme of the electronics inside the fridge, which also contains attenuators for thermalizing the wires and reducing the intensity of the input signal.

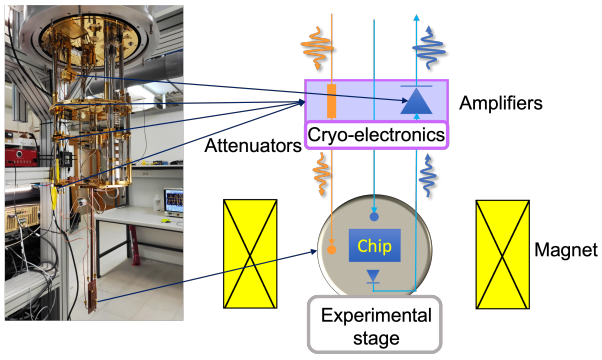

Figure 2.32: Image of the complete DR with the copper cold finger where the samples are placed, together with a scheme of the electronics inside the DR.

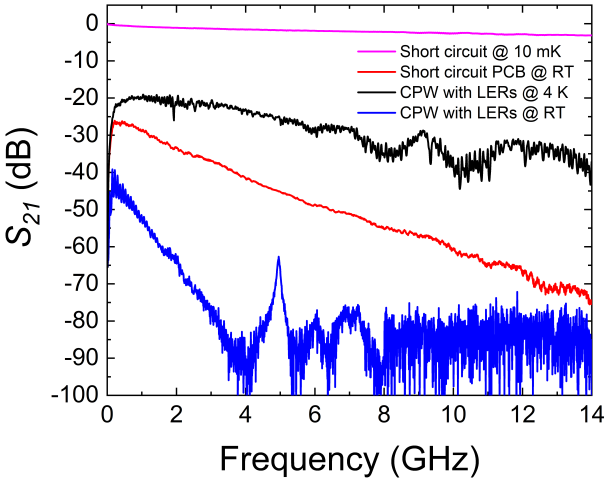

Figure 2.33: Comparison between the transmission signal obtained using a wire as a short circuit at 10 K and at room temperature, a transmission line coupled to LC resonators at 4 K and this transmission line at room temperature, after the installation of the cryogenic amplifiers, copper coaxial cables and the cold finger. The maximum transmission is -20 dB due to the effect of the attenuators (-50 dB) and the amplifiers (+30 dB).

Bibliography

[1] Universidad de Zaragoza, Servicio de Apoyo a la Investigación, Servicio de Medidas Físicas.

[2] R. Bachmann, F. J. DiSalvo Jr., T. H. Geballe, R. L. Greene, R. E. Howard, C. N. King, H. C. Kirsch, K. N. Lee, R. E. Schwall, H.-U. Thomas, and R. B. Zubeck. Heat Capacity Measurements on Small Samples at Low Temperatures. *Review of Scientific Instruments*, 43:205–214, 1972.

[3] A. D. Kent, S. von Molnár, S. Gider, and D. D. Awschalom. Properties and measurement of scanning tunneling microscope fabricated ferromagnetic particle arrays. *Journal of Applied Physics*, 76:6656–6660, 1994.

[4] E. H. Hall. On a New Action of the Magnet on Electric Currents. *American Journal of Mathematics*, 2:287–292, 1879.

[5] R. L. Fagaly. Superconducting quantum interference device instruments and applications. *Review of Scientific Instruments*, 77:101101 (45), 2006.

[6] M. Mück and R. McDermott. Radio-frequency amplifiers based on dc SQUIDs. *Superconductor Science and Technology*, 23:093001 (11), 2010.

[7] G. E. Pake and T. L. Estle. *The physical principles of electron paramagnetic resonance*. W. A. Benjamin, Advanced Book Program, 1973.

[8] M. Brustolon and E. Giamello. *Electron Paramagnetic Resonance: A Practitioner's Toolkit*. John Wiley & Sons, 2008.

[9] I. Gimeno, A. Urtizberea, J. Román-Roche, D. Zueco, A. Camón, P. J. Alonso, O. Roubeau, and F. Luis. Broad-band spectroscopy of a vanadyl porphyrin: a model electronuclear spin qudit. *Chemical Science*, 12:5621–5630, 2021.

[10] C. Mack. *Introduction to Semiconductor Lithography: The Science of Microfabrication*. John Wiley & Sons, 2007.

[11] J. I. Goldstein, D. E. Newbury, P. Echlin, D. C. Joy, C. Fiori, and E. Lifshin. *Scanning Electron Microscopy and X-Ray Microanalysis*. Springer US, 1981.

[12] J. Orloff, M. Utlaut, and L. Swanson. *High Resolution Focused Ion Beams: FIB and its Applications: The Physics of Liquid Metal Ion Sources and Ion Optics and Their Application to Focused Ion Beam Technology*. Springer US, 2003.

[13] I. Utke, P. Hoffmann, and J. Melngailis. Gas-assisted focused electron beam and ion beam processing and fabrication. *Journal of Vacuum Science & Technology B: Microelectronics and Nanometer Structures Processing, Measurement, and Phenomena*, 26(4):1197–1276, 2008.

[14] Universidad de Zaragoza, Laboratorio de Microscopías Avanzadas.

[15] R. D. Piner, J. Zhu, F. Xu, S. Hong, and C. A. Mirkin. "Dip-Pen" Nanolitography. *Science*, 283:661–663, 1999.

[16] D. S. Ginger, H. Zhang, and C. A. Mirkin. The Evolution of Dip-Pen Nanolitography. *Angewandte Chemie (International Edition in English)*, 43:30–45, 2004.

[17] I. Grout. Chapter 3 - pcb design. In Ian Grout, editor, *Digital Systems Design with FPGAs and CPLDs*, pages 123–176. Newnes, Burlington, 2008.

[18] J. M. Hornibrook, E. E. Mitchell, and D. J. Reilly. Superconducting Resonators with Parasitic Electromagnetic Environments. *arXiv*, 2012.

[19] Keysight. *Understanding the Fundamental Principles of Vector Network Analysis*, 2020.

[20] Agilent. *Network Analyzer Basics*, 2004.

[21] Rohde & Schwarz. *R&S ZVB Vector Network Analyzer*, 2011.

[22] M. N. Wilson. *Superconducting Magnets*. Monographs on Cryogenics. Clarendon Press, 1987.

[23] C. Ebner and D. O. Edwards. The low temperature thermodynamic properties of superfluid solutions of ^{3}He in ^{4}He. *Physics Reports*, 2:77–154, 1971.

[24] A. T. A. M. de Waele. Basic Operation of Cryocoolers and Related Thermal Machines. *Journal of Low Temperature Physics*, 164:179–236, 2011.

[25] BlueFors Cryogenics. *BF-LD-Series cryogen-free dilution refrigerator system user manual*, 2016.

[26] H. Nakagawa and T. Hata. Dilution Refrigerator for Nuclear Refrigeration and Cryogenic Thermometry Studies. *International Journal of Thermophysics*, 35:999–1018, 2014.

3

Theoretical Basis for the Coupling of Molecular Spin Qubits to Superconducting Circuits

3.1 Introduction

In this thesis, we have dealt with the interpretation of measurements performed on superconducting circuits, transmission lines and resonators, coupled to different samples of molecular spin qubits. Therefore, it is of crucial importance for the analysis of these data to have a proper theory describing the transmission of microwave radiation through such devices. This theory is described in this chapter, together with the properties of the coupling between superconducting circuits and molecular spin qubits. In section 3.2 we introduce basic concepts of spin qubits and introduce the different parameters that characterise its behaviour. Section 3.3 introduces the coupling between a molecular spin qubit and a superconducting circuit, while its properties are analysed in section 3.4. Finally, in section 3.5 we derive, by means of input-output theory, a expression for the microwave transmission through a superconducting circuit coupled to molecular spin qubits.[1;2]

3.2 Spin qubits and decoherence processes

Spin qubits are one of the multiple candidates to encode quantum information in a hypothetical quantum computer,[3;4] along with others such as superconducting qubits[5] or trapped ions.[6] They are one of the simplest choices to realize a qubit, since the states $|0\rangle$ and $|1\rangle$ of the qubit can be encoded in two of the discrete spin projections of the system. There are some properties that make spin in molecular hosts particularly attractive: their inherent close to perfect reproducibility, the possibility to achieve high spin values; and the ability to tune their properties (for example their resonance frequency or decay times) by chemical design. These advantages motivate the study of the feasability of a quantum processor based on these systems.

Let's see how a spin qubit behaves in the presence of a magnetic field and radiation. For simplicity, we will consider an isotropic spin 1/2 system. The analysis can easily be extrapolated to systems with higher spin values. In the presence of an external magnetic field $\vec{H}$, we can describe its response by a Hamiltonian defined by the Zeeman interaction:[7]

$$\mathcal{H} = -\vec{\mu}\vec{H} = g_S \mu_B \vec{S}\vec{H}, \tag{3.1}$$

where $\vec{\mu} = g\mu_B\vec{S}$ is the magnetic moment of the spin system, g is the g-factor related to the gyromagnetic ratio $\gamma = g\mu_B$, μ_B is the Bohr magneton and $\vec{S}$ is the spin vector operator with components S_x, S_y and S_z. For convenience, we have omitted the $\hbar$ (or h if we work with linear frequencies), and this will be done during all this chapter. The magnetic field splits the levels associated to the two spin projections $m_S = -1/2$ and $m_S = 1/2$, as shown in Fig. 3.1(a), with a field-dependent resonance frequency $\Omega_S = g_S\mu_B H = \gamma H$.

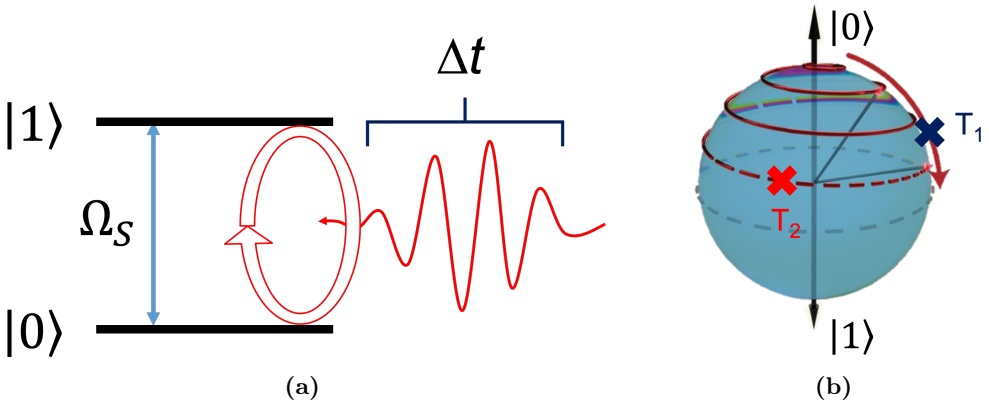

Figure 3.1: (a) Energy splitting Ω_S between the two levels associated with the spin projections of a $S = 1/2$ at a given magnetic field H. If a resonant ($\omega_r = \Omega_S$) magnetic field pulse of duration Δt is applied to the system, the spin will oscillate coherently between its two projections with a frequency Ω_R, known as Rabi frequency. This phenomenom is known as Rabi oscillations.[8] (b) Representation of the two spin eigenstates by means of the Bloch sphere. The evolution from state $|0\rangle$ to $|1\rangle$ is accompanied by a Larmor precession around the quantization axis. Relaxation processes, characterised by T_1, introduce jumps in the state latitude, while dephasing processes characterised by T_2 affect its longitude.

The accessible states of this qubit can be represented by the so-called Bloch sphere, whose north and south poles correspond to the states $|0\rangle$ and $|1\rangle$ respectively (see Fig. 3.1). Starting from the ground state $|0\rangle$, it is possible to generate any arbitrary superposition by applying a resonant pulse of frequency $\omega_r = \Omega_S$:

$$W(t) = W_0 \cos \omega_r t. \tag{3.2}$$

After a given time t, the state evolves to:[8]

$$|\psi\rangle\,(t) = \cos\frac{\Omega_\mathrm{R} t}{2}\,|0\rangle + e^{i\Phi(t)} \sin\frac{\Omega_\mathrm{R} t}{2}\,|1\rangle\,, \tag{3.3}$$

This corresponds to a coherent oscillation from $|0\rangle$ to $|1\rangle$, known as Rabi oscillation, at the Rabi frequency:

$$\Omega_\mathrm{R} = \langle 1\,|W_0|\,0\rangle\,. \tag{3.4}$$

These oscillations are accompanied by a precession around the quantization axis at the Larmor frequency $\omega_\mathrm{L} = \Omega_S$, which determines the phase $\Phi(t) = \Omega_S t$ of the wavefunction. For the simplest case in which the perturbation is given by a transverse microwave magnetic field, $W_0 = g\mu_\mathrm{B} S_x h_x$, where h_x is the amplitude of this field. The Rabi frequency associated to this perturbation is then $\Omega_\mathrm{R} = g_S \mu_\mathrm{B} h_x/2$. It follows that the larger the amplitude, the faster the quantum operations.

The main problem qubits have to face is that, due to their interaction with the environment, there are additional terms that modify the time evolution with respect to that predicted by Eq. (3.3). These terms introduce two types of fluctuations of the wavefunction, known as bit and phase flips. Bit flips are caused by interactions that tend to bring the system to its thermal equilibrium, *e.g.* the coupling to vibrational modes, inducing transitions between the qubit states. These errors can be represented by fluctuations of the state latitude in the Bloch sphere, and are characterised by a time T_1 known as relaxation time. On the other hand, phase flips are produced by interactions that modify the phase of the wavefunction. They are represented by fluctuations of the state longitude in the Bloch sphere, without changes on the qubit energy. Since the phase is determined by the level splitting given by Eq. (3.1), this decoherence often

arises from fluctuations of the local magnetic field, *e.g.* those generated by the dynamics of nuclear spins. Their characteristic time T_2, also called decoherence time, is usually shorter than T_1, being these processes the ones that limit the available time to perform operations on a qubit.

The implementation of quantum algorithms using qubits require the Rabi frequency to be greater than the rate at which qubit errors occur. In a spin qubit coupled to a superconducting circuit, the Rabi frequency is given by the coupling between both systems. In next section we will study the properties of this coupling depending on the type of the spin qubit and the superconducting circuit.

3.3 Coupling to cavity fields

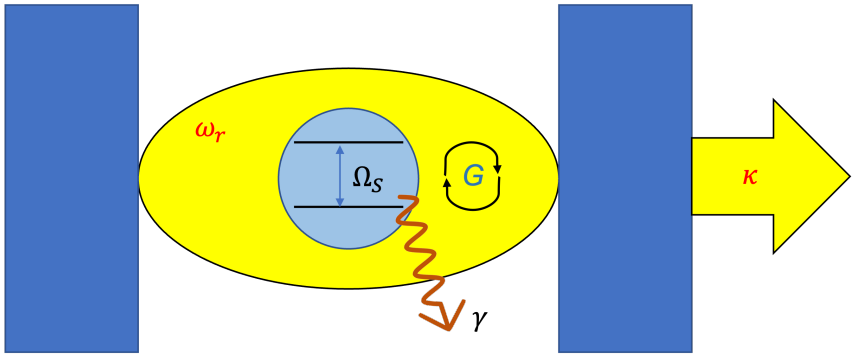

Figure 3.2: Scheme of a basic cavity QED system and its parameters.

Cavity QED studies the interaction between quantum radiation, or photons, trapped in resonant cavities and quantum mechanical systems with a discrete energy spectrum, for example spin qubits. These systems can be coupled by either magnetic or electric fields. An example of one of these cavity QED systems is shown schematically in Fig. 3.2. It provides a realisation of the scheme described in previous section of a spin coupled to a time-dependent perturbation. The Rabi frequency is now given by the coupling between both systems. Here, we discuss how it depends in their properties.

If the transmission through the cavity is monitored, changes will be observed if the spin emits or absorbs photons from the cavity. If the coupling intensity is strong enough and there is only one photon stored in the cavity, the qubit will oscillate coherently between two quantum states. The full system can be described by the Jaynes-Cummings Hamiltonian:[9]

$$\mathcal{H} = \mathcal{H}_s + \mathcal{H}_c + \mathcal{H}_{sc} = \frac{\Omega_S}{2}\sigma^z + \omega_r\left(a^\dagger a + \frac{1}{2}\right) + G\left(a^\dagger\sigma^- + a\sigma^+\right) + \mathcal{H}_\kappa + \mathcal{H}_\gamma, \tag{3.5}$$

where ω_r is the cavity resonance frequency, Ω_S is the frequency of the transition between the two energy levels of the qubit, G is the coupling strength between the two systems, dependent on the intensity of the electric or magnetic field at the qubit's site, $\mathcal{H}_\kappa$ describes the losses of the cavity, being $\kappa = \frac{\omega_r}{Q}$ the decay rate and Q the quality factor of the cavity, and $\mathcal{H}_\gamma$ describes the decay of the qubit into other channels, being related to T_1 and T_2 decay times.

Considering first that there is no damping, the Hamiltonian (3.5) can be diagonalised. If we define the detuning parameter $\Delta = \Omega_S - \omega_r$, the qubit eigenstates as $|\uparrow\rangle$ and $|\downarrow\rangle$, and the cavity eigenstates as $|n\rangle$, with $n = 0, 1, 2,...$, the ground state of the system is $|\uparrow, 0\rangle$, with energy

$E_{\uparrow,0} = -\Delta/2$, while the remaining energy values and eigenstates of the system are the following:

$$\begin{aligned} E_{\pm,n} &= (n+1)\,\omega_r \pm \frac{1}{2}\sqrt{4G^2\,(n+1) + \Delta^2} \\ |+,n\rangle &= \cos\theta_n\,|\downarrow,n\rangle + \sin\theta_n\,|\uparrow,n+1\rangle \\ |-,n\rangle &= -\sin\theta_n\,|\downarrow,n\rangle + \cos\theta_n\,|\uparrow,n+1\rangle \\ \tan 2\theta_n &= \frac{2G\sqrt{n+1}}{\Delta} \end{aligned} \tag{3.6}$$

If the qubit and the cavity are tuned ($\Delta = 0$), then each pair of states $|+,n\rangle$ and $|-,n\rangle$ will be symmetrical and antisymmetrical superpositions of $|\downarrow,n\rangle$ and $|\uparrow,n+1\rangle$ with equal amplitudes, separated by an energy $2G\sqrt{n+1}$. Considering a single excitation, both states will be separated by an energy $2G$. This means that a qubit in the initial state $|\downarrow\rangle$ coupled to an empty cavity will coherently oscillate to the state $|\uparrow\rangle$ and back at a Rabi frequency $\Omega_{\mathrm{R}} = 2G$.

In the dispersive case ($\Delta >> G$ with $\omega_r \sim \Omega_S$), if we consider a single excitation the system eigenvectors become:

$$\begin{aligned} |-,0\rangle &\sim \frac{-G}{\Delta}\,|\downarrow,0\rangle + |\uparrow,1\rangle \\ |+,0\rangle &\sim |\downarrow,0\rangle + \frac{G}{\Delta}\,|\uparrow,1\rangle \end{aligned} \tag{3.7}$$

which are approximately the qubit eigenstates with small mixings with other states with the same number of excitations. In this regime, the transmission of the cavity depends on the state of the qubit. The resonance frequency becomes $\omega_r - G^2/\Delta$ for $|\uparrow\rangle$ and $\omega_r + G^2/\Delta$ for $|\downarrow\rangle$. This is another very attractive property of circuit QED schemes, which is widely used to perform non-demolition measurements of diverse qubits, especially superconducting circuits. One of the goals of this thesis work is to maximise G to make this readout technique also feasible for molecular spin qubits.[10]

3.4 Properties of the spin-photon coupling

In the previous scheme, the coupling strength G between the cavity and the qubit indicated the frequency at which the system would oscillate between the spin up and spin down states, thus the speed at which quantum operations can be performed in this setup. In this section we show how the value of G depends on several parameters of the qubit or the cavity.

If we have a spin described by a Hamiltonian $\mathcal{H}_S$, coupled to the magnetic field generated by a superconducting quantum circuit, ruled by $\mathcal{H}_q$, the dissipationless version of Eq. (3.5) can be written as:

$$\mathcal{H} = \mathcal{H}_q + \mathcal{H}_s - g_S\mu_{\mathrm{B}}\vec{B}_q C_q \vec{S}, \tag{3.8}$$

where $\vec{B}_q$ is the microwave magnetic field generated by the superconducting circuit where the spin is located and C_q is an operator that acts on the resonator and raises or lowers the circuit state by lowering or raising the spin state.

If we choose two levels of our spin system, $|0\rangle$ and $|1\rangle$, we can define the spin-photon coupling strength previously introduced with the Jaynes-Cummings model from the off-diagonal elements of the spin-photon Hamiltonian:

$$\begin{aligned} G &\equiv g_S\mu_{\mathrm{B}}\left|\left\langle 0\left|\vec{B}_q\cdot\vec{S}\right|1\right\rangle\right| \\ &= g_S\mu_{\mathrm{B}}\left|B_{q,X}\,\langle 0\,|S_X|\,1\rangle + B_{q,Y}\,\langle 0\,|S_Y|\,1\rangle + B_{q,Z}\,\langle 0\,|S_Z|\,1\rangle\right|, \end{aligned} \tag{3.9}$$

while the energy difference between these two spin levels is defined as:

$$\Omega_S \equiv \langle 1 | \mathcal{H}_\mathcal{S} | 1 \rangle - \langle 0 | \mathcal{H}_\mathcal{S} | 0 \rangle . \tag{3.10}$$

We can take several choices of the spin states $|0\rangle$ and $|1\rangle$ depending on the spin system. In the case of a $S = 1/2$ system, considered in sections 3.2 and 3.3, the $|0\rangle$ state would be the ground state $|\uparrow\rangle$, while $|1\rangle$ would be the excited state $|\downarrow\rangle$. When working with higher spin states, we can focus on any two states whose energy difference is close enough to the circuit transition frequency ω_r, and then treat the spin system as a two-level system.

The strong coupling regime is achieved when the spins are tuned to the superconducting circuit ($\Omega_S \simeq \omega_r$) and the coupling strength G is strong enough compared to the decoherence sources ($G >> \gamma$ and $G >> \kappa$). As can be seen from Eq. (3.9), G depends on both the form of the wave functions $|0\rangle$ and $|1\rangle$ and the intensity of the microwave field generated by the superconducting circuit, which depends on its design and geometry. In the following sections, these factors will be studied.

3.4.1 Dependence of G on the matrix elements

Coupling of an isotropic $S = 1/2$ system

If we again consider an isotropic $S = 1/2$ system, its Hamiltonian contains only the Zeeman interaction, being valid Eq. (3.1). It leads to the field-dependent energy level scheme shown in Fig. 3.3(a). The matrix elements $\langle 0 | S_i | 1 \rangle$, where $i = X, Y, Z$, can be easily calculated:

$$\begin{aligned}
\langle 0 | S_X | 1 \rangle &= \left\langle -1/2 \left| \frac{S_+ + S_-}{2} \right| 1/2 \right\rangle = \frac{1}{2} \\
\langle 0 | S_Y | 1 \rangle &= \left\langle -1/2 \left| \frac{S_+ - S_-}{2i} \right| 1/2 \right\rangle = \frac{i}{2} \\
\langle 0 | S_Z | 1 \rangle &= 0.
\end{aligned} \tag{3.11}$$

These matrix elements are independent of H. Introducing these values in Eq. (3.9), we obtain:

$$G = g_S \mu_\mathrm{B} B_q \frac{1}{2} = \mu_\mathrm{B} B_q, \tag{3.12}$$

where we have considered that the microwave field generated by the circuit is in the XY plane since the S_Z matrix element is zero, and we have taken $g_S = 2$.

Coupling of an anisotropic spin system with $S > 1/2$

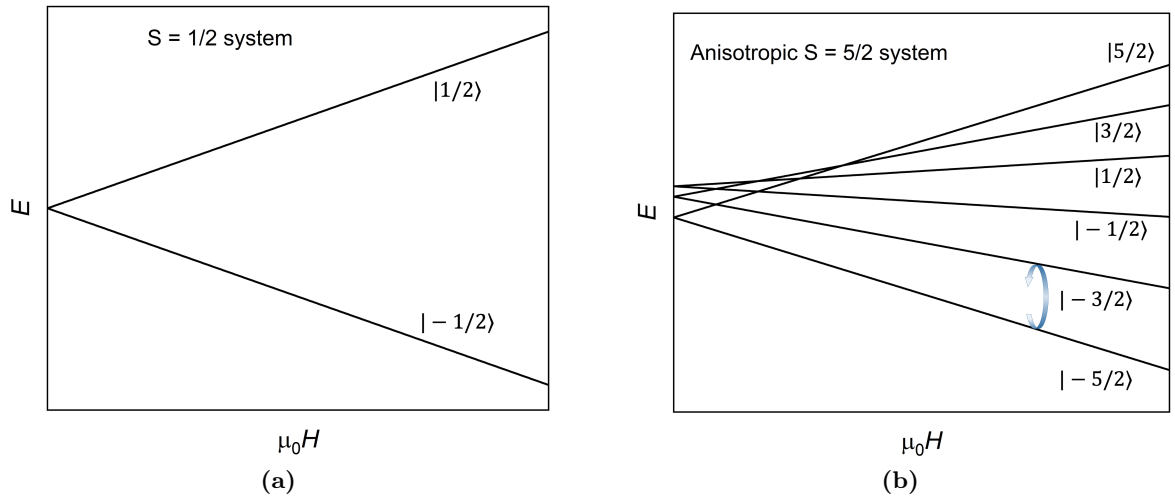

Figure 3.3: Energy diagrams of (a) an isotropic spin 1/2 system and (b) an anisotropic spin 5/2 system in a magnetic field.

Let's now consider the slightly more complex case of a spin system with $S > 1/2$. We can describe it with the following Hamiltonian:

$$\mathcal{H}_S = -DS_z^2 + g_S \mu_B \vec{H} \cdot \vec{S}, \tag{3.13}$$

where D is the uniaxial anisotropy constant which accounts for the zero-field splitting of the energy levels. An example of the Zeeman diagram obtained for a $S = 5/2$ system is shown in Fig. 3.3(b). An initial requirement a system like this should fulfil in order to properly encode a qubit is being anisotropic. This is needed in order to correctly address a single transition with an external resonant excitation. In this case, we can consider two orthogonal spin states of the system with an adequate transition frequency between them and $\Delta m_S = 1$, for example $|S\rangle$ and $|S-1\rangle$, and name them $|0\rangle$ and $|1\rangle$. The matrix elements are then:

$$\begin{aligned}
\langle 0|S_X|1\rangle &= \left\langle 0 \left| \frac{S_+ + S_-}{2} \right| 1 \right\rangle = \frac{1}{2}\langle 0|S_-|1\rangle = \frac{1}{2}\sqrt{S(S+1) - m_0(m_0+1)} \\
\langle 0|S_Y|1\rangle &= \frac{i}{2}\sqrt{S(S+1) - m_0(m_0+1)} \\
\langle 0|S_Z|1\rangle &= 0,
\end{aligned} \tag{3.14}$$

where m_0 is the S_Z eigenvalue of the state chosen to encode $|0\rangle$. Inserting (3.14) in Eq. (3.9), and taking B_q parallel to the X axis, thus perpendicular to the anisotropy axis and to the external magnetic field in Z which produce the splitting between the energy levels:

$$G = g_S \mu_B B_q \frac{1}{2}\sqrt{S(S+1) - m_0(m_0+1)}. \tag{3.15}$$

The value of m_0 depends on each spin system. If $m_0 = 0$, *e.g.* for an integer spin with planar ($D < 0$) magnetic anisotropy, then the coupling is proportional to S, while if $m_0 = -S$, then $G \propto \sqrt{S}$. In any case, the matrix element depends now on the value of the spin, thus it is larger than what we have obtained for the $S = 1/2$ case (see Eq. (3.11)). This fact allows us to search for anisotropic high-spin systems and use two of their spin states as our computational basis. However, the zero-field splitting of high-spin systems is often very large compared to the typical resonance frequencies of superconducting resonators[11;12]. With regard to this, it would be convenient to use systems with low anisotropy, thus low zero-field splittings, and high spin values. In chapter 6 we will introduce an example of this type of systems.

Quantum tunneling: coupling to a spin-clock transition

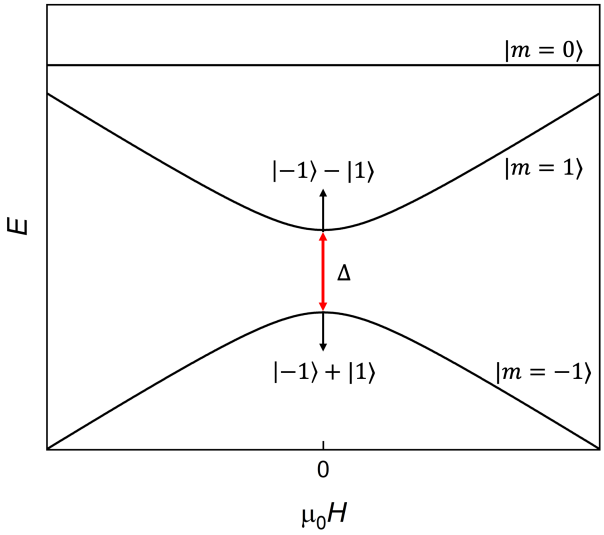

Figure 3.4: Energy levels of a $S = 1$ system described by the Hamiltonian (3.16). The graph shows the energy gap Δ between the entangled states.

In an anisotropic high-spin system, the competition between the Zeeman and the anisotropy terms of the Hamiltonian (or the entanglement between electronic and nuclear spin) can produce a mixing among different energy levels.[13;14] This phenomenom can be illustrated in a simple way by the following Hamiltonian:

$$\mathcal{H}_S = -DS_z^2 + E\left(S_x^2 - S_y^2\right) + g_S\mu_B\vec{H}\cdot\vec{S}, \tag{3.16}$$

where the zero-field splitting is now described by a uniaxial term, with anisotropy constant D, and an orthorhombic diagonal term, with constant E. The latter accounts for the mixing between the states $|m\rangle$ and $|-m\rangle$. The energy diagram of an integer spin system described by (3.16) is illustrated in Fig. 3.4 for the simplest case of $S = 1$. For $H \simeq 0$, this Hamiltonian gives rise to the following eigenstates that we can take as $|0\rangle$ and $|1\rangle$:

$$\begin{aligned} |0\rangle &\simeq \frac{1}{\sqrt{2}}\left(|m\rangle + |-m\rangle\right) \\ |1\rangle &\simeq \frac{1}{\sqrt{2}}\left(|m\rangle - |-m\rangle\right), \end{aligned} \tag{3.17}$$

where m can be any value from S to 0. The off-diagonal term gives rise to a quantum gap Δ at zero field, which for $S = 1$ is $\Delta = E/2$. In this case, the matrix elements are the following:

$$\begin{aligned} &\langle 0|S_X|1\rangle = \frac{1}{4}\left(-\sqrt{S(S+1)+m(-m+1)}\delta_{-m+1,m} + \sqrt{S(S+1)-m(m-1)}\delta_{m-1,-m}\right) = 0 \\ &\langle 0|S_Y|1\rangle = 0 \\ &\langle 0|S_Z|1\rangle = \frac{1}{2}\left(\langle m|S_Z|m\rangle - \langle -m|S_Z|-m\rangle\right) = m. \end{aligned} \tag{3.18}$$

It then follows that only $\langle 0|S_Z|1\rangle$ is different from zero, being possible to achieve stronger coupling strengths using high spin systems showing superposition states with high m. In this case, the microwave magnetic field generated by the superconducting circuit should be parallel to the anisotropy axis of the system, instead of perpendicular as in the previous subsection. This transition is associated with the appearance of an avoided crossing between levels associated to states $|0\rangle$ and $|1\rangle$, being the matrix element maximum at its centre. This level anticrossing

produces yet another very advantageous effect if we want to achieve the strong coupling regime: the cancellation of the first derivative of the transition frequency with respect to the applied magnetic field makes the qubit phase less sensitive to magnetic field fluctuations, and usually implies a sharp increase of the coherence at the anticrossing.[15] Therefore, such systems make it possible to enhance the coupling and the coherence at the same time.

In chapter 6 we will study two systems where these superposition states take place. In HoW_{10}, a molecule with $J = 8$ and ground state with $m_J = \pm 4$, the anisotropy term B_{44} connects the $|+4\rangle$ and $|-4\rangle$ spin projections, producing four anticrossings, or spin-clock transitions, due to the $I = 7/2$ nuclear spin. On the other hand, the vanadyl porphyrin $\mathbf{1^{VO}}$ shows several of these anticrossings at low magnetic fields due to the electronuclear entanglement between its $S = 1/2$ and $I = 7/2$ electronic and nuclear spins.

3.4.2 Dependence of G on the dimensionality of the superconducting circuit

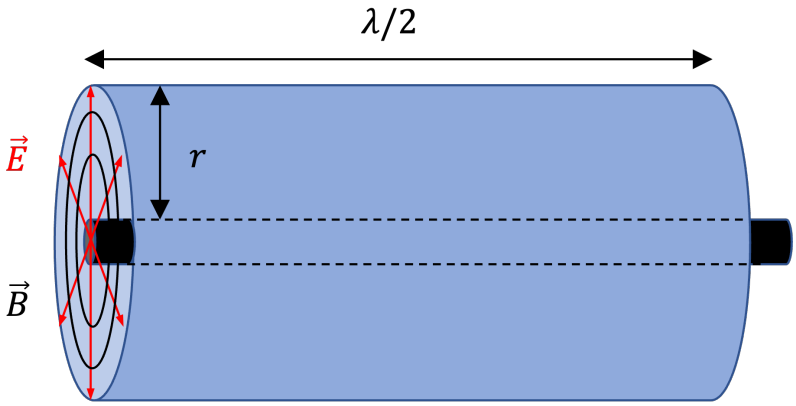

Figure 3.5: Example of a one-dimensional transmission-line cavity, based on a simple coaxial geometry.

The previous analysis indicates how the coupling depends on the nature of the spin states involved in the considered transition. Now, we focus on the evolution of G with the dimensions of the quantum circuit, which can be studied by performing a simple calculation.[16;17] As a first approximation, the coupling is given by the electric (magnetic) field strength at the qubit site times its electric (magnetic) dipole moment:

$$G \simeq dE_0 = \mu B_0, \tag{3.19}$$

being E_0 and B_0 the root-mean-square electric and magnetic field amplitudes, respectively, at the qubit site due to vacuum fluctuations. Given a photon of energy $h\omega$, the average field strength can be calculated remembering that the integral of the field amplitude over the cavity volume is equal to half the energy of a photon (zero-point energy of the cavity):

$$\frac{\omega}{2} = \frac{1}{2}\int_V \varepsilon_0 |E_0|^2 \, dV = \frac{1}{2}\int_V \frac{|B_0|^2}{\mu_0} dV, \tag{3.20}$$

where we have taken $\varepsilon = \varepsilon_0$ and $\mu = \mu_0$. From (3.20) we can obtain the expression for the field intensity in terms of the cavity dimensions:

$$\begin{aligned} E_0 &= \sqrt{\frac{h\omega}{\varepsilon_0 V}} \\ B_0 &= \sqrt{\frac{h\omega\mu_0}{V}}. \end{aligned} \tag{3.21}$$

This result shows that the magnetic field, thus the coupling strength, is proportional to $1/\sqrt{V}$, being V the mode volumen of the cavity. Taking into account that the mode volume of a 3D cavity is much larger than that of a one-dimensional cavity, the enhancement of g in circuit QED compared to cavity QED is rather clear.

In circuit QED, we can consider a 1D transmission line cavity like the one shown in Fig. 3.5. It must be half a wavelength long, but can be much smaller in the transverse direction. The mode volume of this cavity is then:

$$V = \frac{\pi r^2 \lambda}{2}, \tag{3.22}$$

which is much smaller than the mode volume of a 3D cavity provided that $r << \lambda$. Introducing this volume in Eq. (3.21), and using the fact that $\lambda = c/\omega$ we finally obtain:

$$\begin{aligned} E_0 &= \frac{\omega}{r}\sqrt{\frac{2}{\pi\varepsilon_0 c}} \\ B_0 &= \frac{\omega}{r}\sqrt{\frac{2\mu_0}{\pi c}}. \end{aligned} \tag{3.23}$$

Equation (3.23) shows that the field intensity can be enhanced by increasing the resonance frequency of the circuit or by reducing the cavity radius. Increasing the frequency is not always an option, since it is limited by the spin energy levels and the hardware we work with. This means that the easiest way to increase the magnetic field intensity is to reduce the lateral dimension r of the cavity. This is not possible for all type of 3D microwave cavities, being the lateral dimension limited by the radiation wavelength. In circuit QED, these 3D cavities are replaced on-chip resonant circuits, *e.g.* coplanar waveguides (CPW) like the one shown in Fig. 3.6. The transmission properties of these systems are determined by the constituent materials and the ratios between the widths of the central line and the gaps.[18] This allows us decreasing the lateral dimension of the system, for example reducing the diameter of the central line, without modifying the transmission properties. Nanoconstrictions can also be fabricated on these circuits. These structures reduce even more the lateral dimension r of the circuit, thus enhance the microwave magnetic field intensity in its vicinity. If it is short enough compared to the length of the transmission line, the properties of the system are not critically affected.[19]

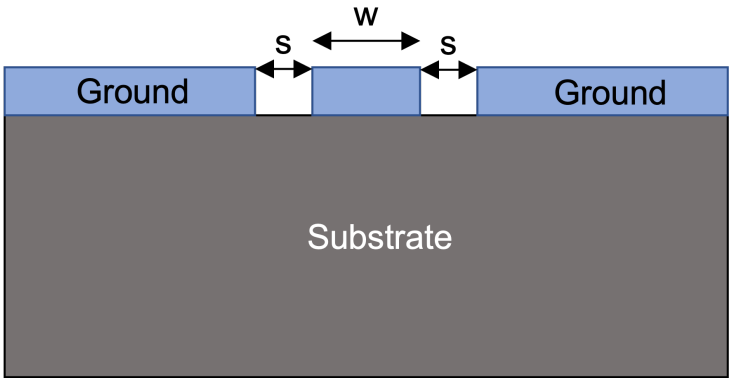

Figure 3.6: Scheme of a coplanar waveguide (CPW).

3.4.3 Dependence of G on the size of the central line

From the previous section it is clear that the more confined the current, the greater the intensity of the microwave magnetic (and electric) field, and thus the single spin-photon coupling. We will

now study the behaviour of the coupling when the width of the central line of a CPW resonator is reduced.

Equation (3.15) shows that the single spin-photon coupling of a spin coupled to any type of cavity is proportional to the intensity of the microwave magnetic field. The profile of this field can be easily simulated for a CPW resonator by finite element methods.[20] We can then evaluate the coupling of a single spin located on the surface of the central line, obtaining the results shown in Fig. 3.7.[21] Here, we have considered two different molecules, DPPH and GdW_{30}. The first one is a free radical with spin 1/2, while GdW_{30} is a molecular nanomagnet with $S = 7/2$ and very weak magnetic anisotropy. We can see an enhancement of $G \propto 1/w$, being increased by three orders of magnitude when the line width w is reduced from 10 μm to 10 nm

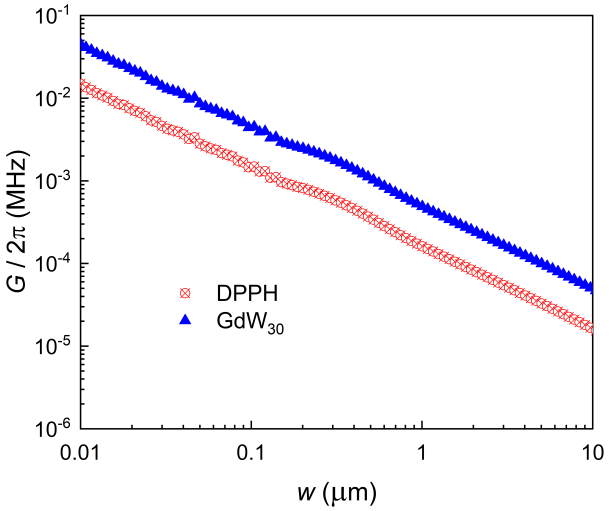

Figure 3.7: Single spin-photon coupling of a free-radical molecule, DPPH, and of a GdW_{30} molecular magnet coupled to a CPW resonator as a function of its central line width. Both spins are located on the surface of the central line. GdW_{30} shows a higher coupling due to its high spin value, $S = 7/2$ (see Eq. (3.15)).

When the width of the central line is reduced, the increase of the microwave magnetic field is accompanied by a reduction of the mode volume. This can be clearly seen if we calculate the collective spin-photon coupling of a molecular crystal with a constant density n of spins per unit volume and length l coupled to a CPW resonator as the one shown in Fig. 3.6. This coupling is then enhanced by $\sqrt{N}$, being N the number of spins:[20;22]:

$$G_N = \frac{g_S \mu_B \sqrt{nl}}{\sqrt{2}} \sqrt{|\langle 0|S_X|1\rangle|^2 \int_S |B_{q,X}|^2 \, dS + |\langle 0|S_Y|1\rangle|^2 \int_S |B_{q,Y}|^2 \, dS}. \tag{3.24}$$

The microwave magnetic field components $B_{q,X}$ and $B_{q,Y}$ can be calculated by finite element methods. By determining these components for the considered resonator, the collective spin-photon coupling strength dependence with the sample height can be calculated for different samples, as shown in Fig. 3.8(a).[20] In this case, a CPW resonator with a 14 μm central line and 7 μm gaps has been considered.

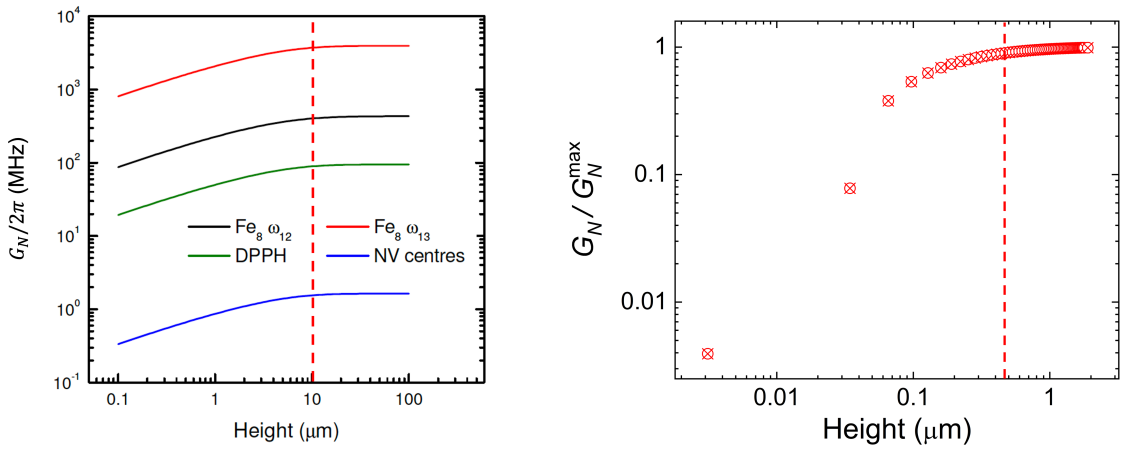

Figure 3.8: (a) Collective coupling of 40 μm×40 μm×height molecular and diamond crystals to a CPW resonator with a 14 μm wide central line as a function of the crystal height.[20] The spin densities are: Fe_8: 5.11×10^{20} spins/cm^3; DPPH: 2.14×10^{21} spins/cm^3; NV centres: 1.1×10^{18} spins/cm^3. (b) Collective coupling of a DPPH crystal located on top of a 50 nm wide, 10 μm long nanoconstriction, normalised by the maximum coupling value. Red dashed lines indicate the maximum crystal height that contributes significantly to the collective coupling, and that therefore defines the height of the magnetic mode. It is reduced from $\sim$ 14 μm to 500 nm near the nanoconstriction, so the spins located beyond this distance do not significantly contribute to the coupling.

Figure 3.8 shows the difference between the mode volumes of a CPW resonator with a 14 μm wide central line and another with a 50 nm nanoconstriction. While the lateral dimension r in the 14 μm wide resonator is $\sim$ 14 μm, when a 50 nm nanoconstriction is considered it is reduced to 500 nm. This implies that the size of the molecular samples need to be adapted to the dimensions of the superconducting circuits, since the maximum height at which a spin will contribute significantly to the coupling will be given by the central line width.

3.5 Transmission through superconducting circuits coupled to spin qubits

In this section we describe the theory that accounts for the transmission of microwave radiation through an open line and a resonator. Although the mathematical derivation of the formulas for the transmission is somewhat laborious, it is necessary as they form the basis to interpret the results of the measurements that will be shown in the following chapters.

3.5.1 Transmission through an open line

Scheme and Hamiltonian

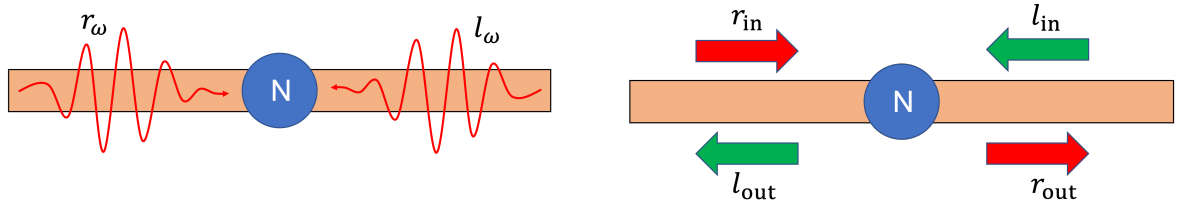

(a) (b)

Figure 3.9: Scheme of an open line coupled to an ensemble of N spins. The ensemble is coupled to both right and left moving photons, described by (a) the annihilation operators r_ω and l_ω respectively or (b) input and output fields r_{in}, l_{in}, r_{out} and l_{out}.

Transmission and reflection formulas are based on the input-output theory,[1;2] which relates the microwave radiation injected into the system (input field) with that transmitted or reflected (output fields). If we consider a spin ensemble coupled to a transmission line (an open line which allows the transmission of photons independently of their frequency), the Hamiltonian which describes the coupled system can be written as:

$$\mathcal{H} = \mathcal{H}_s + \mathcal{H}_l + \mathcal{H}_{sl} = \mathcal{H}_s + \int d\omega\, \omega \left(r_\omega^\dagger r_\omega + l_\omega^\dagger l_\omega \right) + \hat{S} \int d\omega\, G(\omega) \left(r_\omega^\dagger + l_\omega^\dagger + r_\omega + l_\omega \right), \quad (3.25)$$

where we have distinguished between photons moving right or left by the creation (annihilation) operators $r_\omega^\dagger$ (r_ω) and $l_\omega^\dagger$ (l_ω), respectively, and the same single spin-photon coupling $G(\omega)$ has been considered for both. $\hat{S}$ is an operator that accounts for the interaction between the spins and the open line, and ω is the frequency of the photons propagating through the line. An scheme of this system is shown in Fig. 3.9.

The transmission through an open line coupled to a single spin can be defined as:

$$t \equiv \frac{\langle r_{\text{out}} \rangle}{\langle r_{\text{in}} \rangle} \quad (3.26)$$

where r_{in} and r_{out} are the time-dependent input and output fields introduced in Fig. 3.9(b). These fields can be defined from the frequency-dependent annihilation operators as:

$$r_{\text{in}}(t) := \int_0^\infty d\omega \frac{1}{\sqrt{2\pi}} r_\omega(t_0) e^{-i\omega(t-t_0)} \quad (3.27)$$

$$l_{\text{in}}(t) := \int_0^\infty d\omega \frac{1}{\sqrt{2\pi}} l_\omega(t_0) e^{-i\omega(t-t_0)} \quad (3.28)$$

$$r_{\text{out}}(t) := \int_0^\infty d\omega \frac{1}{\sqrt{2\pi}} r_\omega(t_f) e^{-i\omega(t-t_f)} \quad (3.29)$$

$$l_{\text{out}}(t) := \int_0^\infty d\omega \frac{1}{\sqrt{2\pi}} l_\omega(t_f) e^{-i\omega(t-t_f)} \quad (3.30)$$

We need to determine the time evolution of the operators r_ω and l_ω to obtain an expression for the transmission. Knowing the Hamiltonian, we can study the dynamics of the outcoming photons, $\dot{r}_\omega$. In the Heisenberg picture:

$$\dot{r}_\omega = -i\,[r_\omega, \mathcal{H}] = -i\omega r_\omega - i\hat{S} G(\omega), \quad (3.31)$$

where we have taken into account that only the commutators $\left[r_\omega, r_\omega^\dagger r_\omega\right]$ and $\left[r_\omega, r_\omega^\dagger\right]$ are different from zero. We need a particular solution $r_{\omega,\text{inh}}$ of this inhomogeneous equation in order to obtain the time evolution of r_ω:

$$\dot{r}_{\omega,\text{inh}} = -i\omega r_{\omega,\text{inh}} + \dot{f}(t)e^{-i\omega t} = -i\omega r_{\omega,\text{inh}} - i\hat{S}G(\omega) \Longrightarrow r_{\omega,\text{inh}}(t_\text{f}) = -iG(\omega)\int_{t_0}^{t_\text{f}} d\tau\, \hat{S}(\tau)e^{-i\omega(t_\text{f}-\tau)} \tag{3.32}$$

In this equation t_0 indicates the time in which the incident wave packet is injected in the line, while t_f is any time after the interaction between the incident wave packet and the spins has occurred.

The final time evolution of a photon with frequency ω moving right is the sum of the solutions of the homogeneous equation, $\dot{r}_{\omega,\text{h}} = -i\omega r_\omega$ and of the inhomogeneous one, given by (3.32):

$$\begin{aligned} r_\omega(t_\text{f}) = r_{\omega,h}(t_\text{f}) + r_{\omega,\text{inh}}(t_\text{f}) = r_\omega(t_0)e^{-i\omega(t_\text{f}-t_0)} - iG(\omega)\int_{t_0}^{t_\text{f}} d\tau\, \hat{S}(\tau)e^{-i\omega(t_\text{f}-\tau)}d\tau \\ r_\omega e^{i\omega t_\text{f}} = r_\omega e^{i\omega t_0} - iG(\omega)\int_{t_0}^{t_\text{f}} d\tau\, \hat{S}(\tau)e^{i\omega\tau}d\tau \end{aligned} \tag{3.33}$$

Repeating this process for the photons moving left we obtain the equivalent expression:

$$l_\omega e^{i\omega t_f} = l_\omega e^{i\omega t_0} - ig(\omega)\int_{t_0}^{t_f} S(\tau)e^{i\omega\tau}d\tau \tag{3.34}$$

Combining Eqs. (3.33) and (3.34) with the previous definitions of the input and output fields, and making $t_0 \to -\infty$ and $t_\text{f} \to \infty$, we can rewrite the output fields as:

$$\begin{aligned} r_\text{out}(t) = r_\text{in} - i\sum_{n=1}^{N}\int_0^\infty d\omega \frac{G_n(\omega)e^{-i\omega t}}{\sqrt{2\pi}}\int_{-\infty}^{\infty} d\tau\, e^{i\omega\tau}\hat{S}_n(\tau) \\ l_\text{out}(t) = l_\text{in} - i\sum_{n=1}^{N}\int_0^\infty d\omega \frac{G_n(\omega)e^{-i\omega t}}{\sqrt{2\pi}}\int_{-\infty}^{\infty} d\tau\, e^{i\omega\tau}\hat{S}_n(\tau) \end{aligned} \tag{3.35}$$

where we have considered the sum in n of N spins coupled to the line. This result links the input and output fields through the dynamics of the spin operator $\hat{S}(\tau)$.

Replacing Eq. (3.35) in Eq. (3.26), we obtain the following expression for the transmission through an open line coupled to a single spin:

$$t \equiv \frac{\langle r_\text{out}\rangle}{\langle r_\text{in}\rangle} = 1 - \frac{i}{\langle r_\text{in}\rangle}\int_0^\infty d\omega \frac{G(\omega)e^{-i\omega t}}{\sqrt{2\pi}}\int_{-\infty}^{\infty} d\tau\, e^{i\omega\tau}\left\langle \hat{S}(\tau)\right\rangle \tag{3.36}$$

In Eq. (3.36), $\langle r_\text{in}\rangle$ is basically the driving we introduce in the system. This term has the form $\langle r_\text{in}\rangle = \alpha e^{-i\omega_0 t}/2\pi$, where α is the driving amplitude. The interaction Hamiltonian associated to this oscillating driving is then:

$$\mathcal{H}_\text{int} = 2\alpha G(\omega)\hat{S}(t)\cos(\omega t). \tag{3.37}$$

The only parameter we then need to calculate for determining the transmission through the system is the average of the interaction operator $\left\langle \hat{S}(\tau)\right\rangle = \text{Tr}_s\left(\hat{S}\rho_s\right)$. This calculation can be performed by first determining the quantum master equation of the spins. This calculation is shown below.

Derivation of the quantum master equation of an open line coupled to a spin ensemble

The density matrix of the total system, described by Eq. (3.25), obeys the von-Neumann equation:

$$\dot{\rho} = -i\left[\mathcal{H}, \rho\right] = -i\left[\mathcal{H}_s, \rho\right] - i\left[\mathcal{H}_l, \rho\right] - i\left[\mathcal{H}_{sl}, \rho\right] \equiv \left(\mathcal{L}_s + \mathcal{L}_l + \mathcal{L}_{sl}\right)\rho = \mathcal{L}\rho, \tag{3.38}$$

where $\mathcal{L}_s$, $\mathcal{L}_l$ and $\mathcal{L}_{sl}$ are the Liouvillian operators of the spins, the line and the interaction between them, respectively. Equation (3.38) determines the evolution of $\rho(t)$ if $\rho(0)$ and all the interactions are known. If we suppose that the spins and the transmission line were uncoupled before $t = 0$, $\rho(0)$ factorizes as:

$$\rho(0) = \rho_l(0) \otimes \rho_s(0), \tag{3.39}$$

where $\rho_s(0)$ is an arbitrary initial condition of the Hilbert space of the spin system and $\rho_l(0) = \rho_l^e$ is an equilibrium distribution of the Hilbert space of the transmission line, so that $\mathcal{L}_l\rho_l^e = 0$. This means that the density matrix of the transmission line does not evolve over time if the interaction with the spins is not taken into account. With these considerations, the evolution of ρ is:

$$\rho(t) = e^{-it\mathcal{H}}\rho(0)e^{it\mathcal{H}} = e^{t\mathcal{L}}\left(\rho_l^e \otimes \rho_s(0)\right). \tag{3.40}$$

The density matrix of the spins can be obtained by taking the trace of the total density matrix over the line states:

$$\rho_s(t) = \mathrm{Tr}_l\rho(t) = \mathrm{Tr}_l e^{t\mathcal{L}}\left(\rho_l^e \otimes \rho_s(0)\right). \tag{3.41}$$

Equation (3.41) cannot be solved directly. We need to introduce an expansion parameter α, so that $\mathcal{L}_{sl}$ is changed to $\alpha\mathcal{L}_{sl}$. Using the interaction representation σ and perturbation theory:

$$\rho(t) = e^{t(\mathcal{L}_s+\mathcal{L}_l)}\sigma(t) \equiv e^{t\mathcal{L}_0}\sigma(t), \tag{3.42}$$

where $\mathcal{L}_0$ is the unperturbed Liouvillian operator, $\mathcal{L}_0 = \mathcal{L}_s + \mathcal{L}_l$. The operator $\mathcal{L}_s$ acts over the spin states, so it commutes with the trace over the line states, and $\mathcal{L}_l$ does not affect the trace over the line states because we are considering an equilibrium state of the transmission line ρ_l^e ($\mathcal{L}_l\rho_l^e = 0$). Knowing this, we obtain an expression for $\rho_s(t)$:

$$\rho_s(t) = e^{t\mathcal{L}_s}\mathrm{Tr}_l\sigma(t). \tag{3.43}$$

We can now calculate the evolution of $\sigma(t)$:

$$\begin{aligned}\dot{\rho}(t) &= \frac{d}{dt}\left(e^{t\mathcal{L}_0}\sigma(t)\right) = \frac{d}{dt}\left(e^{-it\mathcal{H}_0}\sigma(t)e^{it\mathcal{H}_0}\right) = -i\left[\mathcal{H}_0, e^{-it\mathcal{H}_0}\sigma(t)e^{it\mathcal{H}_0}\right] + e^{-it\mathcal{H}_0}\dot{\sigma}(t)e^{it\mathcal{H}_0} = \\ &= \mathcal{L}_0 e^{t\mathcal{L}_0}\sigma(t) + e^{t\mathcal{L}_0}\dot{\sigma}(t)\end{aligned} \tag{3.44}$$

$$\begin{aligned}\Rightarrow \dot{\sigma}(t) &= e^{-t\mathcal{L}_0}\left(\dot{\rho}(t) - \mathcal{L}_0 e^{t\mathcal{L}_0}\sigma(t)\right) = e^{-t\mathcal{L}_0}\left(\left(\mathcal{L}_0 + \alpha\mathcal{L}_{sl}\right)e^{t\mathcal{L}_0}\sigma(t) - \mathcal{L}_0 e^{t\mathcal{L}_0}\sigma(t)\right) = \\ &= \alpha e^{-t\mathcal{L}_0}\mathcal{L}_{sl}e^{t\mathcal{L}_0}\sigma(t) \equiv \alpha\mathcal{L}_{sl}(t)\sigma(t)\end{aligned} \tag{3.45}$$

Equation (3.45) can be approximately solved to second order in αt:

$$\begin{aligned}\sigma(t) &= \sigma(0) + \alpha\int_0^t dt_1\mathcal{L}_{sl}(t_1)\sigma(0) + \alpha^2\int_0^t dt_1\int_0^{t_1} dt_2\mathcal{L}_{sl}(t_1)\mathcal{L}_{sl}(t_2)\sigma(0) = \\ &= \sigma(0) + \alpha\int_0^t dt_1\mathcal{L}_{sl}(t_1)\rho(0) + \alpha^2\int_0^t dt_1\int_0^{t_1} dt_2\mathcal{L}_{sl}(t_1)\mathcal{L}_{sl}(t_2)\rho(0),\end{aligned} \tag{3.46}$$

where we have considered $\sigma(0) = \rho(0)$. From Eq. (3.43) we need to calculate the trace of $\sigma(t)$ over the line states. Considering the previous expression, this trace is:

$$\begin{aligned}\mathrm{Tr}_l\sigma(t) &= \mathrm{Tr}_l\sigma(0) + \alpha^2\mathrm{Tr}_l\int_0^t dt_1\int_0^{t_1} dt_2\mathcal{L}_{sl}(t_1)\mathcal{L}_{sl}(t_2)\sigma(0) = \\ &= \rho_s(0) + \alpha^2\int_0^t dt_1\int_0^{t_1} dt_2\mathrm{Tr}_l\left\{\mathcal{L}_{sl}(t_1)\mathcal{L}_{sl}(t_2)\rho_l^e\right\}\rho_s(0). \end{aligned} \tag{3.47}$$

We can now differentiate Eq. (3.47) and, combining the result with Eq. (3.43), we finally obtain an expression for the evolution of $\rho_s(t)$:

$$\frac{d}{dt}\rho_s(t) = \frac{d}{dt}\left(e^{t\mathcal{L}_s}\mathrm{Tr}_l\sigma(t)\right) = \left(\mathcal{L}_s + \alpha^2\int_0^\infty d\tau\mathrm{Tr}_l\left\{\mathcal{L}_{sl}\mathcal{L}_{sl}(-\tau)\rho_l^e\right\}\right)\rho_s(t). \tag{3.48}$$

The second term in Eq. (3.48) can be written as the following double commutator:

$$\begin{aligned}\mathcal{L}_{sl}\mathcal{L}_{sl}(-\tau)\rho_l^e\rho_s(t) &= \mathcal{L}_{sl}e^{\tau\mathcal{L}_0}\mathcal{L}_{sl}e^{-\tau\mathcal{L}_0}\rho_l^e\rho_s(t) = \\ &= -\left[\mathcal{H}_{sl}(t),\left[\mathcal{H}_{sl}(t'),\rho_l^e\rho_s(t)\right]\right]. \end{aligned} \tag{3.49}$$

In a general way, we can consider an interaction Hamiltonian $\mathcal{H}_{sl}(t) = \sum_i S_i(t)\otimes L_i(t)$, where S_i and L_i are operators acting over the spin and line states respectively. We need to calculate the trace of this interaction Hamiltonian over the line states:

$$\begin{aligned}&\mathrm{Tr}_l\left[\mathcal{H}_{sl}(t),\left[\mathcal{H}_{sl}(t'),\rho_l^e\rho_s(t)\right]\right] = \mathrm{Tr}_lQ = \\ &= \sum_{i,j}\mathrm{Tr}_l\left\{S_i(t)S_j(t')\rho_s(t)\mathrm{Tr}_l\left(L_i(t)L_j(t')\rho_l^e\right) - S_i(t)\rho_s(t)S_j(t')\mathrm{Tr}_l\left(L_i(t)\rho_l^eL_j(t')\right) - \right. \\ &\left. -S_j(t')\rho_s(t)S_i(t)\mathrm{Tr}_l\left(L_j(t')\rho_l^eL_i(t)\right) + \rho_s(t)S_j(t')S_i(t)\mathrm{Tr}_l\left(\rho_l^eL_j(t')L_i(t)\right)\right\}. \end{aligned} \tag{3.50}$$

We can define the two time correlators $c_{ij}(t,t') = \langle L_i(t)L_j(t')\rangle$. Equation (3.50) then reads:

$$\begin{aligned}\mathrm{Tr}_lQ &= \sum_{i,j}\left\{c_{ij}(t,t')\left[S_i(t)S_j(t')\rho_s(t) - S_j(t')\rho_s(t)S_i(t)\right] + \right. \\ &\left. c_{ji}(t',t)\left[\rho_s(t)S_j(t')S_i(t) - S_i(t)\rho_s(t)S_j(t')\right]\right\} = \\ &= \sum_{i,j}\left\{c_{ij}(t,t')\left[S_i(t),S_j(t')\rho_s(t)\right] - c_{ji}(t',t)\left[S_i(t),\rho_s(t)S_j(t')\right]\right\}. \end{aligned} \tag{3.51}$$

It is easy to check that the two time correlators depend on $t-t'$ and that $c_{ij}(t-t') = c_{ji}^*(t'-t)$ if $L = L^\dagger$. Taking this into account and defining $\tau = t-t'$, the integral of Eq. (3.48) becomes:

$$\int_0^\infty d\tau\mathrm{Tr}_lQ = \int_0^\infty d\tau\sum_{i,j}\left\{c_{ij}(\tau)\left[S_i(t),S_j(t')\rho_s(t)\right] - c_{ji}^*(\tau)\left[S_i(t),\rho_s(t)S_j(t')\right]\right\}. \tag{3.52}$$

We can replace $S_i(t)$ and $S_j(t')$ by their spectral decompositions:

$$S_i(t) = \sum_\omega S_i(\omega)e^{i\omega t}\ ,\ S_i(\omega) = S_i^\dagger(-\omega), \tag{3.53}$$

so the previous integral can be written as:

$$\begin{aligned}\int_0^\infty d\tau\mathrm{Tr}_lQ = \int_0^\infty d\tau\sum_{i,j}\sum_{\omega,\omega'}\Big\{&c_{ij}(\tau)e^{-i\omega t}e^{i\omega' t'}\left[S_i^\dagger(\omega),S_j(\omega')\rho_s(t)\right] - \\ &-c_{ji}^*(\tau)e^{-i\omega t}e^{i\omega' t'}\left[S_i(\omega),\rho_s(t)S_j^\dagger(\omega')\right]\Big\}. \end{aligned} \tag{3.54}$$

Now, using the equality $e^{-i\omega t}e^{i\omega' t'} = e^{-i(\omega-\omega')t}e^{-i\omega'(t-t')}$ and the rotating wave approximation:

$$\int_0^\infty d\tau \mathrm{Tr}_l Q = \int_0^\infty d\tau \sum_{i,j,\omega} \left\{ s_{ij}(\tau)e^{-i\omega\tau}\left[S_i^\dagger(\omega), S_j(\omega)\rho_s(t)\right] - c_{ji}^*(\tau)e^{-i\omega\tau}\left[S_i(\omega), \rho_s(t)S_j^\dagger(\omega)\right]\right\}. \tag{3.55}$$

We can define the following terms:

$$c_{ij}(\omega) = \frac{1}{2}\int_0^\infty d\tau\, c_{ij}(\tau)e^{-i\omega\tau} \tag{3.56}$$

$$\Gamma_{ij}(\omega) = \frac{1}{2}\int_0^\infty d\tau \left\{c_{ij}(\tau)e^{-i\omega\tau} + c_{ji}^*(\tau)e^{i\omega\tau}\right\} = \int_{-\infty}^\infty d\tau\, c_{ij}(\tau)e^{-i\omega\tau}, \tag{3.57}$$

$$\gamma_{ij}(\omega) = \frac{1}{2i}\int_0^\infty d\tau \left\{c_{ij}(\tau)e^{-i\omega\tau} - c_{ji}^*(\tau)e^{i\omega\tau}\right\}. \tag{3.58}$$

Using these terms and after some algebra with the commutators of Eq. (3.55), we finally arrive to the following general expression for the quantum master equation of the spins:

$$\frac{d}{dt}\rho_s(t) = -i\left[\mathcal{H}_s, \rho_s(t)\right] + \sum_{i,j,\omega}\Gamma_{ij}(\omega)\left[2S_j(\omega)\rho_s(t)S_i^\dagger(\omega) - \left\{S_i^\dagger(\omega)S_j(\omega), \rho_s(t)\right\}\right]. \tag{3.59}$$

Now, we will consider the interaction Hamiltonian of the spins-line system:

$$\mathcal{H}_{sl}(t) = \sum_{i,j} S_{ij}P_{ij}e^{i\omega_{ji}t} \otimes \int d\omega\, G(\omega)\left(r_\omega^\dagger e^{-i\omega t} + l_\omega^\dagger e^{-i\omega t} + r_\omega e^{i\omega t} + l_\omega e^{i\omega t}\right), \tag{3.60}$$

where $\omega_{ji} = \omega_j - \omega_i$ is the frequency difference between spin states i and j, $S_{ij} = \langle i|S|j\rangle$ and $P_{ij} = |i\rangle\langle j|$ are relaxation operators connecting allowed transitions $i \leftrightarrow j$. With this Hamiltonian, we can calculate the two time correlators $c_{\omega\omega'}(\tau) = \langle B_\omega(\tau)B_{\omega'}\rangle$, obtaining:

$$c_{\omega\omega'}(\tau) = \int d\omega\, G^2(\omega)\left\{\cos(\omega\tau)\left[2n(\omega)+1\right] + i\sin(\omega\tau)\right\}, \tag{3.61}$$

being $n(\omega) = \left(e^{\beta\omega_{ji}} - 1\right)^{-1}$ the bosonic occupation number. Introducing Eq. (3.61) in Eq. (3.57) gives the following expression for $\Gamma(\omega)$:

$$\begin{aligned}\Gamma(\omega) &= \int_{-\infty}^\infty d\tau\, c(\tau)e^{-i\omega\tau} = \int_{-\infty}^\infty d\tau \int d\omega'\, G^2(\omega')\left[\left(n(\omega')+1\right)e^{i(\omega'-\omega)\tau} + e^{i(-\omega'-\omega)\tau}n(\omega')\right] \\ &= \begin{cases} 2\pi G^2(\omega)\left[n(\omega)+1\right] & ,\ \omega > 0 \\ 2\pi G^2(\omega)n(\omega) & ,\ \omega < 0 \end{cases}.\end{aligned} \tag{3.62}$$

Introducing this term in Eq. (3.59) and considering that we are driving the system with the oscillatory interaction introduced in Eq. (3.37), we finally obtain the quantum master equation of an spin coupled to a transmission line:

$$\begin{aligned}\frac{d}{dt}\rho_s(t) =& -i\left[\mathcal{H}_s, \rho_s(t)\right] + 2\sum_{\omega_{ij}}\Gamma_{ij}(\omega_{ij})\left[P_{ij}\rho_s(t)P_{ij}^\dagger - \frac{1}{2}\left\{P_{ij}^\dagger P_{ij}, \rho_s(t)\right\}\right] - \\ &- i2\alpha g(\omega)\cos(\omega t)\left[S(t), \rho_s(t)\right] + \mathcal{D}\rho_s(t)\mathcal{D} - \frac{1}{2}\left\{\mathcal{D}^2, \rho_s(t)\right\}.\end{aligned} \tag{3.63}$$

The thermal rates $\Gamma_{ij}(\omega_{ij})$ are:

$$\begin{aligned}\Gamma_{ij}(\omega_{ij}>0) &= \left[2\pi g^2(\omega_{ij})\left|\langle i\left|S\right|j\rangle\right|^2+\tilde{\gamma}_{ij}\right]\left[n(\omega_{ij})+1\right]\equiv\mathcal{G}_{ij}+\gamma_{ij}\\ \Gamma_{ij}(\omega_{ij}<0) &= \left[2\pi g^2(\omega_{ij})\left|\langle i\left|S\right|j\rangle\right|^2+\tilde{\gamma}_{ij}\right]n(\omega_{ij}) = e^{-\beta\omega_{ji}}\Gamma_{ij}(\omega_{ji}).\end{aligned} \tag{3.64}$$

We have considered the intrinsic losses of the spin via the parameter $\tilde{\gamma}_{ij}\left[n(\omega_{ij}+1)\right]=\gamma_{ij}$, which corresponds to the inverse of the relaxation time, T_1^{-1}, for the transition $i\leftrightarrow j$. $\mathcal{D}$ is a diagonal matrix accounting for pure dephasing due to phase flips. This term is phenomenological and will not be considered in the calculation of $\left\langle\hat{S}(\tau)\right\rangle$. Finally, the 2 in front of the sum appears because the master equation is coupled both to left (l_ω) and right (r_ω) modes.

Calculation of the transmission through an open line coupled to a spin ensemble

To obtain the transmission through a spin coupled to a transmission line, we need to calculate $\left\langle\hat{S}(\tau)\right\rangle=\mathrm{Tr}_s(\hat{S}\rho_s)$ using the master equation (3.63). Considering that we are within the linear response theory regime, we can write:

$$\left\langle\hat{S}(\tau)\right\rangle=\hat{S}(\omega)e^{i\omega_0\tau}+\hat{S}^*(\omega)e^{-i\omega_0\tau}. \tag{3.65}$$

Replacing Eq. (3.65) in Eq. (3.35), we get:

$$\langle r_{out}(t)\rangle=\langle r_{in}(t)\rangle-i\sqrt{2\pi}G(\omega_0)\hat{S}(\omega_0)e^{-i\omega_0 t}, \tag{3.66}$$

and introducing Eq. (3.66) in Eq. (3.36):

$$t^{(1)}(\omega)=1-i2\pi G(\omega_0)\frac{1}{\alpha}\hat{S}(\omega_0). \tag{3.67}$$

We can now use the definition of susceptibility, $\hat{S}(\omega)=\alpha G(\omega)\chi_{\hat{S},\hat{S}}(\omega)$, obtaining the transmission as a function of the latter:

$$t^{(1)}(\omega)=1-i2\pi G(\omega)^2\chi_{S,S}(\omega). \tag{3.68}$$

The susceptibility $\chi_{\hat{S},\hat{S}}$ can be written as:

$$\chi_{\hat{S},\hat{S}}\cong-i\sum_{\omega_{ij}}\left|\left\langle i\left|\hat{S}\right|j\right\rangle\right|^2\frac{e^{-\beta\omega_j}-e^{-\beta\omega_i}}{\mathcal{Z}_0}\frac{1}{\Gamma_{ij}+i(\omega_{ij}-\omega)}, \tag{3.69}$$

where $\mathcal{Z}_0$ is the partition function of the system. Introducing this expression in Eq. (3.68), we obtain the transmission through an open line coupled to a single spin:

$$t^{(1)}(\omega)=1-\sum_{\omega_{ij}}\frac{\mathcal{G}_{ij}\Delta P_{ij}}{\mathcal{G}_{ij}+\gamma_{ij}+i(\omega_{ij}-\omega)}, \tag{3.70}$$

where $\Delta P_{ij}=\frac{e^{-\beta\omega_j}-e^{-\beta\omega_i}}{\mathcal{Z}_0}$ and $\mathcal{G}_{ij}=2\pi G^2(\omega_{ij})\left|\left\langle i\left|\hat{S}\right|j\right\rangle\right|^2\left[n(\omega_{ij})+1\right]$.

The total transmission for a line coupled to an ensemble of N spins can be computed using the transfer matrix:

$$t=\frac{1}{1-\sum_n r_n^{(1)}/t_n^{(1)}}, \tag{3.71}$$

with

$$\frac{r_n^{(1)}}{t_n^{(1)}} = \frac{t_n^{(1)} - 1}{t_n^{(1)}} \simeq \sum_{i,j} -\frac{\mathcal{G}_{n,ij}\Delta P_{ij}}{\gamma + i(\omega_{ij} - \omega)}. \tag{3.72}$$

We have assumed that the spontaneous emission in the line $\mathcal{G}_n$ for each spin can differ since each of them is at a different position with respect to the line.

3.5.2 Transmission through a resonator

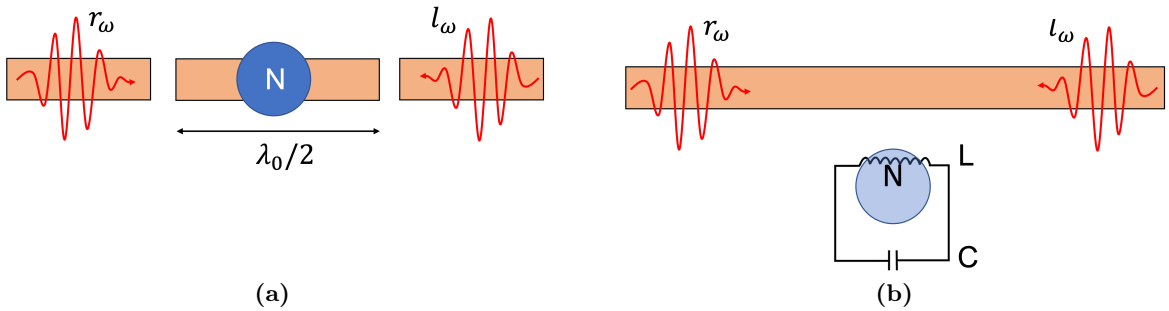

Figure 3.10: Scheme of (a) a CPW resonator coupled to an ensemble of N spins and (b) a LER coupled to an ensemble of N spins and to an open line.

The system under study now is an spin ensemble coupled to a lumped element resonator (LER) or a CPW resonator, being the resonator coupled at the same time to a transmission line. The schemes of both systems are shown in Fig. 3.10 The CPW resonator consists of a transmission line segment, with length $\lambda/2$, separated from the main transmission line by two capacitors that act as the mirrors of the cavity shown in Fig. 3.2. This 2D cavity produces stationary waves of wavelength $l = n\lambda_0/2$, where $n = 1, 2, ...$ indicates the harmonic we are considering. On the other hand, LERs are formed by an LC resonator inductively or capacitively coupled to a feedline.

We will first calculate the transmission for the simpler case of a bare resonator (no spins), and later we will obtain it for the complete system.

Bare resonator

The system we are considering now is a resonator coupled to a transmission line. The full system can be described by means of the Jaynes-Cummings Hamiltonian: [9]

$$\begin{aligned}\mathcal{H} &= \mathcal{H}_{\text{res}} + \mathcal{H}_{\text{line}} + \mathcal{H}_1 = \\ &= \omega_r a_0^\dagger a_0 + \int d\omega\, \omega \left(r_\omega^\dagger r_\omega + l_\omega^\dagger l_\omega\right) + \left(a_0^\dagger + a_0\right) \int d\omega\, G(\omega) \left(r_\omega^\dagger + l_\omega^\dagger + r_\omega + l_\omega\right) \simeq \\ &\simeq \omega_r a_0^\dagger a_0 + \int d\omega\, \omega \left(r_\omega^\dagger r_\omega + l_\omega^\dagger l_\omega\right) + a_0 \int d\omega\, G(\omega) \left(r_\omega^\dagger + l_\omega^\dagger\right) + a_0^\dagger \int d\omega\, G(\omega) \left(r_\omega + l_\omega\right).\end{aligned} \tag{3.73}$$

Here, $\mathcal{H}_1$ is the interaction Hamiltonian between the resonator and the line, ω_r is the resonance frequency of the resonator and a_0 and $a_0^\dagger$ are the annihilation and creation operators acting over the resonator states.

The transmission through this system can be derived from the same Eq. (3.36) we used in the previous section. The difference is that we are considering a resonator, so the term $\left\langle \hat{S}(\tau) \right\rangle$ is

now $\langle a_0(\tau)\rangle$. As in the previous section, we can obtain this expression by means of the quantum master equation of the system (here, the resonator).

Quantum master equation of a bare resonator

In order to derive the quantum master equation of a resonator, we first have to determine the double commutator shown in Eq. (3.49). Replacing t and t' with τ:

$$-\left[\mathcal{H}_1,\left[\mathcal{H}_1(-\tau),\rho^e_{\text{line}}\rho_{\text{res}}\right]\right] = -\int d\omega\, G(\omega)\int d\omega'\, G(\omega')$$
$$\left[a_0\left(r^\dagger_{\omega'}+l^\dagger_{\omega'}\right)+a_0^\dagger\left(r_{\omega'}+l_{\omega'}\right),\left[a_0\left(r^\dagger_{\omega}+l^\dagger_{\omega}\right)e^{i\tau(\omega_r-\omega)}+a_0^\dagger\left(r_{\omega}+l_{\omega}\right)e^{-i\tau(\omega_r-\omega)},\rho^e_{\text{line}}\rho_{\text{res}}\right]\right]. \tag{3.74}$$

Here, we have considered that the time evolution of the operators a_0, r_ω and l_ω is given by:

$$\dot{a}_0 = -i\omega_r a_0 \;\Rightarrow\; a_0(-\tau) = e^{i\omega_r\tau}a_0, \tag{3.75}$$

$$\dot{r}_\omega = -i\omega r_\omega \;\Rightarrow\; r_\omega(-\tau) = e^{i\omega\tau}r_\omega \tag{3.76}$$

$$\dot{l}_\omega = -i\omega l_\omega \;\Rightarrow\; l_\omega(-\tau) = e^{i\omega\tau}l_\omega \tag{3.77}$$

Using the rotating wave approximation, we can eliminate one of the integrals of Eq. (3.74), keeping the one in ω. If we now take the trace over the line states, only the terms with $r_\omega r^\dagger_\omega$, $r^\dagger_\omega r_\omega$, $l_\omega l^\dagger_\omega$ and $l^\dagger_\omega l_\omega$ will not vanish. It then follows that:

$$\begin{aligned}
&\text{Tr}_{\text{line}}\left\{-\left[\mathcal{H}_1,\left[\mathcal{H}_1(-\tau),\rho^e_{\text{line}}\rho_{\text{res}}\right]\right]\right\} = \\
&= -2\int d\omega\, G^2(\omega)\left[n(\omega)\left(a_0a_0^\dagger\rho_{\text{res}} - a_0^\dagger\rho_{\text{res}}a_0\right)+(n(\omega)+1)\left(\rho_{\text{res}}a_0^\dagger a_0 - a_0\rho_{\text{res}}a_0^\dagger\right)\right]e^{-i\tau(\omega_r-\omega)} \\
&- 2\int d\omega\, G^2(\omega)\left[n(\omega)\left(\rho_{\text{res}}a_0a_0^\dagger - a_0^\dagger\rho_{\text{res}}a_0\right)+(n(\omega)+1)\left(a_0^\dagger a_0\rho_{\text{res}} - a_0\rho_{\text{res}}a_0^\dagger\right)\right]e^{i\tau(\omega_r-\omega)}.
\end{aligned} \tag{3.78}$$

We can now perform the integration over τ:

$$\begin{aligned}
&\int_0^\infty d\tau\,\text{Tr}_{\text{line}}\left\{-\left[\mathcal{H}_1,\left[\mathcal{H}_1(-\tau),\rho^e_{\text{line}}\rho_{\text{res}}\right]\right]\right\} = \\
&= 4\pi G^2(\omega_r)n(\omega_r)\left(a_0^\dagger\rho_{\text{res}}a_0 - \frac{a_0a_0^\dagger\rho_{\text{res}}+\rho_{\text{res}}a_0a_0^\dagger}{2}\right)+ \\
&+ 4\pi G^2(\omega_r)\left[n(\omega_r)+1\right]\left(a_0\rho_{\text{res}}a_0^\dagger - \frac{a_0^\dagger a_0\rho_{\text{res}}+\rho_{\text{res}}a_0^\dagger a_0}{2}\right).
\end{aligned} \tag{3.79}$$

Finally, introducing this result in Eq. (3.48) and considering that we are driving the resonator with an oscillatory interaction $\mathcal{H}_{int} = 2\lambda(a_0+a_0^\dagger)\cos(\omega_d t)$, being λ the amplitude of the driving, we obtain the quantum master equation for the bare resonator coupled to a transmission line:

$$\begin{aligned}
\frac{d}{dt}\rho_{\text{res}}(t) = &-i\omega_r\left[a_0^\dagger a_0,\rho_{\text{res}}\right]+4\pi G^2(\omega_r)n(\omega_r)\left(a_0^\dagger\rho_{\text{res}}a_0 - \frac{a_0a_0^\dagger\rho_{\text{res}}+\rho_{\text{res}}a_0a_0^\dagger}{2}\right)+ \\
&+4\pi G^2(\omega_r)\left[n(\omega_r)+1\right]\left(a_0\rho_{\text{res}}a_0^\dagger - \frac{a_0^\dagger a_0\rho_{\text{res}}+\rho_{\text{res}}a_0^\dagger a_0}{2}\right).
\end{aligned} \tag{3.80}$$

Calculation of the transmission through a bare resonator

Now we can calculate the average of a_0. Using the master equation (3.80), the time evolution of $\langle a_0 \rangle$ is:

$$\frac{d}{dt}\langle a_0 \rangle = -\left[i\omega_r + 2\pi G^2(\omega_r)\right]\langle a_0 \rangle - i\lambda\left(e^{i\omega_d t} + e^{-i\omega_d t}\right). \tag{3.81}$$

This equation can be solved by the sum of the solution of the homogeneous equation $\left[-i\omega_r + 2\pi G^2(\omega_r)\right]\langle a_0 \rangle$ and a particular solution of the inhomogeneous equation. Considering that the system is in equilibrium at $t = 0$, so $\langle a_0 \rangle (0) = 0$, the time evolution of $\langle a_0 \rangle$ is then:

$$\langle a_0 \rangle (t) = -i\lambda \frac{1 - e^{-\left[i(\omega_r - \omega_d) + 2\pi G^2(\omega_r)\right]t}}{i(\omega_r - \omega_d) + 2\pi G^2(\omega_r)} e^{-i\omega_d t} \simeq \frac{-i\lambda}{i(\omega_r - \omega_d) + 2\pi G^2(\omega_r)} e^{-i\omega_d t}. \tag{3.82}$$

Combining Eqs. (3.35), (3.36) and (3.82), and taking into account that our system is a resonator ($\left\langle \hat{S} \right\rangle (\tau) \equiv \langle a_0 \rangle (\tau)$), we obtain the transmission of the bare resonator:

$$t = 1 - \frac{2\pi G^2(\omega_d)}{i(\omega_r - \omega_d) + 2\pi G^2(\omega_r)}. \tag{3.83}$$

We can consider that the coupling $G(\omega_d)$ is only relevant if $\omega_d \simeq \omega_r$. Defining $\kappa = 4\pi G^2$, the transmission is finally:

$$t = 1 - \frac{\frac{\kappa}{2}}{i(\omega_r - \omega_d) + \frac{\kappa}{2}}. \tag{3.84}$$

Equation (3.84) describes the transmission through a lumped element resonator coupled to a transmission line. In case of having a coplanar waveguide resonator, the transmission is given only by the second term of the previous expression. It would be maximum in resonance instead of minimum, going to zero as ω_d moves away from ω_r. It can be seen that the coupling to the transmission line gives rise to the decay of the cavity photon modes, *i.e.* it is responsible for the cavity dissipation at a rate κ.

Resonator coupled to a spin ensemble

Let's now consider as our system under study a resonator coupled to a spin ensemble, shown schematically in Fig. 3.10(b). The Jaynes-Cummings Hamiltonian becomes then:[9]

$$\mathcal{H}_{\text{system}} = \mathcal{H}_{\text{res}} + \mathcal{H}_{\text{spins}} + \mathcal{H}_{rs} \simeq \omega_r a_0^\dagger a_0 + \Omega_S b^\dagger b + G\sqrt{N}(a_0 b^\dagger + a_0^\dagger b), \tag{3.85}$$

being N the number of spins and Ω_S the energy difference between the two spin states involved in the relevant transition.

The time evolution of $\langle a_0 \rangle$ and $\langle b \rangle$, if we drive the resonator with an oscillating interaction $\mathcal{H}_{int} = 2\lambda(a_0 + a_0^\dagger)\cos(\omega_d t)$ with amplitude λ, is given by the following equations:

$$\frac{d}{dt}\langle a_0 \rangle = -\left(i\omega_r + \frac{\kappa}{2}\right)\langle a_0 \rangle - iG\sqrt{N}\langle b \rangle - i\lambda\left(e^{i\omega_d t} + e^{-i\omega_d t}\right), \tag{3.86}$$

$$\frac{d}{dt}\langle b \rangle = -iG\sqrt{N}\langle a_0 \rangle - \left(i\Omega_S + \frac{\Gamma}{2}\right)\langle b \rangle, \tag{3.87}$$

where Γ is here approximately $2/T_2$. The only relevant term of the driving interaction is the one that goes with $e^{-i\omega_d t}$. As in the previous section, we can consider that a solution to these equations with $\langle a_0 \rangle$ and $\langle b \rangle$ being proportional to $e^{-i\omega_d t}$. Given this, if we define the operators $\langle \tilde{a}_0 \rangle = \langle a_0 \rangle e^{i\omega_d t}$ and $\left\langle \tilde{b} \right\rangle = \langle b \rangle e^{i\omega_d t}$, they will be constant in time. We can write the time evolution of these operators in the matrix representation:

$$\frac{d}{dt}\begin{pmatrix} \langle \tilde{a}_0 \rangle \\ \left\langle \tilde{b} \right\rangle \end{pmatrix} = \begin{pmatrix} 0 \\ 0 \end{pmatrix} = \begin{pmatrix} -\left[i(\omega_r - \omega_d) + \frac{\kappa}{2}\right] & -iG\sqrt{N} \\ -iG\sqrt{N} & -\left[i(\Omega_S - \omega_d) + \frac{\Gamma}{2}\right] \end{pmatrix} \begin{pmatrix} \langle \tilde{a}_0 \rangle \\ \left\langle \tilde{b} \right\rangle \end{pmatrix} - \begin{pmatrix} i\lambda \\ 0 \end{pmatrix} \tag{3.88}$$

From here, we can find the solution for $\langle \tilde{a}_0 \rangle$:

$$\langle \tilde{a}_0 \rangle = \frac{-i\lambda}{i\left(\omega_r - \omega_d\right) + \frac{\kappa}{2} + \frac{\left(G\sqrt{N}\right)^2}{i\left(\Omega_S - \omega_d\right) + \frac{\Gamma}{2}}} = \langle a_0 \rangle e^{i\omega_d t}. \tag{3.89}$$

Combining the expression of $\langle a_0 \rangle$ with Eqs. (3.35) and (3.36), we get the final transmission through a resonator coupled to a spin ensemble, and this system coupled to a transmission line:

$$t = 1 - \frac{\frac{\kappa}{2}}{i\left[\left(\omega_r - \omega_d\right) + \frac{\left(\omega_d - \Omega_S\right)\left(G\sqrt{N}\right)^2}{\left(\Omega_S - \omega_d\right)^2 + \left(\frac{\Gamma}{2}\right)^2}\right] + \left[\frac{\kappa}{2} + \frac{\frac{\Gamma}{2}\left(G\sqrt{N}\right)^2}{\left(\Omega_S - \omega_d\right)^2 + \left(\frac{\Gamma}{2}\right)^2}\right]}. \tag{3.90}$$

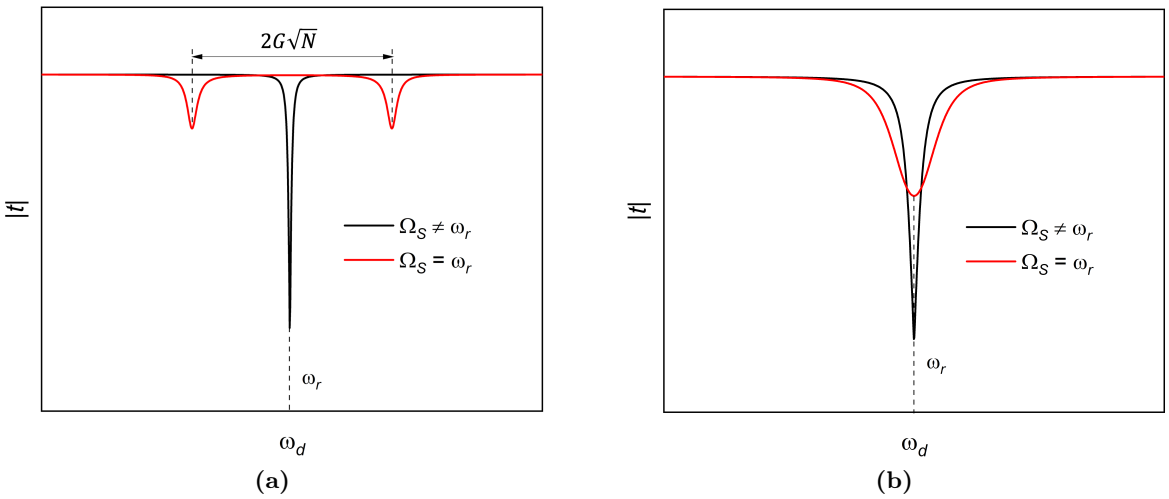

Figure 3.11: Examples of the transmission through a LER coupled to a spin ensemble and a transmission line (Fig. 3.10(b)) in (a) strong coupling and (b) weak coupling regime. In the strong coupling regime, when the resonator and the spins are tuned ($\Omega_S = \omega_r$), the original cavity resonance splits in two peaks separated by a frequency shift $2G\sqrt{N}$. On the other hand, in the weak coupling regime the original peak is preserved, with an increase in its width when the spin system is tuned to the resonator.

The transmission is minimum when the imaginary part of the denominator of Eq. (3.90) vanishes at a driving frequency ω_d. Depending on whether we are in the strong coupling

($G\sqrt{N} >> \Gamma/2$) or weak coupling ($G\sqrt{N} << \Gamma/2$) regime, the driving frequency at which this transmission minimum takes place changes. In the strong coupling regime, the imaginary part of Eq. (3.90) vanishes when:

$$(\omega_r - \omega_d)(\omega_S - \omega_d) \simeq \left(G\sqrt{N}\right)^2 \quad \Rightarrow \omega_{d,\pm} = \frac{\omega_r + \Omega_S}{2} \pm \sqrt{\left(\frac{\omega_r - \Omega_S}{2}\right)^2 + \left(G\sqrt{N}\right)^2}. \quad (3.91)$$

In resonance ($\omega_r = \Omega_S$), we obtain $\omega_{d,\pm} = \omega_r \pm G\sqrt{N}$. Introducing this driving frequency in the real part of the denominator of Eq. (3.90), we find that the peak width in resonance is $\tilde{\kappa} = \kappa + \Gamma$. This situation is shown in Fig. 3.11(a).

On the other hand, if we are in the weak coupling regime (Fig. 3.11(b)) we can consider that the imaginary part of the transmission vanishes at a driving frequency $\omega_d \simeq \omega_r$. In this case, the transmission in minimum when:

$$\omega_d = \omega_r + \frac{(\omega_r - \Omega_S)\left(G\sqrt{N}\right)^2}{(\Omega_S - \omega_r)^2 + \left(\frac{\Gamma}{2}\right)^2}, \quad (3.92)$$

while the modified peak width reads:

$$\tilde{\kappa} = \kappa + \frac{\left(G\sqrt{N}\right)^2 \frac{\Gamma}{2}}{(\Omega_S - \omega_r)^2 + \left(\frac{\Gamma}{2}\right)^2}. \quad (3.93)$$

Fano resonances

In some experiments shown in this thesis, the observed resonances show a Fano behaviour. This type of resonance appears when a discrete quantum state interferes with a continuum band of states.[23] The dynamics of this system can be described using a model of two coupled oscillators, being only one of them (our resonator) driven and coupled to a spin ensemble. The equation of motion of the full system, considering that the spin ensemble is coupled to the resonator with resonance frequency ω_r, is then:

$$\begin{pmatrix} \dot{x}_r \\ \dot{x}_2 \\ \dot{x}_s \end{pmatrix} = \vec{M} \cdot \vec{x} - i\vec{f} = \begin{pmatrix} \omega_r - \omega - i\gamma_r & \lambda & G \\ \lambda & \omega_2 - \omega - i\gamma_2 & 0 \\ G & 0 & -\Omega_S - \omega - i\gamma_S \end{pmatrix} \begin{pmatrix} x_r \\ x_2 \\ x_s \end{pmatrix} - i \begin{pmatrix} f_r \\ 0 \\ 0 \end{pmatrix} \quad (3.94)$$

where γ_r, γ_2 and γ_S are the linewidths of the resonator peak, the symmetric peak and the spins respectively, λ is the coupling between the two resonances, G is the coupling between the spin ensemble and the asymmetric resonance and f_r is the driving term. Solving this system involves calculating the inverse matrix of $\vec{M}$, being it so complex that it is impossible to obtain a compact equation for the transmission. The measurements that show this behaviour have been analysed using a python script, developed by a member of our research group (Víctor Rollano), which finds numerically the inverse matrix of (3.94) and compares the simulated and experimental transmissions, being capable to fit all the parameters of our system.

Bibliography

[1] C. W. Gardiner and M. J. Collett. Input and output in damped quantum systems: Quantum stochastic differential equations and the master equation. *Physical Review A*, 31:3761–3774, 1985.

[2] S. Fan, Ş. E. Kocabaş, and J.-T. Shen. Input-output formalism for few-photon transport in one-dimensional nanophotonic waveguides coupled to a qubit. *Physical Review A*, 82:063821, 2010.

[3] S. Bertaina, S. Gambarelli, A. Tkachuk, I. N. Kurkin, B. Malkin, A. Stepanov, and B. Barbara. Rare-earth solid-state qubits. *Nature Nanotechnology*, 2:39–42, 2007.

[4] D. D. Awschalom, L. C. Bassett, A. S. Dzurak, E. L. Hu, and J. R. Petta. Quantum Spintronics: Engineering and Manipulating Atom-Like Spins in Semiconductors. *Science*, 339:1174–1179, 2013.

[5] Y. Makhlin, G. Schön, and A. Shnirman. Quantum-state engineering with Josephson-junction devices. *Reviews of Modern Physics*, 73:357–400, 2001.

[6] J. I. Cirac and P. Zoller. Quantum Computations with Cold Trapped Ions. *Physical Review Letters*, 74:4091–4094, 1995.

[7] C. Cohen-Tannoudji, B. Diu, and F. Laloë. *Mécanique Quantique*, volume 2. Hermann, 1997.

[8] I. I. Rabi. Space quantization in a gyrating magnetic field. *Physical Review*, 51:652–654, 1937.

[9] E. T. Jaynes and F. W. Cummings. Comparison of quantum and semiclassical radiation theories with application to the beam maser. *Proceedings of the IEEE*, 51:89–109, 1963.

[10] A. Gómez-León, F. Luis, and D. Zueco. Dispersive Readout of Molecular Spin Qudits. *Physical Review Applied*, 17:064030, 2022.

[11] A. Blais, R.-S. Huang, A. Wallraff, S. M. Girvin, and R. J. Schoelkopf. Cavity quantum electrodynamics for superconducting electrical circuits: An architecture for quantum computation. *Physical Review A*, 69:062320, 2004.

[12] A. Wallraff, D. I. Schuster, A. Blais, L. Frunzio, R.-S. Huang, J. Majer, S. Kumar, S. M. Girvin, and R. J. Schoelkopf. Strong coupling of a single photon to a superconducting qubit using circuit quantum electrodynamics. *Nature*, 431:162–167, 2004.

[13] C. A. Collett, K.-I. Ellers, N. Russo, K. R. Kittilstved, G. A. Timco, R. E. P. Winpenny, and J. R. Friedman. A Clock Transition in the Cr_7Mn Molecular Nanomagnet. *Magnetochemistry*, 5:4, 2019.

[14] M. Rubín-Osanz, F. Lambert, F. Shao, E. Rivière, R. Guillot, N. Suaud, N. Guihéry, D. Zueco, A.-L. Barra, T. Mallah, and F. Luis. Chemical tuning of spin clock transitions in molecular monomers based on nuclear spin-free Ni(II). *Chemical Science*, 12:5123–5133, 2021.

[15] M. Shiddiq, D. Komijani, Y. Duan, A. Gaita-Ariño, E. Coronado, and S. Hill. Enhancing coherence in molecular spin qubits via atomic clock transitions. *Nature*, 531:348–351, 2016.

[16] R. J. Schoelkopf and S. M. Girvin. Wiring up quantum systems. *Nature*, 451:664–669, 2008.

[17] M. Devoret, S. Girvin, and R. Schoelkopf. Circuit-QED: How strong can the coupling between a Josephson junction atom and a transmission line resonator be? *Annalen der Physik*, 16:767–779, 2007.

[18] R. N. Simons. *Coplanar Waveguide Circuits, Components, and Systems.* Wiley-IEEE Press, 1986.

[19] M. D. Jenkins, U. Naether, M. Ciria, J. Sesé, J. Atkinson, C. Sánchez-Azqueta, E. del Barco, J. Majer, D. Zueco, and F. Luis. Nanoscale constrictions in superconducting coplanar waveguide resonators. *Applied Physics Letters*, 105:162601, 2014.

[20] M. D. Jenkins. *Coupling quantum circuits to magnetic molecular qubits.* PhD thesis, Universidad de Zaragoza, 2015.

[21] M. D. Jenkins, D. Zueco, O. Roubeau, G. Aromi, J. Majer, and F. Luis. A scalable architecture for quantum computation with molecular nanomagnets. *Dalton Transactions*, 45:16682–16693, 2016.

[22] M. Tavis and F. W. Cummings. Exact solution for an N-Molecule—Radiation-Field Hamiltonian. *Physical Review*, 170:379–384, 1968.

[23] U. Fano. Effects of Configuration Interaction on Intensities and Phase Shifts. *Physical Review*, 124:1866–1878, 1961.

4

Enhanced Spin-Photon Coupling near Superconducting Nanobridges

4.1 Introduction

In chapter 3 we saw that the spin-photon coupling between a superconducting circuit and a molecular spin depends on the intensity of the magnetic field generated by the circuit. In this sense, superconducting coplanar resonators concentrate the microwave magnetic field in smaller regions than conventional three-dimensional cavities, achieving higher field intensities and thus stronger couplings.[1] It has been shown that a single microwave photon generated by a high quality coplanar resonator can be coherently coupled to a superconducting qubit,[2] which made circuit QED the leading platform for the development of solid-state quantum processors. The microwave photons trapped in this architecture can be also employed for coherent single qubit control,[2] for dispersive qubit readout,[3] and for wiring-up individual qubits using the resonator as a quantum bus.[4;5;6;7]

Currently, several approaches have been developed trying to apply the same technology to spin qubits, in a hybrid architecture. For this, one needs to enhance the spin-photon coupling and the detection sensitivity, which would enable working with small spin ensembles and, eventually, with single spin qubits. Some of these approaches imply the use of parametric amplifiers to amplify the output signal,[8] or of lumped element resonators with low impedances.[9] The latter will be considered in chapter 5.

In this chapter we explore a third approach, already introduced in section 3.4.3, based on reducing the effective volume of the cavity magnetic field. In a CPW resonator, this can be achieved by decreasing locally the width of the resonator's transmission line[10;11;12] via the fabrication of a nanoscopic constriction. Sections 4.2 and 4.3 are dedicated to the fabrication and test at very low temperature of these nanoconstrictions in CPW resonators.

For this study we use molecules of the organic free radical 2, 2-diphenyl-1-picrylhydrazyl, hereafter referred to as DPPH. This molecule hosts an unpaired electron with electronic spin $S = 1/2$ and an almost isotropic gyromagnetic factor $g \simeq 2$, thus it provides a close to model realization of the simplest spin qubit (see section 3.2). The inhomogeneous broadening generated by dipolar interactions is reduced by direct exchange interactions between nearest neighbours.[13;14] The spin resonance linewidth γ is then dominated by the homogeneous broadening given by $1/T_2$, where $T_2 \simeq 80 - 120$ ns is the spin coherence time of the free radical.

Whereas the single spin-photon coupling, G_1, is usually too weak to realize a coherent exchange of quantum information, the collective enhancement of the radiation emission and absorption predicts that the collective spin-photon coupling, G_N, is enhanced by $\sqrt{N}$.[15] Considering a two-level system, G_N shows the following expression:

$$G_N = G_1\sqrt{N_{\text{eff}}} = G_1\sqrt{N\frac{\langle S_z\rangle_T}{S}} = G_1\sqrt{N\tanh\left(\frac{h\Omega_S}{2k_BT}\right)}, \tag{4.1}$$

where N_{eff} is the number of spins effectively coupled to the superconducting circuit, given by the temperature-dependent spin polarization, and Ω_S is the splitting between the two spin levels induced by the magnetic field. Expression (4.1) tells us that the collective coupling can be enhanced by increasing the total number of spins or by decreasing temperature. Regarding this approach, ensembles of molecules,[16] electron spins,[17] or atoms[18] have been proposed to be coupled to a superconducting resonator. In this chapter, different ensembles of DPPH molecules have been considered, studying the evolution of the collective coupling while changing the number of spins effectively coupled to the superconducting circuit. The effect on the collective coupling G_N of a nanoconstriction fabricated on a CPW resonator is discussed in section 4.4, while the evolution of the single spin-photon coupling has been studied while changing the number of spins coupled to it (section 4.5), temperature (section 4.6) and nanoconstriction width (section 4.7). Section 4.8 is dedicated to the combination of this approach with a new type of resonator, called 2.5D resonator (a combination between a three-dimensional cavity and a CPW resonator), developed at the Atominstitut of the Technical University of Vienna. Finally, section 4.9 summarizes the conclusions of this chapter.

4.2 Fabrication of the circuits and the nanoscopic constrictions

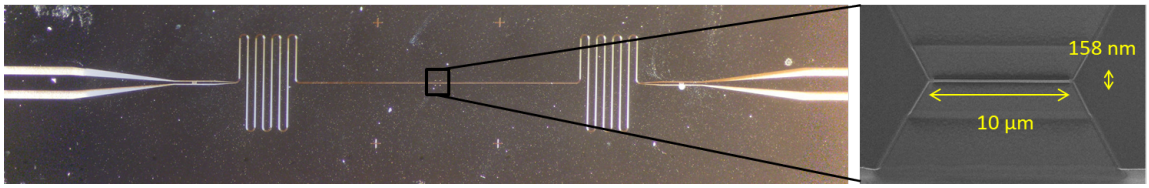

Figure 4.1: (Left) Optical microscopy image of one of the coplanar waveguide resonators used in this work. The meanders on both sides of the CPW resonator increase its length up to 44 mm, and therefore allow tuning its resonance frequency to $\sim$ 1.4 GHz. (Right) Scanning electron microscopy image of the central line of this resonator, after fabricating a 158 nm width nanoconstriction by focused ion beam nanolithography.

The coplanar superconducting resonators used in this study were fabricated by ultra-violet lithography on a 150 nm thick Nb film deposited on top of a sapphire waffer (see section 2.3.1 for more details about this technique). Figure 4.1 shows a representative image of one of these devices. Sapphire was used as the substrate because of its low dielectric losses and excellent insulating properties. The circuit consists of large feedlines with 400 μm central lines and 200 μm gaps that narrow down to a 14 μm central line with 7 μm gaps after the gap capacitors. These finger-design gap capacitors are responsible for turning the transmission line into a resonator. They cut the line at two points and define a cavity with resonant modes determined by the geometry, $L = \frac{n\lambda}{2}$, where the length L of this cavity was chosen to be 44 mm by making a meander across the surface, obtaining a resonance frequency of 1.4 GHz.

The nanoconstrictions were fabricated in the central line of the resonators by using the SEM/FIB system Helios Nanolab Dual Beam introduced in section 2.3.2. The central line was narrowed from 14 μm to a minimum width of 40 nm, along a distance of 10 μm at the midpoint of the central line (Fig. 4.1). These structures were fabricated by focusing a narrow beam of Ga^+ ions onto the niobium layer, scanning with it the area to be removed in two phases. In the first one, the resonator width was reduced to around 1 μm using a large beam current, allowing us to reach this size within a few minutes. Secondly, the final nanobridge was fabricated using small beam currents, below 20 pA, that allowed us to precisely perform thinner structures and to minimize the Nb layer that is implanted with Ga^+ ions. To avoid the risk of electrostatic discharges during the entire process, a small platinum bridge connecting the resonator central

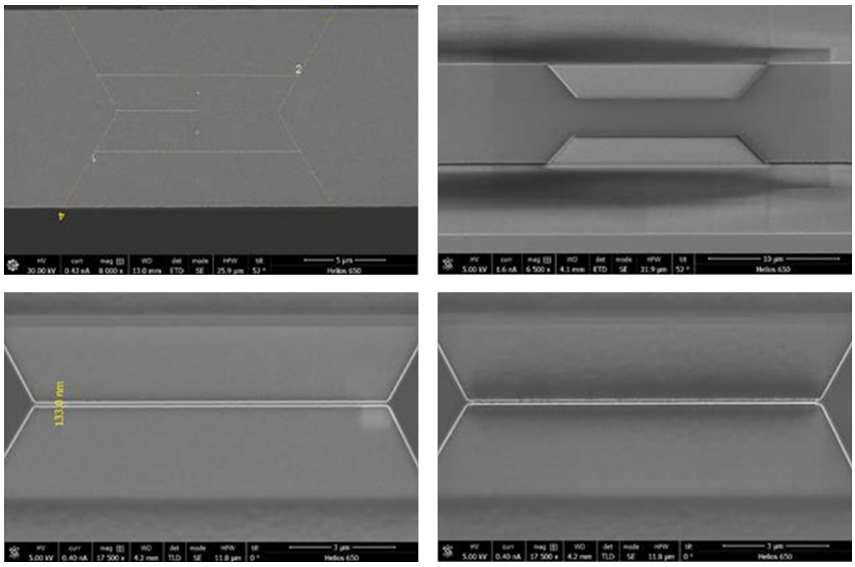

Figure 4.2: Fabrication steps of a nanoconstriction at the central line of a CPW resonator. First, the pattern is designed (top left). Then, a Ga^+ focused ion beam with a large current removes the niobium until we reach a width of around 1 μm (top right). Finally, the current is reduced below 20 pA to reach the final nanoconstriction design (bottom).

line with its ground plates was deposited prior to the fabrication of the constrictions, and these plates were connected to the system ground with carbon tape. This contact to ground allows the beam current used to etch the niobium to be dissipated through the circuit, rather than causing an electrostatic discharge. Once the etching is finished, the platinum bridge is removed with the focused ion beam. The fabrication steps of one of these nanoconstrictions are shown in Fig. 4.2.

4.3 Test of the CPW resonators at very low temperature

A preliminary study of the behaviour of the 14 μm wide CPW resonator with temperature is shown in this section. It was carried out at the Atominstitut of the Technical University of Vienna.

The studied CPW resonator, shown in Fig. 4.1(a), was introduced in an adiabatic demagnetization refrigerator (ADR), a refrigerator that exploits the magnetocaloric effect for achieving temperatures of a few mK (> 50 mK in our case). The transmission characteristics of the device were studied for several temperatures and input powers by connecting it to a VNA (see section 2.5.2) with which the microwave transmission was measured while changing the frequency and power of the input signal.

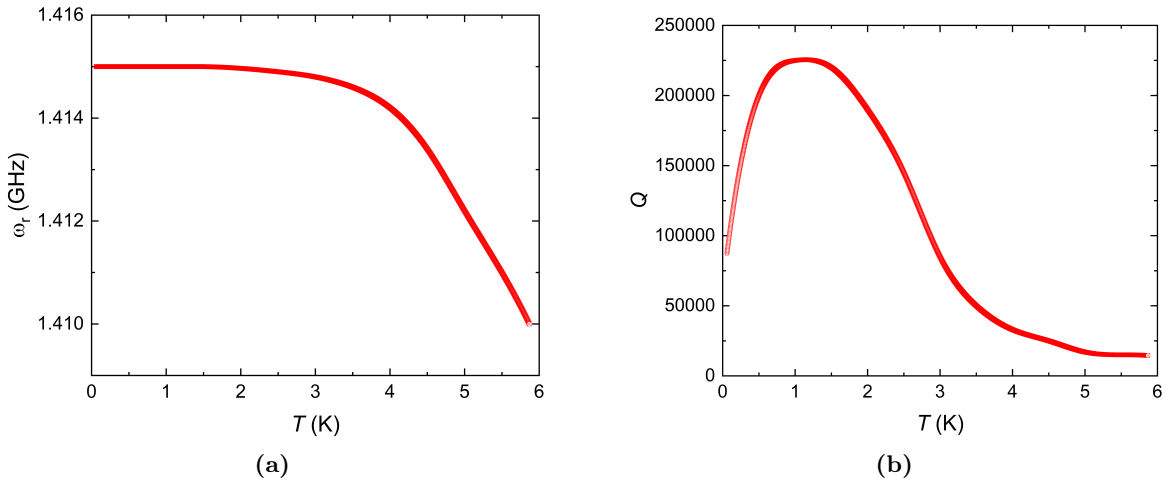

Figure 4.3: Temperature dependence of (a) the resonance frequency ω_r and (b) the quality factor Q of the resonator shown in Fig. 4.1(a), for an input power of -20 dBm. Q shows a maximum value of $\sim 2.2 \cdot 10^5$, corresponding to a linewidth of 6 kHz, at a temperature of 1 K.

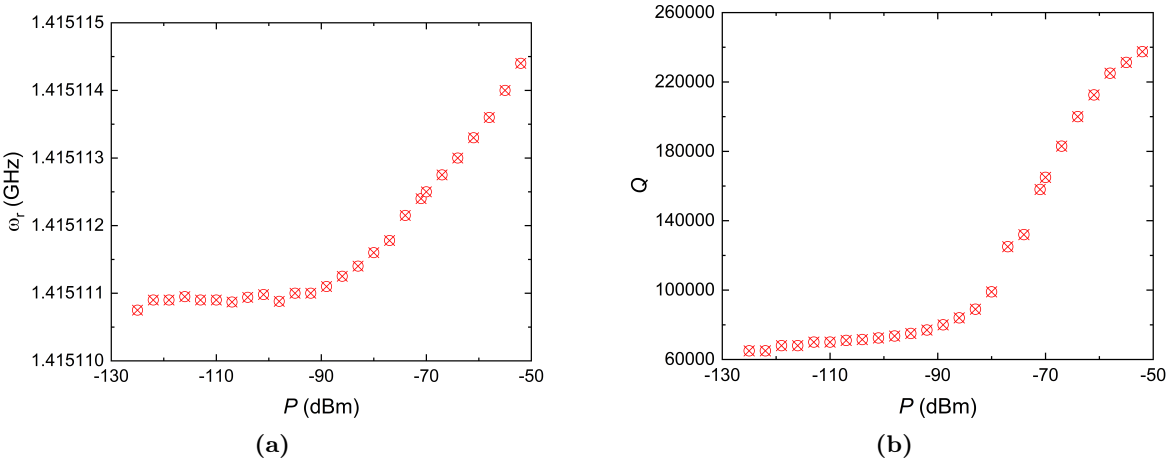

Figure 4.4: Input power dependence of (a) the resonance frequency and (b) the quality factor of the resonator shown in Fig. 4.1(a), for a temperature of 100 mK.

Figures 4.3 and 4.4 show the evolution of the resonance frequency ω_r and the quality factor $Q = \dfrac{\omega_r}{\Delta\omega}$ while changing the temperature and the input power. For an input power of -20 dBm and a temperature of 1 K, Q presents a maximum value of $\sim 2.2 \times 10^5$, which corresponds to a resonance width of 6 kHz for a resonance frequency of 1.4145 GHz. This value is low enough compared to the typical spin linewidths of DPPH, which are close to 2 MHz. This indicates that, for a sufficiently high amount of DPPH molecules deposited on this resonator, any change of the resonance frequency and of the width κ should be easily detectable.

Previous studies show that the overall behaviour of CPW resonators is not significantly modified because of the presence of a nanoconstriction.[11] They locally enhance the magnetic field, thus the spin-photon coupling near the nanoconstriction. We can then assume that, although the nanobridge will produce little changes on the resonance frequency and the quality factor, they will not be critical, allowing us to properly couple DPPH organic radical molecules to this resonator.

4.4 Coupling of model spin qubits to coplanar waveguide resonators: effect of the nanoconstrictions on the collective coupling

4.4.1 Coupling to very large spin ensembles

In this section we study the coupling of DPPH organic radical molecules, whose structure is shown in Fig. 4.5(a). Here, we explore if the presence of a nanoconstriction enhances the collective coupling G_N. For this, we first show results obtained for very large ensembles, and then we show how the sensitivity and the coupling limit the minimum number of molecules that can be detected.

The unpaired electron that each DPPH molecule hosts confers it an electronic spin $S = 1/2$ and an isotropic gyromagnetic factor $g_S \simeq 2$. The Hamiltonian which describes the molecule is then:

$$\mathcal{H} = g_S \mu_B H S, \tag{4.2}$$

where only the isotropic Zeeman effect is considered. The quantization axis of the system will be parallel to the applied magnetic field, being necessary to generate a microwave field perpendicular to this dc magnetic field to generate a transition between the spin states $|-1/2\rangle$ and $|+1/2\rangle$ of the molecule. Under this situation, the system shows a resonance line at frequency $\Omega_S = 2\mu_B H/h$, thus proportional to the magnetic field with a slope of 28 GHz/T.

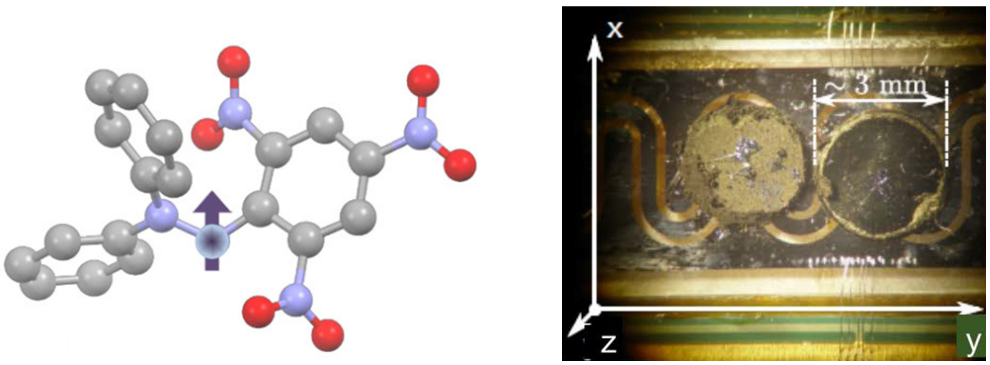

(a) **(b)**

Figure 4.5: (a) Structure of a DPPH organic radical molecule. It contains carbon (grey), oxygen (red) and nitrogen (blue) atoms. (b) Optical microscopy image of a CPW resonator with a 400 μm wide central transmission line hosting two pressed pellets of polycrystalline DPPH. The total number of deposited spins is approximately 10^{19} spins.

Figure 4.5(b) shows two pellets of polycristalline DPPH deposited on top of a CPW resonator with a 400 μm wide central line. This device was introduced in a liquid helium cryostat at 4.2 K that hosts a vector magnet, and connected to a vector network analyser for measuring the microwave transmission through the system. The magnetic field was applied along the X axis of Fig. 4.5(b).

Figure 4.6 shows the evolution of the microwave transmission with magnetic field and input frequency at 4.2 K. A clear absorption signal corresponding to the coupling between DPPH spins and the resonator is observed at an applied field of 60 mT. We can detect two peaks when the spins and the resonator are tuned, while the original resonance is recovered when they are detuned. This anti-crossing indicates that we have achieved the strong coupling regime that takes place when the collective spin-photon coupling is higher than the decoherence rate, thanks to the high amount of molecules that have been deposited on the resonator. We can note that

the resonance shown in Fig. 4.6 is displaced from 54 mT, the field at which it should appear considering $g_S \simeq 2$, to 60 mT. Considering that all the remaining measurements agree with $g_S \simeq 2$, we can assume this is due to an error in the magnet calibration.

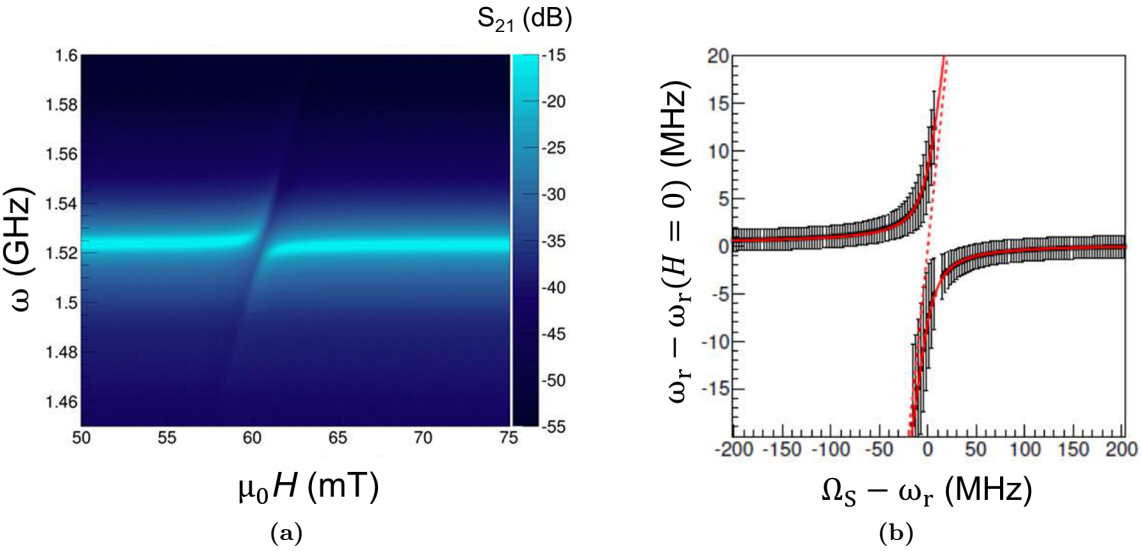

(a) (b)

Figure 4.6: (a) 2D plot of the microwave transmission through the two DPPH pellets coupled to the 1.4 GHz CPW resonator with a 400 μm wide central line shown in Fig. 4.5(b). This measurement was done at a temperature $T = 4.2$ K. A clear absorption signal can be appreciated at 60 mT. (b) Magnetic field dependence of the resonance frequency obtaiend with the data shown in (a). When the resonator and the spins are tuned, an anti-crossing, which is characteristic of the strong coupling regime, appears. A least-square fit to Eq. (4.3) gives us a coupling value $G_N/2\pi \simeq 8.2$ MHz.

The coupling between the spins and the superconducting resonators results in a modification of the characteristics of the resonance: the transmission is reduced, the resonance frequency of the resonator is shifted, and the peak is broadened. All these effects are maximized when the spins and the resonator are tuned, *i.e.* when $\Omega_S \simeq \omega_r$. In the case of achieving the strong coupling regime (when $G_N > \gamma$), a new effect is added to the previous ones: the appearance of two peaks when the spins and the resonator are tuned. The resonance frequencies of these two peaks are given by:

$$\omega_{\pm} = \frac{\omega_r + \Omega_S}{2} \pm \frac{\sqrt{4G_N^2 + (\Omega_S - \omega_r)^2}}{2}. \tag{4.3}$$

Fitting the evolution of ω_r with Eq. (4.3), we can determine the value of the collective spin-photon coupling achieved with the sample shown in Fig. 4.5(b). With this analysis, shown in Fig. 4.6(b), a collective coupling $G_N/2\pi \simeq 8.2$ MHz and a spin linewidth $\gamma \sim 5 - 7$ MHz are obtained, indicating that we are in the vicinity of the strong coupling regime for $N_{\text{eff}} \sim 10^{18}$. This number of molecules effectively coupled to the resonator has been calculated using Eq. (4.1).

4.4.2 Coupling to smaller spin ensembles: effect of the nanoconstriction

The number of molecules coupled to the CPW resonators was then reduced by using devices with narrower central lines and depositing smaller ensembles. Multiple microwave transmission measurements were performed at $T = 4.2$ K on two 14 μm-width CPW resonators, one without constriction and the other with the 158 nm wide nanoconstriction shown in Fig. 4.1. To illustrate the underlying physics, we first discuss measurements performed for a very small spin ensemble

with $N_{eff} \simeq 4 \times 10^7$. Measurements were done for the same amount of DPPH molecules, deposited by dip-pen nanolithography (DPN, see section 2.4 for an explanation of this technique). The molecular ink used in these depositions was prepared by dissolving 10-20 mg/ml of DPPH in *N,N*-Dimethylformamide (DMF) with 5-10% glycerol in volume. DMF preserves the chemical properties of DPPH, while glycerol increases the viscosity and slows the ink evaporation. After the deposition, one of which is shown in Fig. 4.7(a), the resonators were introduced in a liquid helium cryostat at 4.2 K that hosts a vector magnet, and connected to a vector network analyser for measuring the microwave transmission through the system. The input power was attenuated by -52 dB, to avoid exceeding the critical current at the nanoconstriction. [11]

The microwave transmission was measured for magnetic field applied along the Z laboratory axis shown in Fig. 4.7(a), ranging from 30 to 60 mT in the case of the resonator without constriction, and from 40 to 60 mT for the resonator with the nanoconstriction. The spins coupled to the 14 μm wide resonator give no measurable signal, showing that the collective coupling is much smaller than even the bare resonator width κ. In contrast, the coupling becomes clearly visible when using a resonator with a 158 nm wide nanoconstriction fabricated at the centre of its central transmission line (Fig. 4.8). This provides direct evidence for the enhancement of the collective spin-photon coupling, G_N, thanks to the nanoconstriction.

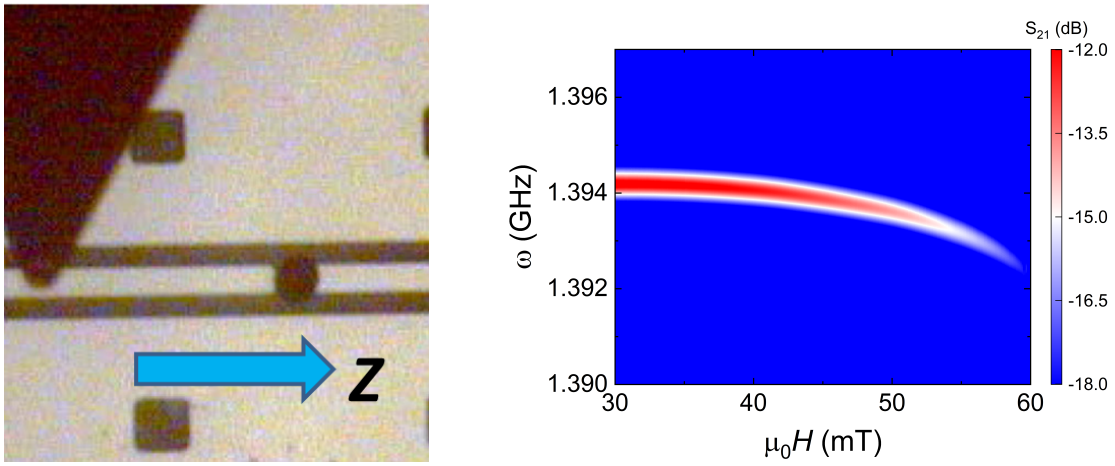

(a) **(b)**

Figure 4.7: (a) Optical microscopy image of the deposition of a DPPH deposit by DPN nanolithography on a 1.4 GHz CPW resonator with a 14 μm wide central line without nanoconstriction, together with the Z laboratory axis. (b) 2D plot of the microwave transmission through this sample. The measurement was done at $T = 4.2$ K and with magnetic field applied along the Z laboratory axis. The effective number of spins coupled to the resonator at this temperature is $N_{\text{eff}} \approx 4 \times 10^7$.

Compared to the previous measurement with the 400 μm wide resonator, when two peaks were detected (see Fig. 4.6), it is clear that the strong coupling regime is not achieved now due to the lower number of molecules coupled to the resonator. The tuning between the resonance frequencies of DPPH and the resonator is achieved at a magnetic field $\mu_0 H \simeq 50$ mT. This value agrees with the field at which signal absorption has been detected (Fig. 4.8). The measurements performed on the original device, without a nanobridge, do not show any variation of κ at this field.

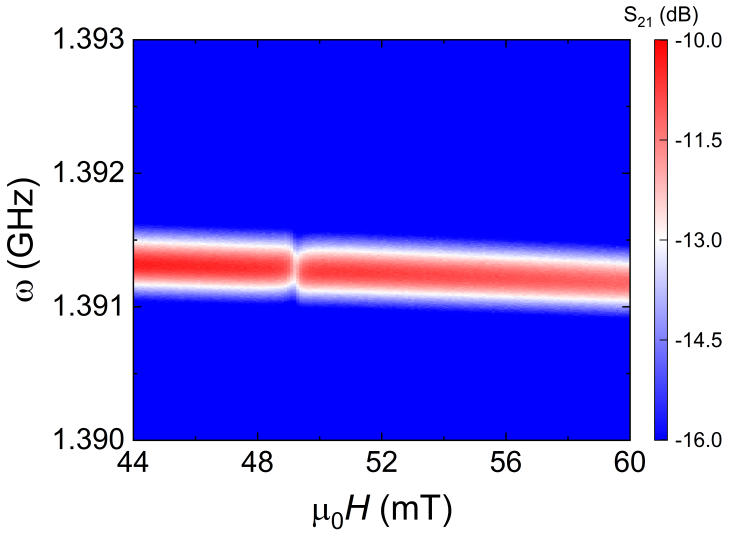

Figure 4.8: 2D plot of the microwave transmission through a DPPH sample coupled to the 1.4 GHz CPW resonator with a 14 μm wide central line shown in Fig. 4.7(a), now with a nanoconstriction of width 158 nm. The measurement was done at $T = 4.2$ K and with magnetic field applied along the Z laboratory axis. The effective number of spins coupled to the resonator at this temperature is $N_{\text{eff}} \approx 4 \times 10^7$.

In the weak coupling regime (when $G_N < \gamma$), the behaviour of the resonance width κ can be described by the following expression:[19]

$$\tilde{\kappa} = \kappa_r + \frac{G_N^2 \gamma}{(\omega_r - \Omega_S)^2 + \gamma^2} \tag{4.4}$$

where κ_r is the broadening of the cavity when it is detuned from the spin ensemble. A fit based on Eq. (4.4) (Fig. 4.9) gives a value for the collective coupling $G_N = 570 \pm 20$ kHz in the case of the resonator with nanoconstriction. These results demonstrate that the nanoconstriction enhances the local magnetic field, and thus the spin-photon coupling, in a region near it. In the following section we will study this improvement of the coupling while varying the number of spins coupled to the system.

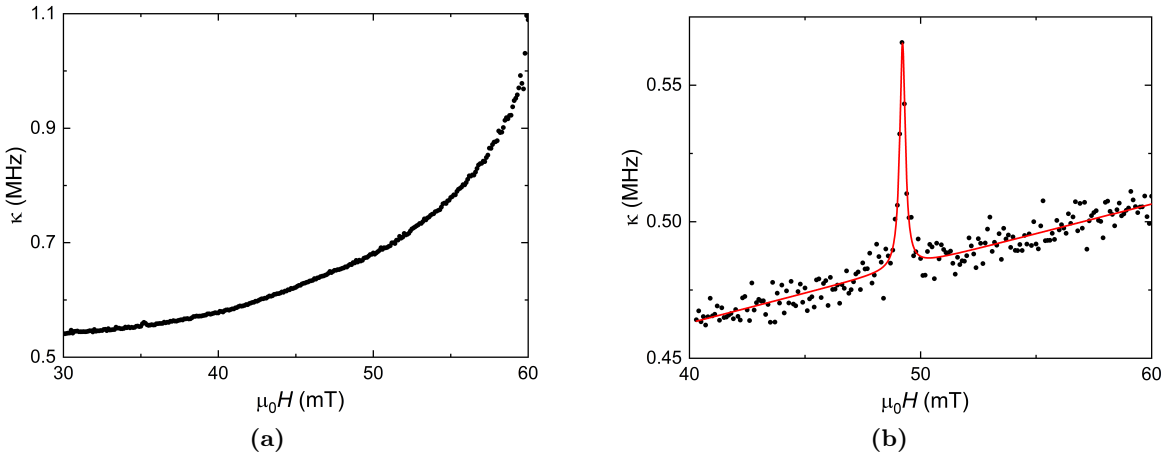

Figure 4.9: Curves of κ measured for the transmission measurements shown in Figs. 4.7(b) and 4.8, for the resonators (a) without and (b) with the 158 nm wide nanoconstriction. The collective coupling in the case of the measurement done without constriction seems to be below its sensitivity limit. The fit on (b) has been performed using Eq. (4.4).

4.5 Spin-photon coupling versus spin number: determination of the single spin-photon coupling strength

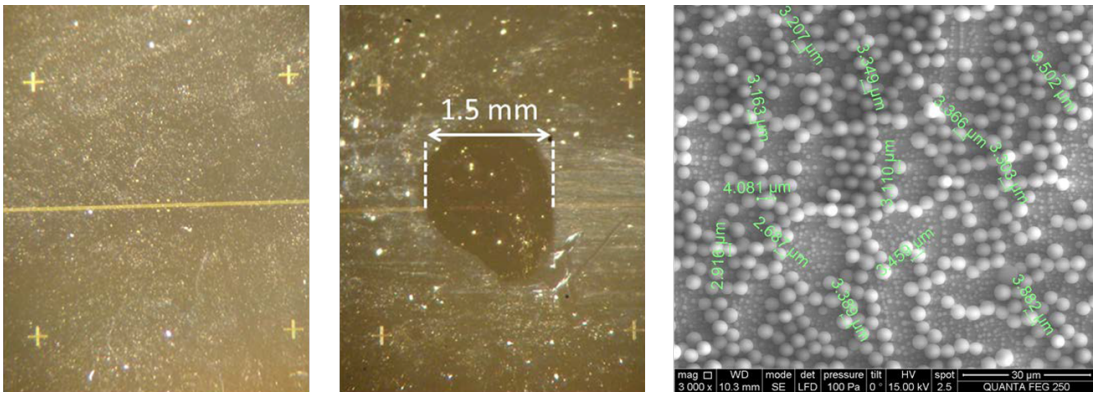

Figure 4.10: Optical microscopy images of a CPW resonator with a 14 μm wide central line before (left) and after (centre) the deposition of a drop of DPPH with concentration 40 mg/ml, done using a micropipette, together with a SEM image (right) of the deposit after the solvent has evaporated, showing the distribution and morphology of DPPH aggregates.

In this section we discuss how the spin-photon coupling evolves with the amount of spins effectively coupled to the resonator. From these results and Eq. (4.1), we estimate the average coupling to individual spins. This study was performed by depositing, by DPN or by using a micropipette, DPPH drops of well controlled sizes and concentrations onto the central line of the resonators described in the previous section. An image of a large deposit is shown in Fig. 4.10, which shows the tendency of DPPH to aggregate into quasispherical micro- and nano-droplets. The experiments were performed at 4.2 K by submerging the samples in a liquid helium cryostat, and the microwave transmission was measured using a VNA.

Figure 4.11 shows the dependence of κ on magnetic field for several ensembles of DPPH molecules. Variations in the resonance fields observed for different runs can be associated to small modifications of the resonance frequency due to different amounts of solvent in each deposit. The main conclusion we can extract from these results is that the sensitivity limit is highly improved thanks to the nanoconstriction. It is reduced from about 10^8 spins without constriction to 2×10^6 spins when a 158 nm wide nanoconstriction is fabricated.

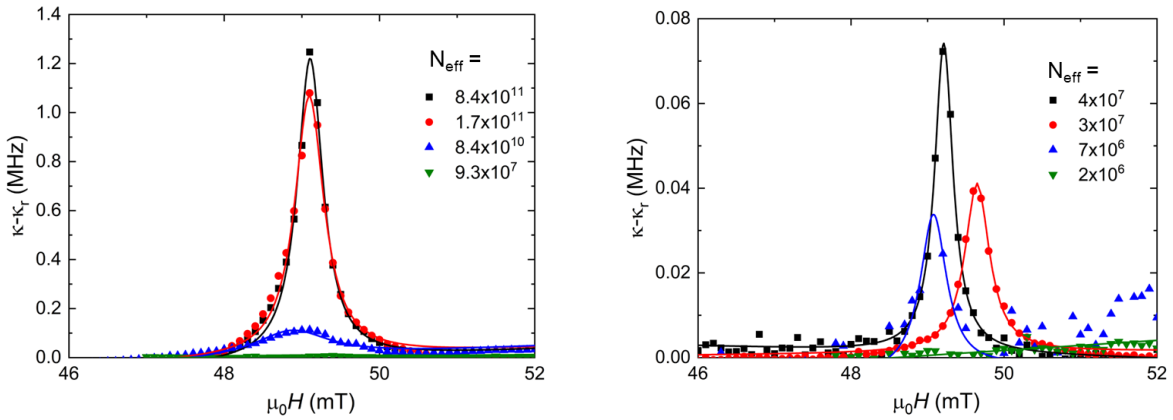

Figure 4.11: Dependence of the resonance width κ with magnetic field for a conventional $w = 14$ μm coplanar resonator (a) and for a resonator with a 158 nm wide constriction (b) coupled to different amounts of DPPH molecules. The effective number of coupled molecules, which takes into account the finite temperature $T = 4.2$ K at which these measurements were performed (Eq. (4.1)), is indicated in the figures. The fits have been performed using Eq. (4.4), which corresponds to the weak coupling limit.

The collective spin-photon coupling and the spin linewidth can be directly obtained by fitting the curves of κ shown in Fig. 4.11 with Eq. (4.4). The values of the spin linewidth γ obtained from these fits are close to 12 MHz for all but the smallest DPPH deposits. This value is compatible with $T_2 \simeq 13$ ns, 6 times lower than the typical values observed for DPPH molecules.[20] This result highlights the dependence of γ on the solvents used.

To determine the dependence of G_N on the size of the spin ensemble, we also need to know the number of spins, N_{eff}, that are effectively coupled to the resonators. The total number of spins, N, interacting with the resonator has been estimated from the topography of the deposits and the geometry of the central line. Let us first consider a resonator without nanoconstriction. SEM images, like the one shown in Fig. 4.10, tell us that the DPPH molecules tend to form aggregates with diameter around 3 μm. While at microscopic scales these aggregates may play a role, at macroscopic scales the sample can be considered to be homogeneous. Taking this into account, N can be estimated from the average number of molecules deposited on the region where the magnetic field of the resonator, thus the coupling to the spins, is significant. We have considered that only those spins located in a 30 μm wide region around the 14 μm wide central line significantly contribute to the coupling (see section 3.4.3 and Fig. 3.8).[21] Using this area, the length of the DPPH drop obtained from the microscopy images (Fig. 4.10), the density and molecular weight of DPPH (1.4 g/cm^3 and 394.92 g/mol respectively) and the concentration of each deposition, the number of spins that contribute to G_N can be determined, ranging from 9.3×10^7 to 8.4×10^{11}.

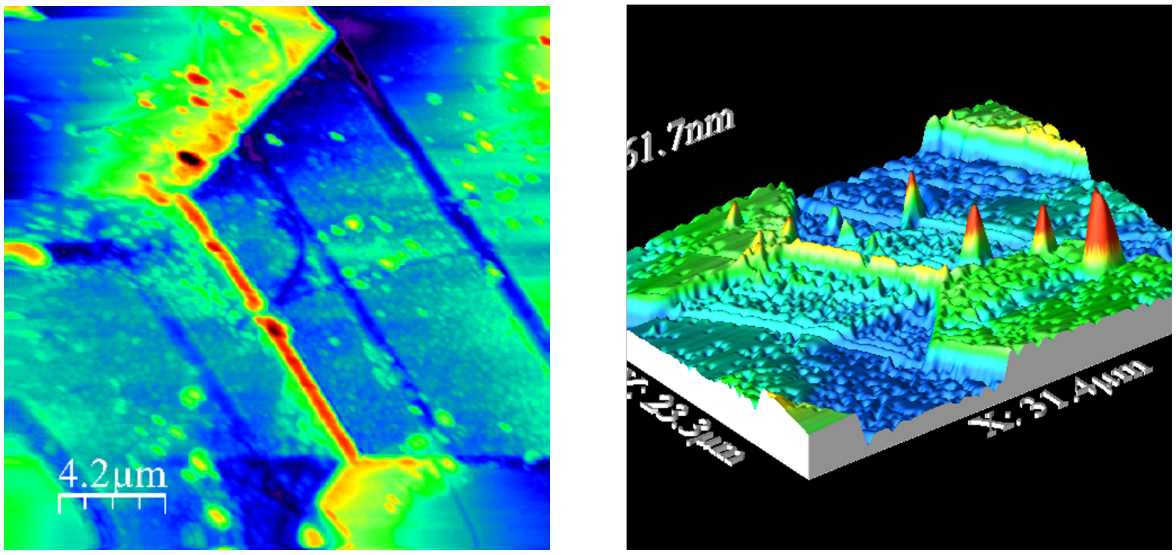

(a) **(b)**

Figure 4.12: AFM 3D topography images of two different depositions of DPPH by DPN in the same 158 nm wide nanoconstriction. In both cases there is a layer of DPPH molecules covering the entire constriction length, but this amount is not enough for measuring any signal corresponding to the molecules. In (b) we can see that nanoaggregates can form on top of the constriction, leading to an appreciable signal related to the coupled spins.

We next turn our attention to the resonator with a 158 nm wide nanoconstriction. Here, the morphology of the deposits plays a major role (see Fig. 4.12 for representative AFM images). The effective number of spins, N_{eff}, actually depends on the typical size of the DPPH drops formed (which varies with concentration at the central line) and on the probability that one of them "falls" sufficiently close to the nanoconstriction. After studying several depositions, we observe that we often have one of the two situations shown in Fig. 4.12. We either have most nanoaggregates far from the relevant area (Fig. 4.12(a)) or we have at least one aggregate on top or very near the nanoconstriction (Fig. 4.12). In the first case, the amount of molecules located on the nanoconstriction (10^7 or so) is not enough for giving any measurable coupling. When nanoagglomerates like those shown in Fig. 4.12(b) are formed near the constriction, a variation in κ can be observed. The number of molecules in both situations can be estimated by considering the dimensions of the nanoconstriction and the aggregate, while its density is taken as that from "pure" DPPH. Repeating this analysis for depositions of the different concentrations used for these experiments, a good estimation of the number of molecules near the constriction in each case can be performed.

Figure 4.13 shows how G_N depends on the number of spins effectively coupled to the resonator for all the measurements performed on both resonators without (Fig. 4.13(a)) and with a 158 nm wide constriction (Fig. 4.13). As mentioned before, less molecules are needed for obtaining a measurable signal in the case of the resonator with the nanoconstriction than when no constriction is used. This translates into a larger slope in the dependence of the G_N versus N_{eff} plot in the former case.

Equation (4.1) predicts how the collective spin-photon coupling is enhanced with the number of spins effectively coupled to the resonator. Our experimental data agree with this prediction, being approximately proportional to $N_{\text{eff}}^{1/2}$. By performing a linear fit, we obtain the average coupling of a cavity photon to a single spin. We find $G_1/2\pi = 3.4 \pm 0.5$ Hz for the conventional resonator and $G_1/2\pi = 85.4 \pm 2.1$ Hz for the resonator with a 158 nm wide constriction. These

data confirm that a strong enhancement in G_1 (by a factor 24 in this case) takes place when the width of the resonator central line is reduced by a factor 100.

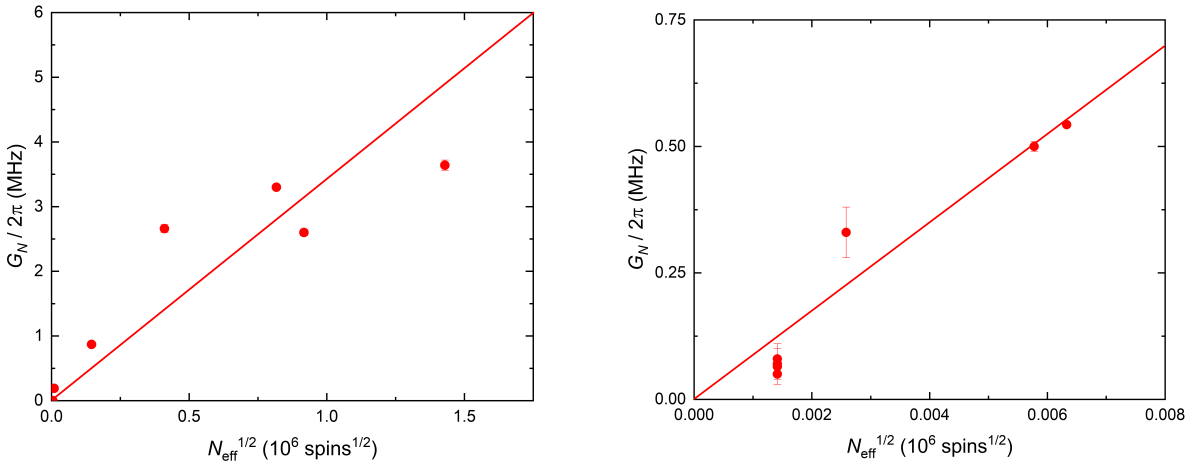

Figure 4.13: Collective spin-photon coupling measured for ensembles of organic free-radical DPPH molecules deposited on a CPW resonator with a 14 μm wide central line (a) without and (b) with a nanoconstriction of width 158 nm. The linear fits have been done considering Eq. (4.1), obtaining the coupling to a single spin in both cases.

4.6 Pushing the limits: Coupling to a 45 nm wide constriction at very low temperatures

4.6.1 Fabrication of the device and deposition of the DPPH molecules

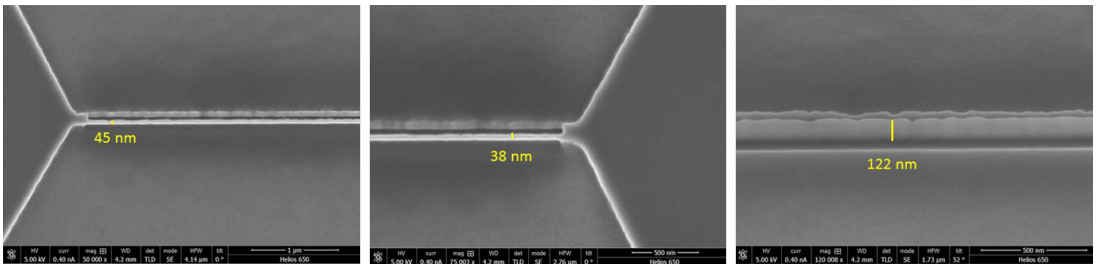

Figure 4.14: SEM images of a 42 nm wide nanoconstriction.

In this section, we describe the experiments performed in close to optimal conditions to achieve the maximum spin-photon coupling. In addition, we measure G_N at very low temperature, which takes N_{eff} close to the total number of molecules N located near the nanoconstriction. Measurements were performed using a resonator with a 14 μm wide central line, where a 42 nm wide nanoconstriction, close to the minimum resolution of this technique, was fabricated (Fig. 4.14). We made a DPN deposition of DPPH molecules at its centre, obtaining the deposits shown in Fig. 4.15.

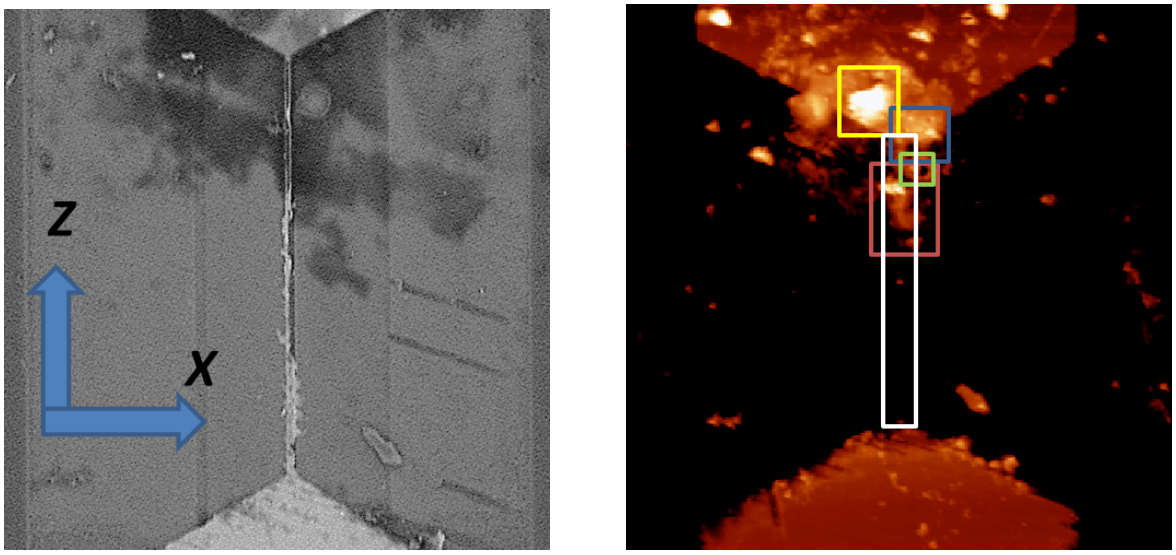

(a) **(b)**

Figure 4.15: (a) SEM and (b) AFM images of the 42 nm wide nanoconstriction after the deposition of DPPH molecules by DPN. Dark areas in (a) correspond to remains of glycerol, while bright spots correspond to DPPH nanoaggregates. Rectangles in (b) indicate the areas that have been analysed by AFM imaging to estimate the number of molecules close enough to the central line to be coupled to it.

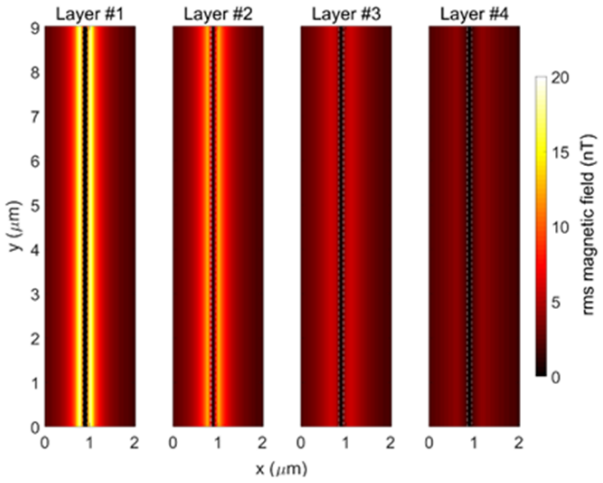

Figure 4.16: Z component (perpendicular to the plane of the resonator, Y component in Fig. 4.15) of the magnetic field generated by a photon at the centre of each simulation cell. This is the component which produces the spin transition in DPPH when the external field is applied along the X axis, as it was the case in the experiments described here. This calculation was performed considering a three-dimensional grid centered over the 42 nm wide nanoconstriction, with a cell size of $100 \times 100 \times 100$ nm^3. The magnetic field was studied in four layers located progressively farther from the chip surface.

Before showing the results of the transmission measurements, we again determine the number of molecules effectively coupled to the CPW resonator. For doing this, we first need to establish a volume around the nanoconstriction in which the DPPH molecules inside couple significantly to the cavity photons. This was done by first performing a simulation of the magnetic field generated by the CPW resonator. Combining this simulation with AFM images of the DPPH

deposition we were able to precisely calculate the coupling energy per spin for the obtained DPPH deposits. A magnetic field simulation is shown in Fig. 4.16. It shows the expected decay of the photon's magnetic field with increasing distance. The spatial distribution of the local magnetic field was calculated considering the root mean square value of the vacuum current fluctuations, $I_{\mathrm{rms}} = \omega_r \sqrt{\pi h / 4 Z_0} = 11.3$ nA, circulating through a resonator with impedance $Z_0 = 50\ \Omega$.[10] The finite-element based software 3D-MLSI, which solves the London equations for a given geometry of a superconducting circuit, was then used for computing the distribution of the magnetic field generated by I_{rms}.[22]

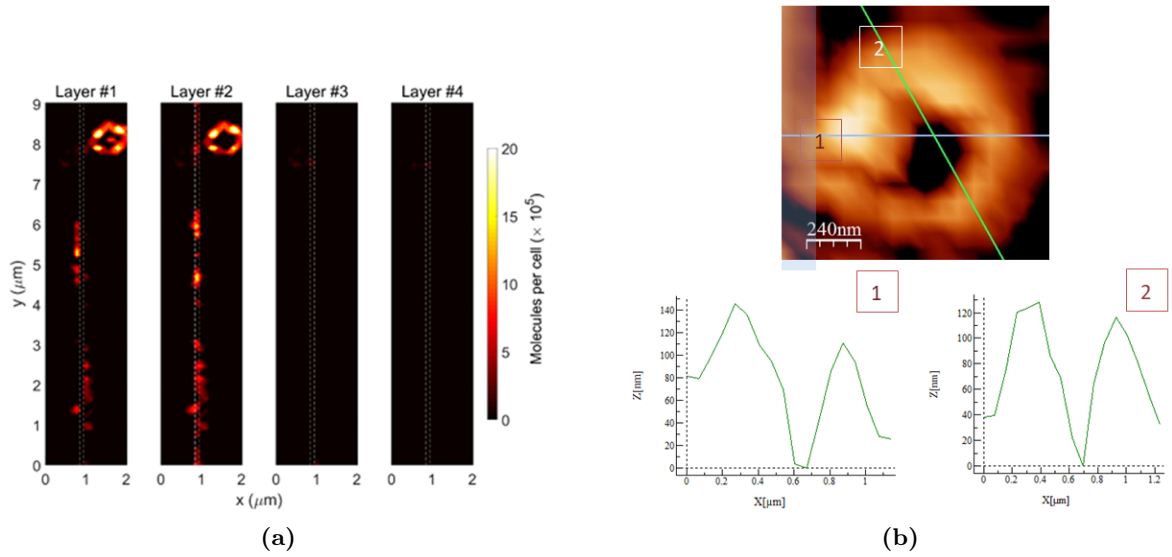

Figure 4.17: (a) Calculation of the distribution of DPPH molecules in the same three-dimensional grid considered in Fig. 4.16. This calculation was performed by a study of several AFM images obtained at different heights. (b) Analysis by AFM of the heights of one of the DPPH clusters shown in (a). Measuring the height profile and the area of each nanoaggregate, the total number of molecules coupled to the nanoconstriction has been determined, obtaining a value of $N \sim 1.6 \times 10^8$ molecules.

Figure 4.17(a) shows the determination by AFM of the number of DPPH molecules in the same three-dimensional grid considered in Fig. 4.16. It can be seen that most of the deposited molecules lie at short distance from the resonator surface. The analysis of the size of one of the detected nanoaggregates is shown in Fig. 4.17(b). By AFM, the height profile of the several detected nanoaggregates indicated in Fig. 4.15(b) has been determined. Then, knowing the surface of each aggregate, thus their volume, and the density and molecular weight of DPPH (1.4 g/cm^3 and 394.92 g/mol respectively), the total number of molecules deposited inside the magnetic mode volume of the resonator has been determined, obtaining a value $N \simeq 1.6 \times 10^8$ molecules. This number of spins is below the minimum amount detectable in the experiments carried out at 4.2 K (see Fig. 4.11), since at 4.2 K the number of spins effectively coupled to the resonator is reduced by a factor 7.9×10^{-3} (see Eq. (4.1)).

4.6.2 Experimental results: transmission as a function of temperature

Now we show the results of the transmission experiments performed with the previous sample at different temperatures. The device was introduced in an adiabatic demagnetization refrigerator (ADR) hosted by the Atominstitut of the Technical University of Vienna, with a base temperature of about 44 mK. Several measurements were performed for temperatures ranging from 44 mK to

1.4 K, and with applied magnetic fields up to 60 mT using a homemade superconducting vector magnet. Due to experimental constraints, this field was applied along the X laboratory axis shown in Fig. 4.15(b), within the plane of the device. The microwave transmission was measured by a VNA, attenuating the input signal down to a level of about 5×10^5 photons, thus smaller than N.

Results of the transmission experiments performed at 44 mK are shown in Fig. 4.18, while the evolution of κ with magnetic field for all the temperatures is shown in Fig. 4.19. Although the number of molecules near the nanoconstriction is below the minimum dose detectable at 4.2 K, as previously shown, the much lower temperature leads to a larger spin polarization, thus a much larger N_{eff}. This accounts for the neat absorption signal that is observed in the results, especially in the measurements done at 44 mK. In this case, a least-squares fit of κ versus magnetic field gives a collective coupling $G_N/2\pi \simeq 1.9$ MHz, and a spin linewidth $\gamma \simeq 65$ MHz. The latter value is 5 times larger than expected from the values of γ previously measured. The additional broadening may be arising from two facts: the smaller size of the transferred DPPH nanoagglomerates, which suggest that DPPH tends to lose crystalline order; DPPH molecules are dispersed in a polymeric matrix. Both effects suppress direct exchange interactions between spins, and thus increase the spin linewidth. Therefore, despite the quite large collective coupling achieved at very low temperature, the results indicate that the system remains in the weak coupling regime.

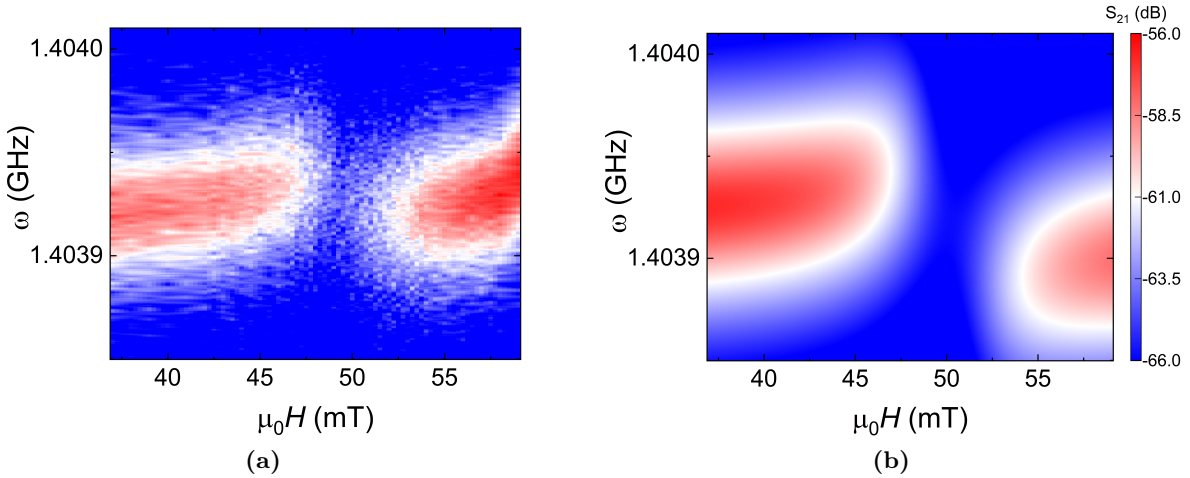

Figure 4.18: (a) Experimental and (b) simulated 2D plots of the microwave transmission through the DPPH deposition shown in Fig. 4.15 on a 1.4 GHz CPW resonator with a 42 nm wide nanoconstriction. The experiment was performed at a temperature of 44 mK. The number of spins close enough to the nanoconstriction was $N \simeq 1.6 \times 10^8$ DPPH molecules, corresponding to $N_{\text{eff}} \simeq 10^8$ spins effectively coupled to the resonator according to Eq. (4.1).

Figure 4.20 shows the evolution of the collective spin-photon coupling G_N with temperature (or with the number of effectively coupled spins, which is temperature dependent as given by Eq. (4.1)). Increasing temperature produces a decrease of the spin polarization and, then, a reduction in the spin-photon coupling. Combining these data and the number N of molecules in the cavity volume, we estimate an average single spin coupling $G_1/2\pi = 186 \pm 7$ Hz. This value is more than twice larger than the one obtained for the 158 nm wide nanoconstriction, and two orders of magnitude higher than the coupling achieved for the 14 μm wide resonator.

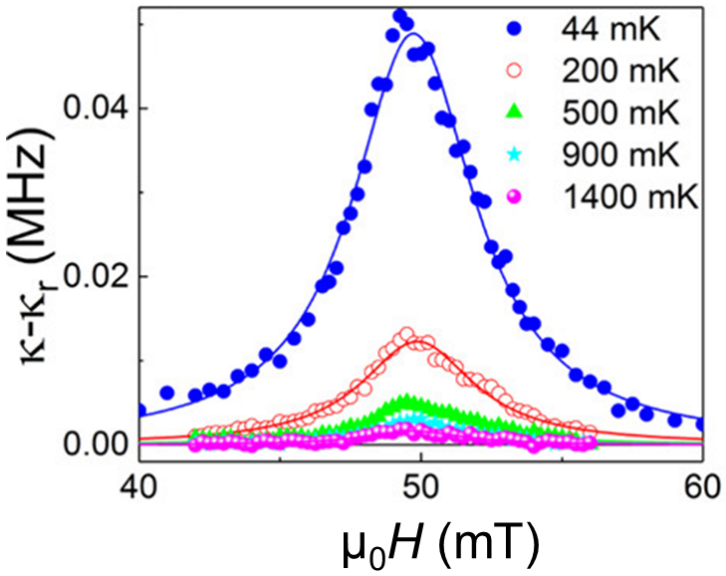

Figure 4.19: Evolution of κ with magnetic field for several temperatures, ranging from 44 mK to 1.4 K. The signal associated with the coupling between the spins and the resonator decreases as temperature rises up. For the minimum temperature achievable, a collective coupling $G_N/2\pi = 1.9$ MHz, and spin linewidth $\gamma = 65$ MHz have been obtained by a least-square fit performed using Eq. (4.4). These values were used to perform the simulation shown in Fig. 4.18(b).

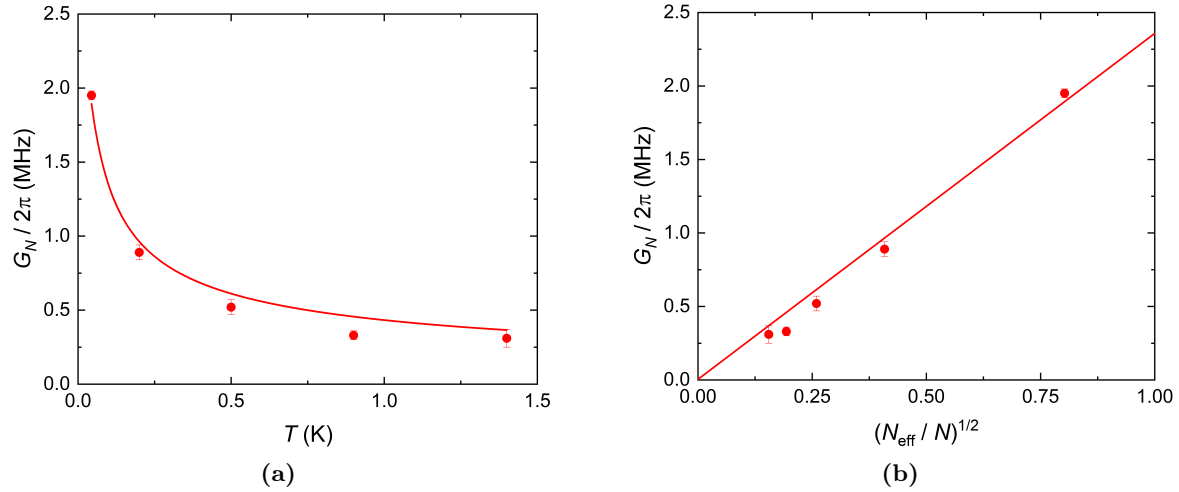

Figure 4.20: (a) Temperature dependence and (b) N_{eff} dependence of G_N, obtained from least-square fits of the κ curves shown in Fig. 4.19, together with least-square fits based on Eq. (4.1). With these fits, a value of $G_N/2\pi \simeq 2.3$ MHz for $T = 0$ is extrapolated, and a single spin-photon coupling $G_1/2\pi = 186 \pm 7$ Hz is obtained.

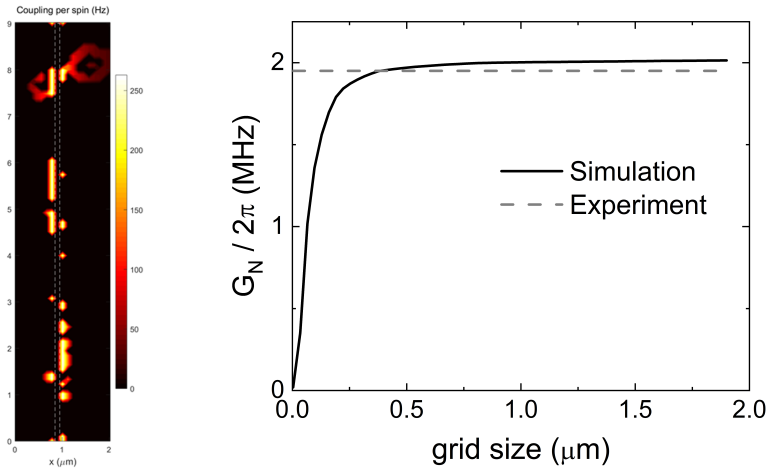

Figure 4.21: (a) Coupling per spin calculated using the data shown in Figs. 4.16 and 4.17. The calculation was performed considering a temperature of 44 mK. (b) Collective spin-photon coupling G_N calculated for the situation shown in (a) for different grid sizes and a temperature of 44 mK, together with the experimental coupling value obtained at this temperature. Spins located at a distance greater than 500 nm from the constriction give an almost negligible contribution to the coupling. From these results, and taking into account the 42 nm wide nanoconstriction shows a length of 10 μm, the effective mode volume can be considered as 1 μm$\times$1 μm$\times$10 μm$=$ 10 μm^3.

The expected collective spin-photon coupling from the detected deposits can be calculated and compared to the experimental results. The calculation of the coupling per spin is shown in Fig. 4.21(a). For the estimation of the spin-photon coupling at each cell, we have multiplied the coupling per spin at a cell times the square root of the number of spins in that cell. Considering a field $\mu_0\vec{h}_i$ at the centre of each cell:[10]

$$G_i = g\mu_B\sqrt{n_i}\left|\left\langle +1/2\left|\vec{h}_i\cdot\vec{S}\right|-1/2\right\rangle\right| \tag{4.5}$$

where n_i is the effective number of spins in the cell at a given temperature. Figure 4.21(a) tells us that the main contribution to the collective coupling will come from the spins located closer to the constriction, since the magnetic field generated by the resonator is stronger.

The collective coupling was calculated for different grid sizes. This calculation was performed by adding up the couplings of all cells as follows:[23]

$$G_N = \sqrt{\sum_i G_i^2} \tag{4.6}$$

This calculation allows determining the effective mode volume of this resonator. The results of the calculation performed at 44 mK, shown in Fig. 4.21(b), tell us that all the spins located within a volume of 10^{-14} L around the nanoconstriction contribute to the collective spin-photon coupling, while G_N saturates for larger volumes. The collective coupling obtained from Eq. 4.6 after summing over this volume is $G_N/2\pi \simeq 2.0$ MHz. and the average single spin coupling is $G_1/2\pi \simeq 200$ Hz. These values agree very well with the experimental ones ($G_N/2\pi \simeq 2.3$ MHz and $G_1/2\pi = 186 \pm 7$ Hz). The small differences can be produced by crystalline defects in DPPH that tend to make part of the molecules diamagnetic. Besides, these calculations allow extracting reliable information on the coupling of individual spins at specific locations with respect to the transmission line.

4.7 Dependence of the spin-photon coupling with nanoconstriction width

The previous results allow an accurate determination of the coupling of single spins to coplanar resonators with central line widths ranging from 400 μm down to 42 nm. The dependence of G_1 on the central line width is shown in Fig. 4.22.

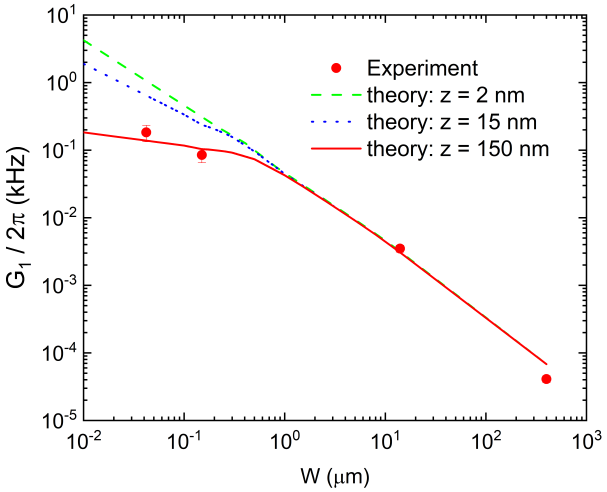

Figure 4.22: Evolution of the average single spin-photon coupling with the width of the CPW resonator central line. The lines are calculations of this coupling considering a spin located at three different heights z over the constriction.

For $w \leq 1$ μm, an enhancement of $G_1 \propto 1/w$ is observed, while for $w \geq 1$ μm this increase in the single spin-photon coupling is slowed down. These results show that decreasing the size of the line that generates the microwave magnetic field provides a promising strategy to achieve quite high couplings. This behaviour can be understood taking into account the geometry of the resonator central line and the topography of the DPPH deposits.

The finite thickness of the niobium film, 150 nm that are reduced near the constriction as shown in Fig. 4.14, decreases the local magnetic field generated by the supercurrents circulating through the resonator, and thus the slope of the theoretical curve when w becomes smaller than the niobium thickness.

The position of the DPPH deposits on the resonator is also critical, specially considering that the coupling enhancement is concentrated in a region with dimensions comparable to w. The numerical calculations of G_1 shown in Fig. 4.22, considering a molecule located at different heights above the nanoconstriction, show that the evolution of G_1 is very influenced by this height. For z close to 0, $G_1 \propto 1/w$ regardless of the constriction width, while for $z \neq 0$ this coupling saturates for $w \leq z$. Hence, an adequate sample integration, making z as close to zero as possible, becomes one of the most important factors to achieve the maximum spin-photon coupling.

Taking into account that the photon energy, thus $G_1 \propto \omega_r$, it is useful to define the dimensionless coupling G_1/ω_r for a comparison between our results and those of the literature. Considering the maximum single spin-photon coupling obtained in this experiments, $G_1/2\pi = 186$ Hz, and a frequency of 1.4 GHz, we obtain $G_1/\omega \simeq 1.3 \times 10^{-7}$. This result is higher than the maximum single spin-photon coupling reported in the literature ($G_1/2\pi \simeq 450$ Hz for a 7 GHz resonator, corresponding to $G_1/\omega_r \simeq 6.4 \times 10^{-8}$,[24] result obtained with lumped-element resonators coupled to impurity spins on their Si substrate. However, the average G_1 is still far from the maximum theoretically attainable single spin-photon coupling, which should reach a value close

to 1 kHz.[10;25] However, the analysis of the coupling of each of the molecules deposited onto the device, shown in Fig. 4.21(a), suggests that such a limit has been achieved for those molecules located right on top of the transmission line, or next to it.

4.8 Searching for new resonator designs: between 2D and 3D

4.8.1 Design, fabrication and test of 2.5D superconducting resonators

We have seen that the single spin-photon coupling can be highly enhanced in CPW resonators when a nanoconstriction is fabricated. However, these devices lack the ability to maximize the coupling by reducing the overall inductance, as the latter needs to be kept sufficiently large to ensure a proper transmission. In this section, we explore a different approach, based on a novel circuit design put forward by Andreas Angerer and co-workers from the Technical University of Vienna. It somehow combines a three-dimensional cavity with a CPW resonator, and we shall therefore call it a "2.5D" resonator. The experiments that will be explained in this section were carried out in the Atominstitut of the Technical University of Vienna, while the DPN depositions took place at INMA.

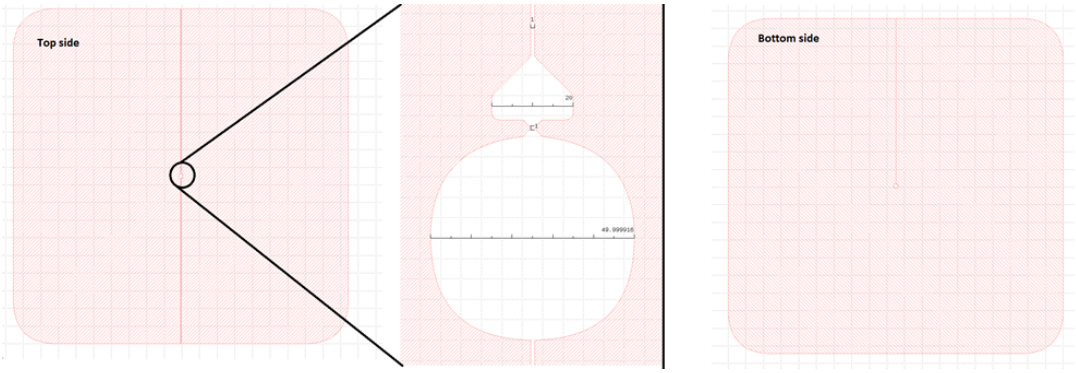

Figure 4.23: Design of the top plate of the 2.5D resonator (left), with a zoom view of its centre showing the inductor joining the two halves of the plate (centre), and design of the bottom plate of the resonator (right). These two plates are placed inside a copper box facing each other, forming a capacitor.

The design of one of these new resonators is shown in Fig. 4.23. It consists of two plates of niobium, each of them deposited on a different sapphire waffer, placed inside a copper box facing each other to form a capacitor. One of these plates has its two halves joined only by a 1 μm wide niobium wire at its centre that acts as a tiny inductor. The whole system acts as an LC resonator with resonance frequency $\omega_r = 1/\sqrt{LC} \simeq 2.5$ GHz. Its innovative design tries to combine some of the best characteristics of two and three-dimensional resonators: the confinement of the photon's electromagnetic field, characteristic of the 2D resonators,[1] and longer coherence times typical of 3D cavities.[26;27]

A 50 nm wide nanoconstriction was fabricated in the inductor with the goal of enhancing the local magnetic field generated by the resonator, similarly to what was observed with the CPW resonators. This constriction was fabricated with the SEM/FIB system Helios Nanolab Dual Beam from the LMA (see section 2.3.2 for more details). The inductor width was reduced from the initial 1 μm to $\sim$ 50 nm along a distance of 2 μm, as shown in Figs. 4.24 and 4.25.

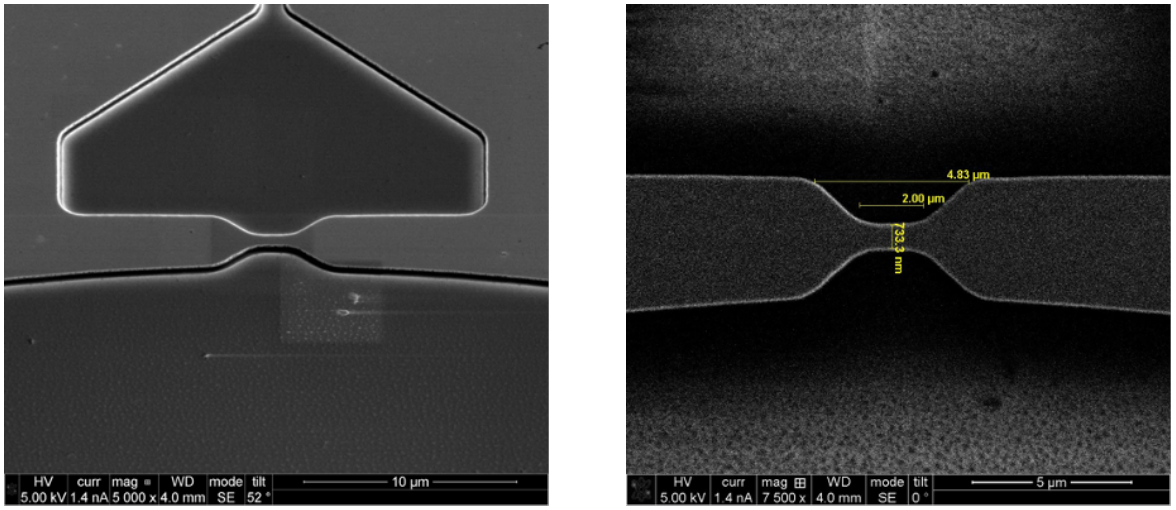

(a) **(b)**

Figure 4.24: SEM images of the inductor of the 2.5D resonator before fabricating the nanoconstriction. The inductor has a width close to 1 μm and a length of 20 μm. It has a preliminary 1 μm wide, 2 μm long constriction.

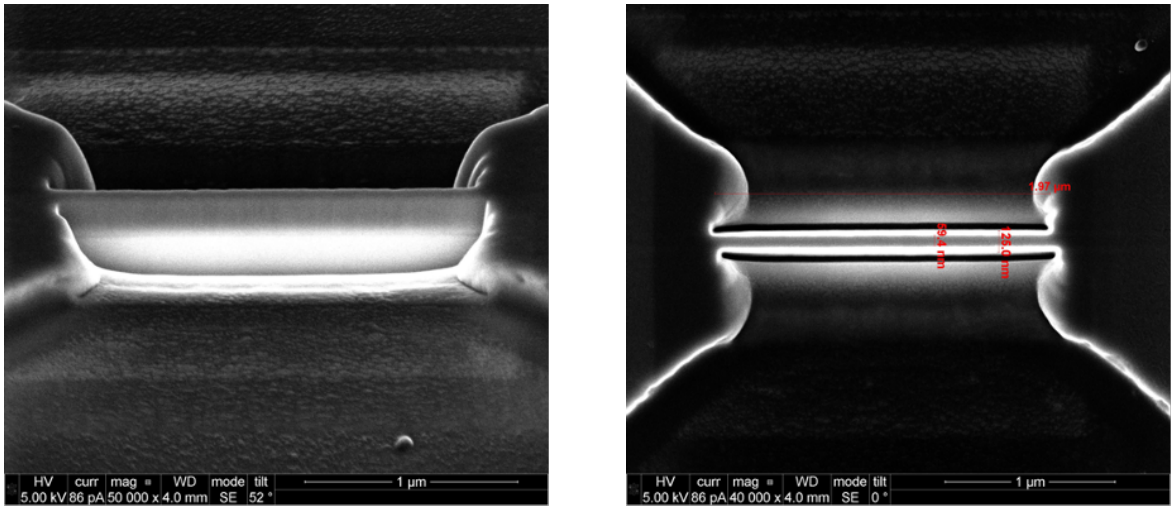

(a) **(b)**

Figure 4.25: SEM images of the central region of the inductor of a 2.5D resonator after fabricating a 50 nm nanoconstriction in it. It shows a minimum width of 59 nm and a length of almost 2 μm.

The transmission characteristics of two of these 2.5D resonators, one with a nanoconstriction and another without it, were studied by means of microwave transmission experiments. They were introduced in an adiabatic demagnetization refrigerator (ADR) with a base temperature of 50 mK, and connected to a VNA with which the microwave transmission was measured while changing the frequency and power of the input signal (see section 2.5.2).

An example of the microwave transmission measured with the resonator with a nanoconstriction fabricated in it, together with the evolution of its quality factor Q with input power is shown in Fig. 4.26. The Fano behaviour of this resonance, that gives rise to an asymmetric line shape, can be clearly seen here. For low input powers (below -30 dBm), Q remains stable at ~ 6400.

For higher input powers, the high current circulating through the nanoconstriction causes a gradual breakdown of the superconductivity, leading to a decrease of the quality factor. The value of Q obtained with this resonator can be compared with the one measured before the nanoconstriction was fabricated (see Table 4.1). Although Q is reduced by a factor 3, κ remains lower than γ of DPPH, thus this circuit is still suitable for performing measurements of the spin-photon coupling.

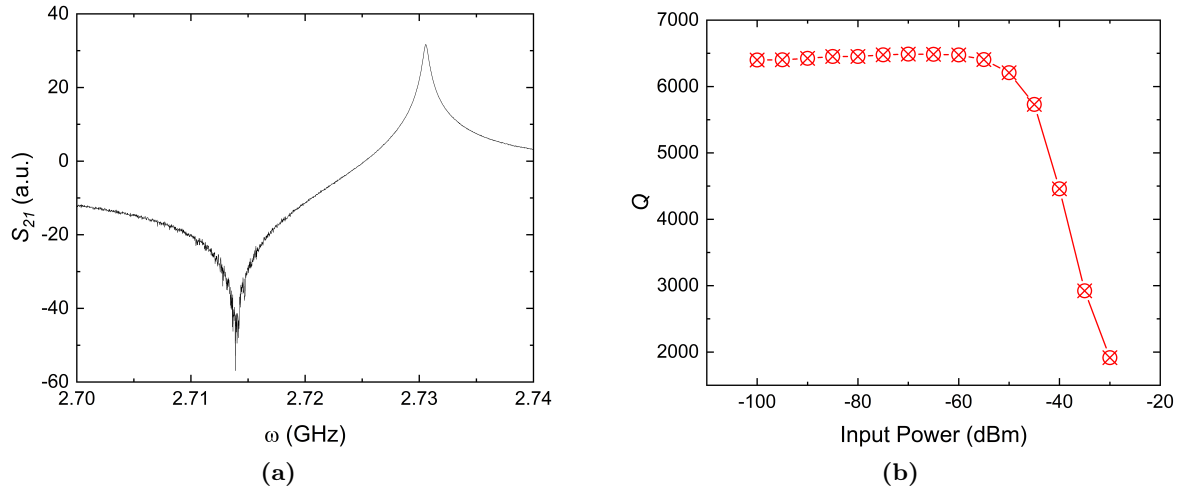

Figure 4.26: (a) Microwave transmission through a 2.5 GHz resonator with the nanoconstriction shown in Fig. 4.25(b), measured at 50 mK with an input power of -55 dBm. Both peaks, minimum and maximum, correspond to the same Fano resonance. (b) Evolution of Q with input power measured for this resonator at this temperature. It remains stable for input powers below -30 dBm.

Q (no constriction)	Q (constriction)
18200	6400

Table 4.1: Values of the quality factor measured in a 2.5 GHz resonator without and with a nanoconstriction.

4.8.2 Study of the coupling to DPPH organic radical molecules

A DPPH sample was deposited by DPN from solution on top of the nanoconstriction. The "ink" had a volume concentration of 40 mg/ml of DPPH in DMF with 10% glycerol. An image of the achieved deposit is shown in Fig. 4.27. Most of the DPPH molecules formed nanoaggregates outside the nanoconstriction. The apparent repulsion of DPPH molecules away from the nanoconstriction may be due to the accumulation of charges during the FIB process employed to fabricate the constriction. Nevertheless, a small DPPH nanodeposit remained on top of the constriction (see Fig. 4.27(b)). By AFM imaging, the nanodeposit was estimated to have a diameter of 38 nm and a height of around 9 nm. Considering these dimensions, the density of "pure" DPPH (1.4 g/cm^3) and its molecular weight (394.32 g/mol), the approximate number of molecules in the nanodeposit is then $N = 2.2 \times 10^5$.

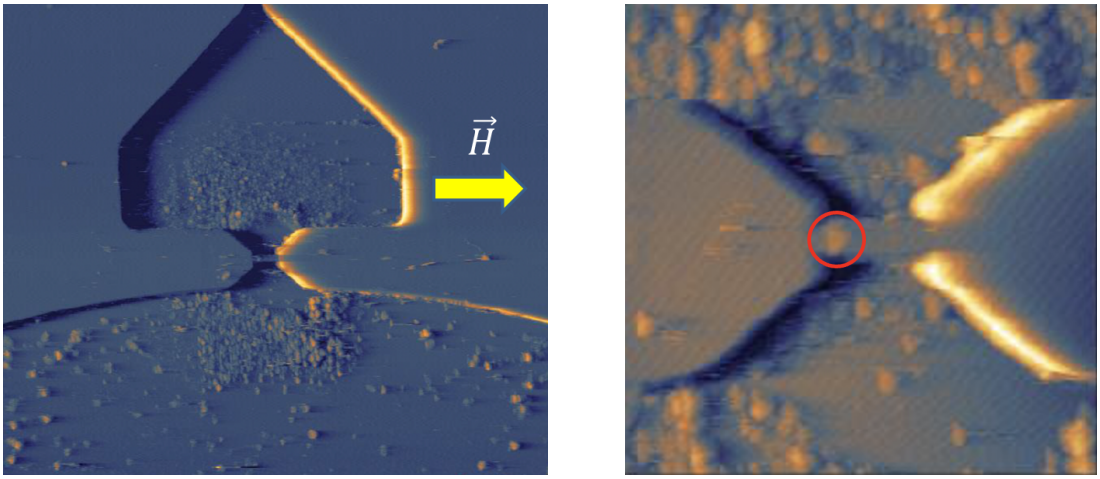

(a) (b)

Figure 4.27: AFM images of the first DPPH deposition on the 50 nm nanoconstriction, using a DPPH sample with concentration 40 mg/ml. The red circle surrounds the deposit that remained on top of the constriction.

Several transmission measurements were done with this device. The magnetic field was applied perpendicular to the microwave field generated by the resonator to maximize the spin-photon coupling. The results of the transmission experiment performed at 50 mK are shown in Figs. 4.28 and 4.29. There is no evidence of any detectable coupling between the DPPH spins and the resonator in neither ω_r or κ, possibly because the number of molecules close enough to the nanoconstriction was too small. The change of the resonance frequency, from 2.7 GHz for the bare chip to 3.27 GHz for the chip with DPPH on it, can be associated to the presence of solvent that changes the dielectric constant, thus the capacitance, of the resonator.

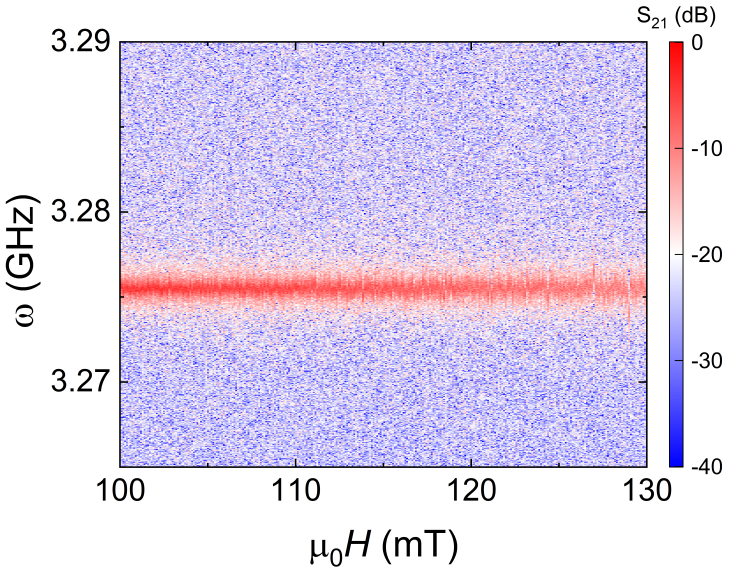

Figure 4.28: 2D plot of the microwave transmission at 50 mK through a 2.5D resonator, with resonance frequency $\sim$ 2.5 GHz and a 50 nm wide constriction, hosting a DPPH nanodeposit (see Fig. 4.27). No absorption signal is appreciated near 117 mT, the magnetic field at which DPPH and resonator frequencies should be tuned.

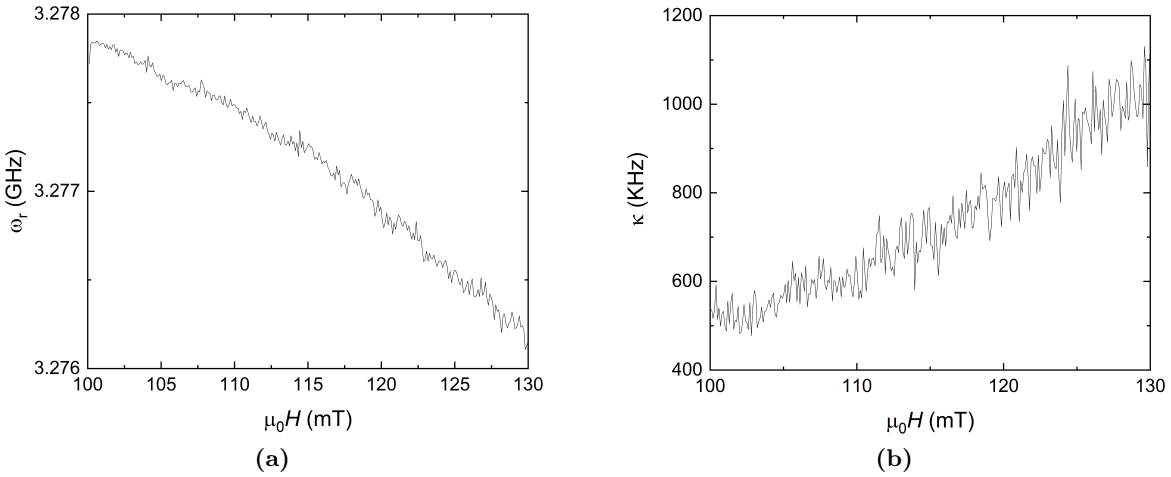

Figure 4.29: Curves of the resonance frequency ω_r (a) and the linewidth κ (b) obtained from the fit of transmission data shown in Fig. 4.28. No absorption signal can be appreciated near 117 mT in any of the two curves.

The resonator was carefully cleaned and a new DPPH deposition was made on the nanoconstriction. In this case, the ink had twice the concentration of DPPH than the first one, 80 mg/ml. An image of this new deposition is shown in Fig. 4.30. The results of the transmission measurements performed with this sample are shown in Figs. 4.31 and 4.32. The experimental conditions were the same as for the previous measurements. Again, no signal associated with a net absorption of photons by the DPPH spins can be observed. As with the first attempt, this can be due to the presence of too few spins close enough to the nanoconstriction.

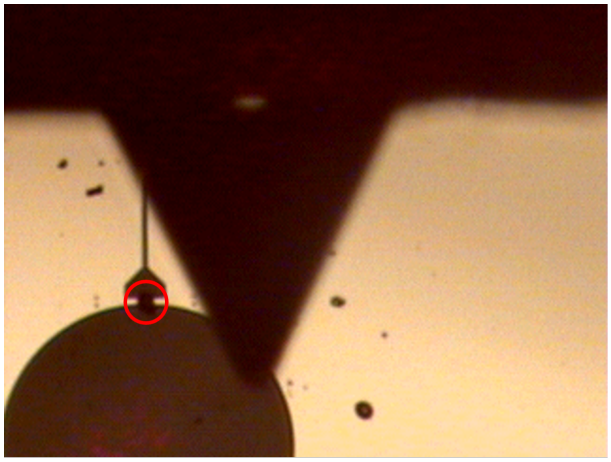

Figure 4.30: Optical microscopy image of the second DPPH deposition performed on the 2.5D resonator with a 50 nm wide nanoconstriction. The red circle surrounds the drop deposited on top of the constriction. The ink used for this deposition had a DPPH concentration of 80 mg/ml.

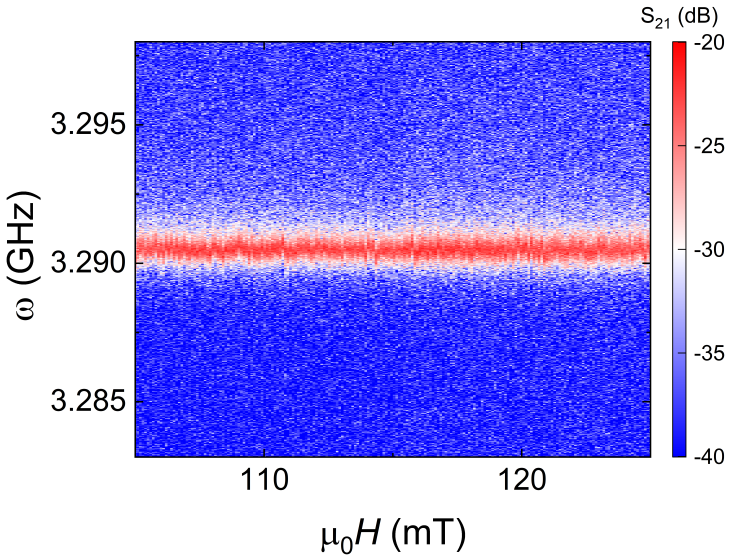

Figure 4.31: 2D plot of the microwave transmission at 50 mK through a 2.5D resonator with resonance frequency $\sim$ 2.5 GHz and a 50 nm wide constriction, hosting a more concentrated DPPH deposit. No absorption signal is appreciated near 117 mT, the magnetic field at which DPPH and resonator should be tuned.

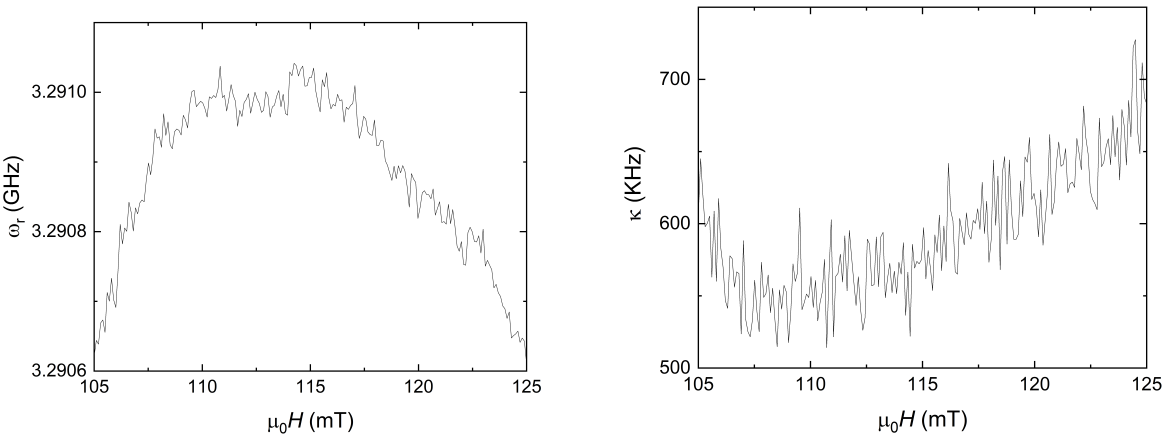

Figure 4.32: Curves of the resonance frequency ω_r (a) and the linewidth κ (b) obtained from fits of the transmission data shown in Fig. 4.31. No absorption signal can be appreciated near 117 mT in any of the two curves.

Due to the difficulties found while depositing DPPH samples with DPN on this resonator, still not clearly understood, a different approach was applied. A third deposition, in this case using a micropipette and the 80 mg/ml ink, was made. An image of this deposit is shown in Fig. 4.33. It widely covers the inductor area, ensuring that there are enough molecules near the constriction to obtain an appreciable signal.

Microwave transmission results obtained with this third sample are shown in Fig. 4.34. We see a very intense absorption signal at 135 mT that can be associated with the resonant coupling of DPPH spins to the cavity photons. This resonance moves from 119 mT, the field at which it should appear considering $g_S \simeq 2$, to 135 mT, corresponding to $g_S \simeq 1.75$, possibly due to an error in the magnet calibration (this region was also studied with the previous samples, and no

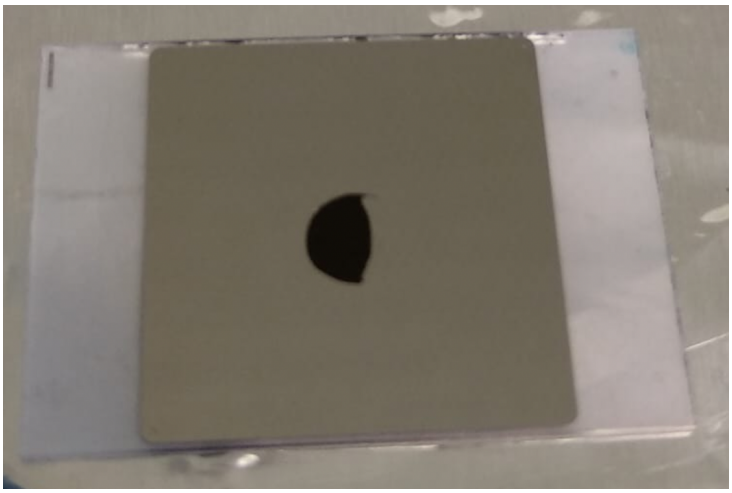

Figure 4.33: Photo of the third DPPH deposition, performed with micropipette on the 2.5D resonator with a 50 nm wide nanoconstriction. The ink used here had a DPPH concentration of 80 mg/ml.

coupling was detected). The microwave transmission was fitted using a python script, developed by a member of our research group (Víctor Rollano), which is capable of fitting the transmission curves as a function of frequency while taking into account the assymetry of the resonances due to Fano interference effects (see Fig. 4.26(a) and chapter 3 for more details). With this fitting, we obtained a collective spin-photon coupling $G_N/2\pi \simeq 51.5$ MHz and a spin linewidth $\gamma \simeq 31.8$ MHz. These values confirm that we have achieved the strong coupling regime with this sample, likely due to the high number of molecules deposited near the inductor in this case. The high value of γ, compared to the homogeneous broadening associated with $T_2 \simeq 80 - 120$ ns can be assigned to the same origin commented in section 4.6.

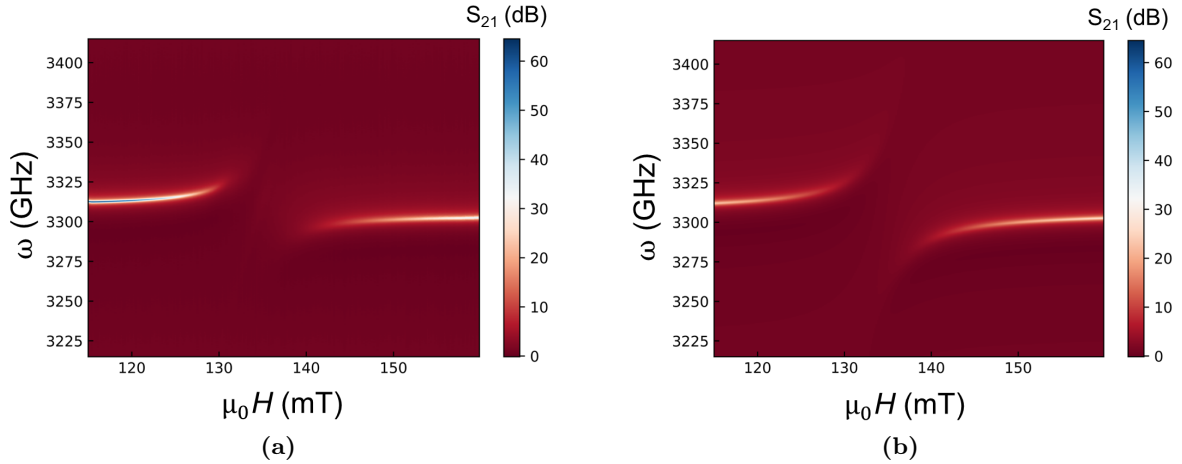

Figure 4.34: (a) Experimental and (b) simulated 2D plots of the microwave transmission measured at 50 mK through the nanoconstriction of the 2.5D resonator, hosting a large and highly concentrated DPPH deposit. A clear absorption signal, associated with the DPPH spins, can be observed near 135 mT. The obtained spin-photon coupling and spin linewidth for this sample are: $G_N/2\pi \simeq 51.5 \pm 2.7$ MHz, $\gamma \simeq 31.8$ MHz.

Finally, a similar deposition was performed on a 2.5 GHz resonator without nanoconstriction. In this way, we can compare the collective spin-photon couplings under identical conditions, with

and without nanoconstriction, thus testing the effect of the latter. The same 80 mg/ml DPPH ink was used. The deposit is shown in Fig. 4.35.

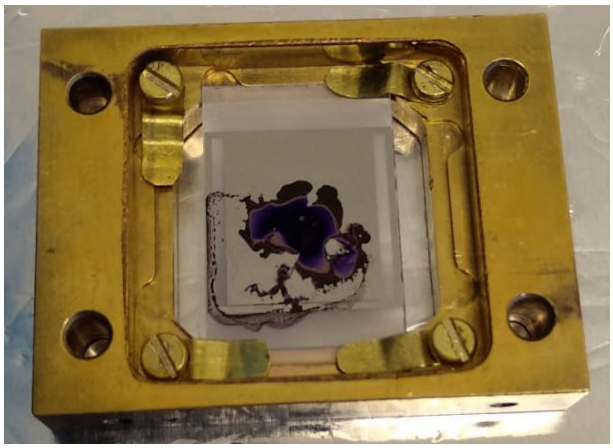

Figure 4.35: Photo of the fourth DPPH deposition, performed with a micropipette on a 2.5D resonator without nanoconstriction. The ink had a DPPH concentration of 80 mg/ml.

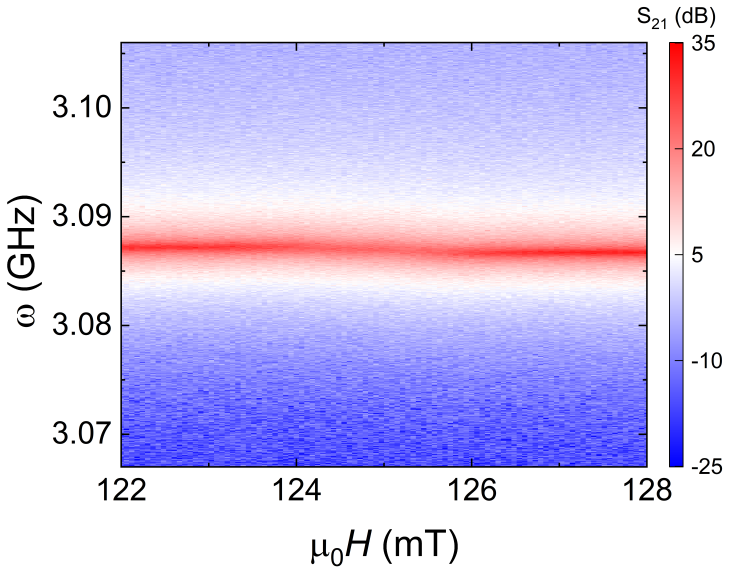

Figure 4.36: 2D plot of the microwave transmission measured at 50 mK through a 2.5D resonator without nanoconstriction hosting a large and highly concentrated DPPH deposit. A small absorption signal, associated with the coupling to the DPPH spins, can be appreciated near 125 mT.

The microwave transmission measured at 50 mK is shown in Fig. 4.36, and the evolution of ω_r and κ with magnetic field are shown in Fig. 4.37. While in the 2D transmission plot it is hard to see any signal corresponding to the absorption of photons by the spins, the curves of ω_r and κ show clear evidence of a net coupling between the spins and the cavity photons. Since in this case we are in the weak coupling regime, the peak observed in Fig. 4.37 has been fitted using Eq. (4.4), obtaining a collective spin-photon coupling $G_N/2\pi \simeq 4.78 \pm 0.04$ MHz and a spin linewidth $\gamma \simeq 29.24 \pm 0.76$ MHz. This value of γ is very similar to the one obtained with the previous deposition performed on the resonator with nanoconstriction, so the presence of the constriction does not seem to be introducing an extra decoherence. The collective spin-photon coupling is now reduced by 1 order of magnitude, showing that the nanoconstriction increases

very much the intensity of the microwave field, and thus the spin-photon coupling to seome of the DPPH molecules, also in these 2.5D resonators.

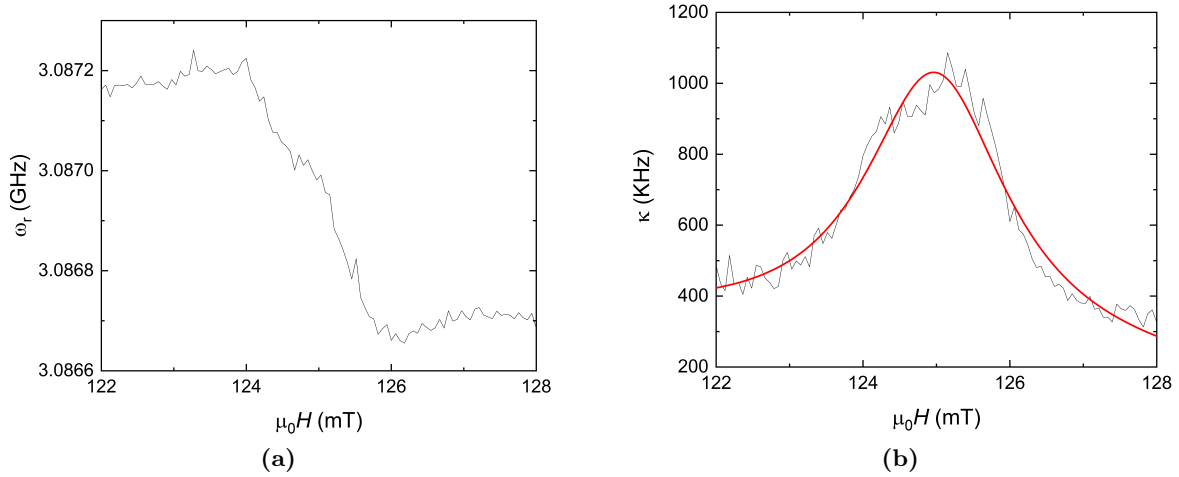

Figure 4.37: Evolution of (a) the resonance frequency ω_r and (b) the linewidth κ obtained from the transmission measurement shown in Fig. 4.36. A sharp drop in ω_r, accompanied by a maximum in κ, can be observed at 125 mT. The fit of κ has been performed using Eq. (4.4).

We will complete the analysis of these results determining the single spin-photon coupling achieved with this 2.5D resonator with and without a nanoconstriction. A quick calculation can tell us approximately the number of molecules effectively coupled to the whole inductor, $N_{\mathrm{t,eff}}$, and effectively coupled to the nanobridge, $N_{\mathrm{c,eff}}$. The inductor has a total length of 20 μm and a width of 2 μm, while there is an initial 1 μm wide, 2 μm long constriction in its centre (see Fig. 4.24). Using similar arguments as those discussed previously for CPW resonators, the mode volume of the inductor can be estimated as $V_t = 18 \times 4 \times 4 + 2 \times 2 \times 2$ μm^3. On the other hand, as can be seen in Fig. 4.25, the nanobridge presents a length of 2 μm and a width of about 50 nm, which can be associated to a mode volume $V_c = 2 \times 1 \times 1$ μm^3 (see section 4.6 above). Considering these volumes, the DPPH concentration of 80 mg/ml, the molecular weigth of DPPH (394.32 g/mol) and the thermal factor introduced in Eq. (4.1) for a temperature of 50 mK, which reduces the number of spins coupled to the resonator by a factor of 0.894 the number of molecules effectively coupled to the whole inductor an to the nanoconstriction are:

$$N_{\mathrm{t,eff}} = \frac{2.96 \times 10^{-10} \cdot 80 \cdot 6.022 \times 10^{23} \cdot 0.894}{394320} = 3.26 \times 10^{10}, \tag{4.7}$$

$$N_{\mathrm{c,eff}} = \frac{2 \times 10^{-12} \cdot 80 \cdot 6.022 \times 10^{23} \cdot 0.894}{394320} = 2.25 \times 10^{8}. \tag{4.8}$$

The average single spin-photon coupling of the inductor without nanoconstriction, $G_{1,nc}$, can then be determined considering $N_{\mathrm{t,eff}}$ and the value of G_N obtained with it:

$$G_{1,nc} = \frac{G_{N,nc}}{\sqrt{N_{\mathrm{t,eff}}}} = \frac{4.78 \times 10^6}{\sqrt{3.26 \times 10^{10}}} = 26.5 \pm 0.2 \text{ Hz}. \tag{4.9}$$

This value is pretty similar to that predicted for a CPW resonator with a 2 μm wide central line (Fig. 4.22). The enhancement of the single spin-photon coupling produced by the nanobridge can be determined considering that now we have $N_{\mathrm{c,eff}}$ molecules coupled to the nanoconstriction with a single spin-photon coupling $G_{1,c}$, and $N_{\mathrm{t,eff}} - N_{\mathrm{c,eff}}$ molecules coupled to the inductor

with the value of $G_{1,nc}$ previously calculated. The total spin-photon coupling is approximately then given by:

$$G_N = \sqrt{(N_{\text{t,eff}} - N_{\text{c,eff}}) \cdot G_{1,nc}^2 + N_{\text{c,eff}} \cdot G_{1,c}}. \tag{4.10}$$

We have obtained a value of $G_N = 52 \pm 3$ MHz from the fitting performed on the microwave transmission data from the resonator with a nanoconstriction (Fig. 4.34). With this value, the number of spins on the inductor and the nanoconstriction area, and the single spin-photon coupling to the inductor, we can finally determine the average single spin-photon coupling to the nanoconstriction fabricated in this 2.5D resonator:

$$G_{1,c} = \sqrt{\frac{G_N^2 - (N_{\text{t,eff}} - N_{\text{c,eff}}) \cdot G_{1,nc}}{N_{\text{c,eff}}}} = 3.4 \pm 0.2 \text{ kHz}. \tag{4.11}$$

The nanobridge fabricated on this resonator enhances the single spin-photon coupling by two orders of magnitude when the width of the inductor is reduced from 1 μm down to 50 nm. This improvement is one order of magnitude higher than that obtained with the CPW resonators, with which the maximum single spin-photon coupling we obtained was around 200 Hz for a 50 nm wide nanobridge. Although the larger coupling can be in part (up to a factor 2) associated to the higher resonance frequency of these cavities, these results confirm that higher photon fields can be generated by this type of resonator compared to the CPW ones. This opens a new way for enhancing the spin-photon coupling by using LC resonators.

4.9 Conclusions

During this chapter, we have validated a method to improve the coupling of molecular spins to photons trapped in CPW resonators. Average single spin-photon couplings of about 180 Hz for CPW resonators with central linewidths close to 40 nm have been achieved, being this coupling a factor 60 higher than the one achieved with CPW resonators with central linewidths of 14 μm. Maximum couplings on the order of kHz have been estimated for distances between the spins and the device close to zero, showing that an adequate sample integration is critical to achieve the highest possible coupling.

We have verified that the collective spin-photon coupling follows a linear dependence with $\sqrt{N_{\text{eff}}}$, being a way to improve this coupling to increase the number of molecules near the resonator. We have also checked that temperature is a critical factor, being necessary to reduce it to a few mK to increase the number of molecules effectively coupled to the resonator.

Different types of resonators can be used to obtain an increase of the single spin-photon coupling. In section 4.8, a new design of resonator, the so-called 2.5D resonator, has been studied. With this device, a single spin-photon coupling of 3.4 kHz has been achieved with a 50 nm wide nanoconstriction, being this value one order of magnitude higher than the 186 Hz obtained with the CPW resonators with a similar nanoconstriction. The dimensionless coupling associated to these results, $G_1/\omega \simeq 1.03 \times 10^{-6}$, shows a record value, being one order of magnitude higher that the maximum spin-photon coupling obtained with CPW resonators with nanoconstrictions ($G_1/\omega \simeq 1.3 \times 10^{-7}$) and two orders of magnitude higher that the previous maximum single spin-photon coupling reported in the literature ($G_1/2\pi \simeq 450$ Hz for a 7 GHz resonator, corresponding to $G_1/\omega_r \simeq 6.4 \times 10^{-8}$.[24] This improvement is due to the resonator design, being an LC circuit with a very low inductance, thus a very high local microwave field close to it. Depositing the samples closer to the device surface, or designing LC resonators with even lower inductances, could allow us to improve even more this single spin-photon coupling.

The results described in this chapter show that reducing locally the width of the inductor of a microwave on-chip resonator provides a relatively simple, yet quite effective, method to enhance the coupling of these devices to spin qubits. Besides, this works with different resonator designs. For instance, it can be implemented into specially designed resonators, which minimize the circuit impedance and the inductance at the same time, maximizing the superconducting current at the inductor.[9;24;28] This implementation should allow enhancing the single spin-photon coupling to values of $G_1/2\pi$ close to 0.1 MHz at frequencies of order $4-5$ GHz. Some sections of chapter 5 will be dedicated to the implementation of these nanoconstrictions in LC resonators with very low impedance coupled to free-radical molecules.

Bibliography

[1] M. Göppl, A. Fragner, M. Baur, R. Bianchetti, S. Filipp, J. M. Fink, P. J. Leek, G. Puebla, L. Steffen, and A. Wallraff. Coplanar waveguide resonators for circuit quantum electrodynamics. *Journal of Applied Physics*, 104:113904, 2008.

[2] A. Wallraff, D. I. Schuster, A. Blais, L. Frunzio, R.-S. Huang, J. Majer, S. Kumar, S. M. Girvin, and R. J. Schoelkopf. Strong coupling of a single photon to a superconducting qubit using circuit quantum electrodynamics. *Nature*, 431:162–167, 2004.

[3] A. Wallraff, D. I. Schuster, A. Blais, L. Frunzio, J. Majer, M. H. Devoret, S. M. Girvin, and R. J. Schoelkopf. Approaching Unit Visibility for Control of a Superconducting Qubit with Dispersive Readout. *Physical Review Letters*, 95:060501, 2005.

[4] A. Blais, R.-S. Huang, A. Wallraff, S. M. Girvin, and R. J. Schoelkopf. Cavity quantum electrodynamics for superconducting electrical circuits: An architecture for quantum computation. *Physical Review A*, 69:062320, 2004.

[5] J. Majer, J. M. Chow, J. M. Gambetta, J. Koch, B. R. Johnson, J. A. Schreier, L. Frunzio, D. I. Schuster, A. A. Houck, A. Wallraff, A. Blais, M. H. Devoret, S. M. Girvin, and R. J. Schoelkopf. Coupling superconducting qubits via a cavity bus. *Nature*, 449:443–447, 2007.

[6] R. J. Schoelkopf and S. M. Girvin. Wiring up quantum systems. *Nature*, 451:664–669, 2008.

[7] A. Imamoğlu. Cavity QED Based on Collective Magnetic Dipole Coupling: Spin Ensembles as Hybrid Two-Level Systems. *Physical Review Letters*, 102:083602, 2009.

[8] A. Bienfait, J. J. Pla, Y. Kubo, M. Stern, X. Zhou, C. C. Lo, C. D. Weis, T. Schenkel, M. L. W. Thewalt, D. Vion, D. Esteve, B. Julsgaard, K. Mølmer, J. J. L. Morton, and P. Bertet. Reaching the quantum limit of sensitivity in electron spin resonance. *Nature Nanotechnology*, 11:253–257, 2016.

[9] C. Eichler, A. J. Sigillito, S. A. Lyon, and J. R. Petta. Electron Spin Resonance at the Level of 10^4 Spins Using Low Impedance Superconducting Resonators. *Physical Review Letters*, 118:037701, 2017.

[10] M. D. Jenkins, T. Hümmer, M. J. Martínez-Pérez, J. J. García-Ripoll, D. Zueco, and F. Luis. Coupling single-molecule magnets to quantum circuits. *New Journal of Physics*, 15:095007, 2013.

[11] M. D. Jenkins, U. Naether, M. Ciria, J. Sesé, J. Atkinson, C. Sánchez-Azqueta, E. del Barco, J. Majer, D. Zueco, and F. Luis. Nanoscale constrictions in superconducting coplanar waveguide resonators. *Applied Physics Letters*, 105:162601, 2014.

[12] P. Haikka, Y. Kubo, A. Bienfait, P. Bertet, and K. Mølmer. Proposal for detecting a single electron spin in a microwave resonator. *Physical Review A*, 95:022306, 2017.

[13] P. W. Anderson and P. R. Weiss. Exchange Narrowing in Paramagnetic Resonance. *Reviews of Modern Physics*, 25:269–276, 1953.

[14] G. Höcherl and H. C. Wolf. Zur Konzentrationsabhängigkeit der Elektronenspin-Relaxationszeiten von Diphenyl-Picryl-Hydrazyl in fester Phase. *European Physical Journal A*, 183:341–351, 1965.

[15] M. Tavis and F. W. Cummings. Exact solution for an N-Molecule—Radiation-Field Hamiltonian. *Physical Review*, 170:379–384, 1968.

[16] P. Rabl, D. DeMille, J. M. Doyle, M. D. Lukin, R. J. Schoelkopf, and P. Zoller. Hybrid Quantum Processors: Molecular Ensembles as Quantum Memory for Solid State Circuits. *Physical Review Letters*, 97:033003, 2006.

[17] J. H. Wesenberg, A. Ardavan, G. A. D. Briggs, J. J. L. Morton, R. J. Schoelkopf, D. I. Schuster, and K. Mølmer. Quantum Computing with an Electron Spin Ensemble. *Physical Review Letters*, 103:070502, 2009.

[18] J. Verdú, H. Zoubi, Ch. Koller, J. Majer, H. Ritsch, and J. Schmiedmayer. Strong Magnetic Coupling of an Ultracold Gas to a Superconducting Waveguide Cavity. *Physical Review Letters*, 103:043603, 2009.

[19] P. Bushev, A. K. Feofanov, H. Rotzinger, I. Protopopov, J. H. Cole, C. M. Wilson, G. Fischer, A. Lukashenko, and A. V. Ustinov. Ultralow-power spectroscopy of a rare-earth spin ensemble using a superconducting resonator. *Physical Review B*, 84:060501, 2011.

[20] N. D. Yordanov. Is our knowledge about the chemical and physical properties of DPPH enough to consider it as a primary standard for quantitative EPR spectrometry. *Applied Magnetiec Resonance*, 10:339–350, 1996.

[21] M. D. Jenkins. *Coupling quantum circuits to magnetic molecular qubits*. PhD thesis, Universidad de Zaragoza, 2015.

[22] M. M. Khapaev, M. Y. Kupriyanov, E. Goldobin, and M. Siegel. Current distribution simulation for superconducting multi-layered structures. *Superconductor Science and Technology*, 16:24–27, 2003.

[23] Thomas Hümmer, Georg M. Reuther, Peter Hänggi, and David Zueco. Nonequilibrium phases in hybrid arrays with flux qubits and nitrogen-vacancy centers. *Physical Review A*, 85:052320, 2012.

[24] S. Probst, A. Bienfait, Campagne-Ibarcq P., J. J. Pla, B. Albanese, J. F. Da Silva Barbosa, T. Schenkel, D. Vion, D. Esteve, K. Mølmer, J. J. L. Morton, R. Heeres, and P. Bertet. Inductive-detection electron-spin resonance spectroscopy with 65 spins/$\sqrt{\text{Hz}}$ sensitivity. *Applied Physics Letters*, 111:202604, 2017.

[25] M. D. Jenkins, D. Zueco, O. Roubeau, G. Aromi, J. Majer, and F. Luis. A scalable architecture for quantum computation with molecular nanomagnets. *Dalton Transactions*, 45:16682–16693, 2016.

[26] H. Paik, D. I. Schuster, L. S. Bishop, G. Kirchmair, G. Catelani, A. P. Sears, B. R. Johnson, M. J. Reagor, L. Frunzio, L. I. Glazman, S. M. Girvin, M. H. Devoret, and R. J. Schoelkopf. Observation of High Coherence in Josephson Junction Qubits Measured in a Three-Dimensional Circuit QED Architecture. *Physical Review Letters*, 107:240501, 2011.

[27] C. Rigetti, J. M. Gambetta, S. Poletto, B. L. T. Plourde, J. M. Chow, A. D. Córcoles, J. A. Smolin, S. T. Merkel, J. R. Rozen, G. A. Keefe, M. B. Rothwell, M. B. Ketchen, and M. Steffen. Superconducting qubit in a waveguide cavity with a coherence time approaching 0.1 ms. *Physical Review B*, 86:100506, 2012.

[28] B. Sarabi, P. Huang, and N. M. Zimmerman. Possible Hundredfold Enhancement in the Direct Magnetic Coupling of a Single-Atom Electron Spin to a Circuit Resonator. *Physical Review Applied*, 11:014001, 2019.

5

Coupling LC Resonators to High-Coherence Molecular Spin Qubits

5.1 Introduction

In chapter 3 we introduced different ways to achieve the highest possible coupling between molecular spins and superconducting circuits. Chapter 4 illustrates one of these methods, based on fabricating nanoconstrictions in the inductor of a superconducting resonator to locally increase the microwave magnetic field and, therefore, the spin-photon coupling. We also introduced a new type of superconducting resonator that, simply because of its low impedance and low inductance design, could facilitate reaching this strong coupling regime (section 4.8). In this chapter we continue this idea of enhancing the coupling by optimizing the resonator design but via a different manner. In parallel, we try to combine it with novel spin qubits having improved properties as compared to DPPH.

Two type of resonators are mainly used in circuit quantum electrodynamics (cQED) experiments: coplanar waveguide (CPW) resonators and lumped element resonators (LERs). The first one, which consists on a coplanar waveguide with two capacitors that convert it into a resonator, has been introduced in chapter 3 and used in chapter 4. The latter type of resonator is based on resistiveless LC circuits fabricated with superconducting materials. It shows a more versatile design, being able to increase the magnetic or electric coupling to qubits by simply using a low or high impedance, respectively.[1;2] In a device containing several of these LERs, the microwave signal is transmitted through a transmission line coupled inductively or capacitively to them. This allows to freely modify the impedance, inductance and capacitance of these resonators, optimizing them for achieving the highest possible spin-photon coupling, without affecting the microwave transmission of the system.

Another obvious way to improve the relationship between spin-photon coupling and spin decoherence, which eventually determines the achievement of the strong coupling regime, is to use molecules with long T_2 values. This is the case of the perchlorotriphenylmethyl (PTM) radical, a very stable molecule that shows high spin coherence even at room temperature, being a strong potential candidate for quantum technologies.[3] These high T_2 values (from ~ 1 μs at room temperature to tens of μs at very low temperature) could facilitate reaching the strong coupling regime even for moderately high spin-photon couplings: $G_1/2\pi \gtrsim 160$ kHz at room temperature, or $G_1/2\pi \gtrsim 16$ kHz at very low temperatures.

The PTM_r molecule studied in this chapter is shown in Fig. 5.1. The magnetic behaviour of this molecule is reduced to that of the unpaired electron it contains, as occurs with DPPH. The molecule shows an electronic spin $S = 1/2$ and a close to isotropic g-factor $g \simeq 2$. As a first approximation, one can describe the behaviour of this molecule in the presence of an external magnetic field by means of the following Hamiltonian:

$$\mathcal{H} \simeq g\mu_B HS, \tag{5.1}$$

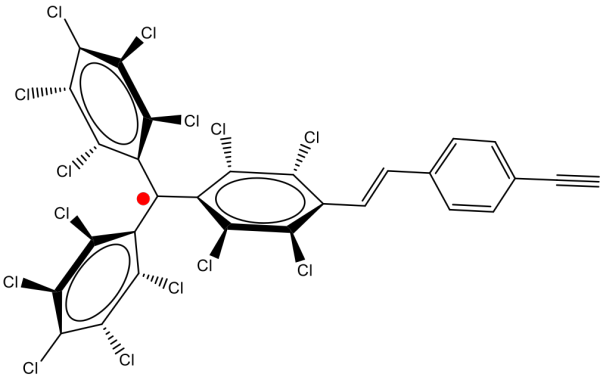

Figure 5.1: Molecular structure of the free-radical PTM molecule.

that only includes an isotropic Zeeman effect is needed. The $S = 1/2$ electronic spin will produce a single resonance line with $\Omega_S/H = 28$ GHz/T associated with the transition between the spin states $|-1/2\rangle$ and $|+1/2\rangle$ of the molecule.

In this chapter, we explore the spin-photon coupling between free-radical PTM molecules and LERs with two different designs. Section 5.2 will be dedicated to the coupling between PTM_r molecules and LERs with different inductances. In section 5.3 we describe the results of experiments that couple these molecules to LERs with very low inductance. In addition, and following the trick described at the previous chapter, we compare the results with the coupling to these same resonators where a nanoconstriction has been fabricated.

5.2 Coupling of PTM free-radical molecules to Lumped Element Resonators with variable designs

5.2.1 Chip design and fabrication

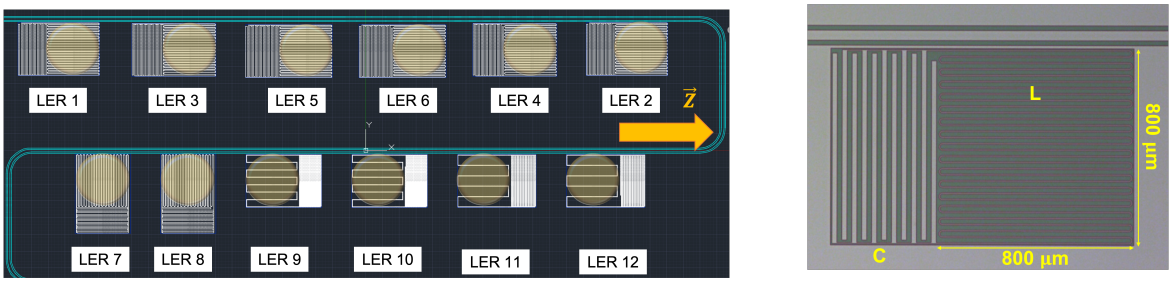

(a) **(b)**

Figure 5.2: (a) Design of the chip with 12 LERs used for the experiments described in this section. Different designs and couplings to the central waveguide can be seen. The yellow circles represent the inductor zone, where the PTM_r samples have been deposited. The microwave magnetic field generated by LERs 7 and 8 has components parallel to the Z laboratory axis and perpendicular to it and to the device. The remaining LERs produce a microwave magnetic field that only has components in the plane perpendicular to the Z axis, being parallel to the device and perpendicular to it. (b) Zoom of one of the LERs, where the dimensions of the inductor are indicated. All LERs show the same inductor size and different capacitor dimensions to define the resonant frequency ω_r.

The chip used in this work was fabricated at CAB by Alicia Gómez, Marina Calero and Maite Magaz. UV lithography (see section 2.3.1) was performed on a 100 nm thick Nb layer deposited on top of a Si wafer. The circuit, whose design is shown in Fig. 5.2, includes 12 LERs coupled to a common 40 μm wide readout transmission line. The gaps between the line and the resonators range from 12 μm to 44 μm. The coupling can be inductive (LERs 7 and 8), capacitive, or both types at the same time (remaining LERs). These two situations will be compared in the next section, showing whether significant changes occur in the results depending on the type of coupling between the LERs and the transmission line.

Each LER consists of a capacitor in parallel with a 800 μm wide square inductor, as shown in Fig. 5.2(b). These LC resonators show resonance frequencies $\omega_r = 1/\sqrt{LC}$ designed to remain between 1.5 and 2.1 GHz, a suitable range for our experimental set-up. The resonance frequencies measured prior to the deposition of PTM_r samples are given in Table 5.1. Using LERs with different inductor designs, we can study the effect of the inductance value on the spin-photon coupling. LERs 1 to 8 present the same geometrical inductance $L_{geo} = 14$ nH, while it was reduced for LERs 9 to 12 by using shorter inductances: LERs 9 and 10 present $L_{geo} = 6$ nH, and LERs 11 and 12, $L_{geo} = 5$ nH. These lower inductances enhance the local magnetic field generated by the inductors, theoretically increasing the spin-photon coupling to each of the spins deposited on top of them.

LER	1	2	3	4	5	6
ω_r (GHz)	1.598	1.601	1.658	1.660	1.727	1.728
LER	7	8	9	10	11	12
ω_r (GHz)	1.805	1.810	1.974	1.975	2.075	2.077

Table 5.1: Resonance frequencies of the bare LERs fabricated on the chip shown in Fig. 5.2, measured at 4 K.

The resonance frequencies can change after a sample is deposited on the devices due to the presence of solvents that modify the dielectric properties of the resonators' environment. Nevertheless, as will be shown in next section, these changes will be small (several tens of MHz) compared to the resonance frequencies shown in Table 5.1, keeping the frequency range similar to the one initially planned.

5.2.2 Coupling Lumped Element Resonators to macroscopic PTM$_r$ ensembles

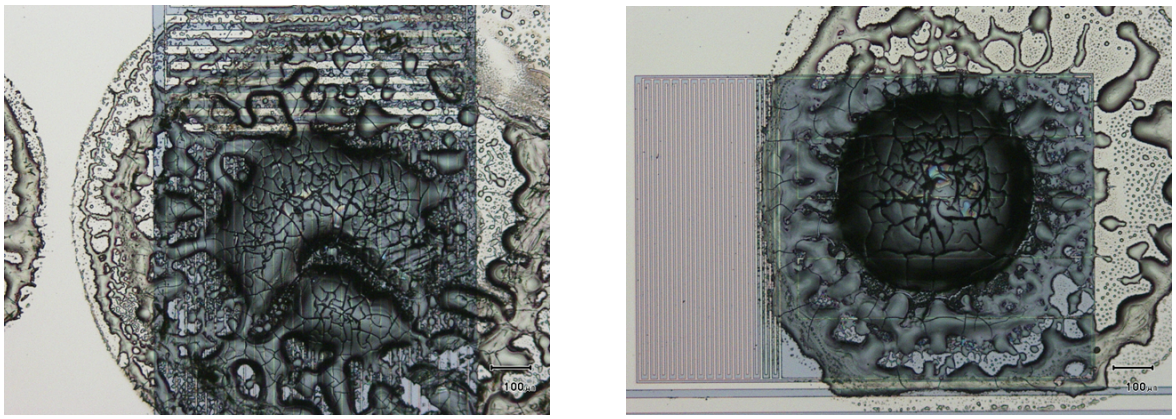

(a) **(b)**

Figure 5.3: Optical microscopy images of the PTM$_r$ samples deposited on the inductor of (a) LER 8 and (b) LER 11. A volume of 1 μL was deposited on each of the 12 LERs, while the PTM$_r$ concentration, the polymer or the type of radical (monoradical or diradical) were changed. The height of the different deposits ranges from 7 μm to 40 μm, which lies inside the magnetic mode height of all the LERs (from 50 μm up to 500 μm depending on the distance between the turns of the inductor).

This section describes the transmission measurements performed on the chip shown in Fig. 5.2, after depositing different PTM$_r$ solutions on each LER. These depositions were performed using a micropipette that allows controlling accurately the volume deposited onto the device. Two examples are shown in Fig. 5.3. The samples were prepared by dissolving a variable weight concentration of PTM$_r$ molecules in a polymeric matrix (poly(pentafluorostyrene), PSF, polystyrene, PS, or a combination of both). This mixture was finally dissolved in chlorobenzene for an adequate deposition of the samples. PSF was chosen due to the reduced PTM$_r$ spin linewidth obtained with it in previous EPR measurements performed by collaborators at ICMAB, compared with that measured using different polymers as poly(methyl methacrylate) (PMMA). In Fig. 5.4 we show two of the EPR curves measured at room temperature, which show a narrower spin resonance for PTM$_r$ dispersed in PSF. This may be motivated by the affinity between the chlorine atoms of the PTM$_r$ molecules and the fluorine atoms of PSF.

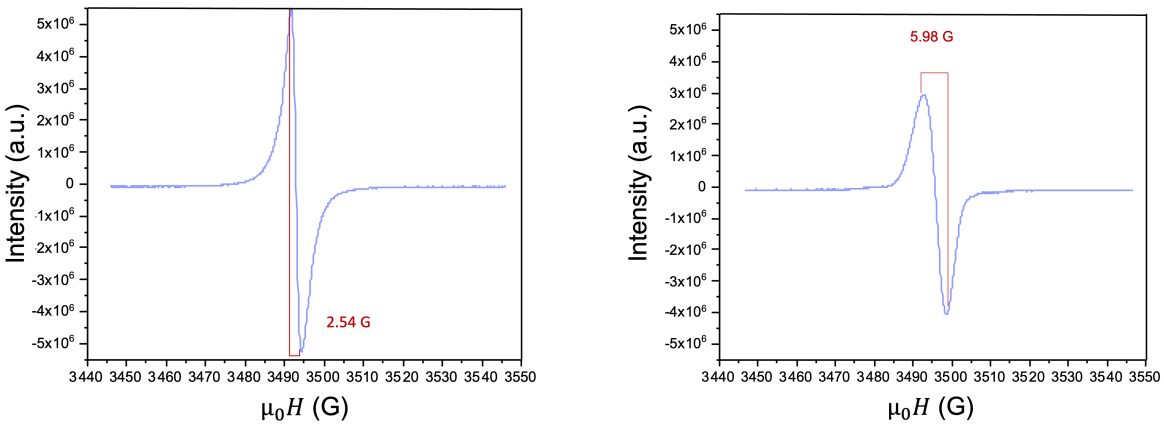

Figure 5.4: EPR spectrum of a solution of 1% PTM_r molecule dispersed in a (a) PSF and (b) PS matrix and dissolved in chlorobenzene. A peak-to-peak width of less than 3 G has been achieved using the PSF polymer, while a linewidth of 6 G is measured when using the PS matrix. These measurements were performed by our collaborators at ICMAB.

Subsequent EPR measurements (see Fig. 5.5), show that the effective T_2 (T_m) is reduced at low temperature due the dynamics of the chlorine atoms that slows down at low temperature. This induces an anisotropic hyperfine interaction of the radical with the nuclear spin ($\mathbf{I} = 3/2$) of the chlorine atoms, broadening the EPR signal.

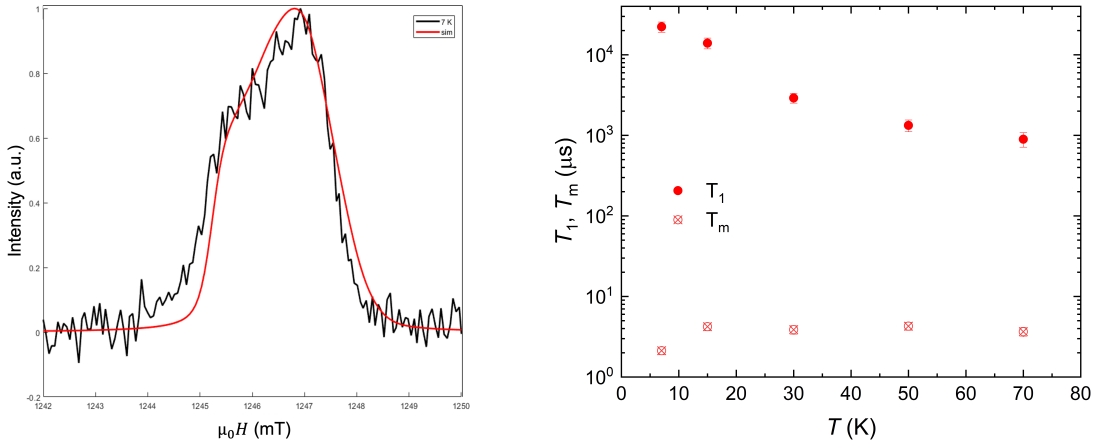

Figure 5.5: (a) ESE spectrum of 200 μL of a solution of 0.1% PTM_r molecule dispersed in PSF. The red line is a simulation of the spectrum assuming an anisotropic hyperfine coupling with 3 nuclear chlorine atom spins. (b) Evolution of T_1 and T_m with temperature, measured by EPR by Joris van Slageren's group of the University of Stuttgart. A maximum value of T_m of 4 μs has been detected for temperatures between 15 K and 50 K.

Table 5.2 gives the characteristic parameters of the samples deposited on the different LERs. 1 μL of a solution of monoradical PTM_r in PSF with variable concentration was deposited on half of the LERs. On the remaining resonators, solutions with diradical PTM_r (which contains two unpaired electrons and shows two independent $S = 1/2$ contributions), and with different polymeric matrices (PS or a combination of PSF and PS) were deposited. These samples were used to carry out a study of the behaviour of the spin linewidth when different polymers and the

diradical are used, trying to optimize the molecular sample to achieve the maximum coupling vs linewidth ratio.

LER	Mono- or diradical	Weight concentration	Polymer	N_{theor}
1	monoradical	0.05	PS	5×10^{12}
2	monoradical	0.05	PSF/PS (10:90)	5×10^{12}
3	diradical	0.05	PSF	5×10^{12}
4	monoradical	0.05	PSF/PS (50:50)	5×10^{12}
5	diradical	0.05	PS	5×10^{12}
6	monoradical	0.05	PSF/PS (90:10)	5×10^{12}
7	monoradical	5	PSF	5×10^{14}
8	monoradical	1	PSF	1×10^{14}
9	monoradical	0.5	PSF	5×10^{13}
10	monoradical	0.1	PSF	1×10^{13}
11	monoradical	0.05	PSF	5×10^{12}
12	monoradical	0.01	PSF	1×10^{12}
Line	diradical	0.05	PS	5×10^{12}

Table 5.2: Specifications of the different depositions performed on the chip shown in Fig. 5.2.

The superconducting device was introduced in a 90 L liquid helium cryostat at 4.2 K hosting a superconducting vector magnet (see section 2.6 for more details). The system was connected to a vector network analyser for measuring the microwave transmission through the circuit. The magnetic field was applied along the Z laboratory axis shown in Fig. 5.2. This geometry ensures that there is a component of the microwave magnetic field generated by the LERs that points perpendicular to the external field, thus able to generate transitions between the $m_S = \pm 1/2$ spin states of PTM_r (see section 3.4). The ranges of magnetic field and frequency explored in these experiments were selected depending on the measured resonator. The broadband microwave transmission through the readout line was studied, with magnetic field ranging from 0 to 0.1 T and frequency from 10 MHz up to 3 GHz.

Figure 5.6 shows the transmission data obtained for all the LERs that were visible. LERs 2, 3 and 12 were not detected, possibly due to damage during its manipulation. LERs 7, 8 and 11 show a clear absorption signal that can be associated to the coupling between the cavity photons and the PTM_r spins. LERs 7 and 8 seem to be swapped in frequency with respect to the values found for the bare chip, since the LER which shows a higher coupling should correspond to the one with more spins deposited on it (LER 7). On the other hand, LERs 1 and 10 show a very weak absorption signal that becomes visible only from the evolution of κ with magnetic field (see Figs. 5.6 and 5.7). Finally, measurements performed with LERs 4, 5, 6 and 9, as well as with the transmission line (not shown), do not show any signal corresponding to the absorption of photons by the spins. This may be due to several factors, depending on the deposition: degradation of the molecular sample; formation of aggregates that increase the local PTM_r concentration and therefore the spin linewidth; increase of the spin linewidth in spins dispersed in PS (LERs 4, 5, 6 and transmission line) or coupling between the two spins of the diradical molecules (LER 5 and transmission line). However, the results obtained with LER 1 indicate that the presence of PS does not seem to affect much the spin linewidth, being this deposition the one which has shown the smallest width (possibly due to the lower spin concentration).

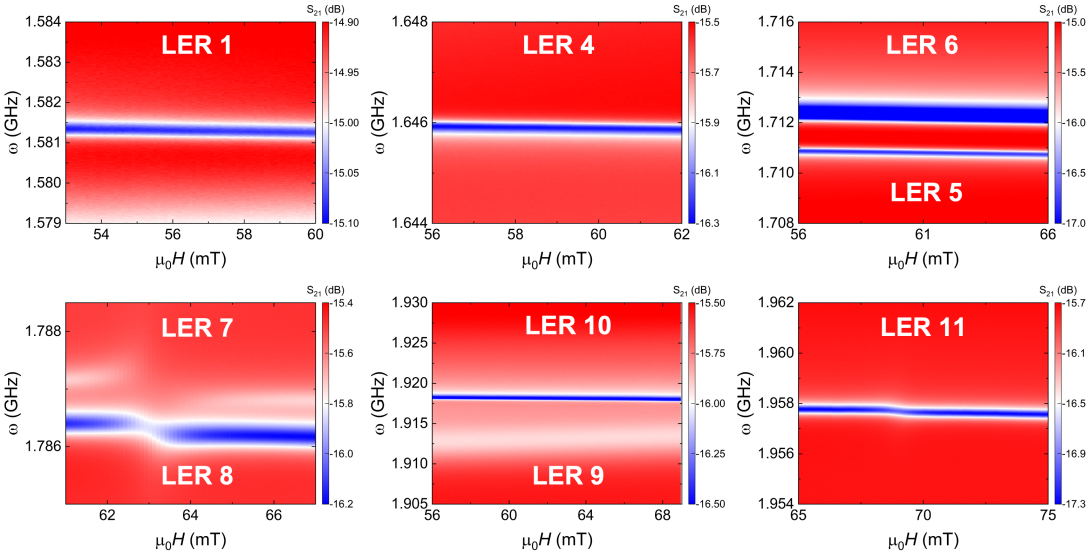

Figure 5.6: 2D plots of the microwave transmission measured at 4.2 K for 9 of the 12 LERs shown in Fig. 5.2. The magnetic field was applied along the Z laboratory axis. The resonances of LERs 2, 3 and 12 were not visible.

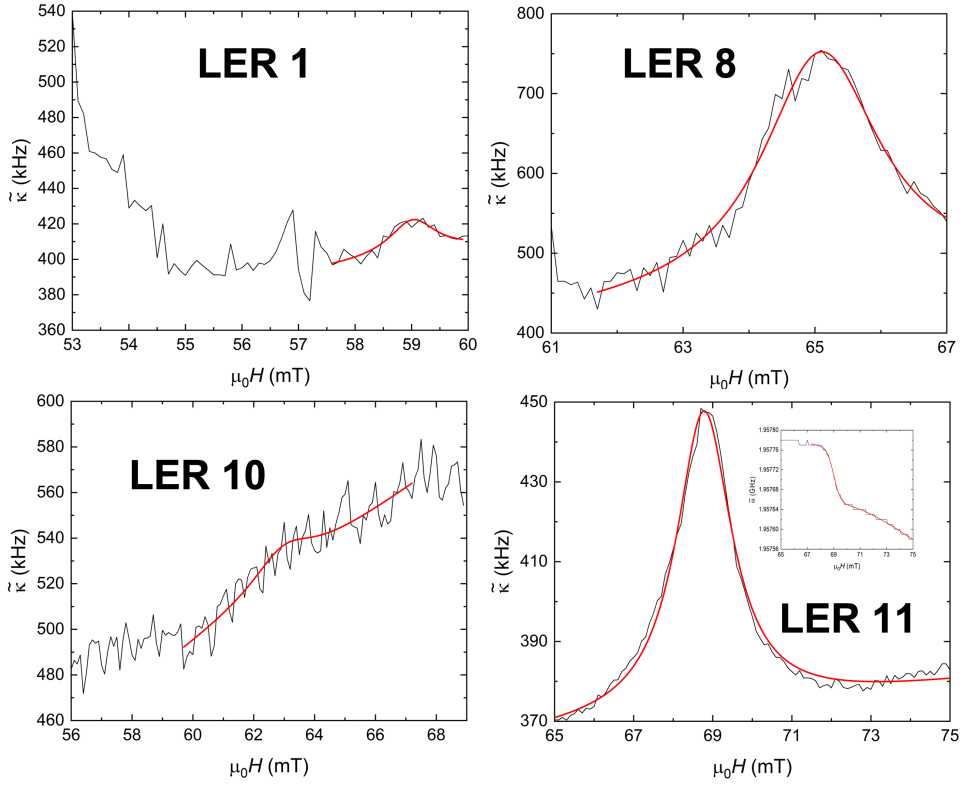

Figure 5.7: Evolution of $\tilde{\kappa}$ with applied magnetic field for LERs 1, 8, 10 and 11. The red solid lines are least-squares fits performed using Eq. (5.2). LER 11 includes an inset with the evolution of $\tilde{\omega}$ with magnetic field, together with a least-squares fit performed using Eq. (5.3)

The collective spin-photon coupling G_N and the spin linewidth γ have been determined by looking at the magnetic field dependence of the cavity resonance broadening κ or the resonance frequency ω_r, in the case of LER 7. The evolution of the resonance frequency has been considered in LER 7 due to the nearly complete disappearance of the resonator signal when it is tuned to

the spins transition, a fact that hinders the analysis of $\kappa(H)$. This may be indicative that we are close to the strong coupling regime with this sample, something that will be analysed in more detail below. For all other LERs, we have considered the following equations for the evolution of κ and ω_r, previously introduced in chapter 3, which are valid in the weak coupling regime: [4]

$$\tilde{\kappa} = \kappa_r + \frac{G_N^2 \gamma}{(\omega_r - \Omega_S)^2 + \gamma^2}, \tag{5.2}$$

$$\tilde{\omega} = \omega_r + \frac{G_N^2 (\omega_r - \Omega_S)}{(\omega_r - \Omega_S)^2 + \gamma^2}, \tag{5.3}$$

where $\tilde{\kappa}$ and $\tilde{\omega}$ are the modified broadening and resonance frequency of the cavity, κ_r and ω_r are the broadening and resonance frequency of the bare cavity, which can be determined when it is detuned from the spin ensemble, and $\Omega_S = g\mu_B B/h$ is the field-dependent resonance frequency of the spins. Using these equations, the fits shown in Fig. 5.7 have been performed. They provide the values of G_N, G_1 and γ shown in Table 5.3 for LERs 1, 8, 10 and 11. The values of G_1 have been determined by considering the theoretical number of spins deposited on each resonator and correcting it with the thermal factor given by the expression (4.1) at 4.2 K (see Table 5.2 and Fig. 5.9).

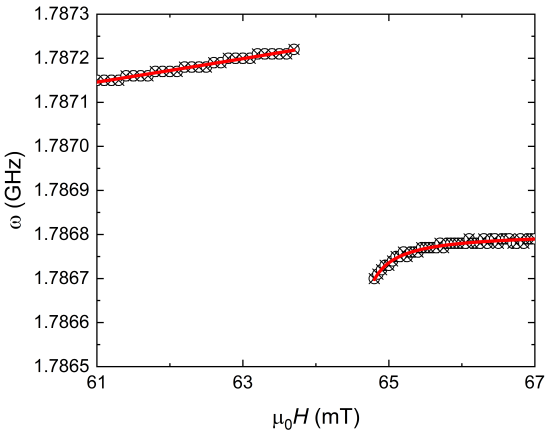

Figure 5.8: Evolution of ω_r of LER 7 with the applied magnetic field, together with the least-square fit performed using Eq. (5.4). With this fit we obtain a coupling value $G_N/2\pi = 5.438 \pm 1.136$ MHz, corresponding to $G_1/2\pi = 2.41 \pm 0.50$ Hz. Although it is the highest coupling value achieved with these samples, it is still far from the minimum value of γ obtained with these samples (13 MHz for LER 1).

Let's consider now the data measured for LER 7. The disappearance of the resonator signal when $\Omega_S \simeq \omega_r$ indicates that we are close to, or even reaching, the strong coupling regime. In this case, Eqs. (5.2) and (5.3) are no longer valid. We have performed a fit considering the evolution of ω_r with magnetic field and using Eq. (5.4), valid in the strong coupling regime:

$$\omega_\pm = \frac{\omega_r + \Omega_S}{2} \pm \frac{\sqrt{4G_N^2 + (\Omega_S - \omega_r)^2}}{2}. \tag{5.4}$$

This fit is shown in Fig. 5.8. We will focus on the strong coupling fit, since Eq. (5.2) tends to underestimate the spin-photon coupling when we are close to the strong coupling regime. We obtain a collective spin-photon coupling $G_N/2\pi \simeq 5.438$ MHz, the highest value of those obtained with this device. This agrees with the fact that this LER is the one of the chip with the largest amount of deposited spins. In fact, $G_1 = G_N/\sqrt{N} \simeq 2.4$ Hz is similar to that achieved

LER	ω_r (GHz)	$\mathbf{G_N/2\pi}$ (MHz)	γ (MHz)	$\mathbf{N_{eff}}$	$\mathbf{G_1/2\pi}$ (Hz)
1	1.652 ± 0.002	0.505 ± 0.022	13.302 ± 1.844	4.5×10^{10}	2.38 ± 0.10
7	1.783 ± 0.006	5.438 ± 1.136	-	5.1×10^{12}	2.41 ± 0.50
8	1.822 ± 0.001	3.023 ± 0.140	30.584 ± 1.933	1.0×10^{12}	2.99 ± 0.14
10	1.763 ± 0.006	0.719 ± 0.072	35.000 ± 6.247	1.1×10^{11}	2.17 ± 0.22
11	1.925 ± 0.001	1.345 ± 0.014	23.877 ± 0.544	5.6×10^{10}	5.69 ± 0.06

Table 5.3: Values of ω_r, $G_N/2\pi$, γ and $G_1/2\pi$ extracted from the fittings shown in Figs. 5.7 and 5.8.

from other devices, thus the large G_N can be ascribed to the large amount of PTM_r molecules coupled to this LER.

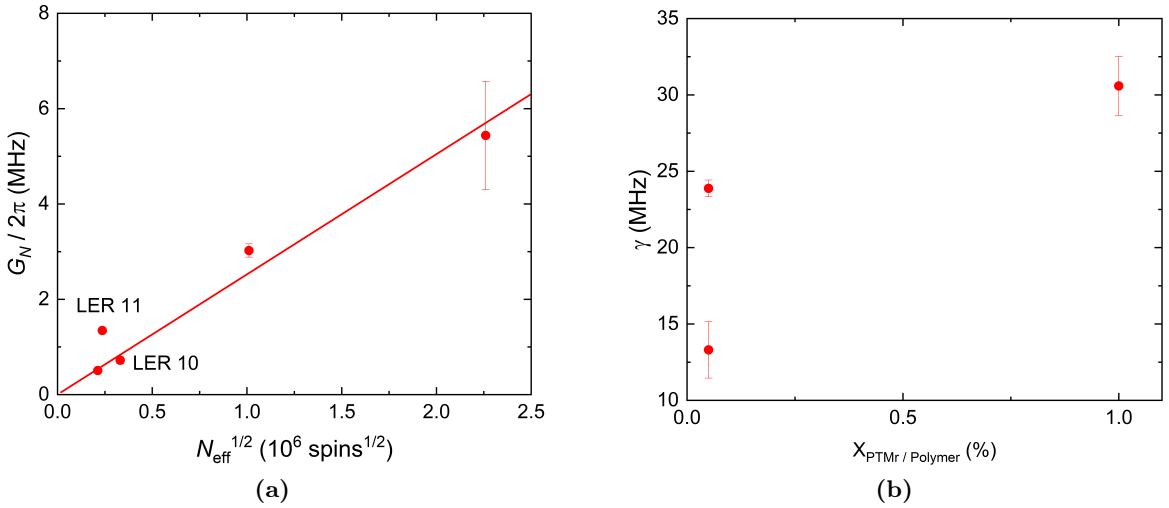

Figure 5.9: (a) Evolution of G_N with the number of spins effectively coupled to the different LERs, together with a least-squares linear fit. The collective spin photon coupling mainly depends here on the number of deposited spins, with an average G_1 value $G_1/2\pi = 2.52 \pm 0.19$ Hz. The G_N obtained for LER 11, higher than for LER 10, may be motivated by the lower inductance of the former. (b) Evolution of γ with the concentration of PTM_r in the polymer (PSF or PS). It shows that the greater the concentration, the higher the spin linewidth.

Looking at the results shown in Table 5.3, some conclusions can be extracted. The first one is that having an inductive coupling to the transmission line (LERs 7 and 8) or inductive-capacitive (remaining LERs) does not seem to significantly modify the microwave field generated by the resonators (LERs 1, 7 and 8 show similar single spin-photon couplings). Although LERs 7 and 8 show higher collective spin-photon couplings, this is likely due to the larger number of spins deposited on their inductors. The second conclusion extracted from these results is that a lower inductance (LER 11) can produce a higher microwave field, which helps enhancing the single spin-photon coupling by a factor of 2 without negatively affecting the resonator properties. Regarding LER 10, the low absorption signal detected made it necessary to fix the value of the spin linewidth at 35 MHz for performing the fit shown in Fig. 5.7. This makes the results obtained for this LER unreliable. Finally, the spin linewidth observed in these measurements, ranging from 13 MHz for the lowest PTM_r concentrations to 35 MHz, do not match with the reduced linewidth of 2.5 G, corresponding to 7 MHz. It has been found that this is due to the behaviour

of the molecular sample after the deposition. When the solvent dries completely, the molecules tend to form aggregates that increase the dipolar interactions between them. This, together with the hyperfine coupling with nuclear spins at chlorine atoms and other inhomogeneous broadening sources, rise the spin linewidth up to values around 20 MHz, regardless of the polymer used. This value is pretty similar to the spin linewidths measured in DPPH in this temperature range. Nevertheless, using PTM_r samples with a very low number of spins would allow us to reduce the spin linewidth, eventually reaching those values corresponding to a T_2 of tens of μs at very low temperature in the single molecule limit.[3]

5.2.3 Evolution of the spin-photon coupling with temperature

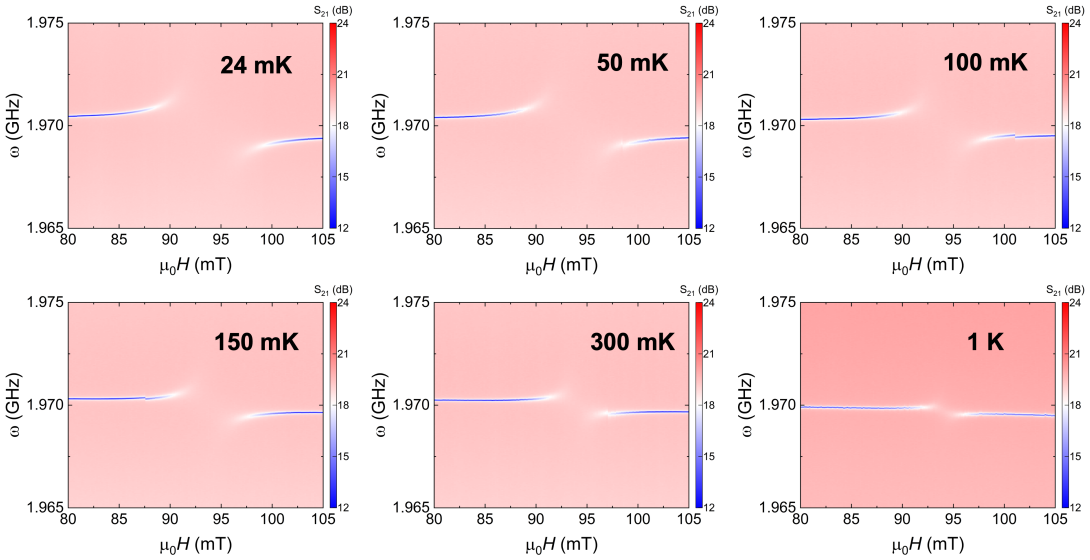

Figure 5.10: 2D plots of the microwave transmission through the PTM_r sample deposited on LER 11, measured at temperatures from 24 mK to 1 K. The reduction of the collective spin-photon coupling with increasing temperature is clearly visible.

In this section, we briefly discuss how G_N for LER 11 depends on temperature, taking N_{eff} closer to the number of molecules N deposited on the inductor. These measurements were performed by introducing the device with the same depositions previously studied in a dilution refrigerator hosted by the Atominstitut of the Technical University of Vienna. The spin-photon coupling was studied performing several transmission measurements with temperatures ranging from 25 mK up to 1 K, and applying magnetic fields from 80 mT to 105 mT with a homemade superconducting vector magnet. In these experiments, the magnetic field was applied in the plane of the device at 90°of the Z laboratory axis shown in Fig. 5.2.

Figure 5.10 shows the microwave transmission through the device near the resonance of LER 11 when Ω_S is tuned through ω_r It can be seen that the collective spin-photon coupling obtained from these measurements is highly enhanced (from 3.5 MHz at 1 K to 10.9 MHz at 24 mK) when temperature is reduced, as expected from Eq. (4.1). This effect is shown directly in Fig. 5.11, where the evolution of the collective spin-photon coupling with temperature and with the relation between the number of effectively coupled spins and the total number of deposited molecules are represented. Combining G_N obtained from these measurements with the number of spins deposited on the inductor (5×10^{12}), we can estimate an average single spin-photon coupling $G_1/2\pi = 4.8 \pm 0.2$ Hz. This value agrees with the one estimated from the experiments at 4.2 K (5.7 ± 0.06 Hz). Regarding the spin coherence, linewidths between 30 and 40 MHz have been obtained, showing that it is almost temperature independent. This reinforces the hypothesis that

there is an inhomogeneous broadening produced by dipolar interactions between molecules and hyperfine couplings between the radical and the chlorine atoms of the molecule. The results show that the obtained $G_1/2\pi = 4.8 \pm 0.2$ Hz is much lower than the spin linewidth or, eventually, lower than $1/T_2$. This difficults the achievement of the strong coupling regime with a single spin if the microwave magnetic field is not increased. This approach will be introduced in next section.

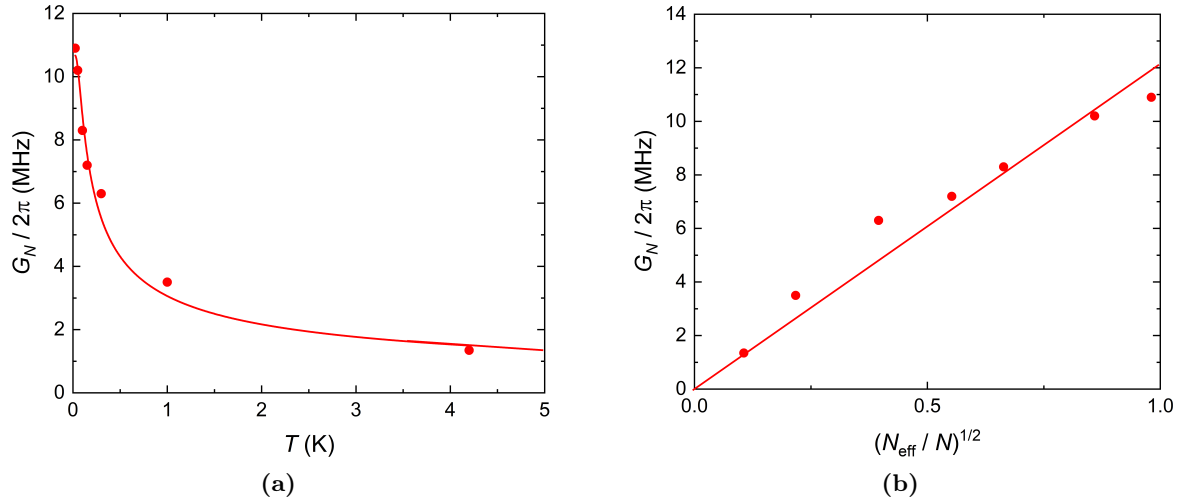

Figure 5.11: (a) Temperature and (b) N_{eff} dependence of G_N, obtained from the transmission measurements shown in Fig. 5.10, together with least-square fits based on Eq. (4.1). A value of $G_N/2\pi \simeq 12.2 \pm 0.5$ MHz for $T = 0$ is extrapolated, and a single spin-photon coupling $G_1/2\pi \simeq 4.8 \pm 0.2$ Hz is obtained. The maximum collective coupling is still lower that the spin linewidth of this sample, between $30 - 40$ MHz, indicating that we are close to but not reaching the strong coupling regime.

5.3 Enhancement of the spin-photon coupling near superconducting nanoconstrictions in LC resonators

We have seen that the largest G_1 was achieved with LERs having the smallest inductance. In this section we study the coupling between PTM_r free-radical molecules and LERs with an inductor consisting on a single wire, which decreases to the minimum the inductance and therefore enhances the microwave magnetic field. The effect of a nanoconstriction fabricated on some of these resonators is also analysed, comparing the coupling values obtained with and without it.

5.3.1 Chip design and fabrication

This device was also fabricated at CAB by Alicia Gómez's group. A 100 nm thick Nb layer deposited on top of a Si substrate was UV lithographed, transferring the design shown in Fig. 5.12. It includes 10 LERs inductively coupled to a 40 μm readout transmission line. All these LERs show the same geometrical inductance $L_{geo} \simeq 0.5$ nH, formed by a single wire, in parallel with a rectangular capacitor. The size of these capacitors was chosen in order to keep the bare resonance frequencies of the LERs, $\omega_r = 1/\sqrt{LC}$, between 1.5 GHz and 3 GHz. These frequencies, measured at CAB before the deposition of PTM_r samples, are shown in Table 5.4.

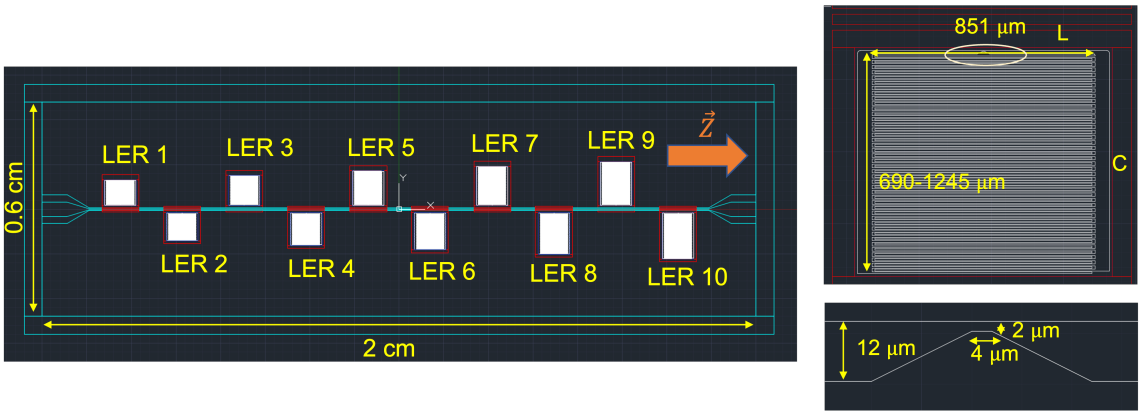

Figure 5.12: Design of the chip with 10 LERs used used in the experiments described in this section. All these resonators show the same inductance, being the capacitance of each one that finally determines their resonance frequencies. All the inductors have a 2 μm wide, 4 μm long initial constriction. At resonance, the magnetic field generated by the inductors is mainly perpendicular to the Z laboratory axis indicated in the figure.

LER	1	2	3	4	5
ω_r (GHz)	2.8308	2.6597	2.5194	2.3896	2.2800
LER	6	7	8	9	10
ω_r (GHz)	2.1756	2.0870	2.0059	1.9331	1.8585

Table 5.4: Resonance frequencies of the LERs fabricated with the design shown in Fig. 5.12, measured at a temperature of 12 mK.

Nanoconstrictions like the one shown in Fig. 5.13(b) were fabricated in half of the LERs present on the chip. The results of chapter 4 show that nanoconstrictions like this greatly enhance the single spin-photon coupling, being a promising approach to achieve the strong coupling regime to a single molecule. These nanoconstrictions, combined with the very low inductance of the LERs studied here, could increase even more the intensity of the microwave magnetic field responsible for causing the spin transitions, thus enhancing the coupling. In next section we will compare the spin-photon coupling achieved with the resonators without and with nanoconstrictions.

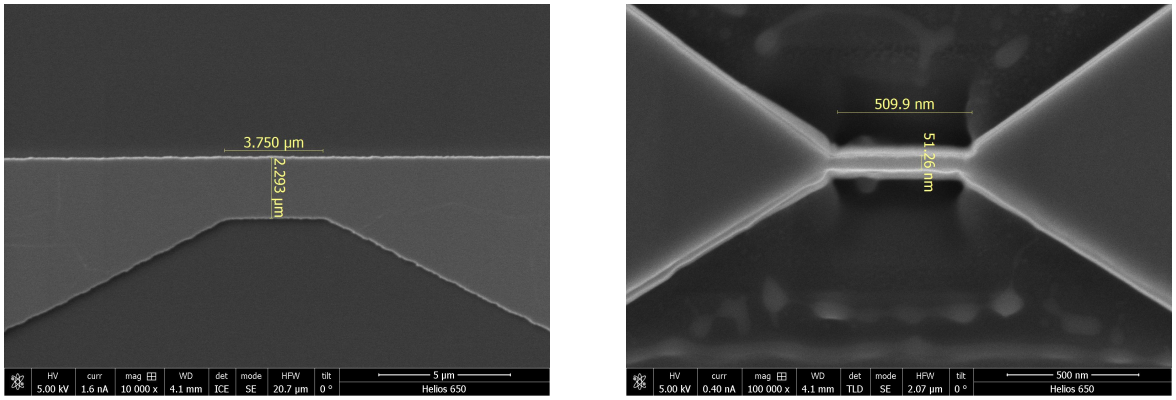

(a) **(b)**

Figure 5.13: SEM images of (a) the 2 μm×4 μm initial constriction fabricated in all LERs by conventional lithography and (b) the 50 nm×500 nm nanoconstriction fabricated in LERs 2, 4, 6, 8 and 10 by FIB lithography at the clean room of INMA.

5.3.2 Coupling of PTM$_r$ molecules to low inductance LERs

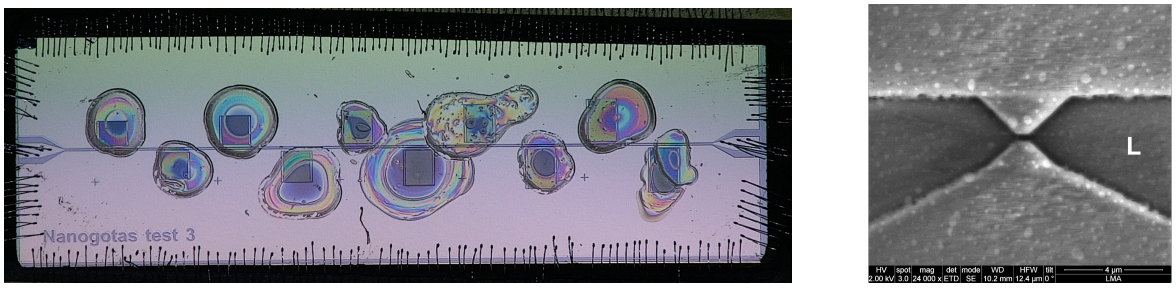

(a) **(b)**

Figure 5.14: (a) Optical microscopy image of the chip showing the different PTM$_r$ depositions. Each drop is formed by 0.1 μL of PTM$_r$ solution. (b) SEM image of the nanoconstriction zone of LER 10. The PTM$_r$ molecules form aggregates that are homogeneously distributed throughout the resonator.

This section is dedicated to the microwave transmission experiments carried out with the previously described chip after depositing different PTM$_r$ samples on each LER, as shown in Fig. 5.14. These samples consist of 0.1 μL of PTM$_r$ solutions in a polystyrene (PS) matrix with five different PTM$_r$/PS ratios, and these mixtures were finally dissolved in undecanol. Table 5.5 indicates the characteristics of each deposition, showing the PTM$_r$ weight concentration related to PS and the estimated number of PTM$_r$ molecules effectively coupled to the inductor and to the nanoconstriction. These calculations are explained in detail below.

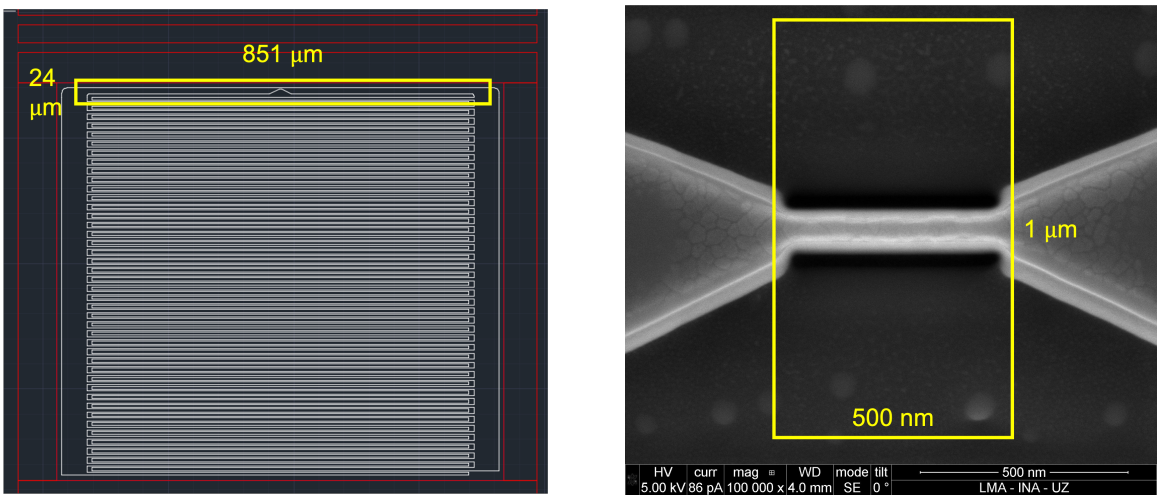

(a) **(b)**

Figure 5.15: illustration of the areas considered to calculate the number of spins coupled (a) to the inductor and (b) to the nanoconstriction.

First, we have considered that the PTM_r molecules are homogeneously distributed on each resonator, as SEM images tend to indicate (Fig. 5.14(b)). The number of molecules near the inductor zone, N_{ind}, can be estimated by first calculating the surface density of spins of every deposition, considering the area of each drop A_{drop} and the total number of deposited spins N_T, and then multipying it by the area of the inductor, shown in Fig. 5.15:

$$N_{\text{ind}} = N_T \frac{851 \cdot 24\,\mu\text{m}^2}{A_{\text{drop}}(\mu\text{m}^2)}. \tag{5.5}$$

Here, we have not considered the height of the drop and the magnetic mode since the drop ($h \sim 7$ μm) is completely contained inside the mode volume ($h \sim 12$ μm), as shown in Figs. 5.16 and 5.17(a).

The number of spins deposited near each constriction N_{cons} can be determined in a similar way, although in this case it is necessary to take into account that the drop height (~ 7 μm) is higher than that of the mode (0.5 μm, see Fig. 5.17):

$$N_{\text{cons}} = N_T \frac{0.5 \cdot 0.5 \cdot 1\,\mu\text{m}^3}{A_{\text{drop}} \cdot 7\,\mu\text{m}^3}, \tag{5.6}$$

The results, corrected by the thermal factor (see Eq. (4.1)), are listed in Table 5.5

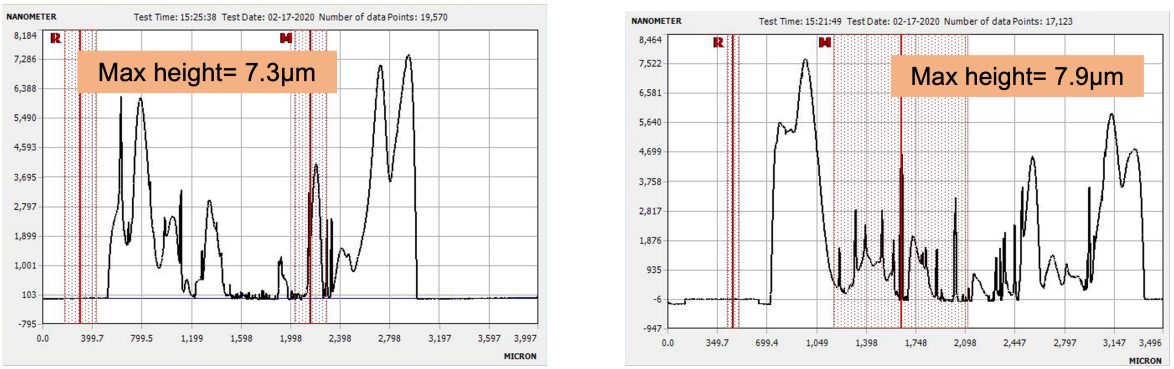

(a) **(b)**

Figure 5.16: Two different AFM measuremens of the height of a drop of PTM_r in PS, showing that it reaches a thickness lower than 10 μm.

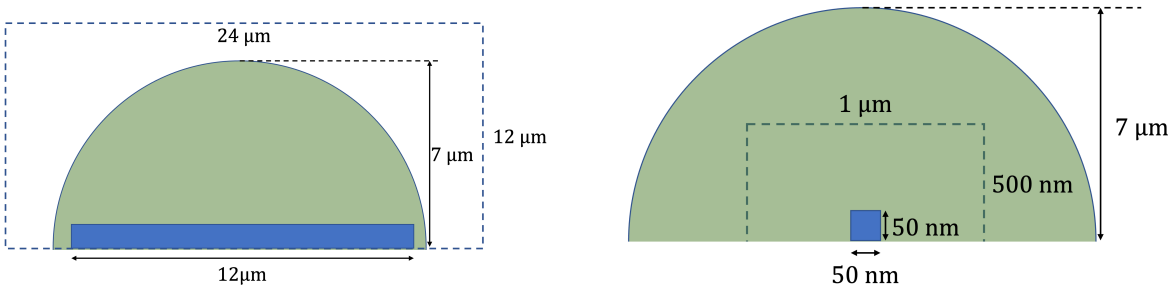

(a) **(b)**

Figure 5.17: Scheme comparing the size of the PTM_r drop and the dimensions of the magnetic mode volumes generated by (a) the inductor and (b) the constriction of each LER. The mode height of the inductor is higher than the drop height, thus all molecules deposited onto the inductor couple to the resonator. In the case of the nanoconstriction, the mode completely confined inside the drop, which means that only a fraction of molecules contribute to the coupling.

The device was introduced into a Bluefors LD-250 cryogen-free dilution refrigerator equipped with a uniaxial magnet (see section 2.6.2 for more details about this refrigerator), which has a base temperature of 10 mK. It was connected to a vector network analyser that measured the microwave propagation through the circuit. The input power was attenuated by -50 dB, while the output signal was amplified by 30 dB. The magnetic field was applied along the Z laboratory axis shown in Fig. 5.12, pointing perpendicular to the microwave magnetic field generated by the inductors.

Figure 5.18 shows the microwave transmission data measured for 9 of the 10 LERs present on the chip (LER 1 was not visible possibly due to damage during its manipulation) at 10 mK. An absorption signal corresponding to the spins coupled to the inductor is clearly visible in the data from LERs 4 to 10, while for LERs 2 and 3 this absorption is hardly distinguishable in these plots, being necessary to plot the evolution of $\tilde{\kappa}$ with magnetic field in order to appreciate it. The differences in the signal intensity between LERs can be associated with two factors: the number of spins deposited near the inductor zone (LER 10 is the one with the most spins, while LER 2 has the fewest); and the presence of a nanoconstriction (it was fabricated in even numbered LERs). The abrupt jumps in the resonances of LERs 2 to 6 are due to the appearance and movement of vortices in the device when a magnetic field is applied. They modify the properties of the resonators and their resonance frequencies, being this effect more pronounced for higher

LER	Weight concentration	Total spins	$N_{eff,i}$	Nanoconstriction	$N_{eff,c}$
1	0.1	1×10^{11}	8.40×10^{8}	No	-
2	0.1	1×10^{11}	1.04×10^{9}	Yes	1.82×10^{3}
3	0.5	5×10^{11}	3.38×10^{9}	No	-
4	0.5	5×10^{11}	3.15×10^{9}	Yes	5.51×10^{3}
5	1	1×10^{12}	1.37×10^{10}	No	-
6	1	1×10^{12}	3.38×10^{9}	Yes	5.90×10^{3}
7	2.5	2.5×10^{12}	1.16×10^{10}	No	-
8	2.5	2.5×10^{12}	2.57×10^{10}	Yes	4.49×10^{4}
9	5	5×10^{12}	3.51×10^{10}	No	-
10	5	5×10^{12}	4.26×10^{10}	Yes	7.45×10^{4}

Table 5.5: Specifications of the different depositions performed on the chip shown in Fig. 5.12, including the total number of spins deposited in 0.1 μL of solution. The effective number of molecules deposited on each inductor ($N_{\text{eff,i}}$) and nanoconstriction ($N_{\text{eff,c}}$) was calculated using Eqs. (5.5) and (5.6) for determining the total number of molecules N_{ind} and N_{cons}, and considering the thermal factor introduced in (4.1) for a temperature of 10 mK.

fields.[5]

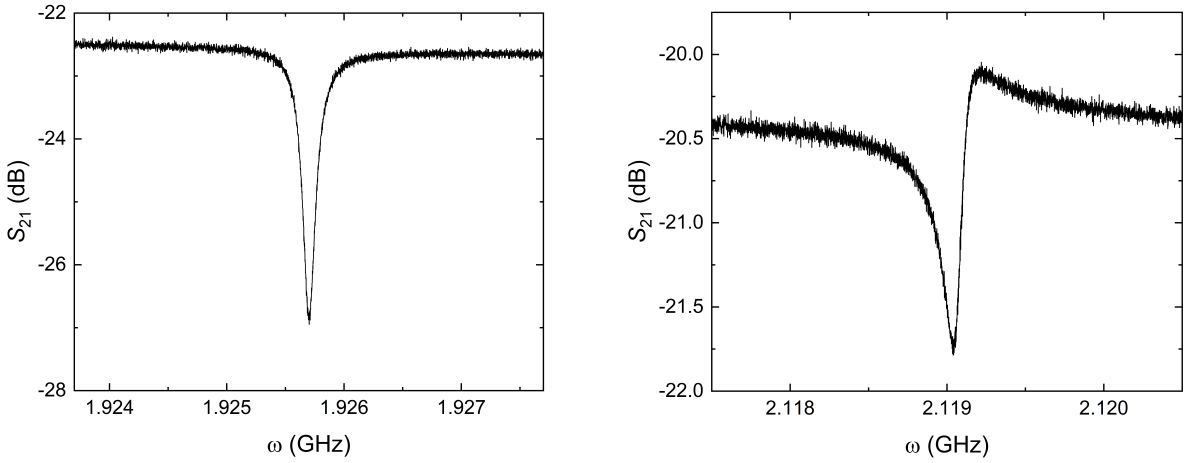

Figure 5.19: Microwave transmission measured with (a) LER 9 at a magnetic field of 51 mT and (b) LER 7 at a magnetic field of 61 mT, where the differences between a Lorentzian peak (LER 9) and an assymetric resonance due to Fano interference (LER 7) can be seen. LERs 2, 8 and 9 show Lorentzian resonances, while the remaining LERs present assymetric peaks.

As shown in Fig. 5.19, the resonances we have measured can present a Lorentzian (Fig. 5.19(a)) or Fano (Fig. 5.19(b)) shape. Lorentzian peaks, observed for LERs 2, 8 and 9, can be studied considering the evolution of $\tilde{\kappa}$ with magnetic field and using Eq. (5.2), since we are in the weak coupling regime. For the remaining LERs, we need to employ the python script described in chapter 4, which takes into account the assymetry of the resonances due to Fano interference effects. Figure 5.20 shows the evolution of $\tilde{\kappa}$ with magnetic field for LERs 2, 8 and 9, together with the least-squares fits performed using Eq. (5.2). In Fig. 5.21, the 2D transmission plots

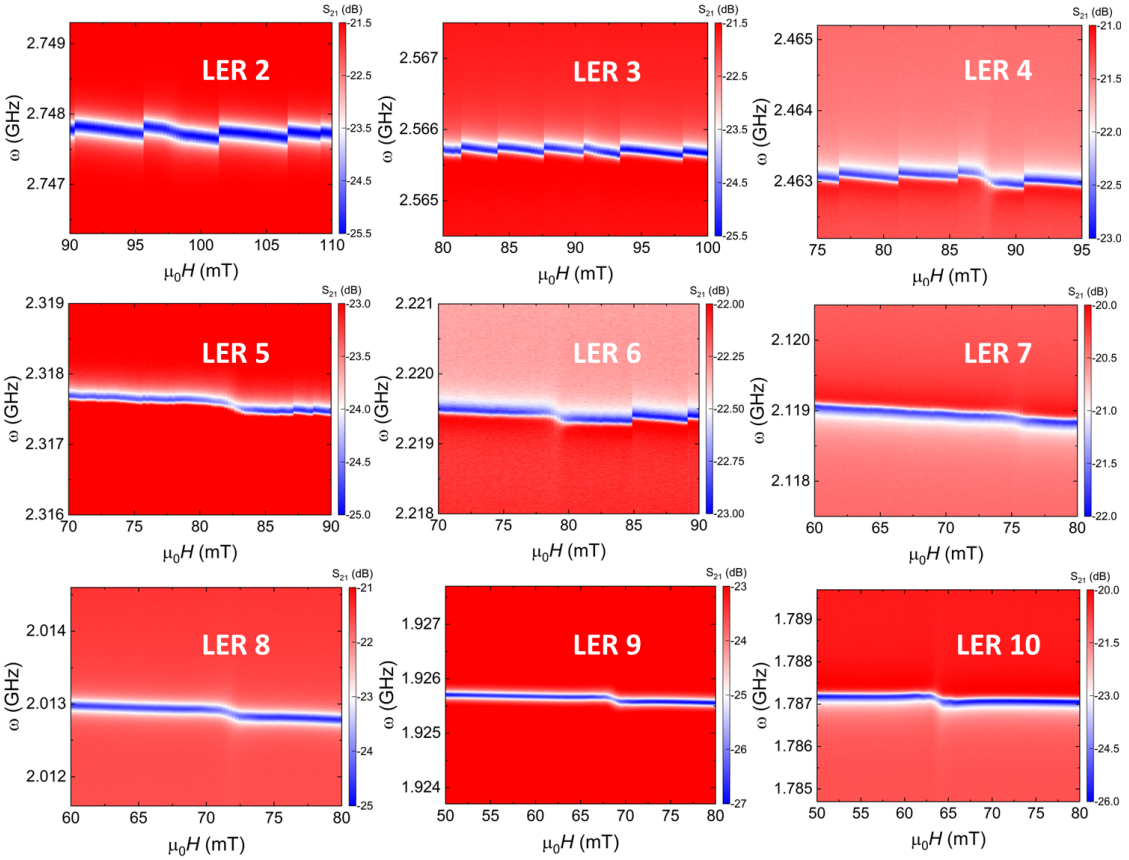

Figure 5.18: 2D plots of the microwave transmission measured at 10 mK for 9 of the 10 LERs shown in Figs. 5.12 and 5.14. The magnetic field was applied along the Z laboratory axis, being perpendicular to the microwave field generated by the resonators. Resonance corresponding to LER 1 was not visible.

generated by fitting the transmission data of the remaining LERs are presented.

In the measurements performed on the LERs having a nanobridge at the centre of the inductor, we can consider that there are two different single spin-photon couplings: one between the cavity photons and the spins on the inductor area, $G_{1,i}$; and a different one (presumably higher) from the spins deposited near the nanoconstriction, $G_{1,c}$. Both couplings contribute to the total spin-photon coupling G_N as follows:

$$G_N \simeq \sqrt{N_{\mathrm{eff,i}} G_{1,\mathrm{i}}^2 + N_{\mathrm{eff,c}} G_{1,\mathrm{c}}^2}, \tag{5.7}$$

where $N_{\mathrm{eff,i}}$ and $N_{\mathrm{eff,c}}$ are, respectively, the spins effectively coupled to the inductor and the nanoconstriction. From Eq. (5.7), and assuming that the distribution of molecules in both devices with and without nanoconstriction is the same, we can estimate the value of $G_{1,\mathrm{c}}$ from G_N and $G_{1,\mathrm{i}}$:

$$G_{1,\mathrm{c}} = \sqrt{\frac{G_N^2 - N_{\mathrm{eff,i}} G_{1,\mathrm{i}}^2}{N_{\mathrm{eff,c}}}} \tag{5.8}$$

We have determined the values of $G_{1,\mathrm{i}}$ from the results of the LERs without a nanoconstriction. Using Eq. (4.1) we have calculated the mean single spin-photon coupling achieved with LERs 3, 5, 7 and 9. These values are shown in Fig. 5.22, together with a linear fit with the resonance frequency taking into account that, having all these resonators the same inductance, the intensity of the microwave magnetic field is expected to be proportional to ω_r.[5]

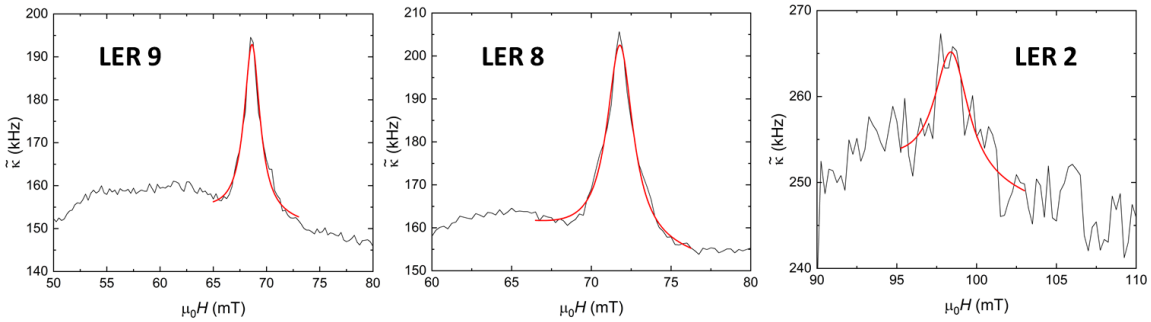

Figure 5.20: Evolution of $\tilde{\kappa}$ with the applied magnetic field for LERs 2 (right), 8 (centre) and 9 (left). A maximum is observed when the resonators and the spins are tuned. The red lines are least-squares fits performed using Eq. (5.2).

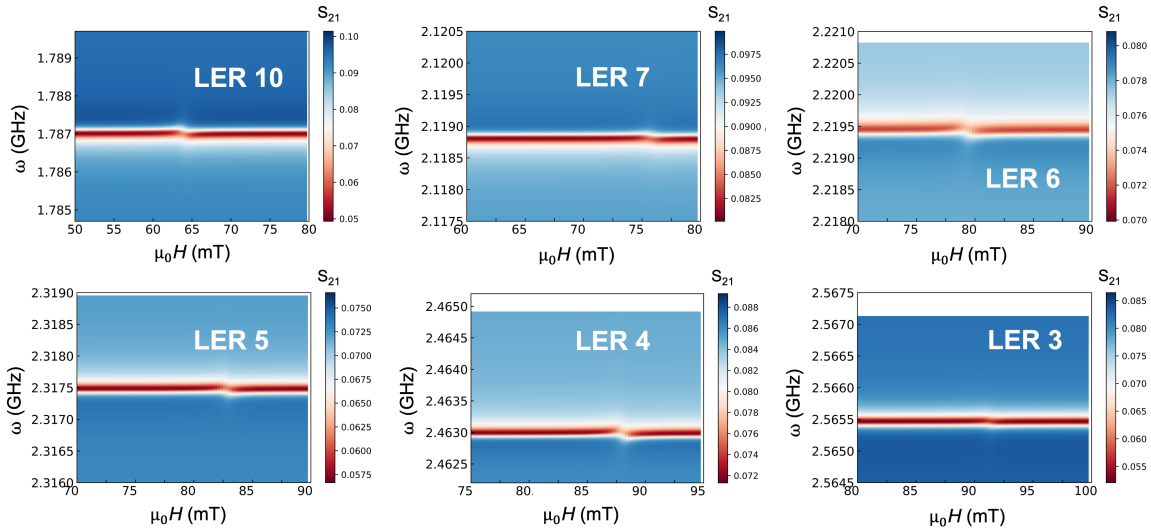

Figure 5.21: Simulated 2D plots of the microwave transmission through LERs 3, 4, 5, 6, 7 and 10 at 10 mK.

Using the linear dependence of G_1 that is obtained from the data shown in Fig. 5.22, we have estimated $G_{1,\mathrm{i}}$, *i.e.* the coupling of the spins located far from the constriction but close to the inductor. The LERs with a nanoconstriction are expected to generate the coupling introduced in Eq. (5.7), so knowing $G_{1,\mathrm{i}}$, G_N, $N_{\mathrm{eff,c}}$ and $N_{\mathrm{eff,i}}$ (shown in Table 5.5), we have calculated the mean single spin-photon coupling achieved by the nanoconstrictions, $\langle G_{1,\mathrm{c}} \rangle$, in LERs 2, 4, 6, 8 and 10 using Eq. (5.8). All these values are given in Table 5.6. These results have been obtained considering that the resonance that is not visible corresponds to LER 1. In case of being another LER the corresponding to this not detected resonance, a new analysis should be performed due to the possible changes of the number of spins corresponding to each LER.

The results shown in Table 5.6 and Fig. 5.23 indicate that the single spin-photon coupling is hugely increased (between three and four orders of magnitude) when a nanoconstriction is fabricated on this type of resonators. Thanks to the smaller inductance we have used now compared to previous sections (0.5 nH vs 5-14 nH), the average single spin-photon coupling of the inductors is higher than before. This is due to the higher current circulating through the inductor of a resonator when its inductance is reduced.

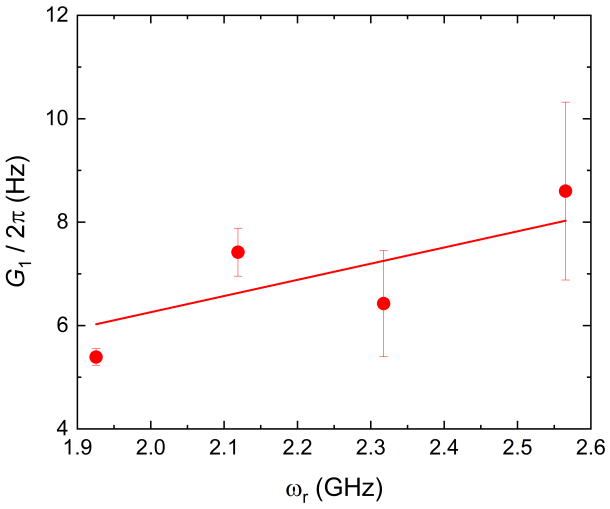

Figure 5.22: Evolution of the single spin-photon coupling measured for LERs 9, 7, 5 and 3, which do not have a nanoconstriction. The red line is a least-squares fit considering a linear dependence of the coupling with the resonance frequency.[5] This fits gives the following dependence of the single spin-photon coupling to the inductor: $G_{1,nc} = (3.129 \pm 0.184) \cdot 10^{-9}\omega$ Hz.

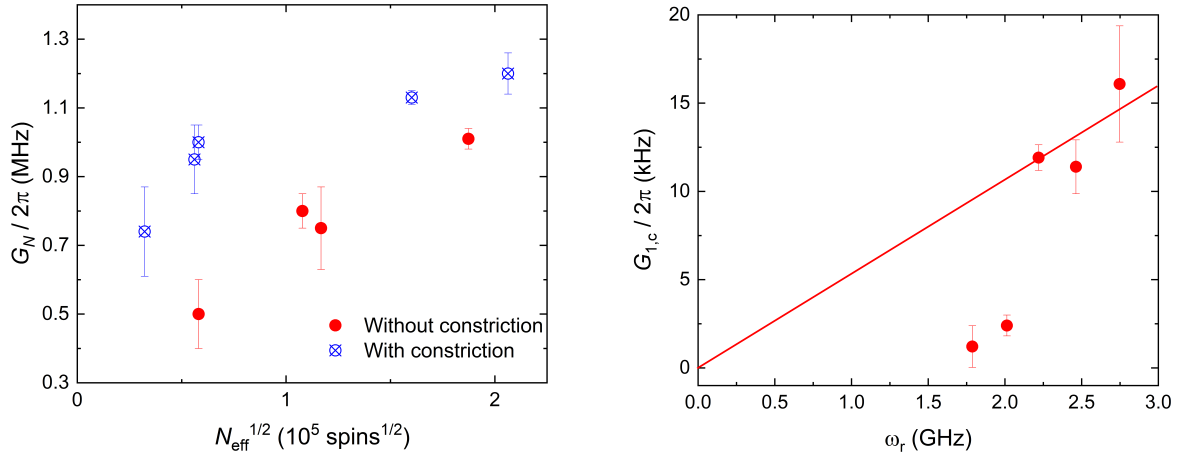

Figure 5.23: Evolution (a) of the collective spin-photon coupling G_N with the number of spins effectively coupled to the different inductors and (b) of the single spin-photon coupling $G_{1,c}/2\pi$ with frequency. The coupling to a single spin increases linearly with the signal frequency, as shown in (b). Here, a linear fit has been performed excluding the data measured for the two lowest frequencies. They seem to be underestimated due to a possible overestimation of the number of spins effectively coupled to the nanobridge.

The values of $G_{1,c}$ shown in Table 5.6 represent the average single spin-photon coupling achieved with the nanoconstriction on each LER. However, just as we have seen in the case of the coplanar resonators (Fig. 4.21), the maximum coupling achieved by individual spins will presumably be larger. In the following lines, we will estimate in a simple way this maximum value for LER 2, the one which shows the larger $G_{1,c}$.

Considering a homogeneous distribution of molecules in the nanoconstriction area, the mean single spin-photon coupling shown in Table 5.6 for LER 2 can be seen as the volume integral of the single spin-photon coupling at each point at a distance r of the constriction. Using the

LER	ω_r (GHz)	$\mathbf{G_N/2\pi}$ (MHz)	γ (MHz)	$\mathbf{G_{1,i}/2\pi}$ (Hz)	$\langle \mathbf{G_{1,c}/2\pi} \rangle$ (kHz)
2	2.755 ± 0.005	0.74 ± 0.13	36.64 ± 10.96	8.60 ± 0.50	16.09 ± 3.29
3	2.566 ± 0.005	0.50 ± 0.10	17.69 ± 1.50	8.60 ± 1.72	-
4	2.463 ± 0.004	0.95 ± 0.10	17.69 ± 1.50	7.71 ± 0.45	11.39 ± 1.52
5	2.318 ± 0.005	0.75 ± 1.20	17.69 ± 1.77	6.42 ± 1.03	-
6	2.220 ± 0.003	1.00 ± 0.05	19.90 ± 3.20	6.94 ± 0.41	11.91 ± 0.72
7	2.119 ± 0.002	0.80 ± 0.05	26.53 ± 3.50	7.42 ± 0.46	-
8	2.013 ± 0.001	1.13 ± 0.02	27.67 ± 1.16	6.30 ± 0.37	$2.40 \pm 0.0.59$
9	1.926 ± 0.001	1.01 ± 0.03	25.26 ± 1.37	5.39 ± 0.16	-
10	1.787 ± 0.001	1.20 ± 0.06	26.53 ± 3.50	5.59 ± 0.33	1.21 ± 1.18

Table 5.6: Values of $G_N/2\pi$, γ, $G_{1,i}/2\pi$ and $G_{1,c}/2\pi$ extracted from the fittings shown in Figs. 5.20 and 5.21.

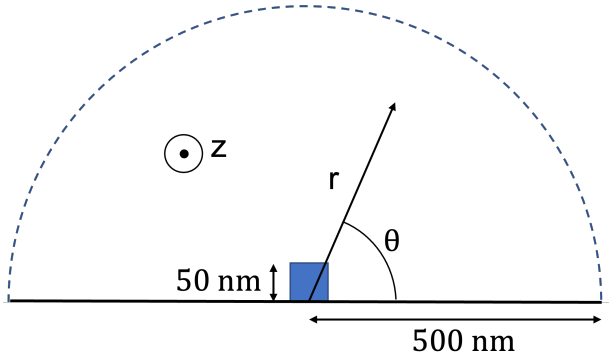

Figure 5.24: Scheme of the cylindrical coordinates considered for the determination of the maximum single spin-photon coupling achieved with LER 10. The distance to the constriction is represented by r, and the z axis is parallel to the nanoconstriction long axis.

cylindrical coordinates shown in Fig. 5.24, and approximating the single spin-photon coupling in a point at a distance $r > w$ of the constriction to:

$$G_{1,c}(r) \simeq G_{1,c}(w)\frac{w}{r}, \tag{5.9}$$

where w is the height of the nanoconstriction (50 nm), this integral becomes:

$$\langle G_{1,c}^2 \rangle \simeq \frac{1}{V}\int_{z=0}^{l}\int_{r=w}^{R}\int_{\theta=0}^{\pi} G_{1,c}^2(r) r dr\, dz\, d\theta = \left[\frac{2 \cdot w^2 \cdot l\pi G_{1,c}^2(w) \ln r}{\pi R^2 \cdot l}\right]_{r=w}^{R} =$$
$$= \frac{G_{1,c}^2(w) \cdot 2w^2 \ln \frac{R}{w}}{R^2} = \frac{G_{1,c}^2(50\ nm) \cdot 2 \cdot 50^2 \ln 10}{500^2}. \tag{5.10}$$

Here, we have considered that the nanoconstriction presents a height w of about 50 nm, a length l of 500 nm as shown in Fig. 5.15, and a magnetic mode with radius $R = 500$ nm.

From Eq. (5.10) the maximum achieved single spin-photon coupling can be extracted. The result is then:

$$G_{1,c}(50\,nm) = \frac{\langle G_{1,c} \rangle}{\sqrt{2 \ln 10}} \cdot \frac{500}{50} = 75.0 \text{ kHz} \tag{5.11}$$

This value is between four and five times greater than the one shown in Table 5.6. This indicates us that, in the case of LER 2, we may have achieved a single spin-photon coupling near 75 kHz

for the molecules located just on top of the nanoconstriction, showing the importance of being able to deposit the molecular samples as close as possible to the circuit. This value is associated with a dimensionless coupling $G_1/\omega \simeq 2.73 \times 10^{-5}$, even higher than the record value obtained in the previous chapter with the 2.5D resonator.

5.4 Conclusions

In this chapter, we have introduced a different type of resonator from those used in the previous chapter: a lumped element resonator consisting on a capacitor in parallel with an inductor. These LERs show a more versatile design than CPW resonators, being possible to modify the resonance frequency and the intensity of the microwave magnetic field by means of the design of their components. We have demonstrated that a reduction of the inductance produces an increase of the microwave field generated by the LERs, and thus an enhancement of the single spin-photon coupling. If the inductance is reduced down to the limit of a single straight wire, as done in section 5.3, the microwave magnetic field should be more intense in the vicinity of the superconducting circuit, while being confined to a smaller volume. This effect has been observed when the inductance has been reduced from 14 nH to 5 nH (section 5.2), and when it has been reduced even more, down to 0.5 nH (section 5.3).

We have checked that the collective spin-photon coupling achieved with PTM_r molecules coupled to lumped element resonators follows a linear dependence with $\sqrt{N_{\text{eff}}}$, being possible to increase the number of deposited molecules in order to enhance it. Nevertheless, this increase in deposited molecules can lead to a worsening of the spin linewidth. The free radical PTM_r shows T_2 values of tens of μs at very low temperature. However, spin linewidths close to 35 MHz were observed in transmission measurements, regardless of the polymer used in the depositions. This increase in the linewidth seems to be motivated by the formation of PTM_r aggregates when the solvent completely dries, together with a hyperfine coupling between nearby spins and other inhomogeneous broadening sources. A high reduction of the spin concentration would be needed in order to increase the spin coherence up to values close to the 7 MHz observed in previous EPR measurements.

We have verified that, when a 50 nm wide constriction is fabricated, the average single spin-photon coupling is highly increased, between three and four orders of magnitude, agreeing with the effect observed in chapter 4 with CPW resonators. The values of $\langle G_{1,c} \rangle$ obtained with these LERs are one order of magnitude higher than those obtained for CPW resonators with a 50 nm wide nanoconstriction, thanks to the reduced inductance of these LERs. They are even higher than the 3.4 kHz achieved with the 2.5D resonator. The dimensionless coupling associated to the constriction of LER 2, $G_{1,c}/\omega \simeq 5.85 \times 10^{-6}$, is pretty similar, and even higher, than that achieved for the 2.5D resonator with a 50 nm constriction ($G_1/\omega \simeq 10^{-6}$). This improvement indicates that the approach of reducing the inductance in on-chip resonators is leading us to achieve record single spin-photon coupling values.

Finally, we have determined the maximum single spin-photon coupling achieved near the nanoconstriction of LER 2, the one that shows a higher mean single spin-photon coupling. This maximum value seems to be close to 75 kHz, much higher than the 16 kHz needed to achieve the strong coupling regime with a PTM_r molecule considering a T_2 of tens of μs. This maximum value of $G_{1,c}$ is achieved by the spins that are closest to the constriction, underlying the crucial importance that depositing the molecular qubits as close as possible to the superconducting circuit has on the practical implementation of this hybrid quantum computation scheme.

Bibliography

[1] A. Bienfait, J. J. Pla, Y. Kubo, X. Zhou, M. Stern, C. C. Lo, C. D. Weis, T. Schenkel, D. Vion, D. Esteve, J. J. L. Morton, and P. Bertet. Controlling spin relaxation with a cavity. *Nature*, 531:74–77, 2016.

[2] A. Stockklauser, P. Scarlino, J. V. Koski, S. Gasparinetti, C. K. Andersen, C. Reichl, W. Wegscheider, T. Ihn, K. Ensslin, and A. Wallraff. Strong Coupling Cavity QED with Gate-Defined Double Quantum Dots Enabled by a High Impedance Resonator. *Physical Review X*, 7:011030, 2017.

[3] Y.-Z. Dai, B.-W. Dong, Y. Kao, Z.-Y. Wang, H.-I. Un, Z. Liu, Z.-J. Lin, L. Li, F.-B. Xie, Y. Lu, M.-X. Xu, T. Lei, Y.-J. Sun, J.-Y. Wang, S. Gao, S.-D. Jiang, and J. Pei. Chemical Modification toward Long Spin Lifetimes in Organic Conjugated Radicals. *ChemPhysChem*, 19:2972–2977, 2018.

[4] P. Bushev, A. K. Feofanov, H. Rotzinger, I. Protopopov, J. H. Cole, C. M. Wilson, G. Fischer, A. Lukashenko, and A. V. Ustinov. Ultralow-power spectroscopy of a rare-earth spin ensemble using a superconducting resonator. *Physical Review B*, 84:060501, 2011.

[5] M. D. Jenkins. *Coupling quantum circuits to magnetic molecular qubits.* PhD thesis, Universidad de Zaragoza, 2015.

6

Coupling Spin Clock Transitions to Quantum Circuits

6.1 Introduction

In previous chapters we have studied two strategies for reaching the coherent coupling regime between molecular spin qubits and superconducting circuits that are both based on the optimisation of the circuit characteristics. Here, we will explot a characteristic property of magnetic molecules. Besides being microscopic, thus fully reproducible and intrinsically quantum, they represent the smallest structure that remains tuneable. The ability to modify the relevant properties by properly choosing the molecular composition and structure allows engineering the qubit spin states and energies[1;2] and enables scaling up computational resources within each molecule (*e.g.* by accommodating several different magnetic atoms in exquisitely defined coordinations[3;4;5;6;7] or by making use of multiple internal spin states[8;9;10;11]). Here, we will show that it can also help optimising the spin-photon coupling.

A way to reconcile a high degree of scalability, *i.e.* a high density of spin qubits, with sufficient isolation from noise sources is to encode the qubit states in a subspace that is robust against magnetic field fluctuations. In the case of molecular systems, this can be achieved by associating 0 and 1 to superpositions of spin-up and spin-down states that arise at "spin-clock" transitions, relatively insensitive to magnetic field changes. In this chapter, we consider how spin level anticrossings influence the coupling to a superconducting resonator.

A paradigmatic example is provided by the sodium salt of the cluster $[Ho(W_5O_{18})_2]^{9-}$,[12;13] hereafter referred to as HoW_{10}, which consists of a single Ho^{3+} ion encapsulated by polyoxometalate moieties (Fig. 6.1). Its fourth-fold coordination symmetry gives rise to fourth-order off-diagonal terms in the spin Hamiltonian that strongly mix the $m_J = \pm 4$ projections of the ground electronic spin doublet. The large quantum tunneling gap $\Delta \simeq 9.1$ GHz generated by such terms, combined with the hyperfine interaction with the $\mathbf{I} = 7/2$ spin of the Ho nucleus, gives rise to a set of level anti-crossings at which the spin coherence time T_2 becomes maximum.[2] This molecule will be studied in section 6.2, where a physical characterization of the molecule and a temperature and field-dependent study of the spin-photon coupling will be presented, with an emphasis on studying the behaviour near avoided level crossings.

A second molecule which also shows "spin-clock" transitions, in this case at low magnetic fields, is the vanadyl porphyrin [VO(TCPPEt)] ($\mathbf{1^{VO}}$, H_2TCPPEt = 5,10,15,20-tetrakis(4-carboxyphenyl)porphine tetraethyl ester). This molecule consists of a single V^{4+} ion at the centre of a N_4 porphyrin. It presents an $S = 1/2$ electronic spin entangled with an $I = 7/2$ nuclear spin, resulting in a series of anharmonically spaced levels. As will be shown in this chapter, the extra states associated with the nuclear spin could help encoding multiple qubits, or a multidimensional qudit.[4;10] This would allow the implementation of non-trivial algorithms, like quantum error correction.[14] Section 6.3 will be dedicated to this sample, studying if it fulfils the conditions to act as a universal 4-qubit processor (or $d = 16$ qudit) as well as the spin-photon coupling between this molecule and lumped element resonators near the clock transitions associated with electronuclear spin entanglement.

6.2 Coupling cavity photons to electronic spin-clock transitions in HoW_{10}

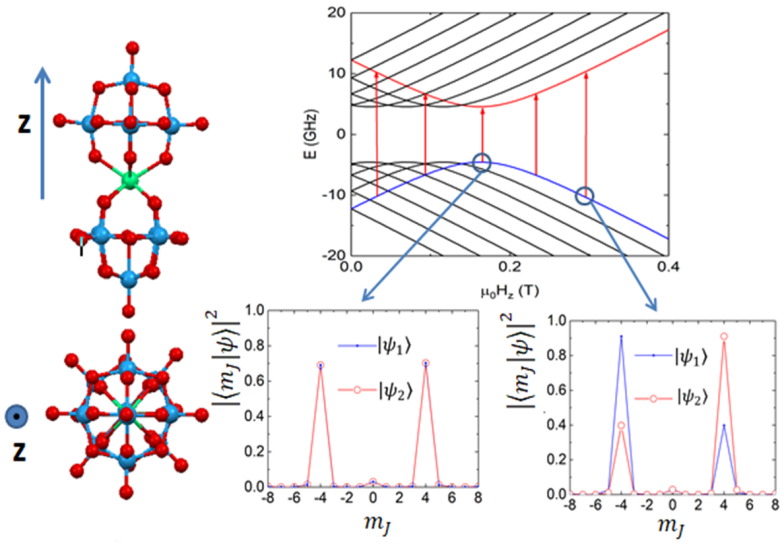

Figure 6.1: Left: two views of the HoW_{10} cluster, showing its four-fold coordination symmetry around its anisotropy axis $\vec{z}$. Right: scheme of magnetic energy levels corresponding to the electronic ground doublet ($m_J = \pm 4$) of HoW_{10} and electronic spin wave functions of two mutually avoiding levels calculated at the indicated magnetic fields (both at and slightly off the clock transition).

In this section we will consider crystals of $Ho_xY_{1-x}W_{10}$, which consist of HoW_{10} molecules diluted into a crystal of diamagnetic YW_{10}. This molecule is a polyoxometalate (POM) consisting of a single lanthanoid ion surrounded by a metal oxide structure that form molecular crystals (Fig. 6.1). Lanthanoid (also known as rare earth) systems present an angular momentum $\mathbf{L}$ different from zero, and a spin-orbit coupling between $\mathbf{L}$ and electronic spin $\mathbf{S}$ larger than the coupling of $\mathbf{L}$ with the crystal field.[15] This makes it necessary to describe these systems using the total angular momentum $\mathbf{J} = \mathbf{S} + \mathbf{I}$, coupled to the crystal field through $\mathbf{L}$. As a result, in the Hamiltonian which describes the magnetic behaviour of lanthanoid systems it is necessary to replace $\mathbf{L}$ and $\mathbf{S}$ by $\mathbf{J}$. It should also include terms to describe the crystal field, which can split the J multiplet into a series of doublets, associated with eigenstates $|\pm m_J\rangle$, and that can induce quantum tunneling between states $|+m_J\rangle$ and $|-m_J\rangle$. Taking this into account, as well as the hyperfine interaction in case of having a non-zero nuclear spin $\mathbf{I}$, the Hamiltonian which describes these molecules is as follows:

$$\mathcal{H} = \sum_{k,q} B_{kq}\hat{O}_k^q + \mu_B \vec{H} \cdot \hat{g}_J \cdot \mathbf{J} + \mathbf{J}\hat{A}\mathbf{I}, \tag{6.1}$$

where the terms $B_{kq}\hat{O}_k^q$ are the Stevens spin operators that describe the crystal field effect on the molecular spin states. The most common Stevens operators are shown in Table 6.1.

The crystal field introduces a zero-field splitting in the energy diagram. This splitting can be tuned by modifying the chemical design of the molecules, allowing us to obtain systems with high spin values, and therefore high couplings, with operating frequencies in a comfortable range for the quantum circuits they would be coupled to.

In the case of HoW_{10}, only the parameters shown in Table 6.2 are non-zero. The Hamiltonian used for HoW_{10} is then

$$\mathcal{H} = B_{20}\hat{O}_2^0 + B_{40}\hat{O}_4^0 + B_{60}\hat{O}_6^0 + B_{44}\hat{O}_4^4 + g_J\mu_B\vec{H}\cdot\mathbf{J} + AJ_zI_z \tag{6.2}$$

k	q	O_k^q
2	0	$3J_z^2 - jI$
	±1	$c_\pm \left[J_z, J_+ \pm J_-\right]_+$
	±2	$c_\pm \left(J_+^2 \pm J_-^2\right)$
4	0	$35J_z^4 - (30j - 25)\, J_z^2 + \left(3j^2 - 6j\right) I$
	±1	$c_\pm \left[7J_z^3 - (3j + 1)\, J_z, J_+ \pm J_-\right]_+$
	±2	$c_\pm \left[7J_z^2 - (j + 5)\, I, J_+^2 \pm J_-^2\right]_+$
	±3	$c_\pm \left[J_z, J_+^3 \pm J_-^3\right]_+$
	±4	$C_\pm \left(J_+^4 \pm J_-^4\right)$
6	0	$231J_z^6 - (315j - 735)\, J_z^4 + \left(105j^2 - 525j + 294\right) J_z^2 - \left(5j^3 - 40j^2 + 60j\right) I$
	±1	$c_\pm \left[33J_z^5 - (30j - 15)\, J_z^3 + \left(5j^2 - 10j + 12\right) J_z, J_+ \pm J_-\right]_+$
	±2	$c_\pm \left[33J_z^4 - (18j + 123)\, J_z^2 + \left(j^2 + 10j + 102\right) I, J_+^2 \pm J_-^2\right]_+$
	±3	$c_\pm \left[11J_z^3 - (3j + 59)\, J_z, J_+^3 \pm J_-^3\right]_+$
	±4	$c_\pm \left[11J_z^2 - (j + 38)\, I, J_+^4 \pm J_-^4\right]_+$
	±5	$c_\pm \left[J_z, J_+^5 \pm J_-^5\right]_+$
	±6	$c_\pm \left(J_+^6 \pm J_-^6\right)$

Here $[A, B]_+ = (AB + BA)/2$, and $j = J(J + 1)$, $c_+ = 1/2$, $c_- = 1/2i$

Table 6.1: Most common extended Stevens operators O_k^q.[16;17]

The molecular structure of HoW_{10}, together with an example of its wavefunctions near and out of a clock transition obtained from (6.2), are shown in Fig. 6.1. The Ho^{3+} ion presents a $J = 8$ electronic angular momentum coupled by the hyperfine interaction with an $I = 7/2$ nuclear spin, and has an isotropic gyromagnetic g-factor $g_J = 5/4$. The integer value of J makes this molecule to be a non-Kramers system, not being able to describe its energy spectrum as a set of spin doublets. The symmetry of the HoW_{10} molecule introduces the diagonal terms up to order 6. These terms produce a degenerated ground state with spin projection $m_J = \pm4$. The non-Kramers behaviour can lead to a spin tunneling effect between opposite spin projections ($+m_J$ and $-m_J$), and level antricrossings. The molecular structure of HoW_{10}, which shows a D_{4d} symmetry, generates the non-diagonal term $B_{44}\hat{O}_4^4$. This term connects states with $\Delta m_J = \pm4$, producing entangled states with both spin orientations $m_J = \pm4$, allowing transitions that would be forbidden otherwise. The combination of these two effects produce the spin-clock transitions that are studied in following sections.

$\mathbf{B_{20}}$ (GHz)	$\mathbf{B_{40}}$ (MHz)	$\mathbf{B_{60}}$ (MHz)	$\mathbf{B_{44}}$ (MHz)	$\mathbf{g_J}$	$\mathbf{A_{zz}}$ (MHz)	$\mathbf{A_{xx}}$, $\mathbf{A_{yy}}$ (MHz)
18.03	209	−1.53	94.3	1.25	830	0

Table 6.2: Hamiltonian parameter set used for all HoW_{10} simulations in this thesis.[13]

6.2.1 Physical characterization: heat capacity and magnetic susceptibility

An initial characterization of pure HoW_{10} samples was done by means of specific heat (using a commercial PPMS system, see section 2.2.1) and magnetic susceptibility measurements (by means of a commercial MPMS system, section 2.2.2).

Regarding the magnetic susceptibility experiments, a pure powder HoW_{10} sample, mixed with Apiezon N grease for an optimal thermalization, was introduced in a plastic capsule. This capsule was placed into the MPMS system, where the susceptibility evolution with temperature was studied between 2 K and 300 K. The final magnetic susceptibility data were obtained by correcting the capsule and grease contributions to the measurement, previously calibrated. These corrected data are shown in Fig. 6.2(a). The fitting curve was calculated by numerically solving the spin Hamiltonian (6.2).

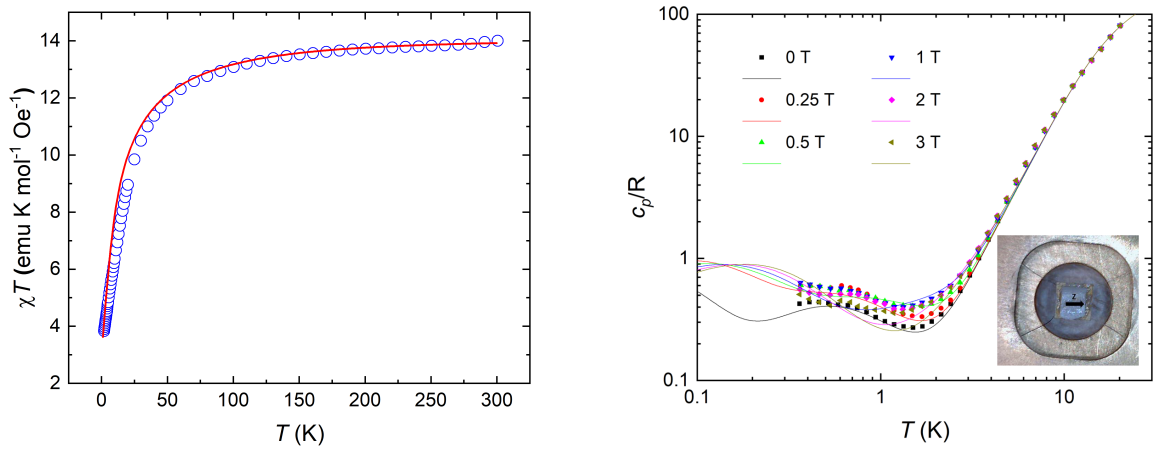

Figure 6.2: (a) DC χT product measured on a powder HoW_{10} sample between 2 and 300 K, and an applied field of 0.1 T, and (b) molar specific heat of a crystal of $Ho_{0.1}Y_{0.9}W_{10}$ measured at several magnetic fields applied parallel to the long crystal axis. The dots are the experimental data and the lines result from numerical calculations of χT and c_P/R that follow from the spin Hamiltonian (6.2) with the parameters reported in the literature.[13]

Considering the eigenstates and energies of the system given by the resolution of the previous Hamiltonian, the dc magnetic susceptibility can be calculated by the following expression:

$$\chi T = T\frac{N_A \mu_B g_J}{ZH}\sum_n \left\langle n\left|\mathbf{J}\cdot\hat{h}\right|n\right\rangle e^{-\beta E_n}, \tag{6.3}$$

where $Z = \sum_m e^{-\beta E_m}$ is the partition function, $\beta = k_B T$ and $\hat{h}$ is the unit vector along the magnetic field orientation. Analysing this expression in the high and low temperature limits, we can find useful information about the sample. For high temperatures, Eq. (6.3) tends to

$$\chi T \simeq N_A \frac{g_J^2 \mu_B^2 J\,(J+1)}{3k_B} \quad (T \to \infty) \tag{6.4}$$

while for low temperatures, we obtain

$$\chi T \simeq N_A \frac{g_J^2 \mu_B^2 m_J^2}{3k_B} \quad (T \to 0) \tag{6.5}$$

In Fig. 6.2(a) we can see that the product χT tends to a value of ~ 14 for high temperatures, which according to Eq. (6.4) corresponds to $J = 8$, the value of the total spin mentioned before. On the other hand, the evolution of the susceptibility for low temperatures fits with the existence of a ground doublet with electronic spin projection $m_J = \pm 4$ as expected from a numerical resolution of the Hamiltonian (6.2).

In order to confirm the existence of the expected tunnel energy gap in HoW_{10}, we performed a series of low temperature specific heat measurements. A diluted crystal ($Ho_{0.1}Y_{0.9}W_{10}$), where the Ho^{3+} ions were replaced with non magnetic Y^{3+} ions, was deposited on top of a calorimeter together with Apiezon N, and the device was introduced in the PPMS system (see section 2.2.1). Several heat capacity curves were measured for different magnetic fields applied along the long crystal axis, and a temperature range between 0.35 and 20 K. The use of a diluted sample can allow us to distinguish the magnetic contribution to the heat capacity from other contributions, like lattice vibrations or dipole-dipole interactions. The measured data are shown in Fig. 6.2(b). In this graph we can see that, for temperatures above 5 K, the curves for all the fields overlap, being the lattice contribution the predominant in this region. For temperatures below 5 K, the magnetic contribution starts to be higher than the lattice one, obtaining different peaks whose positions vary depending on magnetic field. These peaks arise from the energy gap between states with $m_J = +4$ and $m_J = -4$, and the temperatures at which they appear give us information about the size of this gap. Another peak, corresponding to the hyperfine splitting, should appear at lower temperatures, too low to be measured with this device.

The magnetic contribution to the specific heat was calculated by means of the fluctuation-dissipation theorem:

$$\frac{c_M}{R} = \frac{1}{(k_B T)^2} \sum_n \left(\langle E_n^2 \rangle - \langle E_n \rangle^2 \right), \tag{6.6}$$

while the effect of the lattice vibrations at high temperature was simulated using a generalised Debye model:[18]:

$$c = 9 N_A k_B T^3 \left[\frac{1}{\theta_{ac}^3} \int_0^{\theta_{ac}/T} \frac{x^4 e^x}{(e^x - 1)^2} dx + \frac{n_{op}}{\theta_{op}^3} \int_{\theta_{ac}/T}^{\theta_{op}/T} \frac{x^4 e^x}{(e^x - 1)^2} dx \right], \tag{6.7}$$

where two terms were necessary for a correct reproduction of the experimental data. The first one accounts for the contribution of acoustic phonons and the second term for that of the optical phonons and molecular vibrations. Each term has his own Debye temperature (θ_{ac} and θ_{op} respectively) which were fitted separately.

The experimental data together with the fitting curves are shown in Fig. 6.2(b). The fitting parameters of the lattice contribution are $\theta_{ac} = 23$ K, $\theta_{op} = 85$ K and $n_{op} = 65$.

In a system with discrete energy levels, the magnetic contribution to the specific heat produces peaks, or Schottky anomalies, corresponding to the different energy gaps that the system shows. These peaks are at different temperature, T_{max}, depending on the value of the energy gap ($k_B T_{max} \approx 0.417 \Delta E$),[19] so they can provide very interesting information about magnetic systems. HoW_{10} must show two Schottky anomalies corresponding to the tunnel energy gap and the hyperfine splitting.

For a correct reproduction of experimental data, a strain in B_{44}, $\Delta B_{44} = 41$ MHz, thus also of quantum tunneling gaps Δ had to be introduced in order to account for the width of the Schottky anomaly measured at $H = 0$ and $T < 1$ K. This makes the Schottky anomaly to be at a higher temperature than expected (0.6 K instead of 0.2 K). The deviations that can be appreciated in these measurements at low temperature tell us that the spin Hamiltonian (6.2) may need the addition of new terms or strains that would explain the behaviour of c_p. Nevertheless, these new terms should not change the average gap $\Delta = 9.1$ GHz that was measured by broadband spectroscopy measurements shown in next sections.

These two experiments therefore confirm the existence of a ground state with tunnel-split $m_J = \pm 4$ states, with a large quantum energy gap.

6.2.2 Broadband spectroscopy: determination of molecular axes

Knowing the orientation of HoW_{10} molecules in the crystal with respect to the applied magnetic field is crucial for a correct interpretation of the results This orientation was determined by means of broadband spectroscopy for different external magnetic field orientations. In these measurements, a fully concentrated monocrystalline sample was deposited on top of a coplanar superconducting waveguide (CPW), as shown in Fig. 6.3. This system was introduced in a 90 L liquid helium dewar containing a vector magnet (see section 2.6) and connected to a vector network analyser (see section 2.5.2), with which the microwave transmission through the line was measured at 4.2 K. The geometry of the CPW was chosen in order to maximize the coupling between the clock transitions that take place in these molecules and the waveguide. As it was shown in section 3.4.1, the special nature of the spin-clock transitions leads to a vanishing matrix element between the two states involved in the usual configuration of a microwave field perpendicular to the magnetic one applied along the Z laboratory axis. This makes it necessary to generate a microwave field component parallel to the external dc magnetic field.

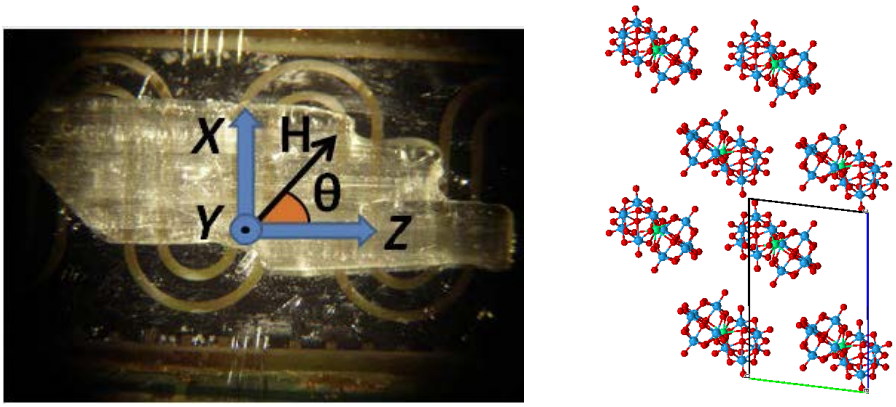

(a) **(b)**

Figure 6.3: (a) Optical microscopy image of the on-chip superconducting waveguide hosting the HoW_{10} single crystal used for the experiments at 4.2 K. Arrows marked with XYZ define the reference laboratory frame, whose axes coincide with those of the superconducting vector magnet that applies and orients in situ the external magnetic field $\vec{H}$. (b) Distribution of the HoW_{10} molecules in the crystal. The short (green) axis corresponds to the long axis of the crystal in (a).

The microwave transmission was measured for different orientations of the external magnetic field applied along the XZ plane of the laboratory frame (see Fig. 6.3). Experimental transmission data are shown in Fig. 6.4. Figure 6.5 shows the plots of the transmission data simulated as described below. In order to enhance the visibility of the effects associated with the coupling between the transmission line and the spins, S_{21} needed to be normalized. The normalized transmission t at magnetic field H_1 and frequency ω_1 is given by

$$t(H_1, \omega_1) = \frac{S_{21}(H_1, \omega_1) - S_{21}(H_2, \omega_1)}{S_{21}^{(0)}(\omega_1)}, \tag{6.8}$$

where $H_2 > H_1$ and $S_{21}^{(0)}$ is the transmission of the transmission line when the spin excitations are outside the studied frequency region. For H_2 close enough to H_1, t approximately corresponds to the derivative of the microwave transmission.

The experimental data neatly show lines associated with the resonant absorption of microwave photons by the spins. Each of them corresponds to an allowed transition between two states

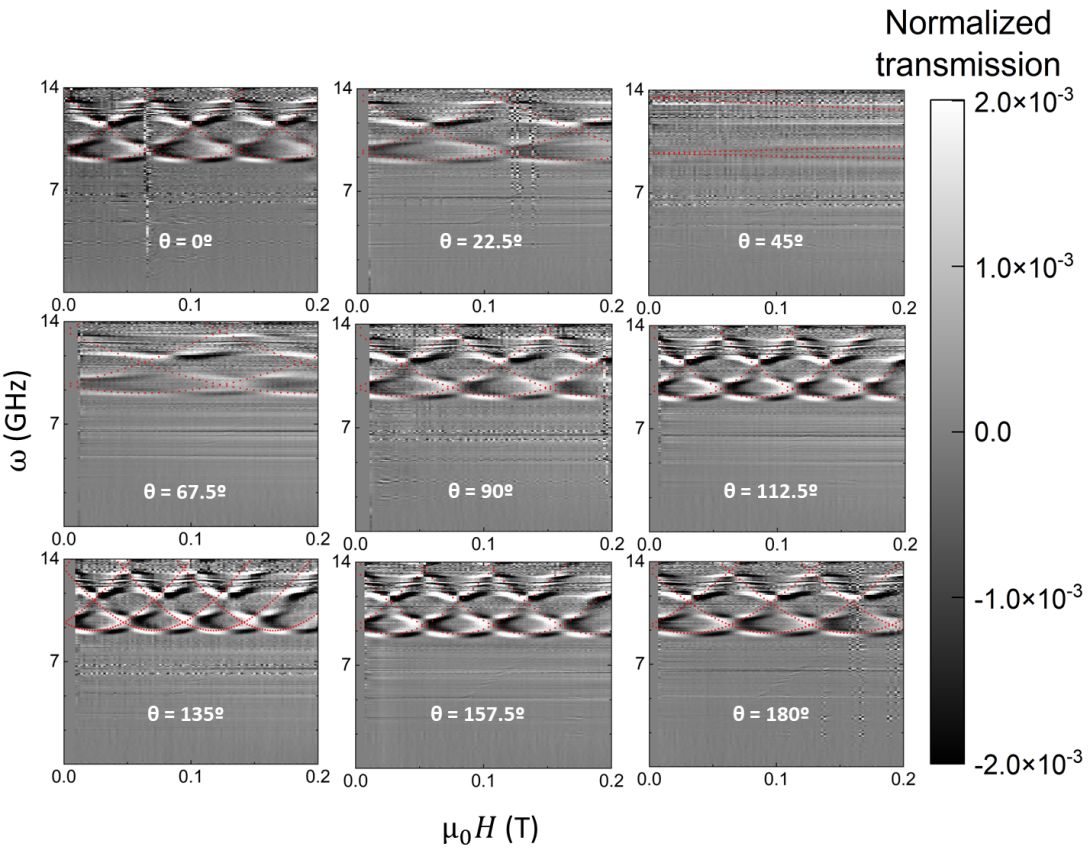

Figure 6.4: 2D plots of the normalized transmission measured, for different orientations of the external magnetic field, on a transmission line coupled to a single crystal of HoW_{10} at a temperature of 4.2 K. Angle θ defines the orientation of $\vec{H}$ with respect to laboratory frame (and the long axis of the device), as shown in Fig. 6.3. Red dotted lines are the positions of the different transitions determined with the spin Hamiltonian (6.2) with the parameters shown in Table 6.2.

having a different electronic spin wave function and the same nuclear spin state, such as those marked by vertical arrows in Fig. 6.1. These resonance lines then provide a complete picture of the low-lying magnetic energy levels in HoW_{10}. In particular, they show the presence of a finite gap $\Delta \simeq 9.1$ GHz in the excitation spectrum associated with 4 different level anti-crossings. The position of these lines can be simulated using the spin Hamiltonian (6.2). As shown by comparing Figs. 6.4 (experiments) and 6.5 (simulations), we find a very good agreement with the same parameters that were determined from EPR experiments performed on magnetically diluted samples (*i.e.* samples in which a $1-x$ fraction of Ho^{3+} ions were replaced with nonmagnetic Y^{3+}).[2] These results show that concentrated crystals retain the same magnetic anisotropy and, together with the heat capacity data, confirm that the strong spin tunnelling, and the associated energy gap, are genuine properties of each molecule.

This assumption has been confirmed by performing transmission measurements with a diluted crystal, $Y_{0.8}Ho_{0.2}W_{10}$, obtaining the 2D plot shown in Fig. 6.6 when the magnetic field is applied along the X laboratory axis. We can see that the gap remains insensitive to the variation of the Ho concentration, while the visibility, and therefore the coupling, has been drastically reduced due to the lower number of magnetic molecules coupled to the CPW. This makes it necessary to decrease temperature when measuring diluted samples, as will be shown in following sections.

The strong magnetic anisotropy of HoW_{10} molecules makes their level splitting almost insensitive to any magnetic field applied on a direction other than the molecular anisotropy axis.

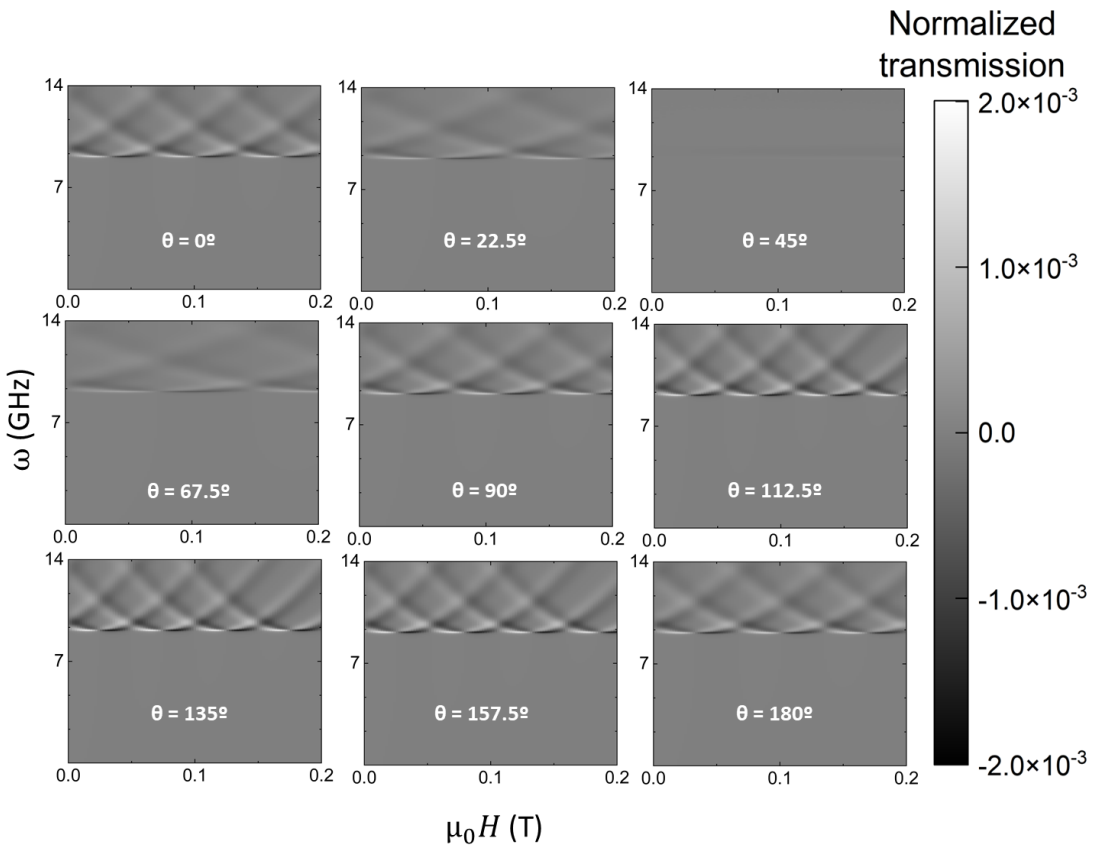

Figure 6.5: 2D plots of the normalized transmission of a transmission line coupled to a single crystal of HoW_{10}, calculated with the Hamiltonian (6.2) for different orientations of the external magnetic field. A gaussian distribution of dipolar fields with a width $\sigma = 6.4$ mT has been used.

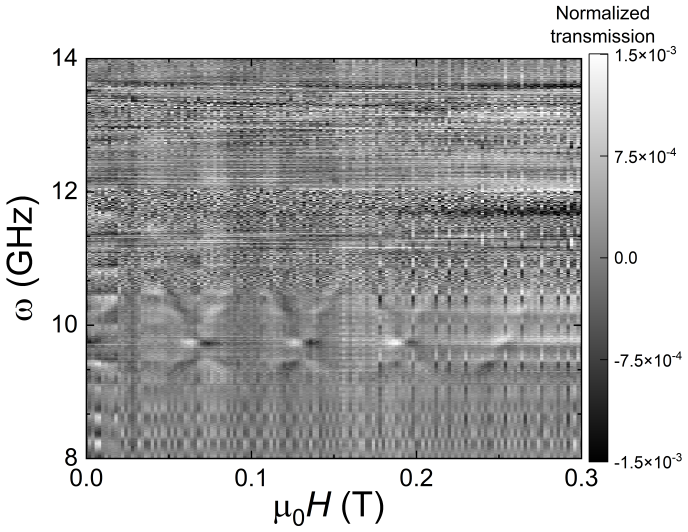

Figure 6.6: 2D plot of the normalized transmission measured for a single crystal of $Y_{0.8}Ho_{0.2}W_{10}$ coupled to a transmission line at a temperature of 4.2 K, when magnetic field is applied along the Z laboratory axis.

This fact has enabled us to determine the orientation of this anisotropy axis by focusing on the positions H_{m_I} of the anticrossings that are visible in the transmission plots. They occur at a given magnetic field parallel to the anisotropy axis, $H_{m_I,z} = 2\,|m_I|\,H_{-1/2,z}$, with $H_{-1/2,z} = 23$ mT.

By fitting the magnetic field at which the anticrossings are observed at different magnetic field orientations, we can obtain the orientation of the molecular anisotropy axis in the laboratory frame. The component $H_{m_I,z}$ of the applied field parallel to the anisotropy axis ($\vec{z}$) can be written as

$$H_{m_I,z} = H_{m_I} \cos\psi = H_{m_I} \left(\sin\theta_z \cos\varphi_z \sin\theta + \cos\theta_z \cos\theta\right) \tag{6.9}$$

where θ is the angle that the magnetic field makes with the laboratory axis Z and θ_z, φ_z are the polar coordinates of the anisotropy axis in the laboratory frame. By applying the magnetic field along different orientations within the XZ plane using a vector magnet (see Fig. 6.7) and using Eq. (6.9), the orientation of the anisotropy axis in the laboratory frame has been determined, obtaining the following values:

$$\theta_z = 134.13^\circ \pm 1.11^\circ \tag{6.10}$$

$$\varphi_z = 27.90^\circ \pm 6.71^\circ \tag{6.11}$$

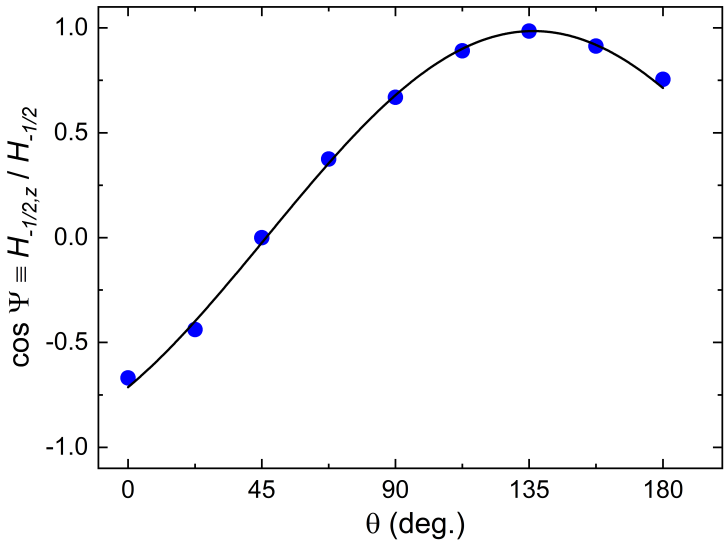

Figure 6.7: Dependence on the magnetic field orientation of the ratio $H_{-1/2,z}/H_{-1/2}$ between the first longitudinal anticrossing field $H_{-1/2,z} = 23$ mT and the observed anticrossing magnetic field $H_{-1/2}$. Angle θ is defined in Fig. 6.3. The solid line is a fit that provides the orientation of the magnetic anisotropy axis $\vec{z}$ with respect to the laboratory axes.

For both the pure and magnetically diluted crystals, the resonance linewidths are of order 100-300 MHz. This broadening seems to be dominated by the dipolar interactions between every magnetic molecule in the crystal, and by the distribution in magnetic anisotropy parameters. By a numerical calculation of the magnetic dipolar fields distribution in HoW_{10}, like the one shown in Fig. 6.8, we have found a field width $\Delta B = 6.4$ mT for the pure sampe and $\Delta B = 2.7$ mT for the magnetically diluted crystal. These distributions correspond to a level broadening $\Delta\omega \simeq 425$ MHz and $\Delta\omega \simeq 180$ MHz for pure and diluted samples respectively, thus enough to account for the observed linewidths.

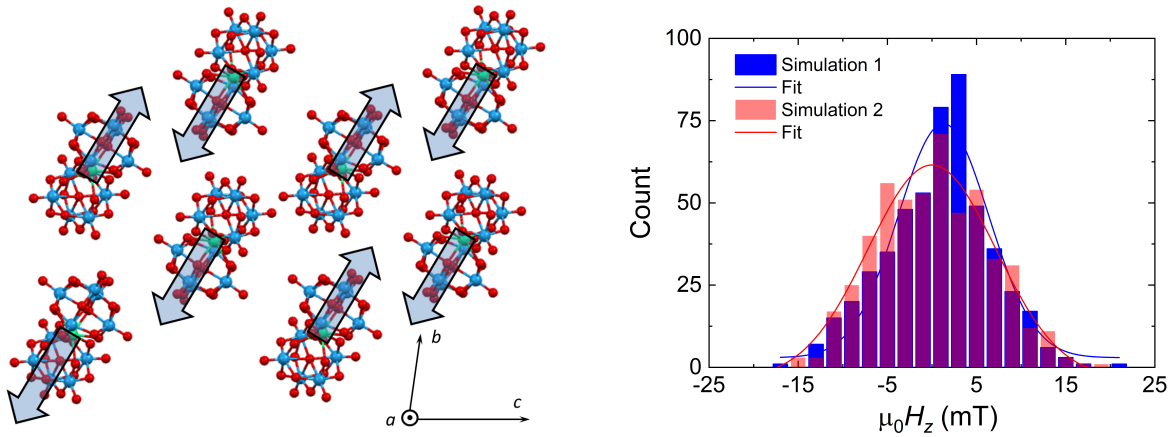

(a) (b)

Figure 6.8: (a) Snapshot of one of the spin configurations used to calculate the dipolar field distribution at the sites of the HoW_{10} crystal lattice. Magnetic moments with magnitude $4g_J\mu_B$ are oriented along the magnetic anisotropy axis z, which corresponds to the long molecular axis. (b) Dipolar magnetic field histograms calculated for an applied magnetic field of 50 mT and two different spin configurations.

6.2.3 Magnetic field dependence of the spin-photon coupling: effect of the spin-clock transitions

Whereas the positions of the resonance lines give access to the energy level scheme, their intensities provide useful information on the wavefunctions of the involved states and about how HoW_{10} spins interact with photons. An important advantage of working with open waveguides is that both frequency and magnetic field can be varied independently of each other. It is therefore possible to monitor how the absorption line shapes vary as a function of H.

For performing experiments at very low temperature and studying the evolution of the spin-photon coupling with field and temperature, a magnetically diluted crystal, $Y_{0.8}Ho_{0.2}W_{10}$, was deposited on top of a CPW and the device was introduced to a cryo-free dilution refrigerator (see section 2.6) equipped with a uniaxial magnet. The temperature of the sample and the chip were varied between 50 mK and about 800 mK. This system contains power attenuators and a cryogenic amplifier, allowing us to introduce very low power in the circuit (down to -85 dBm) and still obtain measurable transmission signals. In this case, the microwave field generated by the CPW used in these experiments was perpendicular to the applied magnetic field, as shown in Fig. 6.9. However, taking into account the orientation of the molecular anisotropy axis, the component of the microwave field parallel to this axis should be strong enough to induce transitions between electronic spin states.

Figure 6.10 shows the normalized microwave transmission measured at a temperature of 300 mK, together with the transmission at one magnetic field comparing the situation near and far from the second spin-clock transition. It can be seen that the visibility of the measured signal becomes higher near the spin-clock transitions than away from them. We have analysed these results and the following ones done at different temperatures using the input-output theory [20;21] adapted to our experimental conditions (see chapter 3), *i.e.* to a close to 1D coplanar waveguide and for finite temperatures. The line shape of a given resonance can then be described with the following expression:

$$\frac{S_{2,1}}{S_{2,1}^{(0)}} = \frac{1}{1+\frac{G}{\gamma+i(\omega_s-\omega)}} \tag{6.12}$$

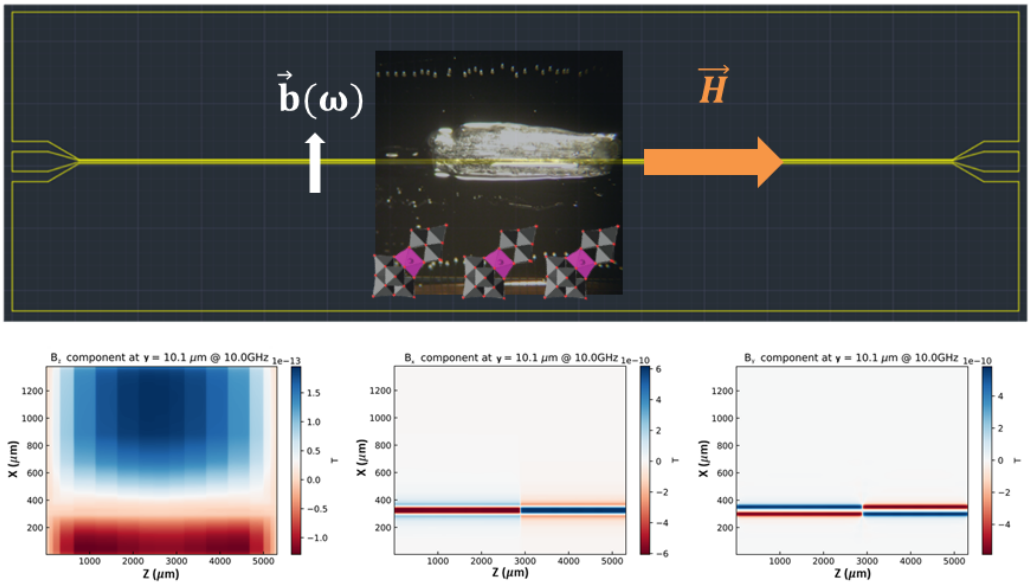

Figure 6.9: Scheme of the setup employed in the transmission experiments carried out at very low temperatures. The chip consists of a 10 μm wide transmission line placed between two ground planes. An $Y_{0.8}Ho_{0.2}W_{10}$ single crystal was placed on top of the line as shown in the figure. The applied magnetic field was parallel to the circuit and to the long crystal axis, while the main component of the microwave magnetic field produced by the transmission line was perpendicular to the applied field and also parallel to the chip, as shown in the bottom graphs.

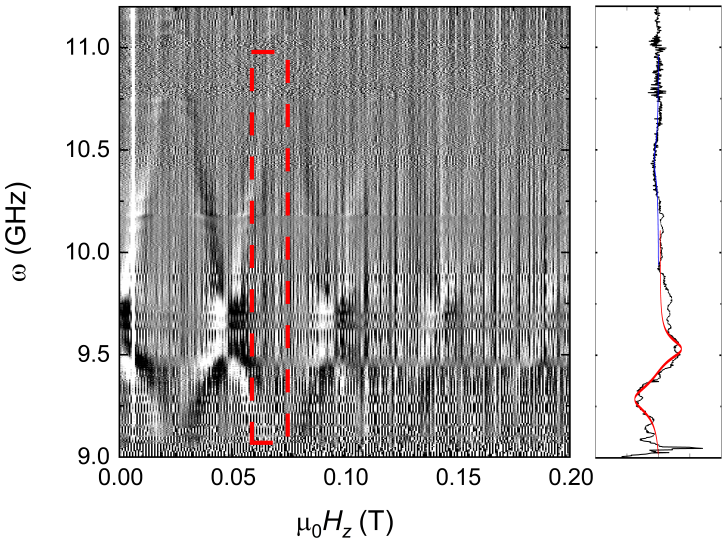

Figure 6.10: Left: 2D plot of the normalized transmission through a coplanar superconducting line coupled to a $Y_{0.8}Ho_{0.2}W_{10}$ crystal as a function of applied magnetic field H_z parallel to the anisotropy axis and frequency ω, for a temperature of 300 mK. Right: normalized transmission measured at $H_z = 69$ mT. Lines are least-square fits based on Eq. (6.12). The visibility is much higher for the transition near the clock than for the one at 10.5 GHz due to the larger overlap between initial and final wavefunctions in the former condition.

where G is the photon-induced transition rate, γ is the linewidth, which mainly reflects the intrinsic spin decay rate, and ω_s is the spin resonance frequency at the given magnetic field.

Given the strong magnetic anisotropy of HoW_{10}, the matrix elements of transverse angular momentum operators nearly vanish. The transition rate G is then approximately proportional to $|\langle\psi_1|J_z|\psi_2\rangle|^2$. Under these conditions, G monitors the overlap between the two wavefunctions. The maximum absorption observed at the clock transition therefore provides experimental evidence, independent from the spectroscopic observation of the ensuing gap, for the formation of quantum superpositions of spin-up and spin-down states.

Using this information, it is possible to perform a quantitative simulation of the transmission curves as a function of magnetic field and frequency. For this, we have used Eq. (6.12), with G given by

$$G = 2\pi g^2(\omega_s)\,|\langle\psi_1|J_z|\psi_2\rangle|^2\,[n(\omega_s)+1]\,\Delta P_{1,2} \tag{6.13}$$

where $g(\omega)$, the only fitting parameter, is a spin-photon coupling density, which depends on the mode density in the transmission line and on geometrical factors (mainly the location of all spins with respect to the circuit and the latter geometry), $n(\omega_s) = [\exp(\hbar\omega_s/k_BT)-1]^{-1}$ is the bosonic occupation number, and $\Delta P_{1,2}$ is the thermal population difference between the spin states involved in the transition.

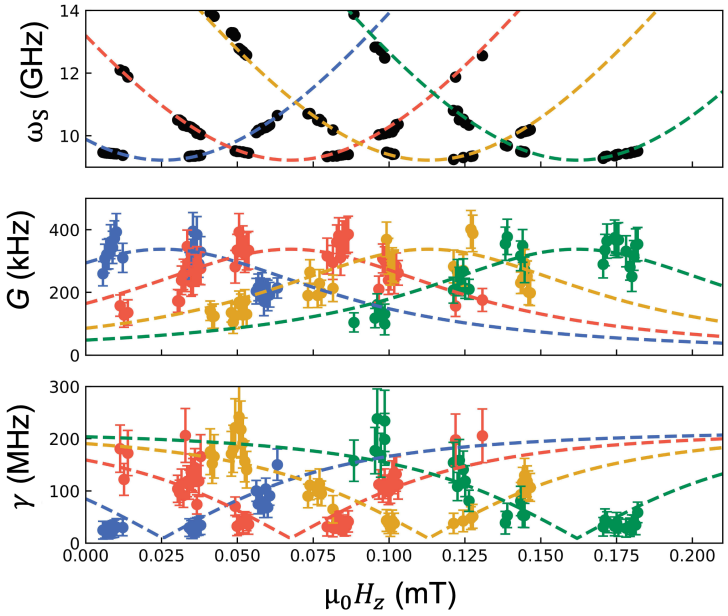

Figure 6.11: Top: Experimental resonance frequency of the different transition lines of $Y_{0.8}Ho_{0.2}W_{10}$ at 650 mK. The theoretical frequency lines are determined by the diagonalisation of Hamiltonian (6.2). Spin-clock transitions lead to four equally spaced minima as a function of magnetic field. Centre and bottom: Spin-photon coupling G and spin linewidth γ obtained from the fit of the resonance lines by using Eq. (6.12). The theoretical lines in the middle panel have been calculated using Eq. (6.13) and the matrix element $|\langle\psi_1|J_z|\psi_2\rangle|^2 = m_J^2\Delta^2/\omega_S^2$, which holds for a two-level system. The lines in the bottom panel are given by Eq. (6.14) with $\gamma_0 = 10$ MHz and $b = 6$ mT.

Using Eq. (6.12) we have been able to fit the two different transitions compared in Fig. 6.10, demonstrating that the visibility, and therefore the coupling, is maximum near a clock transition and decreases as we move away from it. Performing this analysis for the different transitions that take place in the molecule, we have been able to follow the dependence of the spin-photon coupling G and the spin linewidth γ with magnetic field, as can be shown in Fig. 6.11. Here, we can see that the coupling of the transition between two specific states is indeed maximum at the clock transition, regardless of which states they are. At the same time, the narrowing of γ near the clock transitions as the electronic spins become less sensitive to fluctuations of the

magnetic field is experimentally confirmed.[22]. This behaviour can be approximately described by the following expression:[2]

$$\gamma = \gamma_0 + b\frac{\partial \omega_S}{\partial H_z}, \tag{6.14}$$

where the second term is proportional to the effective magnetic moment, which tends to supress the dipolar broadening near a clock transition, and the first considers any other sources of broadening. The fits shown in Fig. 6.11 have been performed with $b \simeq 6$ mT and $\gamma_0 \leq 10$ MHz.

These results are very interesting, taking into account that using spin-clock transitions we are maximizing at the same the spin-photon coupling and the spin coherence time T_2,[2] parameters that are usually opposite to each other. The evolution of the spin-photon coupling with temperature will be shown in next section.

6.2.4 Temperature dependence of the spin-photon coupling

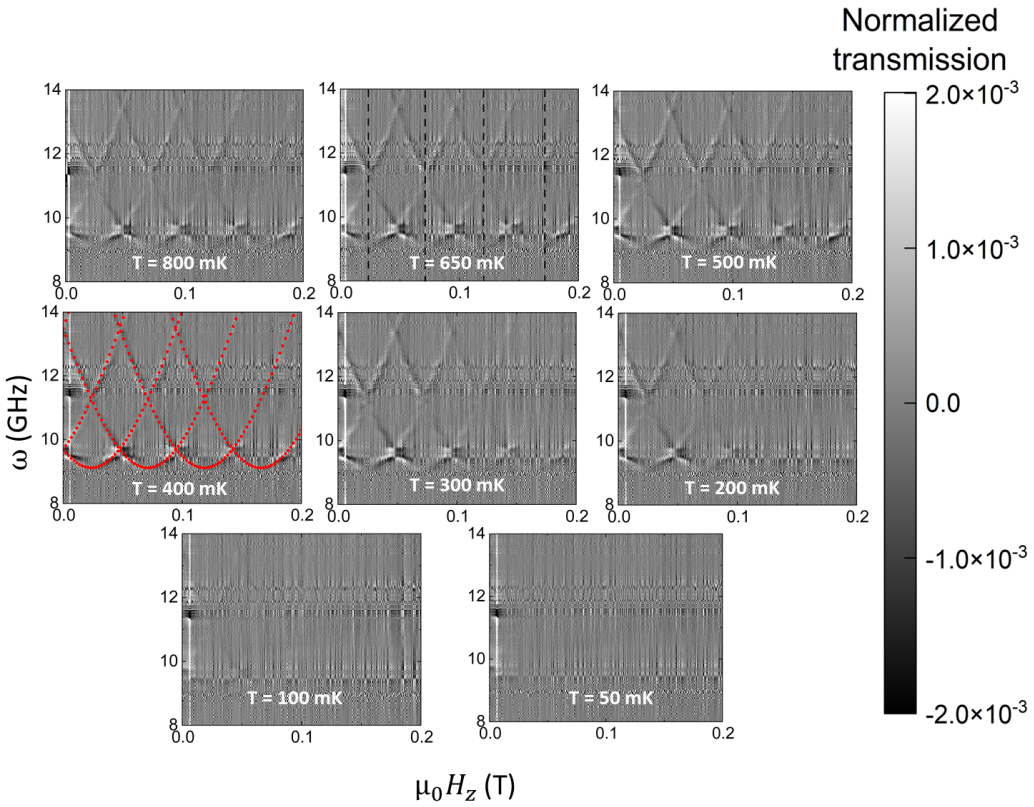

Figure 6.12: 2D plots of the normalized transmission through a coplanar superconducting line coupled to a $Y_{0.8}Ho_{0.2}W_{10}$ crystal, as shown in Fig. 6.9(a), as a function of H_z and ω, for temperatures ranging from 50 mK to 800 mK. Red dotted lines in the experimental plot of 400 mK are the positions of the different transitions determined with the spin Hamiltonian (6.2). Black dotted lines in the 650 mK plot are the positions of the four clock transitions in the sample.

The temperature dependence study of the coupling between the molecules on a $Y_{0.8}Ho_{0.2}W_{10}$ and the superconducting circuit was performed by repeating the previous measurements for several temperatures, from 50 mK to 800 mK. Figure 6.12 shows 2D transmission plots measured at different temperatures, scanning the whole experimental range. The 2D plots show that the resonant lines tend to disappear at lower temperatures because of the decrease in population of the involved spin states. For very low temperatures (< 50 mK), the resonant lines are not visible, while they start to appear while increasing temperature. The spin-clock transition at

lower field is the first to appear in the transmission plots, and the rest are visible in order as temperature is increased. The first spin-clock transition is the one that reaches the maximum visibility first, after which it slowly decreases. The remaining spin-clock transitions reach their maximum visibility in ascending field order while increasing temperature. This behaviour agrees with the observed in the simulated 2D transmission plots shown in Fig. 6.13, performed using Hamiltonian (6.2) and Eq. (6.13). This effect can be understood by taking into account that the spin states involved are both excited states and the effect that the difference in their thermal populations has into the coupling.

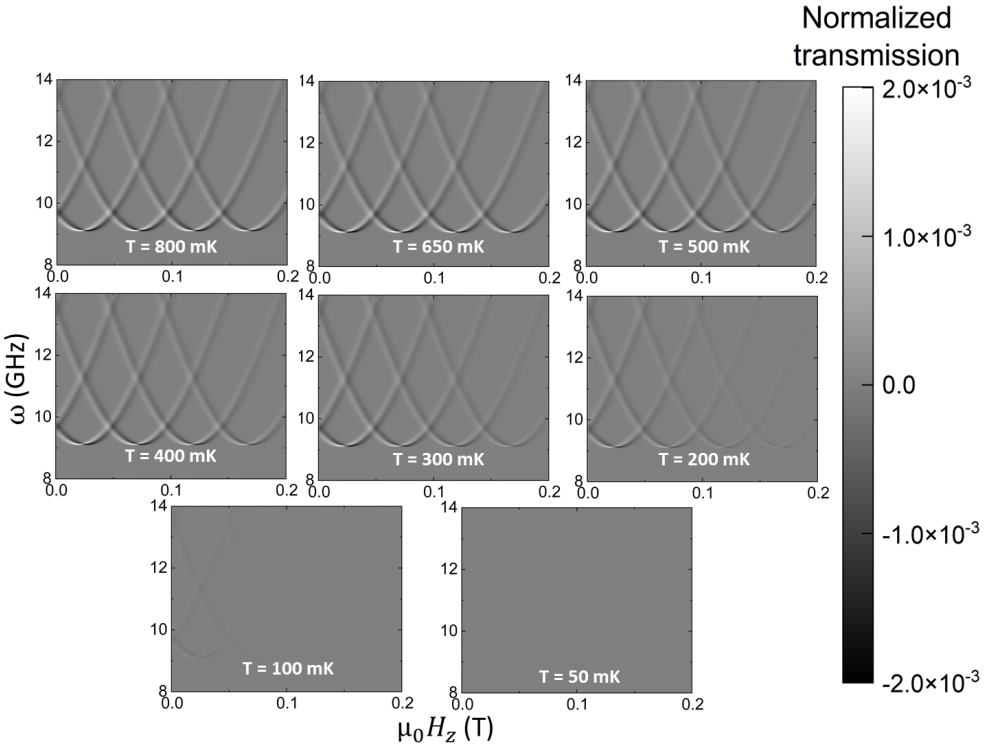

Figure 6.13: 2D plots of the normalized transmission through a coplanar superconducting line coupled to a $Y_{0.8}Ho_{0.2}W_{10}$ crystal, under the same experimental conditions than the previous measurements, calculated with the Hamiltonian (6.2) for different temperatures. A gaussian distribution of dipolar fields with a width $\sigma = 2.7$ mT has been considered.

Finally, the evolution of the spin-photon coupling with temperature for the second clock transition is shown in Fig. 6.14(a). This coupling presents a maximum at a field ~ 60 mT for every measured temperature, where the overlap between the two involved wavefunctions is maximum. Comparing the curves for every temperature, it can be seen that this maximum coupling presents its highest value for a temperature of 400 mK, when the difference in the thermal populations of the two levels involved is maximum, as can be seen in Fig. 6.14(b). The observed and simulated field dependence of the spin-photon couplings shown in Fig. 6.14 do not match very well, due possibly to the difficulties found while fitting the transmission peaks in the noisy signals. Nevertheless, the overall behaviour of the spin-photon coupling with temperature is well accounted for, in particular, the maximum in the coupling of every spin-clock transition at different temperatures and the maximum temperature for the different spin-clock transitions.

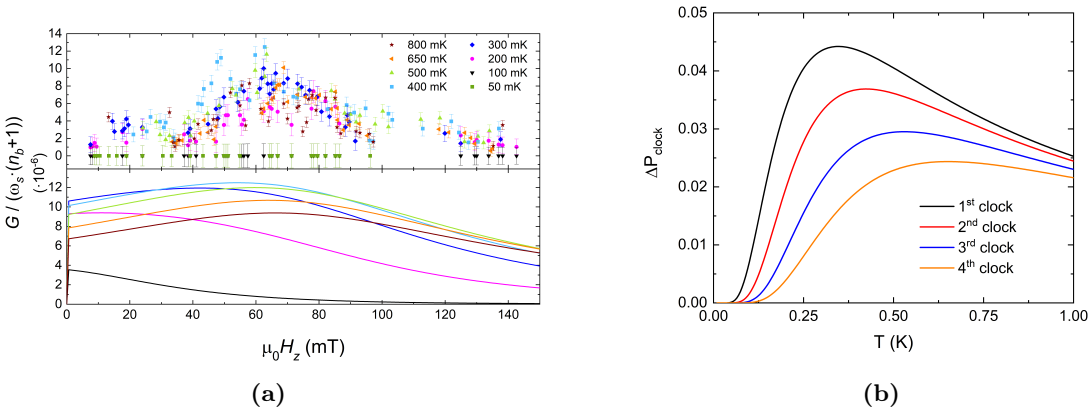

(a) **(b)**

Figure 6.14: (a) Comparison between the spin-photon coupling measured for the second clock transition as a function of magnetic field for different temperatures (top) and simulation of these couplings (bottom). At 100 mK the second clock transition was not visible. (b) Simulation of the thermal population difference calculated for all the clock transitions. Every clock transition shows a maximum in this parameter at a certain temperature. In the case of the second clock transition, this maximum is at ~ 400 mK.

6.2.5 Conclusions

Because of its strong uniaxial anisotropy and the presence of fourth-order transverse anisotropy terms, HoW_{10} is found to have a quantum tunneling gap of 9.1 GHz between superpositions of the $m_J = \pm 4$ electronic spin states. Microwave transmission measurements show that the positions of the spin-clock transitions that take place in this molecule are only sensitive to the applied magnetic field parallel to the molecular anisotropy axis, allowing us to accurately determine the orientation of the molecule in the crystal. Through broadband spectroscopy measurements performed for different temperatures, we have found that the spin-photon coupling is highly increased at spin-clock transitions due to the maximum overlap between the spin states, and the evolution of this coupling with temperature depends mainly on the difference in thermal populations between the involved states, as expected. This stronger coupling to photons in the spin-clock transitions is accompanied, as observed experimentally, by a minimum decoherence, due to an efficient shielding from fluctuating magnetic fields.[2] These results suggest that spin-clock transitions enable attaining coherent coupling in what would otherwise be far from optimum conditions: concentrated spin systems, thus strong dipole-dipole interactions, high temperature, and thus very small spin polarization, etc. Coupling spin clock states to superconducting circuits therefore opens a promising route towards achieving fault-tolerant scalability with chemically engineered spin qubits.

However, the results tell us that HoW_{10} would not be a good qubit candidate due to the nature of its spin-clock transitions. They take place between excited states, making it impossible to correctly initialize the qubit in the $|0\rangle$ state by simply cooling it. Furthermore, the remaining transitions cannot be exploited due to their harmonicity, so we are limited to the spin-clock transitions. In the following section we will explore a system in which these problems are avoided.

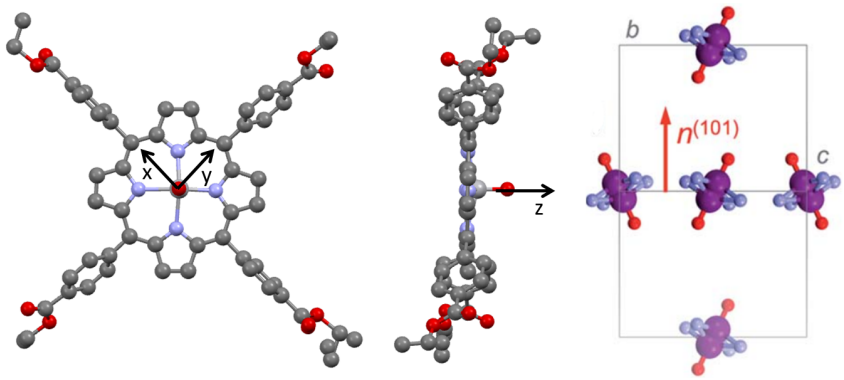

Figure 6.15: (Left) top and (centre) side views of the $\mathbf{1^{VO}}$ molecule, showing the vanadyl group at its centre. (Right) View along the 101 plane of one $\mathbf{1^{VO}}$ unit cell, showing the two different orientations in the crystal. The average V=O orientation corresponds to the normal to the 101 plane.

6.3 Coupling to a vanadyl porphyrin 1^{VO}

This section will be focused on the vanadyl porphyrin, or $\mathbf{1^{VO}}$, shown in Fig. 6.15, which provides a different realization of spin-clock transitions. This molecule basically consists of a vanadyl group at the centre of a porphyrin molecule. The vanadyl group shows a ground state with $\mathbf{S} = 1/2$. Its interaction with the crystal field generated by the molecule effectively quenches its orbital angular momentum $\mathbf{L}$, showing $L_{eff} = 0$.[23] Knowing that the only stable isotope of vanadium is ^{51}V, the nuclear spin of the molecule is $\mathbf{I} = 7/2$, according to the nuclear shell model. This nuclear spin is coupled to the electronic one by the hyperfine interaction. This term, together with the electronic Zeeman effect, make the Hamiltonian necessary to describe the molecule as follows:

$$\mathcal{H} = \mu_B \vec{H} \cdot \hat{g}_S \cdot \mathbf{S} + \mathbf{S}\hat{A}\mathbf{I}. \tag{6.15}$$

This Hamiltonian produces 16 energy levels separated, for high magnetic fields, in two octets with different electronic spin projections. Under these conditions, each level is characterized by well defined electronic and nuclear spin projections. By contrast, for low magnetic fields the eigenstates of the spin Hamiltonian (6.15) approach states of the total angular momentum $\mathbf{F} = \mathbf{S} + \mathbf{I}$, with $\mathbf{F} = 4$ and 3. Due to this, electronic and nuclear spins become entangled, so the previous separation in electronic and nuclear spin projections is not valid in the low field region.

Here, we will first characterize the spin states and level structure of this system, and then we will consider the possibility of enconding a properly addressable spin qudit in it. Finally, we will explore the coupling of these states to cavity photons near spin-clock transitions generated by the action of the anisotropic hyperfine interaction.

6.3.1 Broadband spectroscopy: determination of Hamiltonian parameters

An initial characterization of pure $\mathbf{1^{VO}}$ samples was done by means of broadband spectroscopy measurements. With these experiments, the components of the tensors describing the Zeeman and hyperfine interactions in Eq. (6.15) were determined. As for HoW_{10}, a fully concentrated monocrystalline $\mathbf{1^{VO}}$ sample was deposited on top of a CPW (see Fig. 6.16) and introduced in a 90 L liquid helium dewar containing a superconducting vector magnet. This system was connected to a vector network analyser for measuring the microwave transmission through the system.

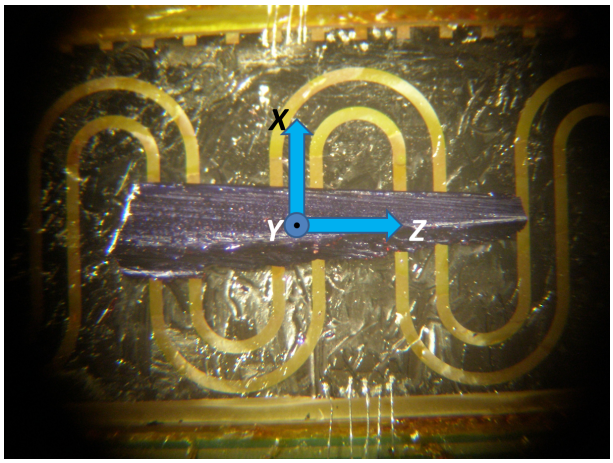

Figure 6.16: Optical microscopy image of the on-chip superconducting waveguide hosting the $\mathbf{1^{VO}}$ single crystal used for the experiments at 4.2 K. Arrows marked with XYZ define the reference frame of the laboratory.

The microwave transmission was measured for the three main orientations of the laboratory frame: X, Y and Z axes shown in Fig. 6.16. Transmission data are shown in Fig. 6.17. They show, for magnetic fields above 0.1 T, eight lines corresponding to the different allowed transitions between states with different electronic spin projection but the same nuclear spin state. Here, the hyperfine interaction acts as a bias field that shifts resonances associated with different nuclear spin projections, obtaining eight almost equidistant resonance lines. Using these data, the components of $\hat{g}$ and $\hat{A}$ can be approximately extracted from the slope of the resonant lines and the distance between them, respectively. Performing this analysis for the three studied orientations, the components of these tensors in the laboratory frame shown in Table 6.3 have been obtained.

$\mathbf{A_{XX}}$ (MHz)	$\mathbf{A_{YY}}$ (MHz)	$\mathbf{A_{ZZ}}$ (MHz)	$\mathbf{g_{XX}}$	$\mathbf{g_{YY}}$	$\mathbf{g_{ZZ}}$
213.57	425.24	254.31	1.99	1.97	1.99

Table 6.3: Hamiltonian parameters referred to the laboratory frame, determined from the experimental transmission plots shown in Fig. 6.17.

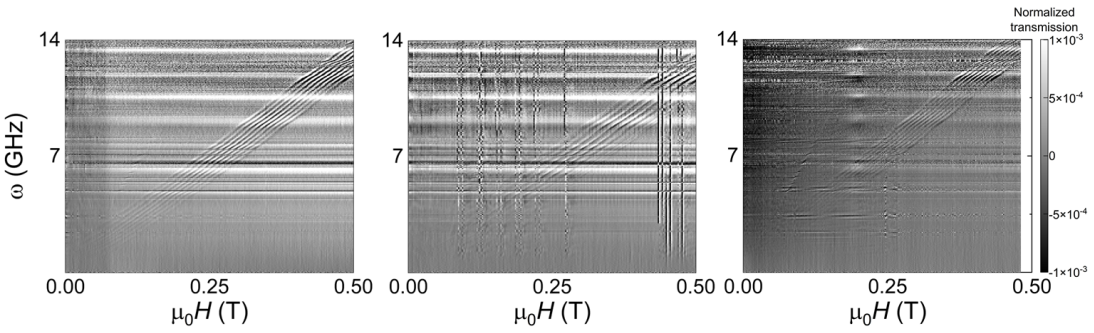

Figure 6.17: 2D plots of the normalized transmission measured on a transmission line coupled to a single crystal of $\mathbf{1^{VO}}$ at a temperature of 4.2 K, for magnetic field applied parallel to the X (left), Y (centre) and Z (right) laboratory axes.

Using the parameters shown in Table 6.3, we have simulated the 2D transmission plots, obtaining those shown in Fig. 6.18 for the three main directions of the laboratory frame. Our simulations agree with the experimental data at high field. At low magnetic field, resonance lines no longer follow a linear dependence with applied field, but this cannot be confirmed with the transmission data shown in Fig. 6.17. This region will be experimentally studied in the following sections at lower temperatures, in order to increase the visibility of the absorption lines.

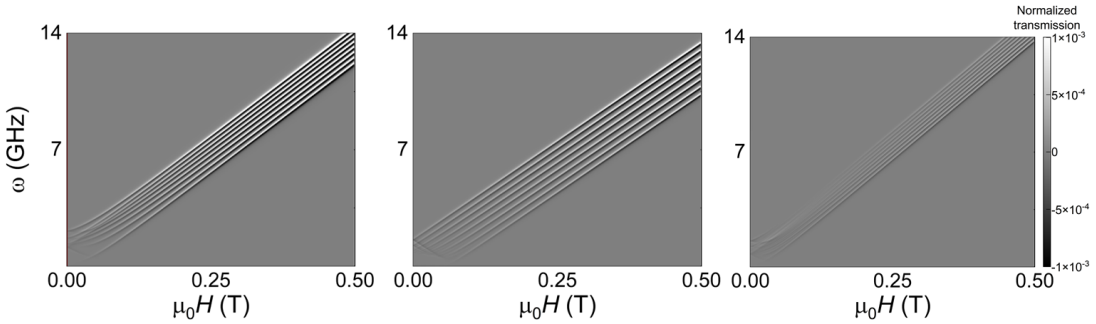

Figure 6.18: 2D plots of the normalized transmission of a transmission line coupled to a single crystal of $\mathbf{1^{VO}}$ at a temperature of 4.2 K, calculated using the Hamiltonian (6.15) with the spin parameters shown in Table 6.3, referred to the laboratory reference frame. The applied magnetic field was considered parallel to the X (left), Y (centre) and Z (right) laboratory axes.

From the experimental transmission plots and the orientation of the $\mathbf{1^{VO}}$ molecules in the crystal, we can determine the Hamiltonian parameters g_{ii} and A_{ii}, referred to the molecular frame. Using the software Mercury[24] we have calculated the angles between the z molecular axis, shown in Fig. 6.15, and the laboratory axes X, Y and Z plotted in Fig. 6.16. The values we find are the following:

$\theta_{\mathbf{X}}$ (°)	$\theta_{\mathbf{Y}}$ (°)	$\theta_{\mathbf{Z}}$ (°)
73.17	28.23	64.67

Table 6.4: Angles between the z molecular axis and the X, Y and Z laboratory axes, where the magnetic field has been applied.

The values of $\hat{g}$ and $\hat{A}$ tensors referred to an arbitrary axis are related to those of the molecular frame by the following equations:[16]

$$g_{\hat{n}} = \sqrt{g_{xx}^2 n_x^2 + g_{yy}^2 n_y^2 + g_{zz}^2 n_z^2} \tag{6.16}$$

$$A_{\hat{n}} = \sqrt{\frac{A_{xx}^2 g_{xx}^2 n_x^2 + A_{yy}^2 g_{yy}^2 n_y^2 + A_{zz}^2 g_{zz}^2 n_z^2}{g_{\hat{n}}^2}} \tag{6.17}$$

$$\hat{n} = \begin{pmatrix} \sin\theta\cos\varphi \\ \sin\theta\sin\varphi \\ \cos\theta \end{pmatrix} \tag{6.18}$$

where $\hat{n}$ is the direction of the applied magnetic field and θ and φ are the spherical coordinates of the unit vector of this field in the molecular frame. Combining these equations with the angles of Table 6.4, and taking into account that the symmetry of the molecule imposes $g_{xx} = g_{yy}$, we

have calculated the values of g_{ii} and A_{ii} parameters referred to the molecular axes:

$$g_{zz} = \sqrt{\frac{g_{ZZ}^2 - \frac{g_{XX}^2 \sin^2\theta_Z}{\sin^2\theta_X}}{\cos^2\theta_Z - \text{cotan}^2\theta_X \sin^2\theta_Z}} = 1.963 \tag{6.19}$$

$$g_{xx} = g_{yy} = \sqrt{\frac{g_{XX}^2 - g_{zz}^2 \cos^2\theta_X}{\sin^2\theta_X}} = 1.99 \tag{6.20}$$

$$A_{zz} = \sqrt{\frac{A_{ZZ}^2 g_{ZZ}^2 \sin^2\theta_X - g_{XX}^2 A_{XX}^2 \sin^2\theta_Z}{g_{zz}^2 \left(\cos^2\theta_Z \sin^2\theta_X - \cos^2\theta_X \sin^2\theta_Z\right)}} = 475 \text{ MHz} \tag{6.21}$$

$$A_{xx} = A_{yy} = \sqrt{\frac{g_{XX}^2 A_{XX}^2 - A_{zz}^2 g_{zz}^2 \cos^2\theta_X}{g_{xx}^2 \sin^2\theta_X}} = 172 \text{ MHz} \tag{6.22}$$

In these experiments only one molecular orientation has been considered. As will be shown with the EPR measurements, the crystal shows three perpendicular directions for which the two orientations of the molecules shown in Fig. 6.15 are magnetically equivalent. Applying the magnetic field along any of these high simmetry directions allows us to deal with the obtained results simplifying the system to a single molecular orientation, characterised by the eight transition lines shown in Fig. 6.17.

6.3.2 Physical characterization: specific heat and magnetic susceptibility

Information about the evolution of the gap between electronic spin up and down states, as well as preliminary information about the spin-lattice relaxation time T_1 was obtained by means of heat capacity and micro-Hall magnetometry measurements (see section 2.2.1 for experimental details of these techniques).

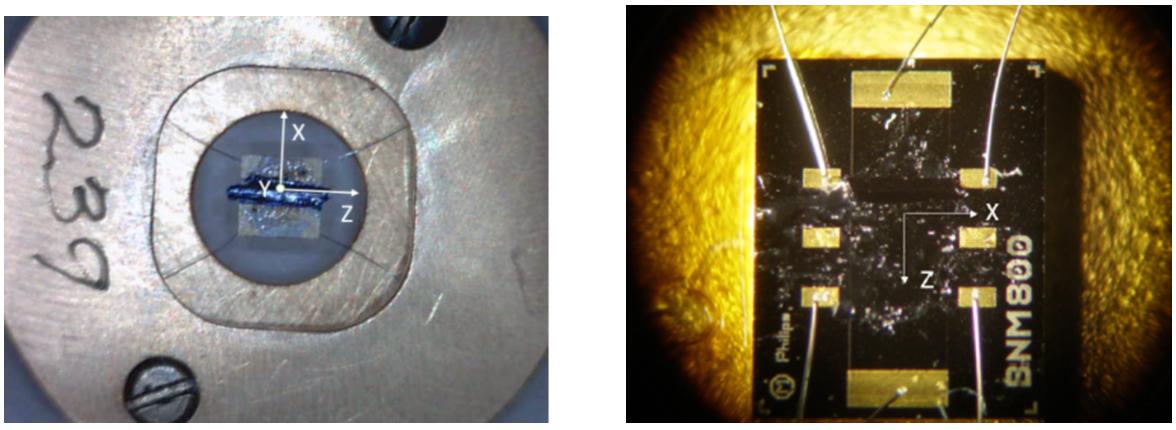

(a) **(b)**

Figure 6.19: Optical microscopy images of (a) the calorimeter used for specific heat measurements, and (b) the micro-Hall magnetometer used for magnetic susceptibility experiments, hosting a $\mathbf{1^{VO}}$ crystal. In both experiments the magnetic field was applied parallel to the Z laboratory axis.

Specific heat is sensitive to the structure of magnetic energy levels. In these experiments, a pure $\mathbf{1^{VO}}$ crystal was deposited on top of a calorimeter together with Apiezon N grease, and this device was introduced in the PPMS system (Fig. 6.19(a)). Here, heat capacity curves were

measured for a temperature range between 0.35 K and 100 K, and applied magnetic fields from 0 to 7 T. The magnetic and lattice contributions to the specific heat were calculated using Eqs. (6.6) and (6.7), being necessary in this case to use one term for acoustic phonons and two terms for optical ones. The measured data, together with the calculations and a zoom of the magnetic contribution to specific heat, are shown in Fig. 6.20. In this case, the fitting parameters of the lattice contribution are $\theta_{ac} = 29$ K, $\theta_{op,1} = 80$ K, $\theta_{op,2} = 280$ K, $n_{op,1} = 15$ and $n_{op,2} = 62$.

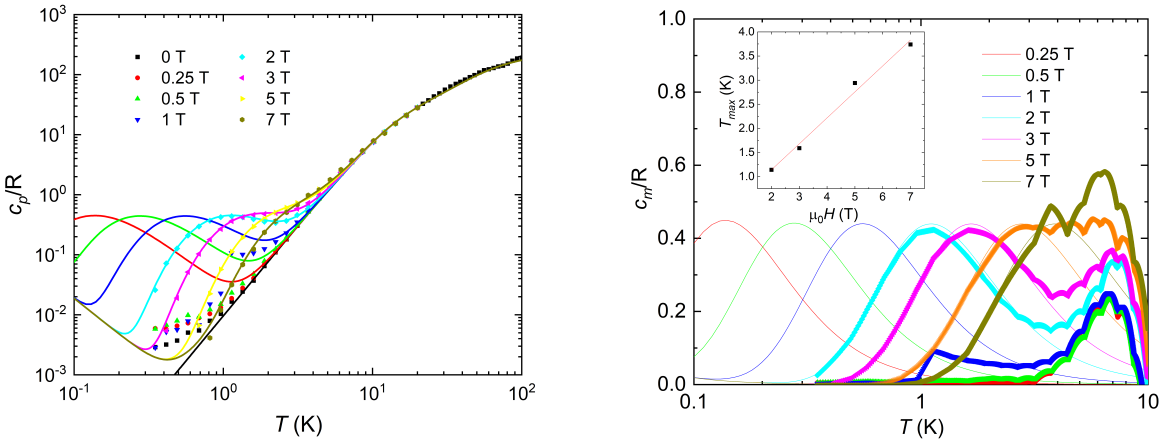

(a) **(b)**

Figure 6.20: (a) Molar specific heat of a crystal of $\mathbf{1^{VO}}$ measured between 0.35 K and 100 K, and at several magnetic fields, together with (b) a zoom of the Schottky anomalies that appear in the system. Inset: variation of the position of these peaks with magnetic field. The linear dependence corresponds to the linear evolution of the energy levels of the molecule.

Besides the lattice contribution, the zero-field c_P/R curve shows only a low temperature tail, likely associated with the hyperfine splitting of the $\mathbf{1^{VO}}$ nuclear spin levels. This splitting is expected to give rise to a Schottky anomaly centered at a temperature of ~ 5 mK, much lower than the achievable temperature of our PPMS. When magnetic field is applied, the Schottky peaks corresponding to the Zeeman splitting between electronic spin up and spin down states can be observed for fields above 2 T. The positions of these peaks follow a linear dependence (Fig. 6.20(b), inset), with slope $m = 0.538 \pm 0.041$ K/T which corresponds to a g_{ZZ} between 1.9 and 2, in good agreement with the values obtained by broadband spectroscopy.

Regarding the c_P/R curves measured for magnetic fields below 2 T (0.25, 0.5 and 1 T), the expected peak is either not detected or reduced with respect to that predicted by the simulations. We attribute this effect to a deviation of the spins from thermal equilibrium. In order to check this possibility, we carried out measurements at 1 T for different experimental times (Fig. 6.21). It follows that phonon-induced relaxation processes become slower than 0.1 s at low temperature, but faster than 4.5 s. This tells us that the spin-lattice relaxation time of $\mathbf{1^{VO}}$ reaches values of a few seconds at sufficiently low temperatures. This phenomenon is confirmed by micro-Hall magnetometry measurements described next.

Magnetization measurements were performed for obtaining preliminary information about the relaxation time T_1 of the $\mathbf{1^{VO}}$ molecule. In these experiments, a pure $\mathbf{1^{VO}}$ crystal was deposited on top of a micro-Hall magnetometer, with the long crystallographic axis parallel to the X laboratory axis, thus perpendicular to the Z laboratory axis and the applied magnetic field (see Fig. 6.19(b)). The sample was then introduced in the PPMS system, where the evolution of magnetization as a function of magnetic field and time was measured.

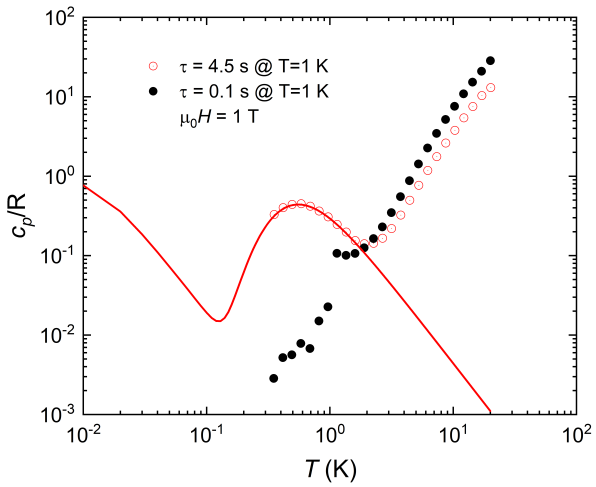

Figure 6.21: Specific heat of $\mathbf{1^{VO}}$ measured at a magnetic field of 1 T for two different experimental times. In the case with a shorter measurement time at 1 K, the spins were unable to attain equilibrium with the crystal lattice and the specific heat could not reach its thermal equilibrium value, shown by the red solid line.

A complete knowledge of the evolution of T_1 is very important for several reasons. First, because T_1 is the ultimate limitation of T_2 when all other sources of decoherence are suppressed. Secondly, T_1 establishes the speed at which the spins decay to the ground state at very low temperature, *i.e.* it determines the speed of the initialization process for the molecular spin qubits. Information of T_1 for several fields and fixed temperature was obtained by means of time dependent magnetization measurements, as will be shown below.

The curves of magnetization against magnetic field for several temperatures are shown in Fig. 6.22. These measurements were performed for a field range between −3.5 T and 3.5 T, with a sweep rate of 1 T/min, and temperatures between 0.4 K and 1 K. The hysteresis loops obtained here provide another evidence of the slow spin dynamics. For temperatures below 1 K, T_1 becomes long enough with respect to the field sweep rate of 1 T/min, so that the system shows magnetic hysteresis loops despite the absence of any activation barrier for the spin reversal.

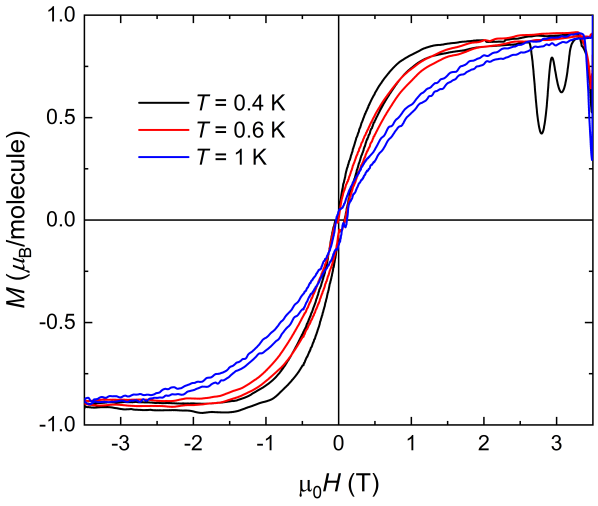

Figure 6.22: Magnetization hysteresis loops of a single crystal of $\mathbf{1^{VO}}$ with magnetic field perpendicular its long axis. The magnetic field sweeping rate was 1 T/min.

Values of T_1 for fixed magnetic fields and temperatures were obtained by performing time dependent magnetization measurements. In this case, a high magnetic field was applied during a certain time and then it was suddenly reduced to a fixed value. In this situation, the magnetization of the sample follows the evolution given by Eq. (6.23):

$$M(t) = M_{eq} - [M_{eq} - M(t=0)]\, e^{-t/T_1}, \tag{6.23}$$

where M_{eq} is the equilibrium magnetization of the sample for the given magnetic field and $M(t=0)$ is the initial magnetization.

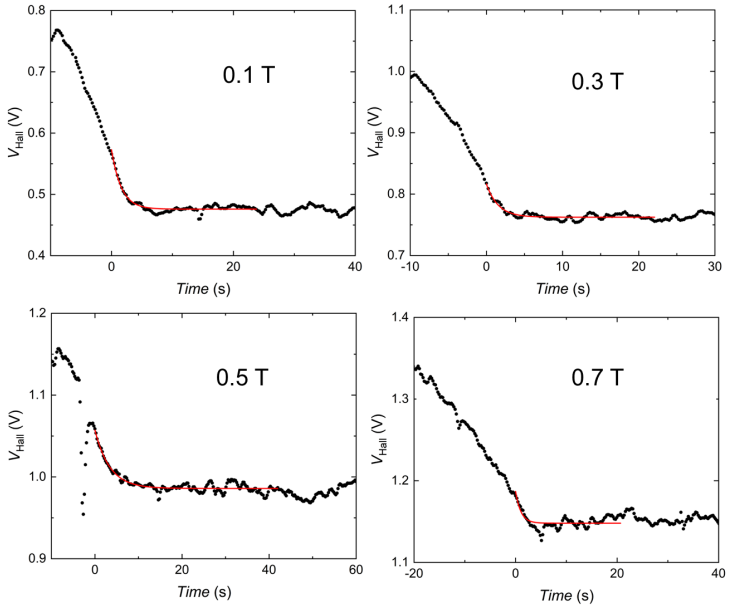

Figure 6.23: Time dependent magnetization measurements performed for magnetic fields of 0.1, 0.3, 0.5 and 0.7 T. The red solid lines are the exponential fits performed using Eq. (6.23).

The magnetization curves obtained for a temperature of 0.4 K are shown in Fig. 6.23. The instant $t = 0$ was determined when the magnetic field, which was monitored in parallel to the μ-Hall voltage, reached its final value (see Fig. 2.6). By performing a fit of these curves using Eq. (6.23), we obtained the following values for T_1:

$\mu_0\mathbf{H}$ (T)	0.1	0.3	0.5	0.7
$\mathbf{T_1}$ (s)	1.605 ± 0.089	1.543 ± 0.138	3.426 ± 0.181	1.047 ± 0.225

Table 6.5: Values of T_1 obtained by time dependent magnetization measurements at a temperature of 0.4 K.

The results confirm that T_1 reaches values of seconds for low temperatures. The evolution of these values with temperature and field will be studied more precisely by time dependent EPR measurements shown in the next section.

6.3.3 EPR experiments: spin coherence and relaxation times

The dynamic response of $\mathbf{1^{VO}}$ while varying temperature was also investigated by means of time dependent EPR measurements (see section 2.2.3). The experiments were performed by Pablo

Alonso and Olivier Roubeau. In this section, the main results of these pulsed EPR measurements will be described.

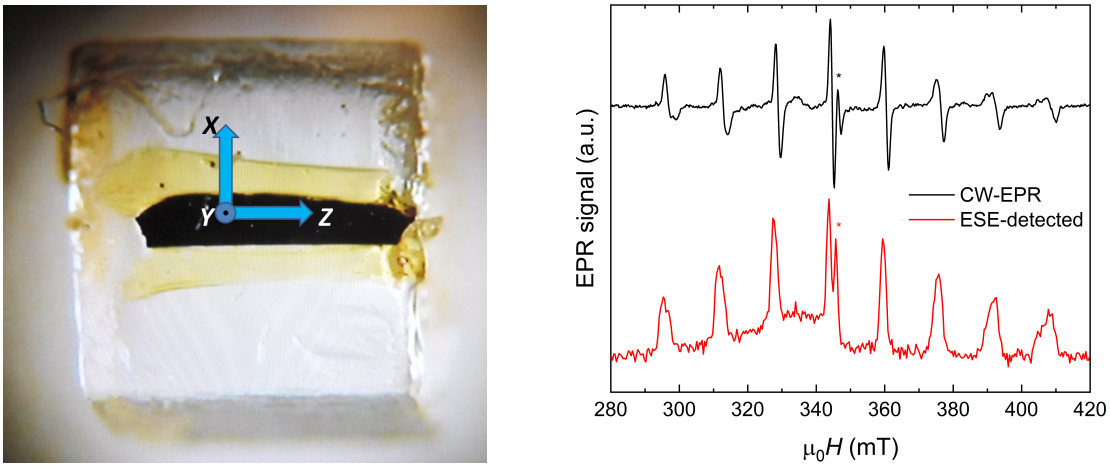

(a) (b)

Figure 6.24: (a) Optical microscopy image of a $\mathbf{1}^{\mathbf{VO}}$ crystal mounted on a $2 \times 2 \times 2$ mm^3 cube-shaped holder with a little GE varnish, together with the XYZ laboratory frame. (b) X-band CW (room temperature) and 2 pulse-ESE-detected (6 K, $\tau = 200$ ns) EPR spectra of $\mathbf{1}^{\mathbf{VO}}_{\mathbf{3\%}}$ with the magnetic field along the y_c axis, for which the splitting between the spin energy levels is maximum. This axis is located on the XY plane and forms an angle of 31° with the Y axis. Stars indicate an isotropic signal at $g = 2.01$ adscribed to a Ti(III) impurity.

CW and 2 pulse (2p)-ESE-detected EPR measurements were done for confirming the Hamiltonian parameters and molecular orientation obtained by broadband spectroscopy. A magnetically diluted single crystal, $\mathbf{1}^{\mathbf{VO}}_{\mathbf{3\%}}$, was mounted on a $2 \times 2 \times 2$ mm^3 cube-shaped holder, and the sample was introduced into the EPR spectrometer (see Fig. 6.24(a)). The CW-EPR and 2p-ESE-EPR spectra obtained at room temperature and 6 K respectively are shown in Fig. 6.24(b). These experiments were done in the X-band, using a microwave cavity with a resonance frequency of 9.848 GHz. The sequence of pulses used for the 2p-ESE-detected EPR measurement was the 2p-spin-echo-sequence explained in section 2.2.3, in this case keeping the time τ between pulses fixed to 200 ns while the magnetic field was changed. The obtained espectra show eight resonant signals corresponding to the eight electronic transitions that take place in each $\mathbf{1}^{\mathbf{VO}}$ molecule at high magnetic field, as shown in section 6.3.1. Both EPR spectra were correctly reproduced using the spin Hamiltonian (6.15) with the parameters obtained in section 6.3.1, thus validating them.

Temperature dependences of the spin relaxation time T_1 and the spin coherence time T_2 were studied by means of pulsed EPR measurements. T_1 was studied by ESE inversion recovery experiments (a scheme of this sequence is shown in Fig. 2.10) at X-band frequencies of a frozen solution $\mathbf{1}^{\mathbf{VO}}_{\mathbf{sol}}$. These experiments were performed for temperatures ranging from 6 K to 120 K and an applied magnetic field of 346.6 mT, corresponding to the most intense resonance line in the CW and ESE-detected spectra. The measurement was repeated for several delay times, t_d, between the initial π inversion pulse and the second one, and a fixed time $\tau = 200$ ns between this $\pi/2$ pulse and the final π pulse. The obtained intensity curves were fitted considering a stretched exponential evolution, obtaining the temperature dependence of T_1 shown in Fig. 6.25. We can see that T_1 decreases continuously while increasing temperature, going from about 50 ms at 6 K to 20 μs at 120 K. This dependence tell us that, at very low temperatures, T_1 could reach values of several seconds as was indeed confirmed by μ-Hall and heat capacity measurements.

These relaxation times are specially long, for example about two times longer than those reported recently as the longest for vanadyl-based compounds.[25] These high values of T_1 ensure that it will not limit the coherence time T_2 at low temperature, being T_1 the ultimate limitation of T_2 when all other decoherence sources are suppressed.

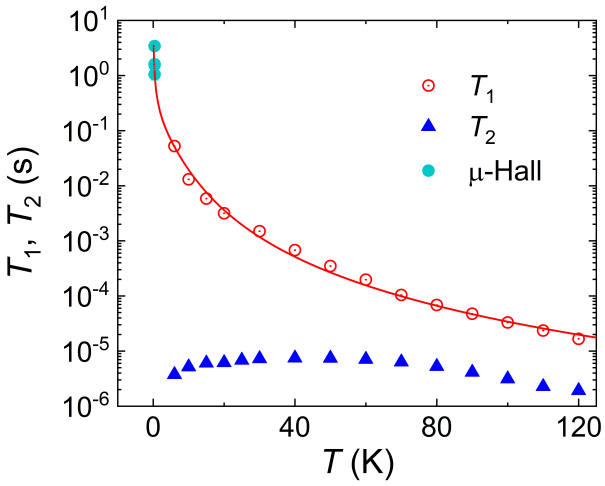

Figure 6.25: Temperature dependence of the relaxation time T_1 and of the coherence time T_2 of the fourth spin transition in $\mathbf{1}^{\mathbf{VO}}_{\mathbf{sol}}$, corresponding to a field of 346.6 mT in the studied frequency region, together with a fit of T_1 data using Eq. (6.24). The values of T_1 obtained by time dependent μ-Hall magnetometry at a temperature of 0.4 K are also included, agreeing with the same model.

For explaining the temperature dependence of T_1 in this molecule, where the transitions are produced between two states, we have considered two relaxation processes: direct and Raman processes.[16] The fitting curve of Fig. 6.25 has been calculated using the following expression:

$$\frac{1}{T_1} = aT + cT^m, \tag{6.24}$$

considering $a = 2.2 \pm 0.2$ s^{-1}K^{-1}, $c = 0.029 \pm 0.003$ s^{-1}K^{-3} and $m = 3$. This result tells us that the direct process is dominant at low temperatures, where the phonon density is lower, while Raman processes are already effective in this region and then dominate the temperature dependence of T_1 at increasing temperatures.

The coherence time T_2 was studied by a 2p-spin-echo sequence at X-band, explained in section 2.2.3, for the frozen solution $\mathbf{1}^{\mathbf{VO}}_{\mathbf{sol}}$ and a diluted single crystal $\mathbf{1}^{\mathbf{VO}}_{\mathbf{3\%}}$. The temperature range was the same that for studying T_1, from 6 K to 120 K. In the case of the frozen solution $\mathbf{1}^{\mathbf{VO}}_{\mathbf{sol}}$, a magnetic field of 346.6 mT was applied, corresponding to the same transition as previously, while 5 different transitions were studied for the single crystal $\mathbf{1}^{\mathbf{VO}}_{\mathbf{3\%}}$. In this case, the magnetic field was applied along the y_c axis, for which the energy splitting is maximum. The intensity curves used for the determination of T_2 were obtained as a function of the time τ between the initial $\pi/2$ pulse and the final π pulse. After fitting the echo intensity decay with a stretched exponential, the temperature dependence of T_2 shown in Fig. 6.25 for the fourth spin transition was finally obtained. The results show that T_2 increases from 3.8 ± 0.2 μs at 6 K to a plateau at 7 μs from 25 K to 60 K. After this, it slowly decreases down to 1.9 ± 0.2 μs at 120 K due to a parallel decrease of T_1, only one order of magnitude higher than T_2 in this region. These values compare well with those found for other V^{IV} molecular spin qubits in frozen solution,[25] being the $\mathbf{1}^{\mathbf{VO}}$ molecule a good qubit candidate, especially taking into account that the solvent used during these experiments was only partly deuterated.

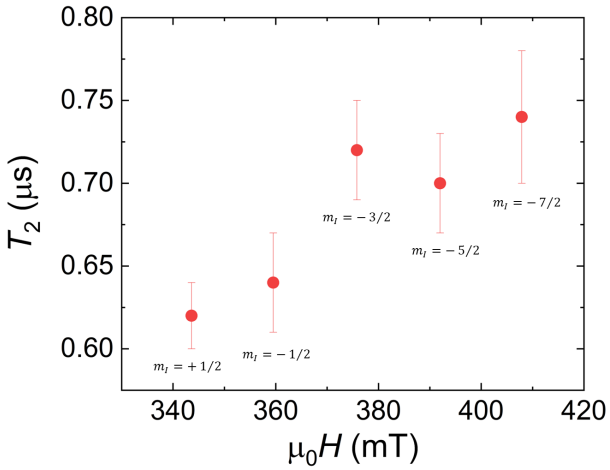

Figure 6.26: Coherence time T_2 measured for $\mathbf{1}_{\mathbf{3}\%}^{\mathbf{VO}}$ at 6 K with the magnetic field applied along the y_C crystal axis.

The results obtained in the solid state are shown in Fig. 6.26. These T_2 values are very similar between them, with a slight increase with magnetic field. This times are significantly lower than the ones seen for $\mathbf{1}_{\mathbf{sol}}^{\mathbf{VO}}$, apparently due to the still relatively high concentration of magnetic molecules of $\mathbf{1}^{\mathbf{VO}}$ in the $\mathbf{1}_{\mathbf{3}\%}^{\mathbf{VO}}$ sample. Crystals with lower $\mathbf{1}^{\mathbf{VO}}$ concentrations may therefore increase T_2 until the values measured in $\mathbf{1}_{\mathbf{sol}}^{\mathbf{VO}}$.

Considering the results obtained for spin relaxation and coherence times, T_1 and T_2, it is clear that the molecule $\mathbf{1}^{\mathbf{VO}}$ provides a good realization of a spin qubit. The obtained T_1 values seem to be the longest obtained for any vanadyl-based compound, reaching values of several seconds at very low temperature. On the other hand, T_2 values are comparable with those found for other vanadyl spin qubits in frozen solution.[25;26] These values could be even improved by further deuterating the solvent mixture. In the next section we explore how to exploit all the spin states that are present in the molecule, including those associated with the nuclear spin, therefore obtaining a qudit candidate.

6.3.4 Very low temperature experiments: electronuclear spin entanglement

The broadband spectroscopy experiments performed at 4.2 K show that the eight observed absorption lines are almost equidistant for applied magnetic fields above 0.1 T. For lower fields, our simulations suggest that resonance lines should not follow a linear dependence on magnetic field due to the existence of level crossings and anticrossings associated with the anisotropic hyperfine interaction. In order to experimentally explore this region, we extended the broadband spectroscopy experiments to very low temperatures by means of a ^{3}He-^{4}He dilution refrigerator introduced in the liquid helium cryostat that hosts the superconducting vector magnet. This refrigerator works in the same way that the cryogen-free dilution refrigerator explained in section 2.6, with the difference that it does no have a pulse tube, making it necessary to insert it in the liquid helium cryostat for achieving temperatures low enough to start the condensing cycle.

The sample and the CPW used for these experiments were the same that for the ones at 4.2 K (see Fig. 6.16). The microwave transmission was measured for several temperatures between 4.2 K and 0.175 K, the minimum temperature attainable with this refrigerator. A comparison between the transmission plots obtained for different temperatures is shown in Fig. 6.27. The increase in the visibility of the absorption lines by decreasing temperature is related to the thermal population difference between the two electronic spin states implied in each of those

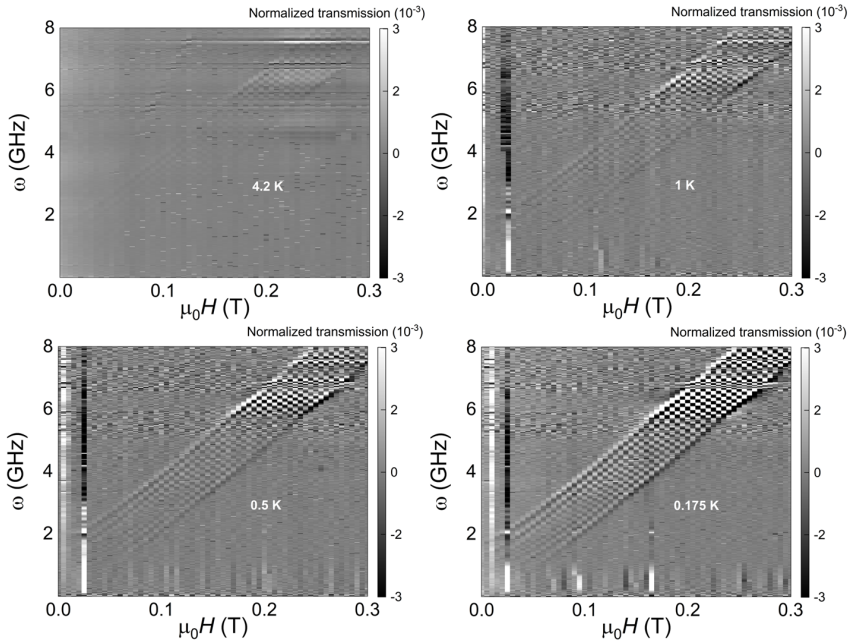

Figure 6.27: 2D plots of the normalized transmission measured on a transmission line coupled to a single crystal of $\mathbf{1^{VO}}$ at different temperatures, for magnetic fields applied parallel to the Z laboratory axis. It can be seen that the visibility of the absorption lines becomes higher when temperature decreases, due to the increase of thermal population differences between initial and final states.

transitions, which increases for lower temperatures.

Let's focus on the measurement done at 0.175 K, shown in Fig. 6.28. The data reveal that resonance lines no longer follow a linear dependence with magnetic field in the low field region ($\mu_0 H < 0.1$ T). This can be seen more clearly in Fig. 6.29, where we plot the frequency separations between nearest resonances. It can be seen that they tend to spread in frequency for low fields, while for higher fields the level scheme becomes almost harmonic.

Figure 6.28 also suggests that additional transitions become allowed in the low field regime. As with the nonlinear field dependence, this can be associated to the entanglement between electronic and nuclear spins, which allows transitions that are forbidden for higher fields when states become simple products of electronic and nuclear spin projections. The connection between electronuclear spin entanglement and the transition rates is shown in Fig. 6.30, where a magnetic field parallel to the molecular anisotropy axis z has been considered for simplicity. In this situation, the wavefunctions of states 7 and 9 (labeled from 0 to 15) at 48 mT are the following:

$$|\Psi_7\rangle\,(48\,\mathrm{mT}) \simeq \frac{1}{\sqrt{2}}\left(|+1/2;\,-7/2\rangle - |-1/2;\,-5/2\rangle\right) \tag{6.25}$$

$$|\Psi_9\rangle\,(48\,\mathrm{mT}) \simeq \frac{1}{\sqrt{2}}\left(-|+1/2;\,-7/2\rangle - |-1/2;\,-5/2\rangle\right), \tag{6.26}$$

that show a maximum entanglement between the electronic and the nuclear spins, while the situation at 300 mT changes to:

$$|\Psi_7\rangle\,(300\,\mathrm{mT}) \simeq |-1/2;\,-7/2\rangle \tag{6.27}$$

$$|\Psi_9\rangle\,(300\,\mathrm{mT}) \simeq |+1/2;\,-5/2\rangle \tag{6.28}$$

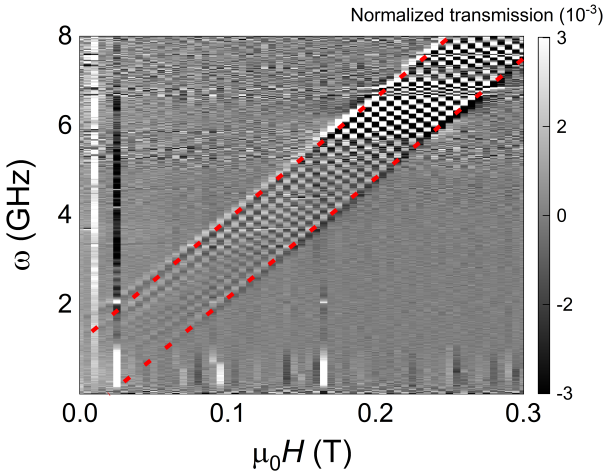

Figure 6.28: 2D plot of the normalized transmission through a CPW coupled to a single crystal of $\mathbf{1^{VO}}$ at a temperature of 0.175 K, for magnetic field applied parallel to the Z laboratory axis. Absorption lines no longer follow a linear dependence, indicated by the thick dashed lines, in this low field region.

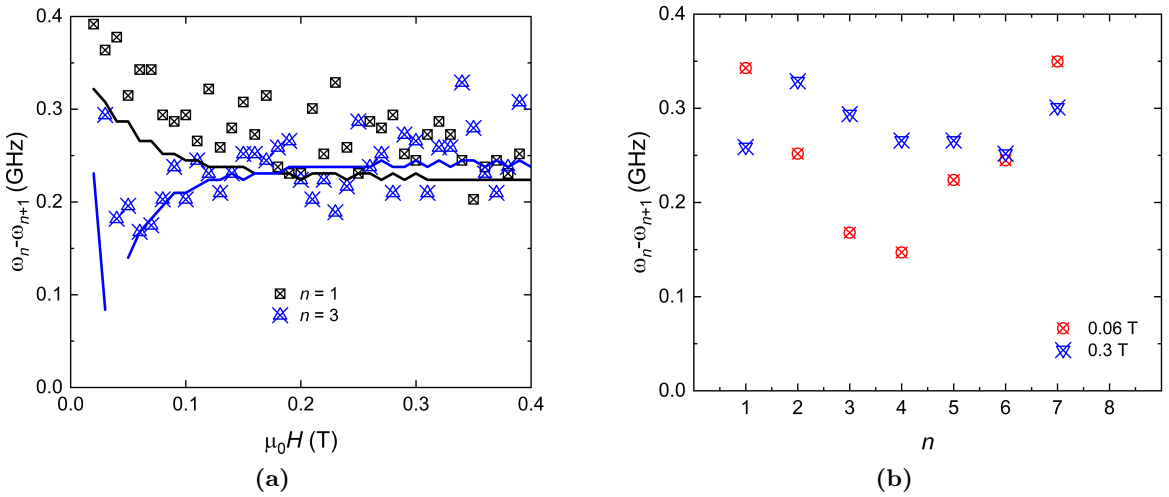

Figure 6.29: Frequency separations between adjacent resonant lines as a function of either magnetic field (a) or the initial state in each transition(b).

In the low field situation, states 7 and 9 can be completely connected by the S_z operator, allowing us to perform transitions between these two states with maximum Rabi frequency. When moving to higher fields, transitions between these states need to be done with S_x (or S_y) and I_x (or I_y) simultaneously. Changing the nuclear spin projection is much slower than modifying only the electronic one, so the Rabi frequency of the considered transition in this region vanishes while increasing the magnetic field.

A good qudit candidate should fulfil two main conditions: its energy diagram should be anharmonic for ensuring a proper addressability of the relevant transitions; and universal operations must be admitted by the molecule, *i.e.* it should be possible to generate any state of the Hilbert space by applicating a sequence of resonant electromagnetic pulses.[27] The first condition has just been verified in the low field regime. Regarding the second condition, we have checked that in this low field region the entanglement between electronic and nuclear spins causes an increase of the Rabi frequency of forbidden transitions at higher fields. Taking this

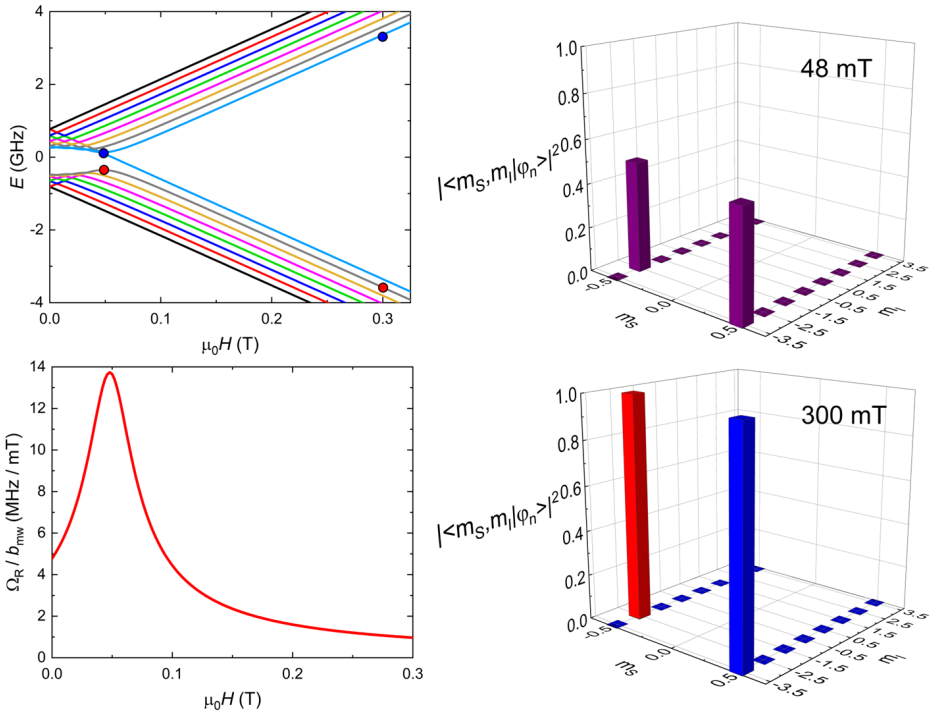

Figure 6.30: Link between electronuclear entanglement and Rabi frequency for a simple situation where the magnetic field is applied along the molecular anisotropy axis z. Left, top: energy level scheme, where the red and blue dots show the energies of levels 7 and 9 at 0.048 T and 0.3 T. Left, bottom: Rabi frequency of the transition associated with these levels, which shows a maximum near the level anticrossing. Right: Wavefunctions of these levels at the same magnetic fields. They become maximally entangled near the anticrossing (thus leading to maximum Ω_R) and factorize as a product of nuclear and electronic spin states at high field.

into account, we need to study if this set of allowed transitions at low fields is large enough to perform universal operations in the molecule. For this, we have first focused on the Rabi frequency at low fields of "electronic" and "nuclear" transitions (those that are associated with changes in the nuclear spin state at high magnetic fields). These Rabi frequencies are shown in Fig. 6.31 for external magnetic field parallel to X laboratory axis and microwave magnetic field parallel to Z, while a plot of these frequencies for a fixed external magnetic field of 0.02 T and microwave magnetic fields under the previous conditions is shown in Fig. 6.32.

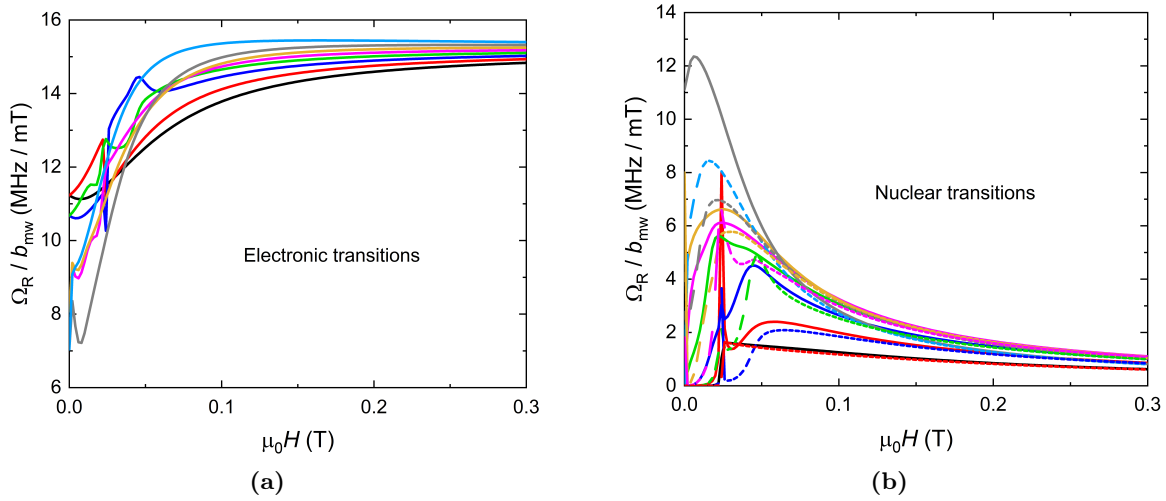

Figure 6.31: Magnetic field dependence of the Rabi frequencies of "electronic" (a) and "nuclear" (b) spin transitions, for external and microwave magnetic fields parallel to the Z laboratory axis. Transitions previously associated with changes in the nuclear spin projection are allowed for low magnetic fields.

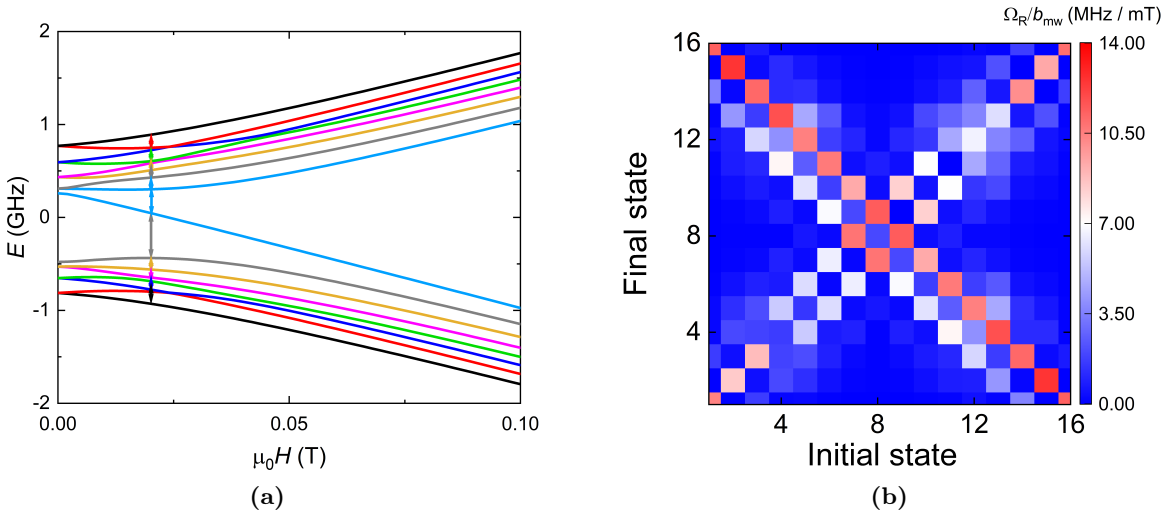

Figure 6.32: (a) Energy diagram of $\mathbf{1^{VO}}$ for a magnetic field applied along the X laboratory axis. (b) Colour map of Rabi frequencies for an applied magnetic field of 0.02 T parallel to X laboratory axis.

Figures 6.31 and 6.32 show that, for low magnetic fields, the Rabi frequencies of "electronic" and "nuclear" transitions are comparable, obtaining a large set of allowed transitions in this field region. Comparing these Rabi frequencies with a decoherence rate $1/T_2 \approx 0.2$ MHz (corresponding to $T_2 = 5$ μs, see Fig. 6.25), we can see that Ω_R is several times larger than $1/T_2$ for most of the considered transitions, allowing us to use them for performing quantum operations.

The question we need to answer now is wether this set of allowed transitions is large enough to perform universal operations. This condition implies that any state of the $d = 16$ dimension Hilbert state can be generated by applying a proper sequence of resonant electromagnetic pulses. This has been studied by calculating the rates W_{nm} at which any basis state n evolves to any other final state m for a typical microwave field amplitude of 1 mT. This evolution needs to be

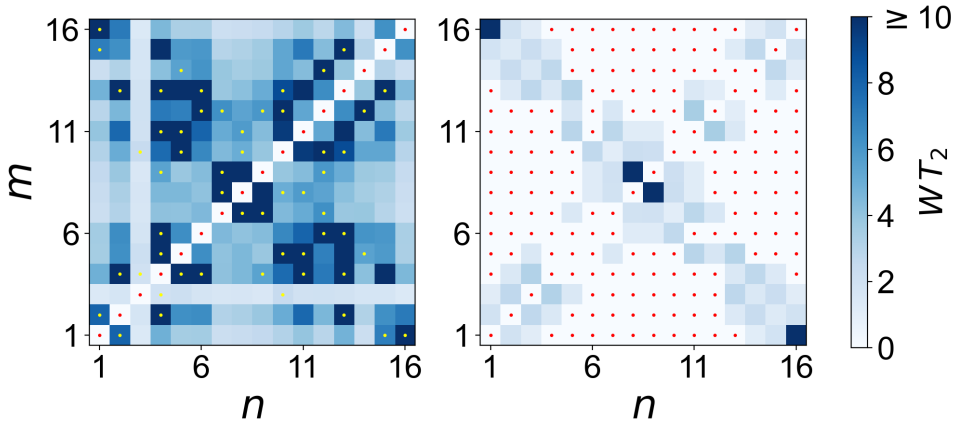

Figure 6.33: Universality plots showing the rates of operations connecting any pair of spin states n and m at 0.02 T (left) and 0.3 T (right) applied in the X laboratory axis, considering an amplitude $b_{\mathrm{mw}} = 1$ mT. A coherence time of 5 μs has been considered. White spots, marked also with a red dot, identify the trivial diagonal spots (identity operation) as well as mutually disconnected states, while yellow dots indicate the connected states.

performed by resonant transitions, so the resonant frequencies should be nondegenerate with that of any other allowed transition. Secondly, to take into account that each electromagnetic pulse has an intrinsic frequency width proportional to Ω_{R}, only transitions whose frequencies differ by more than Ω_{R} have been considered. Finally, we have compared these rates W_{nm} with a decoherence rate $1/T_2 \approx 0.2$ MHz. The results obtained for $\mathbf{1}^{\mathbf{VO}}$ molecules taking all this into account are shown in Figs. 6.33 and 6.34. These plots show that, for sufficiently low magnetic fields, there is a region in which any two basis states can be connected by a sequence of addressable and sufficiently fast resonant transitions. The minimum value of W_{nm}, W_{min}, shown in Fig. 6.34, is the one that limits universality, going to 0 as the external field increases due to the factorization of electronic and nuclear spin states. Results also show us that improving T_2 or the rate of the operations (by increasing b_{mw}) would lead to an increase of the magnetic field region where the system shows universality.

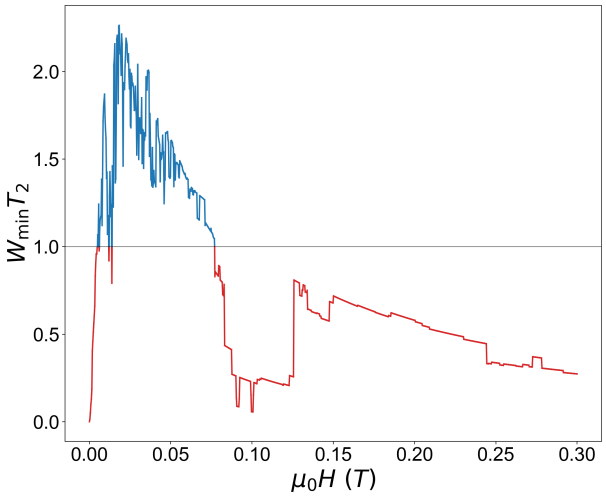

Figure 6.34: Minimum $W_{nm}T_2$ as a function of applied magnetic field in X laboratory axis. The region with $W_{\mathrm{min}} > 1/T_2$ is where universal operations are allowed, while when $W_{\mathrm{min}} < 1/T_2$ electron and nuclear spin states factorize and the system presents a non-universal behaviour. The sudden drop observed around 0.1 T arises from accidental degeneracies between transitions that eliminate some of them.

6.3.5 Coupling of cavity photons to spin-clock transitions in VO-porphyrin molecules

Experimental set-up

With the previous study we have verified that the $\mathbf{1}^{\mathbf{VO}}$ molecule is a good candidate to encode a $d = 16$ qudit or 4 qubits in the low field region ($\mu_0 H < 0.1$ T). Under these conditions, each molecule can be regarded as a microscopic size, small scale quantum processor. A way to exploit this system in proof-of-concept implementations of quantum algorithms, *e.g.* for quantum error correction, is to couple it to transmission lines, for the control of spin states, and to LC resonatos, for the read-out. In this section, we explore this possibility using chips that include both, such as the one shown in Fig. 6.35. The chips are similar to those introduced in chapter 5, but designed to match the resonant frequencies of different spin transitions in $\mathbf{1}^{\mathbf{VO}}$ at low magnetic fields. They were fabricated by our collaborators at CAB. As shown in section 6.2 referred to HoW_{10}, spin-clock transitions can also help to optimize the collective spin-photon coupling of a spin system while keeping the spin linewidth sufficiently small, attaining coherent coupling even in adverse conditions (*e.g.* for concentrated crystals).

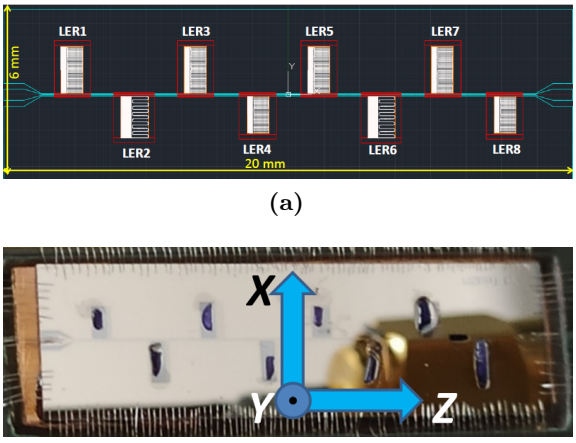

(a)

(b)

Figure 6.35: (a) Scheme of the chip used for studying the coupling of cavity photons to spin-clock transitions in $\mathbf{1}^{\mathbf{VO}}$, together with (b) a picture of the device hosting several $\mathbf{1}^{\mathbf{VO}}$ and $\mathbf{1}^{\mathbf{VO}}_{\mathbf{20\%}}$ crystals on it. The four crystals on the left part are diluted, while the crystals on the right part (four on the resonators and one on top of the transmission line) are fully concentrated.

The study of the spin-clock transitions in the low field region was performed by depositing several fully concentrated ($\mathbf{1}^{\mathbf{VO}}$) and magnetically diluted ($\mathbf{1}^{\mathbf{VO}}_{\mathbf{20\%}}$) single crystals on the different LC resonators of a chip consisting on 8 of these LERs coupled to a common transmission line (Fig. 6.35). The crystals were oriented with their long axis perpendicular to the Z laboratory axis, along which the external magnetic field was applied. At the same time, the microwave field generated by the LERs was perpendicular to this dc magnetic field, and thus parallel to the long crystal axis. The LERs were specifically designed to have resonance frequencies close to those of the different clock transitions shown in Fig. 6.36, obtaining the theoretical resonance frequencies given in Table 6.6. We deposited $\mathbf{1}^{\mathbf{VO}}$ and $\mathbf{1}^{\mathbf{VO}}_{\mathbf{20\%}}$ crystals in pairs of LERs with similar frequencies, allowing us to compare the effect of spin concentration on the spin-photon coupling and the spin linewidth with little variation in frequency and magnetic field. The chip was introduced into the Bluefors LD-250 cryogen-free dilution refrigerator with a uniaxial magnet, described in section 2.6.2, and connected to a VNA that measured the microwave propagation through the device.

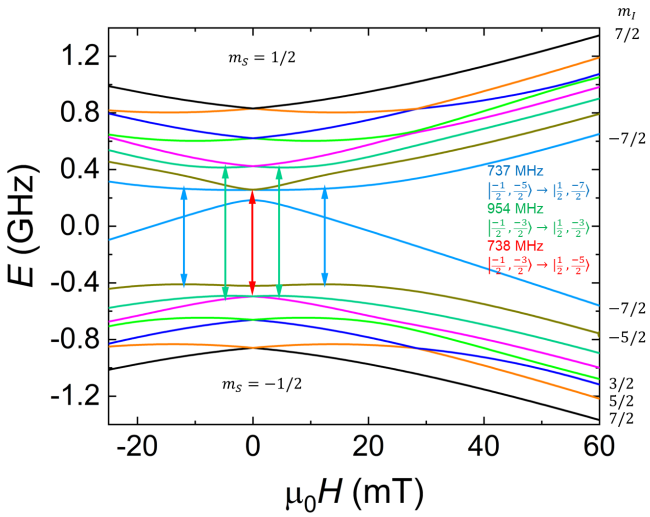

Figure 6.36: Energy diagram of $\mathbf{1^{VO}}$ molecule with the magnetic field applied along the Z laboratory axis, perpendicullar to the crystal z_C axis. The different spin clock transitions are marked with arrays. The states presumably involved in these clock transitions are indicated.

LER number	1*	2*	3*	4*	5	6	7	8
$\mathbf{f_{res}}$ (MHz)	732	939	740	949	748	959	756	969

Table 6.6: Values of the simulated resonance frequencies of the LERs from the chip shown in Fig. 6.35. LERs marked with * are those on which the concentrated crystals were deposited.

Microwave transmission: experiments and analysis

The microwave transmission was measured for all the different LERs applying the magnetic field along the Z laboratory axis, and maintaining a temperature of 10 mK. Transmission data obtained for the seven resonators that could be detected are shown in Fig. 6.37. LER 2 was not visible, possibly due to being damaged during its manipulation.

The transmission data show clear evidences for the coupling of cavity photons to different spin transitions for every sample. In order to properly analyse the results, it is necessary to identify the spin transitions associated to each observed signal. This is difficult in this case, as the electronuclear spin level structure is quite complex, specially at low magnetic fields (see Fig. 6.36). For a better visualization of the results and the correct labelling of the different transitions we have plotted in Fig. 6.38, the frequency of the detected transitions has been plotted with all transition lines in $\mathbf{1^{VO}}$. Here, a slightly different set of Hamiltonian parameters, shown in Table 6.7 has been considered to properly account for the observed transitions.[28] Taking these results into account, we can observe that we are mainly following the evolution of "electronic" transitions between states 7 ($|m_S; m_I\rangle = |-1/2; -7/2\rangle$ at high fields) and 8 ($|+1/2; -7/2\rangle$ at high fields), and also between states 6 ($|-1/2; -5/2\rangle$) and 9 ($|+1/2; -5/2\rangle$). These transitions are characterized by their higher spin-photon coupling compared to non-purely electronic transitions, due to the larger matrix element of the former. An example of the difference between these two types of transitions is shown in Figs. 6.39 and 6.40, where the experimental and fitted 2D plots of the electronuclear transition at 20 mT and the electronic one at 40 mT for LER 1 are shown. Here, it is shown that the coupling is 8 times higher for the pure electronic transition than for the electronuclear one, but also the spin linewidth grows by a factor of 4 for the electronic transition.

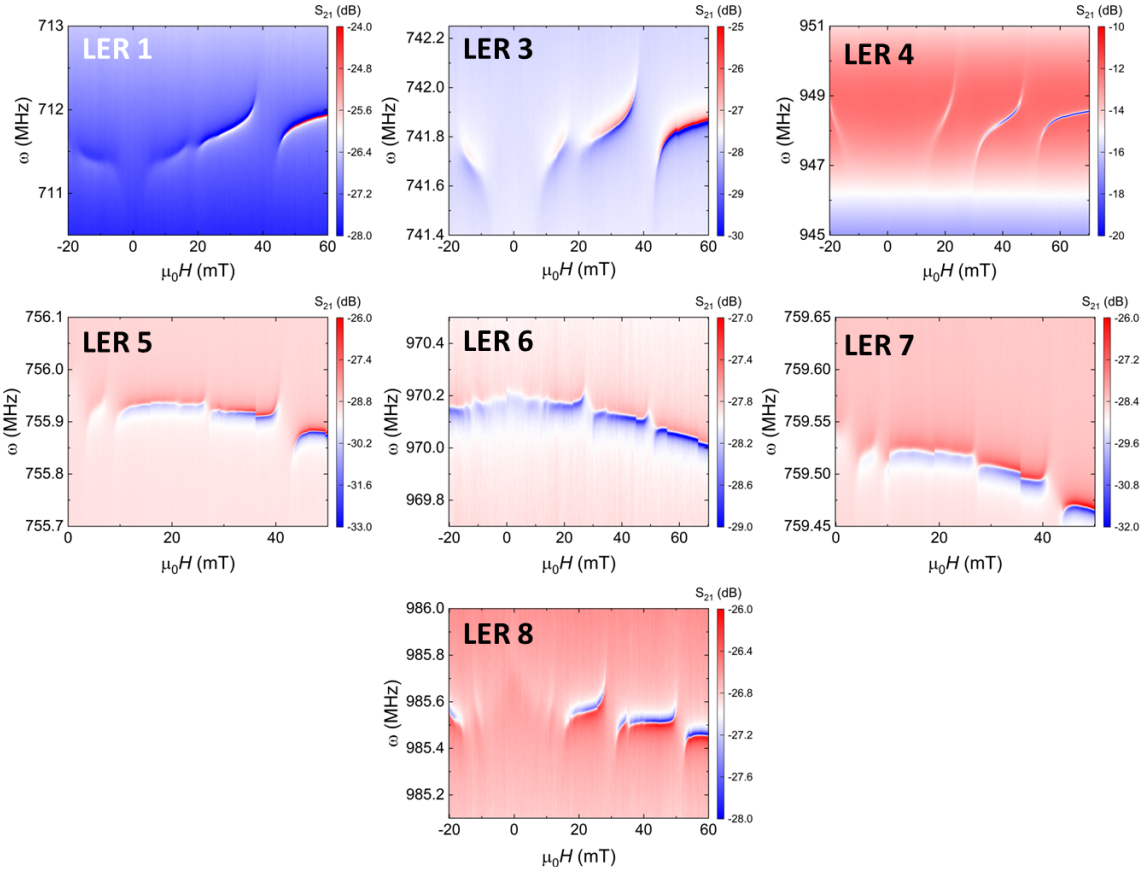

Figure 6.37: 2D plots of the microwave transmission measured at 10 mK for seven of the eight LERs shown in Fig. 6.35. LER 2 was not visible.

$\mathbf{A_{xx}}$ (MHz)	$\mathbf{A_{yy}}$ (MHz)	$\mathbf{A_{zz}}$ (MHz)	$\mathbf{g_{xx}}$	$\mathbf{g_{yy}}$	$\mathbf{g_{zz}}$
158	158	472	1.984	1.984	1.964

Table 6.7: Hamiltonian parameters, referred to the molecular frame, considered for the analysis of the results shown in this section.[28]

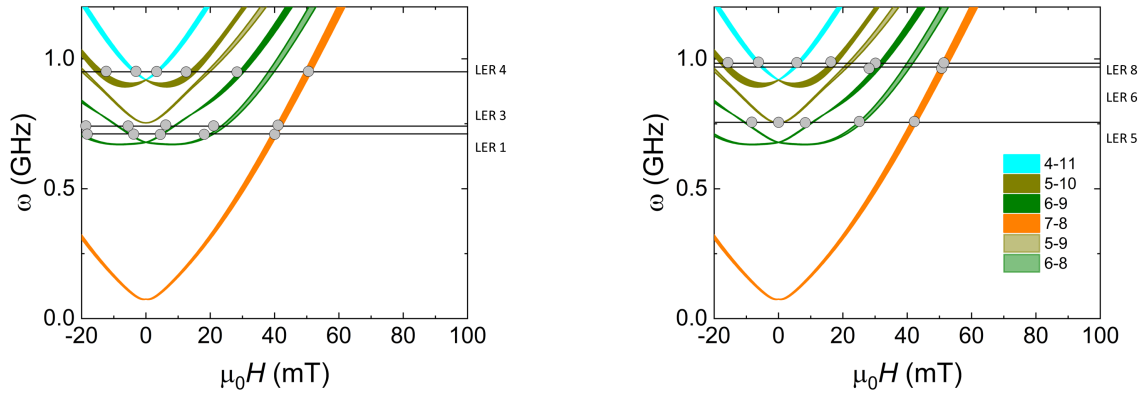

(a) **(b)**

Figure 6.38: Resonance lines of $\mathbf{1^{VO}}$ of interest in the studied region, ordered in the legend from largest to smallest theoretical spin-photon coupling at 10 mK (solid coloured lines), together with the observed transitions in (a) the concentrated and (b) the diluted crystals (dots). The levels are labeled from 0 (ground state) to 15. Theoretical transition lines have been calculated taking into account a possible variation of 20° in the orientations of the deposited crystals, and using the Hamiltonian parameters shown in Table 6.7. The horizontal solid lines show the frequencies of different LERs used in this study

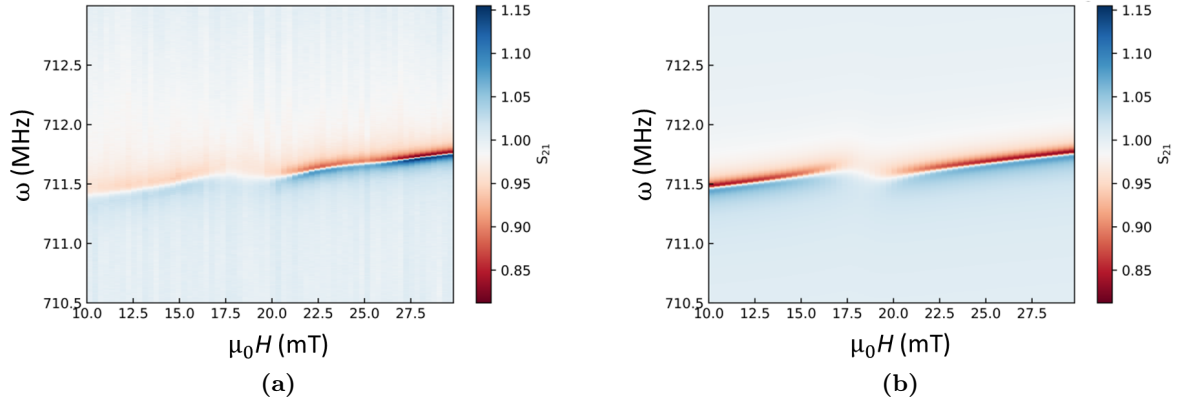

Figure 6.39: (a) Experimental and (b) simulated 2D plots of the electronuclear spin transition between states 6 ($|-1/2; -5/2\rangle$) and 8 ($|+1/2; -7/2\rangle$) observed for LER 1 at 20 mT and a temperature of 10 mK. The fit gives us a coupling between the spins and the circuit photons of 0.6 MHz and a linewidth of 3.5 MHz.

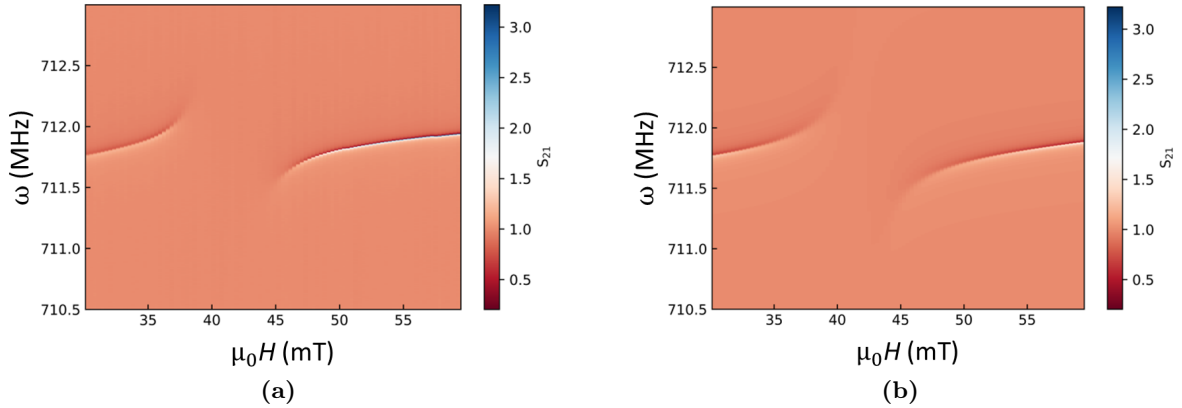

Figure 6.40: (a) Experimental and (b) simulated 2D plots of the electronic spin transition between states 7 ($|-1/2; -7/2\rangle$) and 8 ($|+1/2; -7/2\rangle$) observed for LER 1 at 40 mT and 10 mK. The fit gives us a coupling between the spins and the circuit photons of 4.5 MHz and a linewidth of 14 MHz.

Observing Fig. 6.38, we can see that LERs 4, 6 and 8 are tuned close to the spin-clock transition between states 5 ($|-1/2; -3/2\rangle$) and 10 ($|-1/2; -3/2\rangle$), while LERs 1, 3, 5 and 7 couple to the spin-clock transition between states 6 ($|-1/2; -5/2\rangle$) and 8 ($|+1/2; -7/2\rangle$). Looking at the detected signals, LERs 5 and 7 seem also coupled to the spin-clock transition between states 5 and 9 ($|+1/2; -5/2\rangle$). A zoom of the resonance lines of $\mathbf{1^{VO}}$ near each of these spin-clock transitions has been plotted in Fig. 6.41 for clarity.

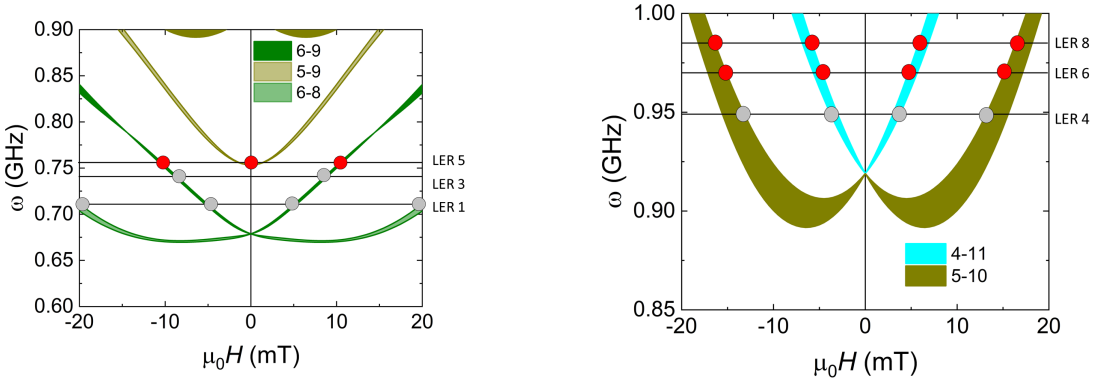

Figure 6.41: Zoom of the resonance lines of $\mathbf{1}^{\mathbf{VO}}$ near the spin-clock transitions between states (a) 6 and 8, and between 5 and 9, and (b) 5 and 10. Red and grey dots are referred to the observed signals with diluted and concentrated samples respectively. The horizontal solid lines show the frequencies of different LERs used in this study.

In Fig. 6.42(a) we take a closer look at the detected spin-clock transition between states 5 and 10 with LER 4. The high value of the spin-photon coupling for this transition, together with the evolution of the energy levels involved in it, cause the resonator signal to disappear for magnetic fields between −10 and 10 mT. In the case of the measurement carried out with the diluted sample in LER 8 (Fig. 6.43(a)), the lower value of the spin-photon coupling allows us to also follow the transition between states 4 and 11 that occurs at lower fields. Observing both graphs, it seems that we are near, or even reaching, the strong coupling regime with both concentrated and diluted crystals. This has been verified by fitting the transmission data with the python script used previously. The 2D transmission plots generated by the fittings of these transitions in LERs 4 and 8 are shown in Figs. 6.42(b) and 6.43(b) respectively. As mentioned before, the results tell us that the coupling to this clock transition is greater for the concentrated sample than for the diluted one, due to the higher number of $\mathbf{1}^{\mathbf{VO}}$ molecules coupled to the circuit in the concentrated crystal. But, remarkably, the spin linewidth does not increase. Notice that the frequency of the LER that hosts the pure crystal is closer to the anticrossing than that of LER 8, which hosts a diluted one. In these conditions, the spin levels tend to become progressively less sensitive to external magnetic field fluctuations, which are at the origin of γ.

Thanks to this property, the strong coupling regime is achieved in the case of the concentrated sample, obtaining a spin-photon coupling between 1.6 and 4 times greater than the spin linewidth depending on the observed transition (5-10 or 4-11). Therefore, as expected, the clock transition can be exploited to work with fully concentrated samples without paying the prize of a stronger decoherence.

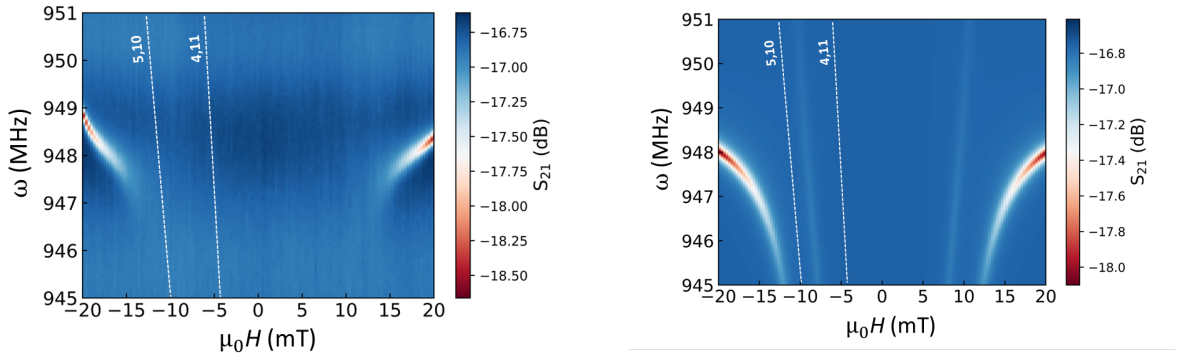

Figure 6.42: (a) Experimental and (b) simulated 2D plots of the spin-clock transition between states 5 and 10, observed for LER 4 (concentrated sample) at −12, −4, 4 and 12 mT, at a temperature of 10 mK. Two transitions needed to be considered due to a crossing between the involved levels at zero field: between states 5 and 10, and between states 4 and 11. The obtained spin-photon couplings and spin linewidths for both transitions are: $G_{5,10} = 5.1$ MHz, $G_{4,11} = 12.2$ MHz, $\gamma_{5,10} = \gamma_{4,11} = 3.2$ MHz.

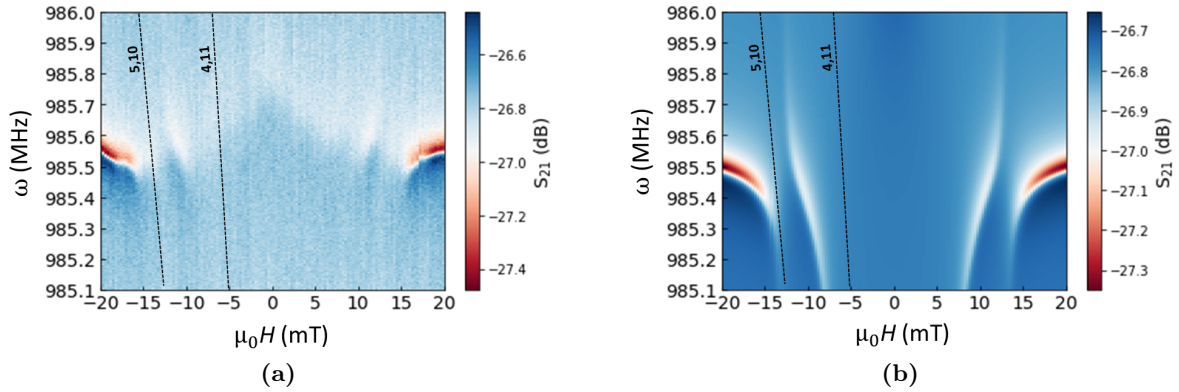

Figure 6.43: (a) Experimental and (b) simulated 2D plots of the spin-clock transition between states 5 and 10, observed for LER 8 (diluted sample) at −15, −5, 5 and 15 mT, at a temperature of 10 mK. The same two transitions that were considered in the concentrated case have been used here. The obtained spin-photon couplings and spin linewidths for both transitions are: $G_{5,10} = 1.3$ MHz, $G_{4,11} = 4.5$ MHz, $\gamma_{5,10} = \gamma_{4,11} = 5.3$ MHz.

Now we will focus on the spin-clock transition between states 6 and 8 that is observed with LERs 1, 3, 5 and 7. Due to the similarity between the results obtained with the pairs of concentrated and diluted crystals, we will show here the analysis of the transitions observed in two of these samples, those placed on LERs 1 and 5. The experimental 2D transmission plots are shown in Figs. 6.44(a) ($\mathbf{1^{VO}}$) and 6.45(a) ($\mathbf{1^{VO}_{20\%}}$). As with LERs 4 and 8, the resonator signal of LER 1, that hosts a pure crystal, vanishes for magnetic fields between −5 and 5 mT due to the high spin-photon couplings achieved, 5 MHz in this region. In this case, the spin-clock transition takes place between two states, 6 ($|-1/2; -5/2\rangle$) and 8 ($|+1/2; -7/2\rangle$), a transition that is forbidden at high fields. This makes the spin-photon coupling to be lower than for the spin-clock transition between states 5 and 10, 0.5 MHz compared to 5.1 MHz. Nevertheless, part of the clock transition involves also states 6 and 9, which show the same nuclear spin projection. This makes the spin-photon coupling of the transition detected at −5 and 5 mT greater than

the one of the electronuclear part of the spin-clock transition, allowing us to achieve the strong coupling regime near this transition.

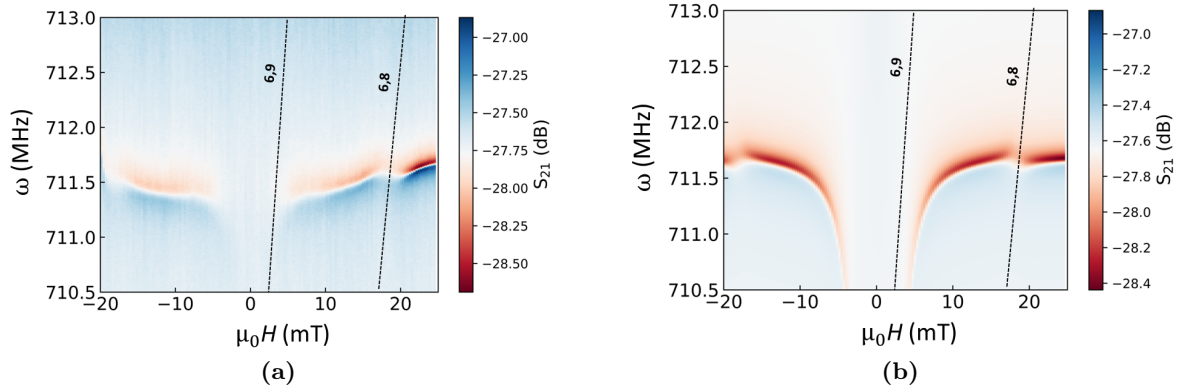

Figure 6.44: (a) Experimental and (b) simulated 2D plots of the spin-clock transition between states 6 and 8, observed for LER 1 (concentrated sample) at −20, −5, 5 and 20 mT, at a temperature of 10 mK. Transitions between the states 6 and 8, and between states 6 and 9 were observed and considered for the fittings. The obtained spin-photon couplings and spin linewidths for both transitions are: $G_{6,8} = 0.5$ MHz, $G_{6,9} = 5$ MHz, $\gamma_{6,8} = 3.7$ MHz, $\gamma_{6,9} = 2.1$ MHz.

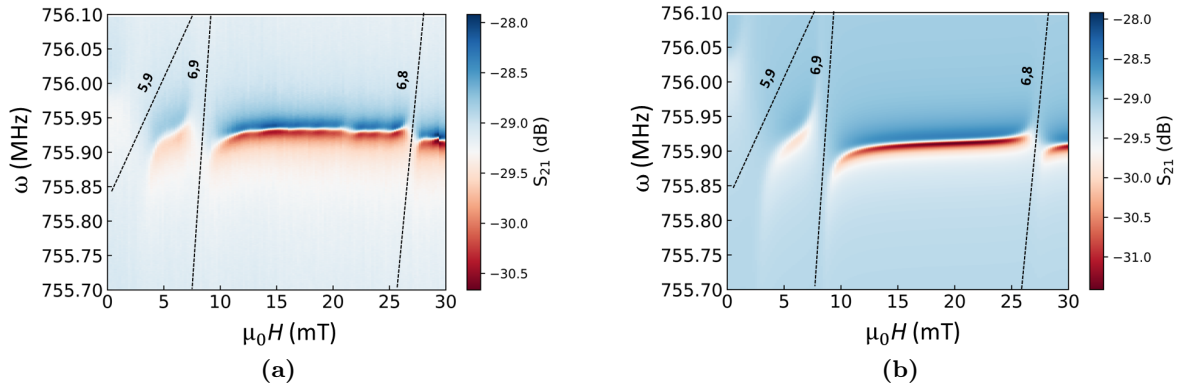

Figure 6.45: (a) Experimental and (b) simulated 2D plots of the spin-clock transition between states 6 and 9, observed for LER 5 (diluted sample) at −10 and 10 mT, between states 6 and 8 at 28 mT, and between states 5 and 9 at 0 mT, at a temperature of 10 mK. The obtained spin-photon couplings and spin linewidths for these transitions are: $G_{6,9} = 0.6$ MHz, $G_{6,8} = 0.1$ MHz, $G_{5,9} = 0.7$ MHz, $\gamma_{6,9} = 3.2$ MHz, $\gamma_{6,8} = 0.7$ MHz, $\gamma_{5,9} = 2.7$ MHz.

Regarding the signals observed in LER 5, and shown in Fig. 6.45, the resonator frequencies are close to the frequency of the spin-clock transition between states 5 and 9 wave functions at zero field, as shown in Fig. 6.41(a) in addition to transitions 6-9 and 6-8. The spin-photon coupling obtained for the transition between states 6 and 9 is 10 times lower than the one observed for the same transition in the concentrated crystal, due to the lower number of coupled molecules, while the coupling for the transition between states 6 and 8 decreases by a factor of 5. At zero field, the resonator signal vanishes because of the coupling to the spin-clock transition between states 5 and 9. Although the strong coupling regime is not achieved in this case, the weak dependence of the transition frequency in this region, characteristic of spin-clock transitions, makes the resonator to remain continuously coupled to the spins between −2.5 and 2.5 mT.

All the spin-photon couplings and linewidths obtained for the spin-clock transitions analysed in these LERs are shown in Table 6.8. For both concentrated and diluted samples, the highest spin-photon coupling has been achieved with the spin transition between states 4 and 11, near the clock transition between states 5 and 10. In terms of the spin linewidth, we find, rather surprisingly and as already anticipated, higher decoherence rates for the diluted crystals. This can be explained by taking into account the distance between the observed signals and the minima of the spin-clock transitions. The frequencies of the LERs with diluted crystals were higher than of those with concentrated samples, and therefore the observed transitions were farther from the frequency minima. The reduced sensitivity of the transition frequency to magnetic field compensates for the higher dipolar interactions and can make the concentrated samples show similar, or even lower, broadening than the diluted ones.

Transition	4-11	5-10	6-9	6-8	5-9
Spin-photon coupling (MHz)	12.2 ± 1.2	5.1 ± 0.3	5.0 ± 0.4	0.50 ± 0.03	–
	4.5 ± 0.4	1.3 ± 0.1	0.60 ± 0.03	0.10 ± 0.01	0.70 ± 0.02
Spin linewidth (MHz)	3.2 ± 0.2	3.2 ± 0.2	2.1 ± 0.1	3.7 ± 0.1	–
	5.3 ± 0.3	5.3 ± 0.3	3.2 ± 0.1	0.70 ± 0.04	2.7 ± 0.1

Table 6.8: Summary of the spin-photon couplings G_N and spin linewidths γ obtained for the studied spin-clock transitions. Values for concentrated (top) and diluted (bottom) samples are shown.

Finally, we can compare the spin-photon couplings and linewidths observed in these clock transitions with that obtained for the electronic transition between states 7 and 8 in both concentrated and diluted samples (Figs. 6.46 and 6.47). While the couplings obtained now are pretty similar, or even higher, than the values obtained for the clock transitions, the decoherence rates have risen as well. It can be verified that working with clock transitions allow us to reduce the decoherence and increase the spin-photon coupling at the same time, even achieving the strong coupling regime with a sufficiently high number of interacting spins.

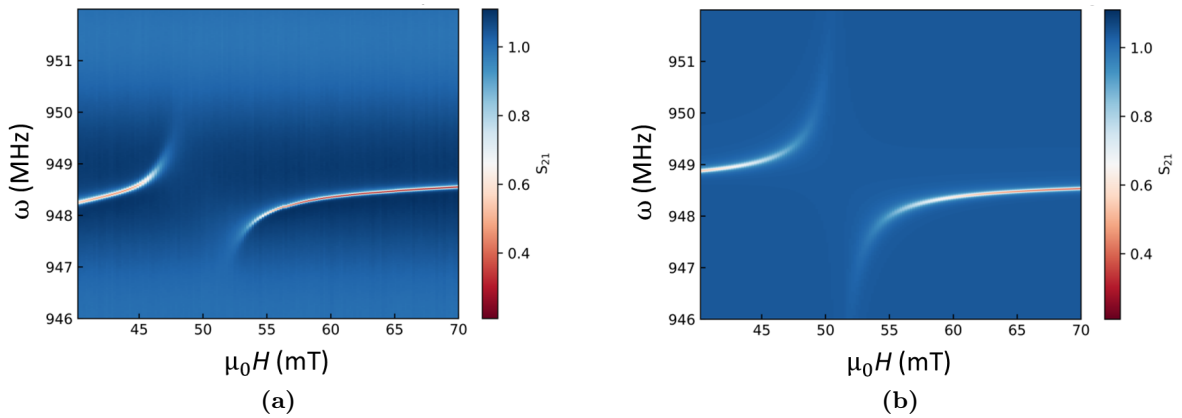

Figure 6.46: (a) Experimental and (b) simulated 2D plots of the electronic transition between states 7 and 8, observed for LER 4 (concentrated crystal) at 50 mT. The simulation gives us a spin-photon coupling of 8 MHz and a linewidth of 14.6 MHz.

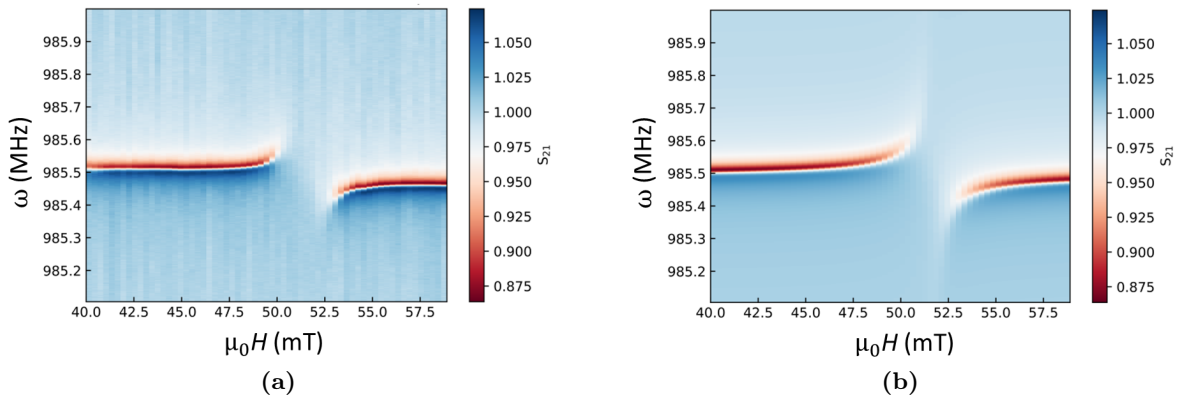

Figure 6.47: (a) Experimental and (b) simulated 2D plots of the electronic transition between states 7 and 8, observed for LER 8 (diluted crystal) at 50 mT and 10 mK. In this case, the obtained spin-photon coupling is 1.7 MHz, and the linewidth is 10.3 MHz.

6.3.6 Conclusions

The results of the study of $\mathbf{1^{VO}}$ molecules show that they show a sufficiently high anharmonicity at low fields, and the possibility to introduce electronuclear spin entanglement by applying the adequate external magnetic field. These two facts allow us to coherently manipulate both electronic and nuclear spin transitions at sufficiently high speeds, being this system able to perform universal quantum operations. Taking also into account the relatively long spin coherence and relaxation times (of a few μs and up to several seconds respectively), we can conclude that $\mathbf{1^{VO}}$ molecules provide quite promising realizations of either a 4-qubit processor or a $d = 16$ qudit.

No quadrupolar term in the Hamiltonian has been required for achieving the needed anharmonicity and universality, only a hyperfine interaction not fully uniaxial nor fully isotropic. This hyperfine interaction produces a set of level anticrossings and clock transitions that enhance the overlap between different states, and thus the operation speed (spin-photon coupling) and the universality.

Molecular qudits like $\mathbf{1^{VO}}$ could allow the integration of quantum error correction at the molecular level. Using 4 qubits, single qubit or single phase flips can be corrected by the simplest repetition code, based on Shor's algorithm.[14] Furthermore, more efficient codes adapted to the level structure of $\mathbf{1^{VO}}$ could be used.[11;29]

In this chapter we have also shown that it is possible to attain long T_2 in diluted $\mathbf{1^{VO}}$ crystals while selectively addressing individual transitions. This could allow us to implement single qubit operations on a crystal using on-chip resonators,[30] rather than single molecular spins. The several spin states of the crystal can be exploited by means of broadband electromagnetic pulses generated by an open transmission line. In the region of relevant frequencies of $\mathbf{1^{VO}}$, it is easy to generate pulses of amplitude of about 1 mT, and this value can be increased by improving the circuit design (see chapter 4). With this pulse amplitude, Rabi frequencies faster than decoherence rates are obtained, bringing molecular spins close to realistic quantum implementations.

Finally, we have shown that the spin-clock transitions that appear at sufficiently low magnetic fields, due to a set of level anticrossings produced by the hyperfine interaction, allow us to improve the spin decoherence while keeping high enough spin-photon couplings. Thanks to this fact, the strong coupling regime has been achieved near these clock transitions even using concentrated systems. This is a necessary ingredient for the application of circuit QED techniques to read out

electronuclear spin states. Therefore, the results reported here represent the first steps to perform proof of concept realizations of qudit based algorithms using molecular crystals coupled at the same time to open transmission lines (for the control) and to LC resonators (for the readout). $\mathbf{1^{VO}}$ provides a promising platform for the implementation of such techniques.

Bibliography

[1] M. J. Martínez-Pérez, S. Cardona-Serra, C. Schlegel, F. Moro, P. J. Alonso, H. Prima-García, J. M. Clemente-Juan, M. Evangelisti, A. Gaita-Ariño, J. Sesé, J. van Slageren, E. Coronado, and F. Luis. Gd-Based Single-Ion Magnets with Tunable Magnetic Anisotropy: Molecular Design of Spin Qubits. *Physical Review Letters*, 108:247213 (5), 2012.

[2] M. Shiddiq, D. Komijani, Y. Duan, A. Gaita-Ariño, E. Coronado, and S. Hill. Enhancing coherence in molecular spin qubits via atomic clock transitions. *Nature*, 531:348–351, 2016.

[3] F. Luis, A. Repollés, M. J. Martínez-Pérez, D. Aguilà, O. Roubeau, D. Zueco, P. J. Alonso, M. Evangelisti, A. Camón, J. Sesé, L. A. Barrios, and G. Aromí. Molecular Prototypes for Spin-Based CNOT and SWAP Quantum Gates. *Physical Review Letters*, 107:117203, 2011.

[4] G. Aromí, D. Aguilà, P. Gamez, F. Luis, and O. Roubeau. Design of magnetic coordination complexes for quantum computing. *Chemical Society Reviews*, 41:537–546, 2012.

[5] D. Aguilà, L. A. Barrios, V. Velasco, O. Roubeau, A. Repollés, P. J. Alonso, J. Sesé, S. J. Teat, F. Luis, and G. Aromí. Heterodimetallic [LnLn'] lanthanide complexes: toward a chemical design of two-qubit molecular spin quantum gates. *Journal of the America Chemical Society*, 136(40):14215–14222, 2014.

[6] J. Ferrando-Soria, E. Moreno-Pineda, A. Chiesa, A. Fernández, S. A. Magee, S. Carretta, P. Santini, I. J. Vitorica-Yrezabal, F. Tuna, G. A. Timco, E. J. L. McInnes, and R. E. P. Winpenny. A modular design of molecular qubits to implement universal quantum gates. *Nature Communications*, 7:11377, 2016.

[7] A. Fernández, J. Ferrando-Soria, E. Moreno-Pineda, F. Tuna, I. J. Vitorica-Yrezabal, C. Knappke, J. Ujma, C. A. Muryn, G. A. Timco, P. E. Barran, A. Ardavan, and R. E. P. Winpenny. Making hybrid [n]-rotaxanes as supramolecular arrays of molecular electron spin qubits. *Nature Communications*, 7:10240, 2016.

[8] M. D. Jenkins, Y. Duan, B. Diosdao, J. J. García-Ripoll, A. Gaita-Ariño, C. Giménez-Saiz, P. J. Alonso, E. Coronado, and F. Luis. Coherent manipulation of three-qubit states in a molecular single-ion magnet. *Physical Review B*, 95:064423, 2017.

[9] C. Godfrin, A. Ferhat, R. Ballou, S. Klyatskaya, M. Ruben, W. Wernsdorfer, and F. Balestro. Operating Quantum States in Single Magnetic Molecules: Implementation of Grover's Quantum Algorithm. *Physical Review Letters*, 119:187702, 2017.

[10] E. Moreno-Pineda, C. Godfrin, F. Balestro, W. Wernsdorfer, and M. Ruben. Molecular spin qudits for quantum algorithms. *Chemical Society Reviews*, 47:501–513, 2018.

[11] R. Hussain, G. Allodi, A. Chiesa, E. Garlatti, D. Mitcov, A. Konstantatos, K. S. Pedersen, R. De Renzi, S. Piligkos, and S. Carretta. Coherent Manipulation of a Molecular Ln-Based Nuclear Qudit Coupled to an Electron Qubit. *Journal of the American Chemical Society*, 140:9814–9818, 2018.

[12] M. A. AlDamen, S. Cardona-Serra, J. M. Clemente-Juan, E. Coronado, A. Gaita-Ariño, C. Martí-Gastaldo, F. Luis, and O. Montero. Mononuclear Lanthanide Single Molecule Magnets Based on the Polyoxometalates $[Ln(W_5O_{18})_2]^{9-}$ and $[Ln(\beta_2\text{-}SiW_{11}O_{39})_2]^{13-}$($Ln^{III}$ =Tb, Dy, Ho, Er, Tm, and Yb). *Inorganic Chemistry*, 48:3467–3479, 2009.

[13] S. Ghosh, S. Datta, L. Friend, S. Cardona-Serra, A. Gaita-Ariño, E. Coronado, and S. Hill. Multi-frequency EPR studies of a mononuclear holmium single-molecule magnet based on the polyoxometalate $[Ho^{III}(W_5O_{18})_2)]^{9-}$. *Dalton Transactions*, 41:13697–13704, 2012.

[14] E. Macaluso, M. Rubín, D. Aguilà, A. Chiesa, L. A. Barrios, J. I. Martínez, P. J. Alonso, O. Roubeau, F. Luis, G. Aromí, and S. Carretta. A heterometallic [LnLn'Ln] lanthanide complex as a qubit with embedded quantum error correction. *Chemical Science*, 11:10337–10343, 2020.

[15] S. Bertaina, S. Gambarelli, A. Tkachuk, I. N. Kurkin, B. Malkin, A. Stepanov, and B. Barbara. Rare-earth solid-state qubits. *Nature Nanotechnology*, 2:39–42, 2007.

[16] A. Abragam and B. Bleaney. *Electron paramagnetic resonance of transition ions*. Dover Publications Inc., 1986.

[17] K. W. H. Stevens. Matrix Elements and Operator Equivalents Connected with the Magnetic Properties of Rare Earth Ions. *Proceedings of the Physical Society. Section A*, 65:209–215, 209.

[18] P. Debye. Zur Theorie der spezifischen Wärmen. *Annalen der Physik*, 344:789–839, 1912.

[19] H. B. Callen. *Thermodynamics and an Introduction to Thermostatistics, 2nd edition*. John Wiley & Sons, 1985.

[20] C. W. Gardiner and M. J. Collett. Input and output in damped quantum systems: Quantum stochastic differential equations and the master equation. *Physical Review A*, 31:3761–3774, 1985.

[21] S. Fan, Ş. E. Kocabaş, and J.-T. Shen. Input-output formalism for few-photon transport in one-dimensional nanophotonic waveguides coupled to a qubit. *Physical Review A*, 82:063821, 2010.

[22] M. Rubín-Osanz, F. Lambert, F. Shao, E. Rivière, R. Guillot, N. Suaud, N. Guihéry, D. Zueco, A.-L. Barra, T. Mallah, and F. Luis. Chemical tuning of spin clock transitions in molecular monomers based on nuclear spin-free Ni(II). *Chemical Science*, 12:5123–5133, 2021.

[23] C. Kittel. *Introduction to Solid State Physics, 8th edition*. John Wiley & Sons, 2005.

[24] Cambridge Crystallographic Data Centre, Mercury.

[25] M. Atzori, S. Benci, E. Morra, L. Tesi, M. Chiesa, R. Torre, L. Sorace, and R. Sessoli. Structural Effects on the Spin Dynamics of Potential Molecular Qubits. *Inorganic Chemistry*, 57:731–740, 2018.

[26] C.-J. Yu, M. J. Graham, J. M. Zadrozny, J. Niklas, M. D. Krzyaniak, M. R. Wasielewski, O. G. Poluektov, and D. E. Freedman. Long Coherence Times in Nuclear Spin-Free Vanadyl Qubits. *Journal of the American Chemical Society*, 138:14678–14685, 2016.

[27] C. V. Kraus, M. M. Wolf, and J. I. Cirac. Quantum simulations under translational symmetry. *Physical Review A*, 75:022303, 2007.

[28] D. Mannikko. *High-Resolution ENDOR Studies on Vanadyl Porphyrins andd Crude-Oil Petroporphyrins*. PhD thesis, University of Washington, 2020.

[29] A. Chiesa, E. Macaluso, F. Petiziol, S. Wimberger, P. Santini, and S. Carretta. Molecular Nanomagnets as Qubits with Embedded Quantum-Error Correction. *The Journal of Physical Chemistry Letters*, 11:8610–8615, 2020.

[30] C. Bonizzoni, A. Ghirri, F. Santanni, M. Atzori, L. Sorace, R. Sessoli, and M. Affronte. Storage and retrieval of microwave pulses with molecular spin ensembles. *npj Quantum Information*, 6:68, 2020.

7 Conclusions

Although the development of quantum processors based on superconducting qubits has shown an impressive progress in the last years, they have not yet achieved the computational power needed to address problems of particular relevance. Besides, scaling these systems and, especially, dealing with their inherent errors, remains very challenging. It is possible that the combination of different systems into a single one could allow the design of an even better quantum computing architecture. Therefore, the study of different qubit systems that might help in some aspects can be very userful.

In this thesis work, we have studied the possibility of combining systems based on circuit quantum electrodynamics and molecular magnets. Molecular spins are an interesting alternative to superconducting qubits because of their chemical tunability and the fact that two molecules of the same compound are identical. However, we need to achieve the strong coupling regime with a single molecule in order to design a quantum processor with these systems. For this reason, during this work we have experimentally studied different methods for achieving this goal.

More specifically, we have focussed on several ways of enhancing the spin-photon coupling between molecular samples and superconducting circuits, as the first steps towards the fabrication of a quantum processor based on the combination of these systems. We will now give a summary of the main conclusions we have reached in this work.

Firstly, we have shown that the fabrication of a 40 nm wide nanobridge on the central line of a 14 μm wide CPW resonator enhances the single spin-photon coupling by a factor 60, achieving values of about 180 Hz. This coupling can be even higher, on the order of kHz, if the distance between the molecular samples and the superconducting circuits is close to zero, due to the large decay of the microwave magnetic field generated by the nanoconstriction with distance. This approach has been introduced in a new type of resonator, the so-called 2.5D resonator, with which single spin-photon couplings higher than 3 kHz have been achieved with a 50 nm wide nanoconstriction. This resonator consists on an LC circuit with a very low inductance introduced on a 3D cavity. The reduced inductance produces a local microwave magnetic field higher than that of CPW resonators, showing that the combination of nanoconstrictions with low inductance resonators is a very promising way to achieve high single spin-photon couplings.

Another way to achieve the strong coupling regime is to use molecules with high coherence. This is the case of the molecule PTM_r, a free radical that shows T_2 values of tens of μs at very low temperature. We have studied the coupling between these molecules and lumped element resonators, a different type of LC resonator consisting on a capacitor in parallel with an inductor, and coupled to a transmission line. Single spin-photon couplings up to 5.7 Hz have been observed when using LERs with high inductance, while values of 1 kHz were achieved when the samples were deposited on LERs with very low inductance and a nanoconstriction. It was even possible to achieve single spin-photon coupling values close to 24 kHz with these low inductance LERs with nanoconstrictions, being this coupling higher than the 16 kHz necessary to achieve the strong coupling regime with a single molecule considering a T_2 value of 10 μs at very low temperature. These samples have shown a spin linewidth up to 35 MHz instead of the 7 MHz observed by previous EPR measurements. This seems to be motivated by the formation of PTM_r aggregates, together with a hyperfine coupling between nearby spins and some other inhomogeneous broadening sources. Nevertheless, by reducing the spin concentration

the coherence could be increased up to the previous 7 MHz, being this system a suitable qubit candidate if the single spin-photon coupling is further enhanced.

The previous results represent a record of the single spin-photon coupling, being the dimensionless coupling G_1/ω_r associated to them higher than the maximum single spin-photon coupling reported in literature.[1] All these results are summarised in Fig. 7.1

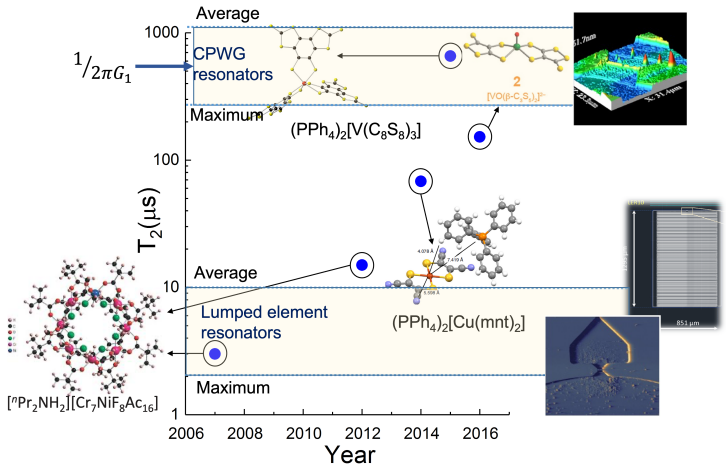

Figure 7.1: Comparison between the average and maximum values of $G_1/2\pi$ estimated in this work for every type of resonator and T_2 of the best molecular qubits. These qubits are $[^nPr_2NH_2]\,[Cr_7NiF_8Ac_{16}]$,[2;3] $(PPh_4)_2\,[Cu\,(mnt)_2]$,[4] $[VO\,(\beta - C_3S_5)_2]^{2-}$,[5] and $(PPh_4)_2\,[V\,(C_8S_8)_3]$.[6]

The effect of spin-clock transitions in the spin-photon coupling has also been studied. In chapter 6 we have introduced two different molecules that show these transitions: HoW_{10} and $\mathbf{1^{VO}}$. In the case of HoW_{10}, its strong uniaxial anisotropy and the presence of fourth-order transverse anisotropy terms generate a quantum tunneling gap of 9.1 GHz between symmetric and antisymmetric superpositions of the $m_J = \pm 4$ electronic spin states. Four different spin-clock transitions take place in this molecule due to its nuclear spin $\mathbf{I} = 7/2$, being the position of these anticrossings only sensitive to the magnetic field applied parallel to the molecular anisotropy axis. Through broadband spectroscopy measurements performed for different temperatures, we have observed that the spin-photon coupling becomes maximum at these clock transitions due to the maximum overlap between the spin states. This enhancement of the coupling is accompanied by a minimum decoherence. These results show that engineering the qubit states can provide a promising method to optimise both the spin coherence and the coupling to circuits, which are often mutually incompatible. This is also a promising way to attain coherent spin-photon coupling in HoW_{10} even far from optimum conditions. However, the nature of spin-clock transitions (they take place between excited states), as well as the harmonicity of the remaining transitions, make this molecule a bit problematic as a qubit candidate.

Regarding the molecule $\mathbf{1^{VO}}$, it has been observed that the entanglement of nuclear and electronic spins introduces a sufficiently high anharmonicity at low fields. In addition, the hyperfine coupling also enhances the Rabi frequencies between nuclear spin states, to values comparable to those of electronic transitions. These two facts allow performing universal quantum operations with this molecule, which can be seen as a 4-qubit processor or a $d = 16$ qudit. Molecular qudits like this could allow the integration of quantum error correction even at the molecular level, being possible to correct single qubit or single phase flips by the simplest repetition code. Finally, we have achieved strong coupling to the spin-clock transitions that appear in $\mathbf{1^{VO}}$ at low fields, even using concentrated systems. This is a key ingredient for the application of circuit QED techniques to read out electronuclear spin states.

In conclusion, we have approached the strong coupling regime with a single molecule by modifying the superconducting circuits or the molecules, reaching values higher than those reported in the literature. Although the results presented within this work are quite promising, further improvements are needed in order to fabricate a molecular quantum processor such as the one shown in the introduction. We are currently trying to improve the microwave magnetic field generated by CPW resonators by combining them with 2D materials. The confinement of photons in a bidimensional structure could produce a significant enhancement of the microwave magnetic field intensity. Systems that show spin-clock transitions with better properties than those shown here are also being studied. Further work is necessary to obtain the best combination of superconducting resonators and molecular samples, being the goal of fabricating a molecular quantum processor achievable in the near future.

Bibliography

[1] S. Probst, A. Bienfait, Campagne-Ibarcq P., J. J. Pla, B. Albanese, J. F. Da Silva Barbosa, T. Schenkel, D. Vion, D. Esteve, K. Mølmer, J. J. L. Morton, R. Heeres, and P. Bertet. Inductive-detection electron-spin resonance spectroscopy with 65 spins/$\sqrt{\text{Hz}}$ sensitivity. *Applied Physics Letters*, 111:202604, 2017.

[2] A. Ardavan, O. Rival, J. J. L. Morton, S. J. Blundell, A. M. Tyryshkin, G. A. Timco, and R. E. P. Winpenny. Will Spin-Relaxation Times in Molecular Magnets Permit Quantum Information Processing? *Physical Review Letters*, 98:057201, 2007.

[3] C. J. Wedge, G. A. Timco, E. T. Spielberg, R. E. George, F. Tuna, S. Rigby, E. J. L. McInnes, R. E. P. Winpenny, S. J. Blundell, and A. Ardavan. Chemical Engineering of Molecular Qubits. *Physical Review Letters*, 108:107204, 2012.

[4] K. Bader, D. Dengler, S. Lenz, B. Endeward, S.-D. Jiang, P. Neugebauer, and J. van Slageren. Room temperature quantum coherence in a potential molecular qubit. *Nature Communications*, 5:5304, 2014.

[5] C.-J. Yu, M. J. Graham, J. M. Zadrozny, J. Niklas, M. D. Krzyaniak, M. R. Wasielewski, O. G. Poluektov, and D. E. Freedman. Long Coherence Times in Nuclear Spin-Free Vanadyl Qubits. *Journal of the American Chemical Society*, 138:14678–14685, 2016.

[6] J. M. Zadrozny, J. Niklas, O. G. Poluektov, and D. E. Freedman. Milisecond coherence time in a tunable molecular electronic spin qubit. *ACS Central Science*, 1:488–492, 2015.

8
Conclusiones

Aunque el desarrollo de procesadores cuánticos basado en qubits superconductores ha mostrado un impresionante progreso a lo largo de los últimos años, aun no se ha podido alcanzar la potencia de computación necesaria para resolver problemas de especial relevancia. Además, escalar estos sistemas y, especialmente, tratar con sus errores inherentes, es todavía muy complejo. Es posible que la combinación de diferentes sistemas en uno solo permita diseñar una arquitectura de computación cuántica mejor que las actuales. Por lo tanto, el estudio de sistemas de qubits distintos que puedan ayudar en determinados aspectos se vuelve muy útil.

En este trabajo de tesis, hemos estudiado la posibilidad de combinar sistemas basados en electrodinámica cuántica de circuitos e imanes moleculares. Los espines moleculares son una alternativa interesante a los qubits superconductores debido a su sintonizabilidad química y al hecho de que dos moléculas del mismo compuesto son idénticas. Sin embargo, para emplear estos sistemas en un procesador cuántico debemos alcanzar el régimen de acoplo fuerte con una única molécula. Por esta razón, durante el presente trabajo hemos estudiado experimentalmente diversos métodos para alcanzar este objetivo.

En concreto, nos hemos centrado en varias formas de mejorar el acoplo espín-fotón entre sistemas moleculares y circuitos superconductores, como un primer paso hacia la fabricación de un procesador cuántico basado en la combinación de ambos sistemas. A continuación haremos un resumen de las conclusiones principales que hemos alcanzado en este trabajo.

En primer lugar, hemos mostrado que la fabricación de una nanoconstricción de 40 nm de ancho en la línea central de un resonador coplanar de 14 μm de ancho aumenta el acoplo individual espín-fotón en un factor 60, alcanzando valores en torno a 180 Hz. Este acoplo puede ser incluso mayor, del orden de kHz, si la distancia entre las muestras moleculares y los circuitos superconductores se acerca a cero, debido al decaimiento con la distancia del campo magnético de microondas generado por la nanoconstricción. Este enfoque se ha introducido en un nuevo tipo de resonador, que hemos llamado resonador 2.5D, con el cual se han alcanzado acoplos individuales espín-fotón mayores de 3 kHz empleando una nanoconstricción de 50 nm de ancho. Este resonador está formado por un circuito LC con una inductancia muy pequeña introducido en una cavidad 3D. Esta inductancia pequeña produce un campo magnetico local de microondas mayor que el de los resonadores coplanares, demostrando que la combinación de nanoconstricciones con resonadores de baja inductancia es una vía prometedora para alcanzar valores elevados de acoplo individual espín-fotón.

Otra forma de alcanzar el régimen de acoplo fuerte consiste en emplear moléculas de elevada coherencia. Este es el caso de la molécula PTM_r, un radical libre que muestra valores de T_2 de decenas de μs a muy baja temperatura. Hemos estudiado el acoplo entre estas moléculas y resonadores de parámetros concentrados (LERs), un tipo de resonador LC formado por un condensador en paralelo con un inductor, y acoplado a una línea de transmisión. Se han observado acoplos individuales espín-fotón de hasta 5,7 Hz al usar LERs con inductancia elevada, mientras que se han alcanzado valores de 1 kHz al depositar las muestras en LERs con inductancias muy pequeñas y una nanoconstricción. Ha sido incluso posible alcanzar valores de acoplo individual espín-fotón cercanos a 24 kHz con estos LERs conbaja impedancia y nanoconstricciones, siendo este acoplo mayor que los 16 kHz necesarios para alcanzar el régimen de acoplo fuerte con una única molécula considerando un valor de T_2 de 10 μs a muy baja temperatura. Estas muestras han

mostrado una anchura de espín de hasta 35 MHz en lugar de los 7 MHz observados en medidas previas de EPR. Esto parece estar motivado por la formación de agregados de PTM_r, junto con un acoplo hiperfino entre espines cercanos y otras fuentes de ensanchamiento inhomogéneo. Sin embargo, reduciendo la concentración de espines se podría aumentar la coherencia hasta los 7 MHz, siendo este sistema un buen candidato a qubit si el acoplo individual espín-fotón se consigue mejorar.

Los resultados anteriores representan un récord en el acoplo individual espín-fotón, siendo su acoplo adimensional G_1/ω_r asociado mayor que el máximo reportado en la literatura.[1] Estos resultados están resumidos en la Fig. 8.1

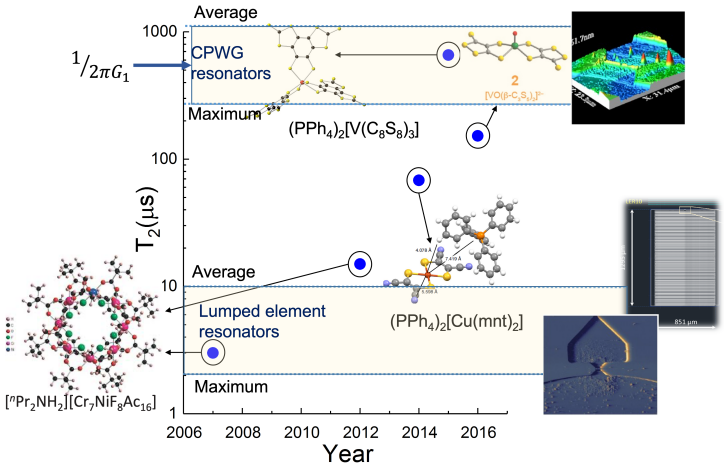

Figura 8.1: Comparación entre los valores promedio y máximos de $G_1/2\pi$ estimados en este trabajo para cada tipo de resonador, y T_2 de los mejores qubits moleculares. Estos qubits son $[^nPr_2NH_2]\,[Cr_7NiF_8Ac_{16}]$,[2;3] $(PPh_4)_2\,[Cu\,(mnt)_2]$,[4] $[VO\,(\beta - C_3S_5)_2]^{2-}$,[5] y $(PPh_4)_2\,[V\,(C_8S_8)_3]$.[6]

El efecto de las transiciones de reloj de espín en el acoplo espín-fotón también se ha estudiado. En el capítulo 6 hemos introducido dos moléculas distintas que presentan estas transiciones: HoW_{10} y $\mathbf{1^{VO}}$. En el caso del HoW_{10}, su elevada anisotropía uniaxial y la presencia de términos de anisotropía transversal de cuarto orden generan un gap cuántico de túnel de 9,1 GHz entre las superposiciones simétricas y antisimétricas de los estados de espín electrónico $m_J = \pm 4$. En esta molécula tienen lugar cuatro transiciones de reloj de espín diferentes debido a su espín nuclear $\mathbf{I} = 7/2$, siendo la posición de estos anticruzamientos sensible únicamente al campo magnético aplicado paralelo a eje de anisotropía molecular. Mediante medidas de espectroscopía de banda ancha realizadas a distintas temperaturas, hemos observado que el acoplo espín-fotón se vuelve máximo en estas transiciones de reloj debido al solapamiento máximo entre los estados de espín. Esta mejora del acoplo viene acompañada por un mínimo de la decoherencia. Estos resultados muestran que la ingeniería de los estados del qubit puede proporcionar un método prometedor para optimizar a la vez la coherencia de espín y el acoplo a circuitos, algo que suele ser incompatible. También es una forma útil de alcanzar acoplo coherente en la molécula HoW_{10} incluso en condiciones no óptimas. De todas formas, la naturaleza de estas transiciones de reloj de espín (tienen lugar entre estados excitados), así como la armonicidad de las transiciones restantes, hacen que esta molécula presente algunos problemas al optar a candidata a qubit.

Respecto a la molécula $\mathbf{1^{VO}}$, se ha observado que el entrelazamiento de los espines electrónico y nuclear introduce una anarmonicidad suficientemente elevada a bajo campo. Además, el acoplo hiperfino también aumenta las frecuencias de Rabi entre los estados de espín nuclear, hasta valores comparables a los de las transiciones electrónicas. Estos dos hechos nos permite realizar operaciones cuánticas universales con esta molécula, que puede verse como un procesador de

4 qubits o un qudit con $d = 16$. Qudits moleculares como este permitirían la integración de la corrección de errores cuántica incluso a nivel molecular, siendo posible corregir cambios de un qubit o de su fase con el código de repetición más simple. Finalmente, hemos alcanzado el acoplo fuerte a transiciones de reloj de espín que aparecen en esta molécula a campos bajos, incluso usando sistemas concentrados. Este es un ingrediente clave en la aplicación de técnicas de electrodinámica cuántica de circuitos para leer estados electronucleares de espín.

En resumen, nos hemos acercado al régimen de acoplo fuerte con una única molécula mediante la modificación de los circuitos superconductores o las moléculas, alcanzando valores mayores que los mostrados en la literatura. Aunque los resultados presentados en esta tesis son prometedores, aun se necesitan avances para fabricar un procesador cuántico molecular como el mostrado en la introducción. Actualmente estamos intentando aumentar el campo magnético de microondas generado por los resonadores coplanares combinándolos con materiales 2D. El confinamiento de los fotones en una estructura bidimensional podría producir una mejora significativa de la intensidad del campo magnético de microondas. También se están estudiando sistemas con transiciones de reloj de espín con mejores propiedades que los mostrados aquí. Aun se necesita más trabajo para obtener la mejor combinación de resonadores superconductores y muestras moleculares, siendo el objetivo de fabricar un procesador cuántico molecular alcanzable en un futuro próximo.

Bibliografía

[1] S. Probst, A. Bienfait, Campagne-Ibarcq P., J. J. Pla, B. Albanese, J. F. Da Silva Barbosa, T. Schenkel, D. Vion, D. Esteve, K. Mølmer, J. J. L. Morton, R. Heeres, and P. Bertet. Inductive-detection electron-spin resonance spectroscopy with 65 spins/$\sqrt{\text{Hz}}$ sensitivity. *Applied Physics Letters*, 111:202604, 2017.

[2] A. Ardavan, O. Rival, J. J. L. Morton, S. J. Blundell, A. M. Tyryshkin, G. A. Timco, and R. E. P. Winpenny. Will Spin-Relaxation Times in Molecular Magnets Permit Quantum Information Processing? *Physical Review Letters*, 98:057201, 2007.

[3] C. J. Wedge, G. A. Timco, E. T. Spielberg, R. E. George, F. Tuna, S. Rigby, E. J. L. McInnes, R. E. P. Winpenny, S. J. Blundell, and A. Ardavan. Chemical Engineering of Molecular Qubits. *Physical Review Letters*, 108:107204, 2012.

[4] K. Bader, D. Dengler, S. Lenz, B. Endeward, S.-D. Jiang, P. Neugebauer, and J. van Slageren. Room temperature quantum coherence in a potential molecular qubit. *Nature Communications*, 5:5304, 2014.

[5] C.-J. Yu, M. J. Graham, J. M. Zadrozny, J. Niklas, M. D. Krzyaniak, M. R. Wasielewski, O. G. Poluektov, and D. E. Freedman. Long Coherence Times in Nuclear Spin-Free Vanadyl Qubits. *Journal of the American Chemical Society*, 138:14678–14685, 2016.

[6] J. M. Zadrozny, J. Niklas, O. G. Poluektov, and D. E. Freedman. Milisecond coherence time in a tunable molecular electronic spin qubit. *ACS Central Science*, 1:488–492, 2015.

List of Publications

[1] A. Urtizberea, E. Natividad, P. J. Alonso, L. Pérez-Martínez, M. A. Andrés, I. Gascón, I. Gimeno, F. Luis, and O. Roubeau. Vanadyl spin qubit 2D arrays and their integration on superconducting resonators. *Materials Horizons*, 7:885–897, 2020.

[2] I. Gimeno, W. Kersten, M. C. Pallarés, P. Hermosilla, M. J. Martínez-Pérez, M. D. Jenkins, A. Angerer, C. Sánchez-Azqueta, D. Zueco, J. Majer, A. Lostao, and F. Luis. Enhanced Molecular Spin-Photon Coupling at Superconducting Nanoconstrictions. *ACS Nano*, 14:8707–8715, 2020.

[3] I. Gimeno, A. Urtizberea, J. Román-Roche, D. Zueco, A. Camón, P. J. Alonso, O. Roubeau, and F. Luis. Broad-band spectroscopy of a vanadyl porphyrin: a model electronuclear spin qudit. *Chemical Science*, 12:5621–5630, 2021.

[4] I. Gimeno, V. Rollano, D. Zueco, Y. Duan, C. Sánchez-Azqueta, T. Astner, A. Gaita-Ariño, S. Hill, J. Majer, E. Coronado, and F. Luis. Coupling spin "clock states" to superconducting circuits. *arXiv*, 2019.

[5] S. Martínez-Losa del Rincón, I. Gimeno, J. Pérez-Bailón, V. Rollano, F. Luis, D. Zueco, and M. J. Martínez-Perez. Measuring the magnon-photon coupling in shaped ferromagnets: tuning of the resonance frequency. *Physical Review Applied (Accepted)*, 2022.